Development of a computationally efficient monolith reactor simulator: CFD-Hybrid model analysis of methane oxidation monolith catalysed systems

Mopeli Khama

Thesis presented for the degree of

DOCTOR OF PHILOSOPHY IN CHEMICAL ENGINEERING

Under the supervision of:
Assoc. Prof. Randhir Rawatlal

In the department of Chemical Engineering

UNIVERSITY OF KWAZULU NATAL

Plagiarism declaration

I hereby undertake that I know the meaning of plagiarism and I declare that all the work that is not mine is properly acknowledged in this document.

_____

Signature

_____

Date

Abstract

The optimisation of complex geometries such as that of monolith reactors can be supported by computation and simulation. However, complex boundaries such as those found in multi-channel monoliths render such simulations of extremely high computational expense. Adding to the computational expense is the strong coupling among reaction kinetics, heat and mass transfer limitations in these channels. This severely limits the possibilities for geometric optimisation.

In the first step toward developing a fast-solving hybrid simulation, a detailed CFD simulation was used to obtain the unsteady state, spatial temperature and concentration (and hence reaction rate) profiles for a range of input conditions. The results of the CFD simulation were then accepted as the benchmark to which faster-solving models were measured against to be considered as viable descriptions. A modified plug flow with effectiveness factor correction for wall mass-transfer was developed and evaluated as the first step towards the development of a multi-channel model.

However, the modified plug model is only applicable to single channel monoliths and cannot account for heat transfer across high-density multi-channel beds. For multichannel simulations, the modified plug flow model is embedded into a hybrid-model framework. The hybrid model is based on the principle that, due to the high density of channels in a monolith, there will exist an equivalent homogeneous cylindrical model that approximates the behaviour of a bundle of channels acting as axial heat sources. This model entails the coupling of analytical solutions to single channel mass and momentum transfer with heat transfer across the single-shell extra-multi-channel space. Due to the application of effectiveness-factor type approaches, it is shown that the model can be represented by algebraic models that accurately represent the partial differential equations (PDEs) that describe monolith reactors.

A close agreement between both temperature and species mole fraction profiles predicted from the modified plug flow model and a detailed CFD model was found with R^2 values of 0.994 for temperature. The time needed to find a converged solution for plug flow model on a*n* Intel(R) Core(TM) i5-5300U CPU @ 2.30GHz workstation was found to be 53 seconds in comparison to 1.3 hours taken by a CFD model. The hybrid

model was itself validated against the CFD multichannel model. The hybrid model axial temperature and species concentration profiles at various radial positions were found to be in a close agreement with CFD simulations, with relative error found to be in the 0.35 % range. The clock time on an Intel(R) Core(TM) i5-5300U CPU @ 2.30GHz workstation was found to be 38 hours for a CFD multi-channel simulation which when compared with the 53 seconds clock time of the hybrid model implies the suitability of hybridisation for the application to geometric optimisation in the design of monolith reactors.

The hybrid-model is developed to facilitate geometric optimization with the view of reducing hot spot formation, pressure drop and manufacturing costs. This is because monolith reactors applied in catalytic partial oxidation of methane are coated with precious metal catalysts, significantly contributing to capital costs. By isolating regions of high catalytic activity, it becomes possible to reduce the amount of precious metal coating required to achieve high conversion.

The fast-solving hybrid model was used in the economic analysis of the catalytic partial oxidation of methane to syngas. Due to the low computational expense of the hybrid model, it was possible to investigate a wide range of design geometry and operating condition .It is shown that, for methane oxidation over a Platinum gauze catalyst, the channel diameter could be optimised to the 0.8 mm level resulting in the highest syngas revenue (R 65754.14 /day). The distribution of the catalytic material on the monolithic walls was found to influence the reactor performance hence the process profitability. The non-uniform distribution was found to significantly reduce the cost of fabrication while maintaining a high syngas productivity. In general, a method is proposed to optimise design and operation of catalytic monolith reactors through the application of fast-solving models.

Key words: Hybrid model, catalytic partial oxidation, modified plug flow model, CFD

Acknowledgements

I would like to give thanks and honour to the Lord almighty for His love, care and mercy that sustained me throughout the duration of my studies.

I'm grateful to thank my supervisor Prof. Randhir Rawatlal for his guidance and support in my studies. I couldn't have completed my studies without your encouragement and the skills you imparted in me, for this I will forever be grateful. To my industrial supervisor Dr Glenn Jones, I really appreacite your input into my work and I want to express my gratitude for your insightful contribution.

Dr Tiziano Maffei, thanks for helping me with catalyticFOAM. Your sacrifice has left a permant imprint my heart. I would like to thank Dr Andrew Gill for encouraging me to attend CHPC winter school and conference and for some fruitful discussions that helped me to understand OpenFOAM.

To my wife 'Mateboho Ntsoaki Khama, you have always been a pillar of strength and the reason for my persistence. My gratitute to you is indescrebable. I'm thankful to my family, ntate Bothata, 'me 'Mamoliehi, ntate Khuto, 'me 'Mantsoaki, Moliehi, Kaliana,Moseli ,Pulane, Letsoara ,Ponts'o and my small boy Eddie.

I'm thankful to the data science and modelling group (Philani, Leandra, Joash, Sameera, Christine and Trisha). The weekly seminars and academic discussions we had kept me going and encourgared me to complete this project. To Philani Biyela, I would like to thank you in a special way for your kindness and always willing assist when need arouse.

My friends have always been there for me and I would like to thank them for such an important role. Kea leboha banna ba heso, Dr Matsutsu, Qotherlo, Lekhobola, Motjemoka, Molaoa, Marasi, Armstrong, Macheli, Leponesa, Mohloki and Karabo.

I would like to thank Johnson Matthey for financial support.

Table of Contents

List of Tables

List of Figures

Chapter 1. Introduction

The Catalytic Partial Oxidation of Methane (CPOM) to syngas has received substantial attention over the past years in part due to the depletion of crude oil (Aschroft et al., 1991; Balachandran et al., 1995; Chisti, 2007). In addition, the partial oxidation of methane provides the cleanest alternative to other fossil fuels and this is ascribed to low ratio of carbon/hydrogen in natural gas which results in significant reduction of carbon dioxide emissions (Corbo and Migliardini, 2007). Given that large reservoirs of natural gas exist, of which methane constitutes a large percentage, the partial oxidation thereof poses an attractive and alternative source of energy to other fossil fuels (Cimino et al., 2012; Pino et al.,2002). Owing to rigorous environmental regulations and potentially increasing carbon taxes, catalytic partial oxidation of methane is an economically attractive process.

The conversion of methane into syngas on noble metal catalysts is mainly by thermochemical techniques for example; steam reforming, partial oxidation and auto-thermal reforming (Rezaei et al., 2011; Meng et al., 2010; Feio et al., 2008). Steam reforming reaction presents an advantage in that it gives high yield of hydrogen; however, this is offset by the endothermic nature of the reaction which results in high capital and production costs as external heating is required. The partial oxidation of methane results in lower H_2/CO ratio and can be started quickly as it requires short contact/ residence time. Since the partial oxidation is exothermic this might necessitate external cooling. On the other hand, auto-thermal reforming being a combination of steam reforming and partial oxidation has been proved to be a more economical approach (Mosayebi et al., 2012). These can be explained by the sufficient heat produced from the exothermic partial oxidation which can then be used in the endothermic steam reforming without requiring any external heating.

1.1. Basic chemistry

The mechanism for methane conversion to syngas is reported to happen in two steps (Korup et al., 2013); first the complete oxidation of methane as demonstrated by Equation 1.3 takes place followed by the endothermic methane reforming reactions (Equation 1.1 and Equation 1.4). It has been reported in some other studies that methane dry reforming as represented by Equation 1.4 does not take place while some

studies report dry reforming to take place (Fan et al., 2010). The methane dry reforming presents many advantages as mentioned, however the commercialisation of the process still poses some significant challenges. This is attributed to the high catalyst deactivation which is caused by carbon deposits on the catalyst active sites. The formation of carbon deposits that block the active sites is extenuated by the use of supported metal catalysts.

$$CH_4 + H_2O \rightarrow 3H_2 + CO \qquad \Delta_rH= +206 \quad kJmol^{-1} \qquad (1.1)$$

$$CH_4 + \frac{1}{2}O_2 \rightarrow 2H_2 + CO \qquad \Delta_rH= -36 \quad kJmol^{-1} \qquad (1.2)$$

$$CH_4 + 2O_2 \rightarrow 2H_2O + CO_2 \qquad \Delta_rH= -803 \quad kJmol^{-1} \qquad (1.3)$$

$$CH_4 + CO_2 \rightarrow 2CO + 2H_2 \qquad \Delta_rH= +247 \quad kJmol^{-1} \qquad (1.4)$$
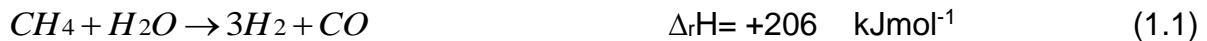
The production of syngas from methane on an industrial level is mainly by steam reforming. The catalytic partial oxidation of methane has not replaced steam reforming on an industrial level due to slow technological progress of the process. The challenges posed by catalytic partial oxidation of methane are the complex interplay of partial and total oxidation which normally results in the low yield of syngas (Neumann and Veser, 2005). The total oxidation of methane can be inhibited by dynamic heat integration and temperature control.

The formation of local hot spot which leads to irreversible catalyst deactivation also contributes to some factors that limit the industrial application for conversion of methane to syngas by catalytic partial oxidation. There have been some attempts to limit the formation of local hot spot, and these include the design of a catalyst with good thermal conductivity to allow for the distribution of the excess heat through the catalyst bed. Given that steam reforming is more endothermic, steam addition to partial oxidation of methane can help stabilise the temperature profile through the catalyst bed (Hegarty et al., 1998)

Carbon dioxide is normally added in the reactor feed to allow for parallel running of the endothermic dry reforming with the exothermic partial oxidation. The addition of carbon dioxide in the reactor feed changes the hydrogen/carbon ratio and depending on the downstream syngas application this might be undesirable. Thus, for the partial

oxidation of methane to replace steam reforming, significant work is needed to address the described challenges.

1.2. Catalyst Design

In the design of a catalyst, the following criteria need to be met for better reactor performance for the catalyst of interest (Liu, 2007).

- Low pressure drop
- High rates of internal mass transfer from the bulk gas phase to the catalyst surface, and high rates of mass transfer from the catalyst surface to the interior of the catalyst.
- High metal loading per reactor volume
- Chemical and mechanical stability

The metal particle size plays a major role in the intrinsic activity of a catalyst. The smaller the size of the particle, the higher the activity. In addition, a smaller particle size limits the formation of coke; hence the catalyst deactivation by the blockage of active sites by carbon deposits can be obviated to a certain degree by an optimum particle size. The optimization of catalyst particle size should be coupled with a strategy to avoid metal encapsulation as this leads to a catalyst with decreased activity (Gannouni et al., 2013). However, there are some challenges that need to be addressed with regards to smaller particle size as they lead to increased pressure drop which is undesirable. The pressure drop at smaller particle size and high surface to volume ratio is extenuated by the use of monolith reactors (Neumann and Veser, 2005). The lower pressure drop in such systems is ascribed to their high porosity.

1.3. Monolith reactors

A representation of a gas flow through a single channel in a monolith reactor is shown in Figure 1 where the gas follows through a single channel and the reactions happen upon the surface of the walls impregnated with a catalytic material.
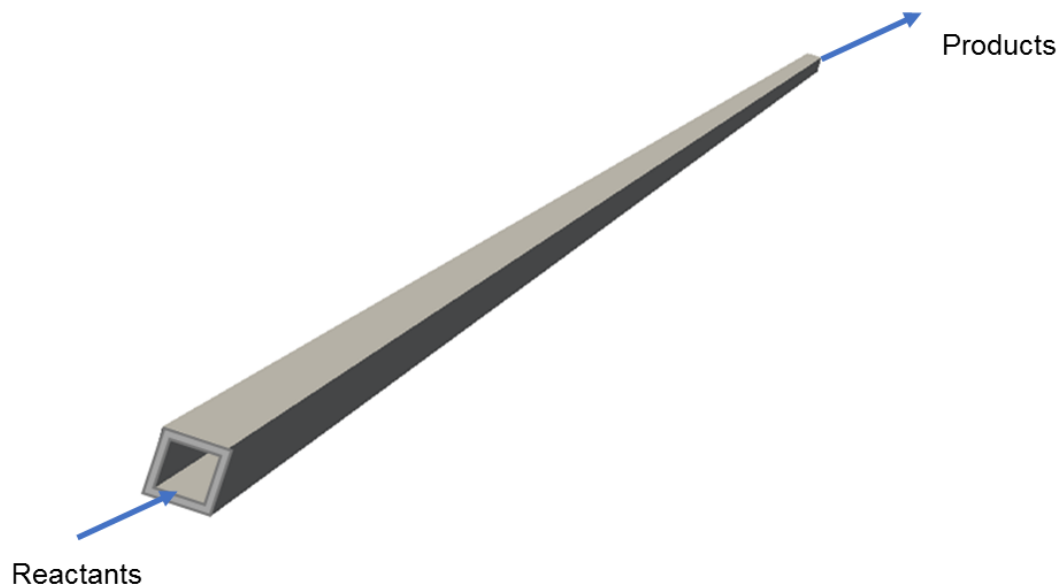
Figure 1: A schematic of a gas flow through a single channel in a monolith reactor

To maintain high conversions of methane to syngas, the processes are usually carried out at high temperatures with the associated high capital and operating costs. These costs can to some extend be mitigated by the use of catalysts, although this results in other challenges such as catalyst poisoning and coking. Even so, these processes remain extremely energy expensive (Larentis et al., 2001; Rafiq, Jakobsen and Hustad, 2012; Arutyunov and Krylov, 2007). It is therefore desirable to optimize the catalytic solution in particular with respect to the geometry of the catalyst support in the reactor. To facilitate geometric optimization, simulations predicting conversion, yield and selectivity in three dimensions are required. It is possible to carry out these simulations using CFD, however, the complete set of Navier-Stokes equations must be simulated over relatively complex geometries and kinetics. Such simulations pose a high computational expense and optimisation algorithms would benefit from use of a quick solving model.

The reaction kinetics in partial oxidation of methane is complicated by the short residence times (reaction happening in milliseconds) and this leads to a possibility of mass transfer limitations. The partial oxidation of methane is exothermic and this can result in severe heat transfer limitations which can result in high temperatures at the catalyst bed (de Smet et al., 2000). The above mentioned conditions render the determination of reaction kinetics in partial oxidation of methane a not straightforward process. Many studies have been dedicated to the determination of reaction kinetics

in methane partial oxidation, and this ranges from using different reactor configurations, taking heat and mass transport limitation into account (Hickman and Schmidt, 1992; Witt and Schmidt, 1996; Srinivasan et al., 1997; Khan and Somorjai, 1985; Quiceno et al., 2006). The study of reaction kinetics that incorporates all the relevant physical and chemical phenomena is required for the accurate determination of intrinsic kinetics as this will aid in the optimization process.

1.4. Design of monolith reactors

Given the challenges and advantages that catalytic partial oxidation presents, it is desirable to carry out research with the view of reducing hot spot and increasing yield and selectivity. The analysis, optimization and design of catalytic partial oxidation requires a rigorous coupling of transport and chemistry. The reactions take place in the reactor walls which are impregnated with the catalytic material. A schematic of a monolith reactor is represented in Figure 2. The catalytic walls might be active enough to effect the desired reaction and conversion, however, the rate of transport of species from the bulk gas phase to the active sites influences the reaction concentration. Computational Fluid Dynamics can be used to determine the local concentration and temperature. Due to the relatively high geometric complexity, large time and length scales, the computational expense involved is significant.

The challenge in developing such a solver emanates from a need to have it include all the described phenomena. A rigorous reactor model must make use of reliable kinetic models. However, the kinetics in this process are complicated by several factors which comprise the distribution of active material on the support, the interaction of the active material with the support, and the complexity of chemisorption (Elnashaie and Elshishini, 1993). In addition, a monolith constitutes many thousands of channels (Figure 2) and the thermal transfer is complicated by the interplay between convective transfer within a channel and the radial transfer among multiple neighbouring channels. The lateral and axial heat transfer in a monolith is represented in Figure 3.

Over the years there has been work done in developing computationally efficient models for the reactive heterogeneous catalytic systems (Hayes et al.,2004; Jahn et al.,1997; Deutschmann et al.,2001). The computationally efficient models expedite the optimization and design processes that can ultimately lead to improved performance of catalytic partial oxidation process.
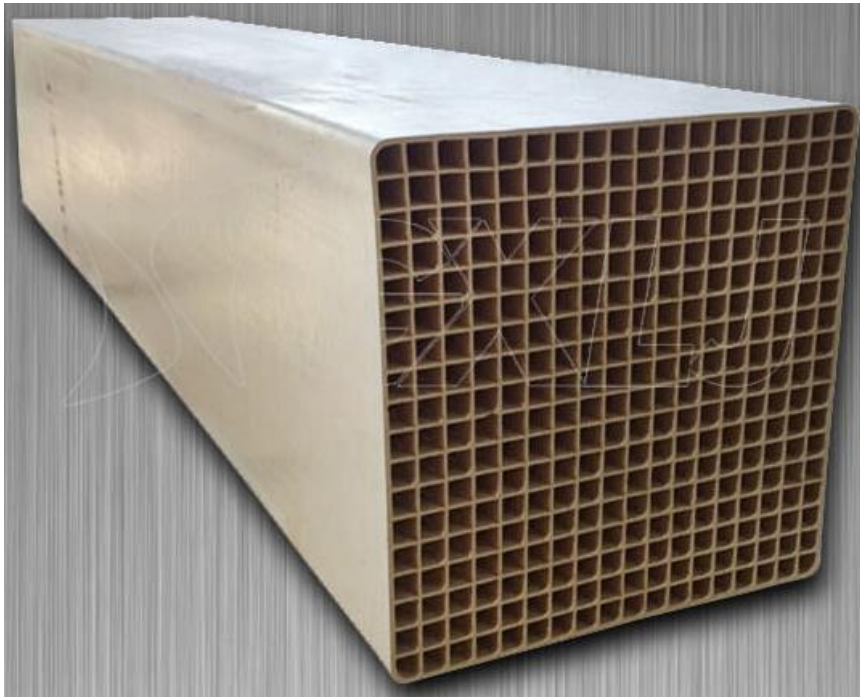
Figure 2: A schematic of a monolith reactor (GXLJ, 2014)

Lateral heat transfer

Axial heat transfer
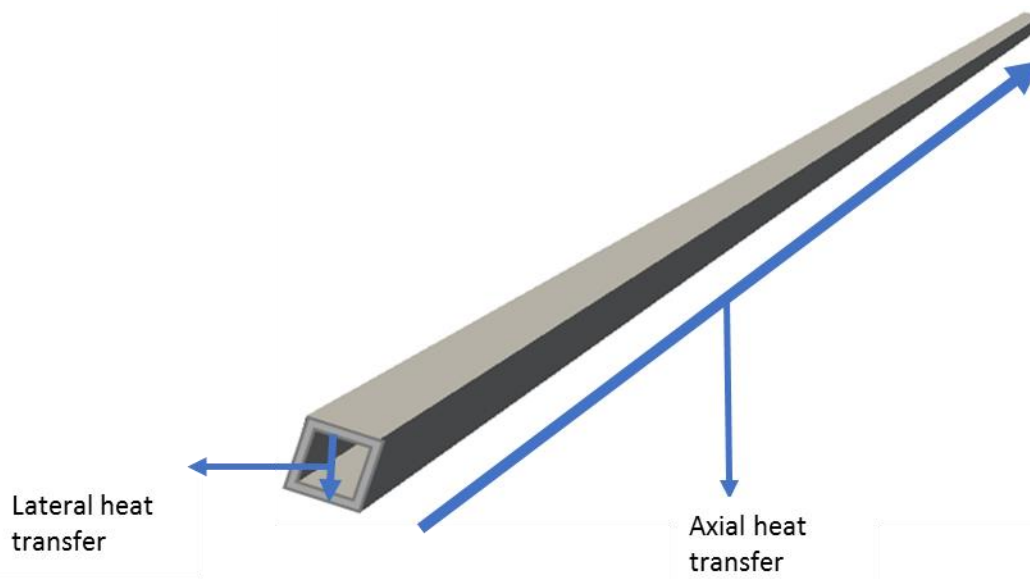
Figure 3: Lateral and axial heat transfer in a monolith

1.5. Simulating monolith reactors

The numerical models should also have the capacity to investigate the reactor configuration as it plays a significant role in the distribution of state variables (temperature and concentration) in partial oxidation of methane. The consumption of oxygen is fully eternal mass transfer limited (Maffei et al., 2014) , as such, the diffusion

path length results in local variations in the distribution of temperature and species mole fraction. The reason for the mentioned observation is that, for catalytic partial oxidation of methane reactions, oxygen is fully consumed within the first few millimetres of the catalytic bed, and given its consumption is dictated by mass transfer regime, a different geometry will lead to a different flow structure (Maestri et al., 2009).

The development of reactor models that will realize the local variations is desirable and this stems from a realization that; the local distribution of temperature varies significantly with different reactor geometries. As a result, given the marked influence temperature has on the stability of a catalyst, it is desirable to predict its distribution from the reactor inlet to the outlet.

1.6. Summary

The catalytic partial oxidation of methane presents many advantages in addressing the environmental regulations and promises to be an answer to global energy demands. By leveraging large existing reservoirs of natural gas and methane it may be possible to significantly reduce the impact of extracting and refining longer chain hydrocarbons. However, there are some significant challenges that need to be addressed in both the design of a catalyst and a reactor. The modelling of this process needs to couple the transport phenomena with reaction kinetics to capture the full dynamic features of the process and thus optimize the process to meet the large-scale industrial requirement and replace the conventional steam reforming.

Chapter 2. Literature Review

2.1.Reaction kinetics

In the study of reactive systems, the study of reaction kinetics is an important first step. The study of chemical kinetics is twofold; the first part entails the determination of reaction mechanisms that gives rise to the overall reaction and the second part deals with the determination of the reaction rate. According to Kee et al. (2003)**,** the reactions that take place in chemically reacting flows can be categorized according to levels of complexity as follows:infinitely fast reactions, global reactions, analytically reduced reactions mechanisms and the detailed reaction mechanisms. The infinitely fast reactions and chemical equilibrium are classified as fast chemistry (not kinetically controlled), while global reactions, analytically reduced reaction mechanisms and detailed reaction mechanisms are classified as finite rate chemistry and kinetically controlled (Kee et al., 2003).

Over the past decades, there has been an intensive study on reaction kinetics of catalytic partial oxidation of methane. de Smet et al. (2000) developed a kinetic model for the catalytic partial oxidation of methane over Pt metal gauze in the presence of transport phenomena. Unlike in some cases where the heat resistance is not considered since only the gas-phase temperature is measured, in their study, heat transfer resistance was taken into account by the measurement of temperature for both the gas phase and the catalyst. The kinetic model under consideration constitutes six reaction steps which takes the methane adsorption to be oxygen assisted. The intrinsic kinetic parameters were determined from the experimental data and the reactor model. They found that the kinetics of surface reactions have a significant influence on CO selectivity, while the conversion of both methane and oxygen was found to be dictated by mass transport. The oxygen assisted adsorption was shown to be in close agreement with experimental results. The catalytic partial oxidation of methane (POM) mechanism is as shown in Table 1.

The first step in the reaction mechanism (Table 1) is oxygen dissociative adsorption. These authors consider oxygen adsorption as competitive. However, there are some cases where oxygen adsorption is considered as non-competitive (Hickman and

Schmidt, 1993). In the latter case, oxygen is assumed to adsorb on specific catalytic sites. The second step is methane dissociative adsorption which results in gaseous water and carbon species. Methane desorption is oxygen-assisted as observed in reaction 2. According to de Smet et al. (2000), reaction 2 proceeds through intermediates such as adsorbed CH_x (where x=1, 2 and 3) and adsorbed OH species. The formation of adsorbed CO species is described in reaction 3 and the adsorbed CO from this step is converted to CO_2 in step 4. Steps 5 and 6 describe the desorption and adsorption of CO.

Table 1: The reaction mechanism and their respective rate equations and kinetic data for partial oxidation of methane (de Smet et al., 2000)

No	Reaction	Rate equation	A.c.q.s$_0$[§]	E$_{act}$	Reference
1	$O_{2,g} + 2* \rightarrow 2O*$	$r_1 = k_1 p_{O_2}{}^2 \theta_*{}^2$	0.023	0	(Elg et al., 1997)
2	$CH_{4,g} + 2O* \rightarrow C* + 2H2O_g + *$	$r_2 = k_2 p_{CH_4} \theta_O{}^2$	$2.39.10^5$	48.2	(de Smet et al., 2000)
3	$C* + O* \rightarrow CO* + *$	$r_3 = k_3 \theta_c \theta_O$	1.10^{13}	62.8	(Hickman and Schmidt, 1993)
4	$CO* + O* \rightarrow CO_{2,g} + *$	$r_4 = k_4 \theta_{co} \theta_o$	1.10^{13}	100	(Campbell et al., 1980)
5	$CO* \rightarrow CO_g + *$	$r_5 = k_5 \theta_{co}$	1.10^{13}	126	(McCabe and Schmidt, 1977)
6	$CO_g + * \rightarrow CO*$	$r_6 = k_6 p_{CO} \theta_*$	0.84	0	(Campbell et al., 1981)

In Table 1, A.c.q.s$_0$[§] represents the rate coefficient for the elementary reaction. Where A is the pre-exponential factor and S$_0$ is the initial sticking coefficient. The steady state mass balance for the surface species as per kinetic model depicted in Table 1 was

done as shown from equations 2.1 to 2.4.

C-balance: $k_2 p_{CH4} \theta_O{}^2 - k_3 \theta_C \theta_O = 0$ $\hspace{3cm}$ (2.1)

CO- balance: $k_3 \theta_C \theta_O - k_4 \theta_{CO} \theta_O - k_5 \theta_{CO} + k_6 p_{CO} \theta_* = 0$ $\hspace{1.5cm}$ (2.2)

O-balance: $2 k_1 p_{O2} \theta_*^2 - 2 k_2 p_{CH4} \theta_O^2 - k_3 \theta_C \theta_O - k_4 \theta_{CO} \theta_O = 0$ $\hspace{1cm}$ (2.3)

Vacant sites: $\theta_* + \theta_{CO} + \theta_O + \theta_C = 1$ $\hspace{2.5cm}$ (2.4)

A kinetic study to derive the kinetic rate equations and parameters was undertaken by Soick et al. (1996). In their work, the reaction mechanism for partial oxidation of methane to syngas was described to happen in four steps, namely; methane dissociation, CO_2 adsorption, CO adsorption and oxidation. The steps are represented in Equations 2.5, 2.11a, 2.11b and 2.10a. The reaction mechanism for their study is shown in Equations (2.5) to (2.11). These researchers modelled the temporal analysis of products (TAP) reactor to determine the adsorption enthalpies, rate constants and activation energies for the surface reaction steps presented in Equations (2.5) to (2.11).

Methane activation

a) $CH_{4(g)} + {}^* \rightarrow CH_x{}^* + (4\text{-}x)H^*$

b) $(x= 1, 2, 3)$ $CH_x{}^* \rightarrow C^* + xH^*$ $\hspace{3cm}$ (2.5)

Total oxidation

a) $CH_x{}^* + (x/2+2)O^* \rightarrow CO_2{}^* + (x/2)H_2O^*$

b) $2H^* + O^* \rightarrow H_2O^*$

c) $H^* + 2O^* \rightarrow 2OH^*$ $\hspace{3cm}$ (2.6)
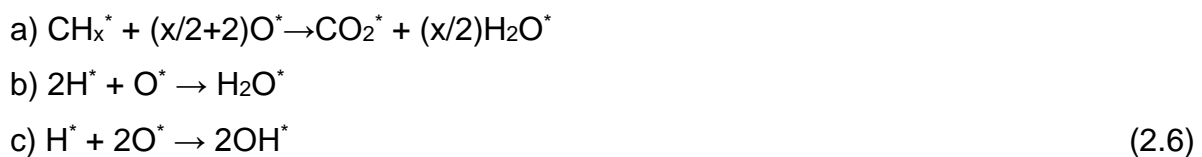
Reserved Boudouard reactions

$CH_x{}^* + CO_2{}^* \leftrightarrow 2CO^* + xH^*$ $\hspace{3cm}$ (2.7

Reforming
a) $CH_x{}^* + H_2O^* \leftrightarrow CO^* + (x+2)H^*$

b) $CH_x{}^* + OH^* \leftrightarrow CO^* + (x+1)H^*$

$\hspace{12cm}$ (2.8)

Surface re-oxidation

$O_{2(g)} + 2^* \rightarrow 2O^*$
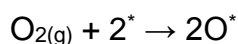
Consecutive oxidation

a) $CO^* + O^* \rightarrow CO_2^*$

b) $2H^* + O^* \rightarrow H_2O^*$
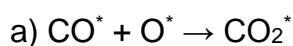
(2.10)

Adsorption equilibria

a) $CO_{2(g)} + {}^* \leftrightarrow CO_2^*$

b) $CO_{(g)} + {}^* \leftrightarrow CO^*$

c) $H_{2(g)} + {}^* \leftrightarrow H_2^*$
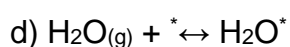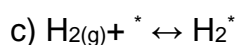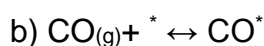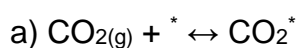
d) $H_2O_{(g)} + {}^* \leftrightarrow H_2O^*$ (2.11)

Quiceno et al. (2006) developed a gas phase and surface reaction mechanism for a steady-state catalytic partial oxidation of methane to syngas over Pt gauze catalyst. These authors state that the first step in the catalytic partial oxidation of methane to syngas involves the cleavage of the C-H bond upon the catalyst surface, and this results in highly reactive CH_3 species. The formation of CO and CO_2 is primarily due to surface reactions that involve methyl groups and oxygen. Their scheme considers the interaction between the surface and gas phase mechanisms and consists of 10 surface species and 24 reactions (Table 2). This interaction is done via the surface species (H, O, OH) and the molecular species (CO, CO_2, CH_4, O_2, H_2, H_2O). The kinetic scheme is robust due to the coupling of surface and gas phase mechanism and can be applied in the simulation of high temperature and short contact times regime.

On partial oxidation of methane, Kostenko et al. (2014) used a model that accounts for the gas-phase and surface reactions to investigate methane partial oxidation to syngas in a porous medium reactor. A kinetic model was described and tested for a mixture of methane, oxygen and steam and the dependency of the composition of final products on temperature and composition of the gas mixture was investigated. The numerical solutions yielded the combustion temperature at which the steam reforming reactions are low and the partial steam conversion in the combustion wave was attributed to the reaction of steam with adsorbed carbon on the porous solid medium.

It is desirable to study the kinetics of methane oxidation to syngas with the view of understanding the reactions that affect the catalyst performance. Korup et al. (2013)

used a polycrystalline Pt foil as a model catalyst for catalytic oxidation of methane to syngas. The study was aimed at demonstrating that upon ignition of methane, oxidation and steam reforming resistant carbon deposits form on a Pt surface and this results in the blockage of a larger portion of the Pt surface atoms. The study was prompted by a need to understand the underlying reasons for slower product formation and reactant consumption in Pt foam catalyst as opposed to Rh foam catalyst. Their findings indicate that the poorer syngas selectivity and slower catalytic oxidation of methane on Pt foam catalyst as opposed to Rh foam catalyst can be ascribed to the formation of oxidation resistant graphitic carbon on the Pt surface sites.

A systematic study of the kinetics of methane oxidation over Pt and Pt-Pd catalysts to investigate the influence of temperature, water and methane concentration on catalyst performance over a range of operating conditions for environmental applications was performed by Abbasi et al. (2012). The findings from their study demonstrated that there is a permanent loss of the significant portion of the activity of both Pt and Pt-Pd catalysts due to exposure to water in the feedstock. These authors concluded that under dry conditions, the fresh Pt-Pd catalyst is more active than the fresh Pt catalyst. The development of mathematical models that investigate the described phenomenon can help reduce experimentation, hence costs and allow for an investigation of a wider range of parameters.

The simulated results based on the surface reaction mechanism by Soick et al. (1996) were reported to result in the underestimation of the reaction rate. This is because the cooperative effect of surface oxygen on methane dissociation was not taken into account. On the other hand, the simulation results based on the surface reaction mechanism by Quiceno et al. (2006) were reported to be in close agreement with methane partial oxidation experiments over Pt gauzes. This close agreement could be attributed to the inclusion of the effect of surface oxgen on methane dissociation by the latter mechanism. However, there are some similarities between the two reaction mechanisms. They both consist of 10 surface species, methane dissociation, oxidation, CO_2 adsorption and CO adsorption.

The simulations in the current work will be based on the reaction mechanism developed by Quiceno et al. (2006) given that it is a robust kinetic scheme for catalytic partial oxidation of methane in high temperatures and short contact times. The reaction

mechanism employed in as shown in Table 2. The kinetic, transport and thermodynamic data are shown in Tables 15, 16 and 17 respectively.

The coupling of gas-phase and surface reaction mechanisms has been reported to be important as it allows for the development of robust kinetic schemes (Campbell et al., 1988; Quiceno et al., 2006). This is explained by the fact that the gas-phase reactions are initiated by radicals and these radicals may desorb from the catalyst surface. The gas-phase reaction mechanism by Quiceno et al. (2006) which consists of 30 species and 150 irreversible reactions is presented in Table 21 (Appendinx E). Although the detailed gas-phase reaction mechanism consists of numerous chemical species (several hundreds), the most important are internal H-atom abstraction, decomposition of hydrocarbons, addition of molecular oxygen and O-O bond scission, H-atom abstraction and β-scission of radicals (Chevalier et al., 1992). The sensitivity and flow analysis are often carried out to remove the insignificant reaction path ways and this helps to speed up the simulations.

Table 2: Surface reactions on a Platinum surface where * depicts surface species whereas g depicts a gas-phase species (Quiceno et al., 2006)

Adsorption-Desorption
$H_{2,g} + 2* \rightarrow 2H*$
$2H* \rightarrow H_{2,g} + 2*$
$O_{2,g} + 2* \rightarrow 2O*$
$2O* \rightarrow O_{2,g} + 2*$
$CH_{4,g} + 2* \rightarrow CH_3* + H*$
$CH_3* + H* \rightarrow CH_{4,g} + 2*$
$H_2O_g + * \rightarrow H_2O*$
$H_2O* \rightarrow H_2O_g + *$
$CO_{2,g} + * \rightarrow CO_2*$
$CO_2* \rightarrow CO_{2,g} + *$
$CO_g + * \rightarrow CO*$
$CO* \rightarrow CO_g + *$

Surface reactions
$H* + O* \rightarrow OH* + *$
$OH* + * \rightarrow H* + O*$
$H* + OH* \rightarrow H_2O* + *$
$H_2O* + * \rightarrow H* + OH*$
$OH* + OH* \rightarrow H_2O* + O*$
$H_2O* + O* \rightarrow OH* + OH*$
$C* + O* \rightarrow CO* + *$
$CO* + * \rightarrow C* + O*$
$CO* + O* \rightarrow CO_2* + *$
$CO_2* + * \rightarrow CO* + O*$
$CO* + OH* \rightarrow CO_2* + H*$
$CO_2* + H* \rightarrow CO* + OH*$
$CH_3* + * \rightarrow CH_2* + *$
$CH_2* + H* \rightarrow CH_3* + *$
$CH_2* + * \rightarrow CH* + H*$
$CH* + H* \rightarrow CH_2* + *$
$CH* + * \rightarrow C* + H*$
$C* + H* \rightarrow CH* + *$
$H_{2,g} + C* \rightarrow CH_2*$
$CH_2* \rightarrow C* + H_{2,g}$
$CH_{4,g} + O* + * \rightarrow CH_3* + OH*$
$CH_{4,g} + OH* + * \rightarrow CH_3* + H_2O*$
$CH_3* + OH* \rightarrow CH_{4,g} + O* + *$
$CH_3* + H_2O* \rightarrow CH_{4,g} + OH* + *$

2.2. Reactor Model

The momentum, heat and mass transfer characteristics must be considered for the model results to be interpreted from the laboratory reactor. In the context of partial oxidation of methane in monolith reactors, a complete set of Navier-Stokes equations has to be simulated over relatively complex kinetics. Upon establishing the intrinsic kinetics as described above, the monolith reactor for partial oxidation is simulated by the coupling of transport and micro-kinetics of surface reactivity (Kolaczkowski et al., 2007; Maghrebi et al., 2013). In a monolith reactor, the gas flows through the channels and the transport of species from the bulk gas phase to the catalyst active sites influences the reaction concentration.

The catalytic partial oxidation of methane is characterised by complex interaction of transport phenomena and chemical reaction kinetics. Additionally, there is competition between partial and total oxidation of methane (Neumann and Veser, 2005). Depending on the reaction conditions, the chemistry may include both homogeneous and heterogeneous reactions. At atmospheric pressure, the homogeneous gas-phase reactions are negligible, however, at elevated pressures, the gas-phase reactions must be considered in the reaction kinetics. Over the past years, intensive research has been undertaken to study the partial oxidation of methane with the consideration of the described phenomena.

For accurate determination of state variables in methane partial oxidation, the governing equations for partial oxidation in monolith reactors are solved using Computational Fluid Dynamics (CFD). In CFD modelling of monolith reactor for heterogenous reactions, the transport processes from CFD are coupled with some external subroutines such as CHEMKIN or DETCHEM to account for surface micro-kinetics (Quiceno et al., 2006; Chen et al., 2018). With the CFD modelling, the reactor configuration, reactor performance and operating protocol can be related.

The multi-channel models are used in cases where there is fuel maldistribution (James et al., 2003). In this case, the fuel is not fully premixed and as a result some channels will have a higher fuel concentration than others. Several multi-channel models have been developed (Flytzani-Stephanopoulos et al., 1986; Cybulski and Moulijn, 1994; Spence et al., 1993; Jahn et al., 1997). The heat transfer models developed by

Flytzani-Stephanopoulos et al. (1986) and Cybulski and Moulijn (1994) do not take into account the homogeneous and heterogeneous reactions. The steady state temperatures of the wall and gas-phase in each channel are described by the boundary-value ODEs. The channels are coupled through the use of heat transfer terms. Both models were reported to predict the results that are in a close agreement with experiments.

The improvement on the multi-channel models was done by Worth et al. (1996) who studied heat tranfer with reactions. The radial temperature gradients between neighbouring channels result in heat exchange, and their model was aimed at studying the interactions among the channels. The temperature variables in the multichannel structure are as shown in Figure 4. Their model constitutes a system of integral equations that are used to describe the radiative heat transfer in a catalytic monolith. A simple approximation of the integral equations was done because the modelling of the channel interactions and the processes in the catalytic monolith often requires the coupling of algebraic models and complex differential equations. The approximation is done as shown in Equation 2.12. The radiative flux from their study was compared with the published data and a good agreement was found.
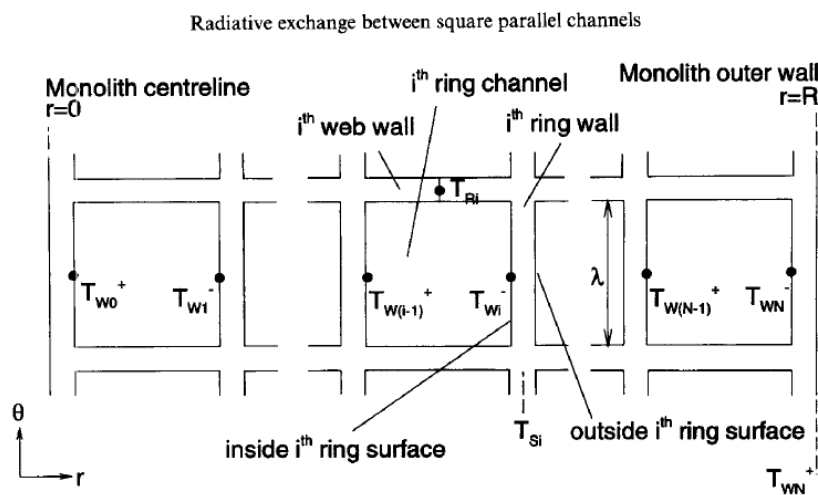
Figure 4: Temperature variables in the multichannel structure (Worth et al., 1996)

$$\int_0^{L/\lambda} q(x) A\left(\left|\frac{x}{\lambda} - \frac{z}{\pi}\right|\right) d\left(\frac{z}{\lambda}\right) \approx q(x) \int_0^{L/x} A\left|\frac{x}{\lambda} - \frac{z}{\lambda}\right| d\left(\frac{z}{\lambda}\right) \qquad (2.12)$$

Where *A* is radiation view factor, *L* is the length of monolith, *q* is the radiative heat loss, *λ* is the channel width.

The non-uniform flow and distribution of the catalytic activity in monolith channel results in significant radial temperature gradients even under adiabatic operation (Jahn et al., 1997). In order to determine the actual temperature profiles in monolith channels at a range of operating conditions, Jahn et al. (1997) developed a 3D model for a monolith with 24 channels. The model uses Fourier equation to consider heat conduction and accumulation in the solid phase. In addition, mass and heat balances in the gas-phase and on the catalyst surface are considered. The temperature and concentration fields are discretized to thousands of ODEs which are integrated on a fast workstation to give transient solutions. The findings from their study indicated that it requires one hour to simulate one minute of real time in the model.

A single channel model that exhibits stable multiple steady states of catalytic combustion was developed by James et al. (2002). This has also been observed experimentally in the work that investigated the transient behaviour of monolith reactors in the catalytic combustion of methane (Cimino et al., 2001). The approach by James et al. (2002) was extended to multichannel monoliths by James et al. (2003). The extension is done by considering heat transfer between channels. The convection term is linearised and this enables it to be expressed in terms of a system of ODEs instead of PDEs. The multiple stable steady states which were seen experimentally and from the single channel model were also seen from their study. The authors concluded that the multichannel model gives a richer behaviour of monolith reactors than a single channel monolith. This is because the model is able to investigate the effect of fuel maldistribution in individual channels.

In addition to the above mentioned models, reactor models such as a 2D elliptic model, 1D heterogeneous model and a 3D flow field coupled with a heat balance and a detailed description of surface and gas-phase chemistries have been used to simulate a short-contact time reactors (De Groote and Froment, 1996; Deutschmann and Schmidt, 1998a). The 3D and 2D elliptic models are based on the CFD code FLUENT.

2.2.1. Multi-scale modelling

The modelling of heterogeneous reacting systems comprises different scales which include micro-scale, meso-scale and macro-scale. The micro-scale level entails the electronic interaction between active sites and the reactant molecules. This process comprises the adsorption of reactant molecules on the active sites, the diffusion of species at the surface, the reaction process, the de-sorption of products from the active sites (Rebughini and Maestri, 2016). All the events result in elementary steps at the surface of the catalyst.

The meso-scale comprises the interplay among the rates of the elementary steps from micro-scale, the distribution of active site at the catalyst surface, the influence of surface coverage on activation energy and the nature of active sites (Stampfl et al., 2002). At the meso-scale level, the simulations are carried out by the use of the reaction theory based models such as mean field theory and Kinetic Monte Carlo (Stoller et al., 2008). The mean field approximation assumes the fast diffusion at the surface thus considering the average values of surface coverage. Kinetic Monte Carlo relaxes the assumption of average surface coverage by considering the spatial and temporal variations and as a result the simulations can be done for longer time steps which is a requirement for the reaction events.

At the macro-scale, transport phenomenon is considered; and it is usually highly coupled with chemistry. At this level, the transport of reactants from the gas phase to the surface of the catalyst are considered. A graphical representation of the different scales is represented in Figure 5. The depiction in Figure 5 shows a wide range of temporal and spatial scales involved from micro-scale to macro-scale. The macro-scale is characterized by long time and length scales and the underlying transport equations are normally non-linear and stiff.
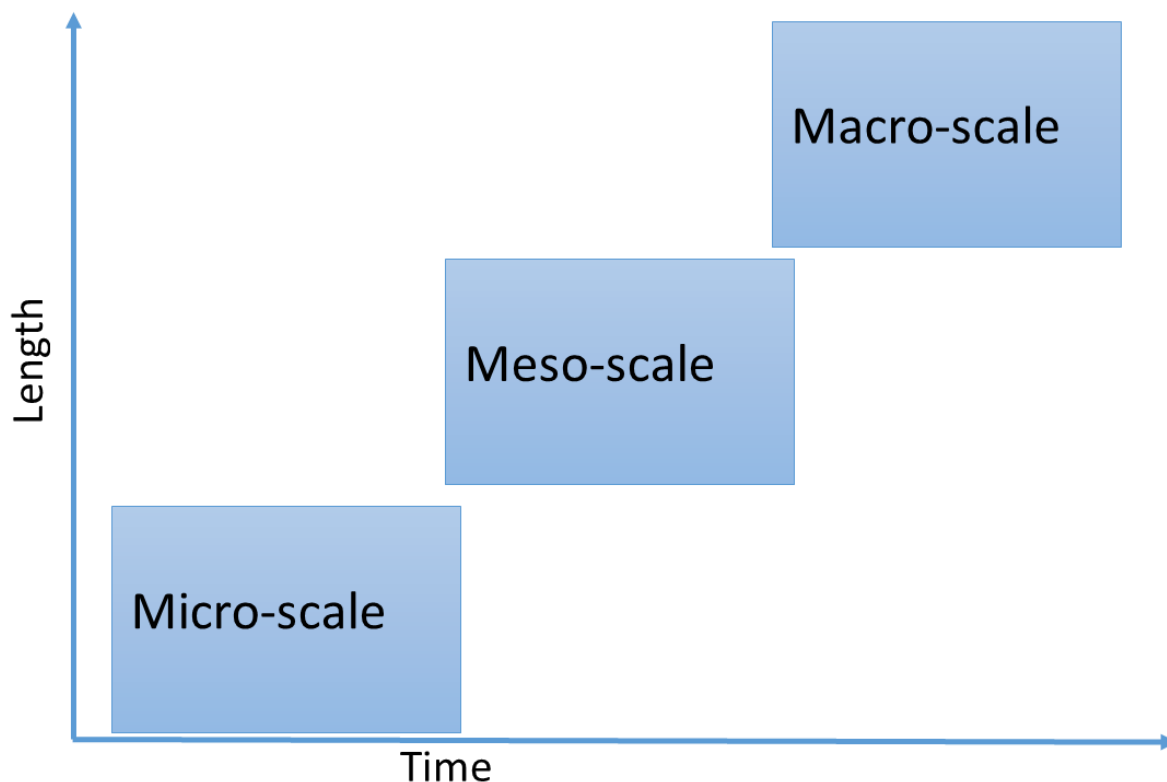
Figure 5: An illustration of the multi-scale at varying temporal and spatial scales

The interplay among all the 3 scales imply that there is a possibility of a propagation of error from micro-scale to macro-scale.

2.2.2. Coupling between the scales

The phenomenological rate equation models, micro-kinetic models and mechanistic rate equation models are used to effect the coupling between micro-scale and meso-scale. The mechanistic rate equation models involve the prior assumption regarding the rate determining step for the reaction mechanism. The shortcoming of this approach lies in the lack of generality as their usage is circumscribed to the operating conditions under which the rate expressions were derived. On the other hand, the micro-kinetic models present a more general and generic approach as there is no assumption made regarding the rate determine step. They can be applied over a range of operating conditions and this is attributed to the fact that they are based on a series of elementary steps (Davis and Davis, 1993). The coupling between the scales is achieved using CFD simulators that couple transport phenomena with micro-kinetics.

2.3. Governing equations for the gas-phase and the catalytic surface

The governing equations that describe fluid flow are momentum, continuity, mass and energy balance equations. These equations are collectively called Navier-Stokes equations and they are normally solved numerically because in most cases analytical solutions are not possible. The numerical solution procedure involves treating the fluid as the continuum and invoking macroscopic properties such as concentration, velocity, pressure and temperature with their temporal and spatial derivatives to describe the system behaviour (Versteeg and Malalasekera, 2007).

The gas-phase conservation equations are individual species, total mass, mixture energy, individual mass fractions and mixture momentum. The conservation equation for the catalytic surface balances the rate of change of surface species with the net formation rate as a result of heterogeneous reactions.

2.4. Numerical simulation of monolith reactors based on CFD

The conservation equations for the gas-phase and catalytic surfaces are well studied and there are several CFD studies reported on their application in monolith reactors (Pawlowski et al., 2018; Iwaniszyn et al., 2017; Inbamrung et al., 2018; Cui and Kær, 2018; Sadeghi et al., 2017; Liu et al., 2005; Irani et al., 2011). The geometric optimization with the view of maximizing the reaction rate was achieved by investigating the influence of channel geometry and fluid behaviour on the reaction performance (Inbamrung et al., 2018). The findings indicate that the smaller channel diameters increase the reaction rate in comparison to larger channel diameters at the same gas hourly space velocity.

Sadeghi et al. (2017) solved the governing equations in the 3D modelling for a range of channel geometries which include triangular, circular, hexagonal and square cross sections. Hexagonal monoliths allow for a more uniform washcoat and have a better thermal mass efficiency compared to square monoliths (Cybulski and Moulijn, 2005). However, a square monolith offers a slightly better or same performance as the hexagonal monolith due to its higher geometric surface area. The findings from their study indicated that the change of the channel geometry from circular to triangular increases the rate of reaction. This is attributed to an increase in the area to volume ratio. Liu et al. (2005) performed a CFD simulation of a novel metal-based monolith

reactor and demonstrated that the external mass transfer of the two-layer channel (one layer is the metallic support and the other layer is a foam metal annular that is deposited on the support surface) is not significantly influenced by the inlet velocity of the mixture, inlet gas temperature and inlet methane concentration.

On the numerical investigation of partial oxidation of methane to syngas, Deutschmann and Schmidt (1998) developed a 2-D reactor model that couples the flow field with the detailed reaction mechanisms for the surface and gas-phase reactions. The study was based on methane partial oxidation on Rh and Pt coated monoliths in a short contact time reactor. The flow field is simulated from Computational Fluid Dynamics (CFD) coupled with external subroutines to consider the detailed chemistry. Their model neglects diffusion in the flow direction and this makes it unsuitable for simulating more complex geometries. In addition, the assumption of no diffusion in the flow direction is not valid for systems with large heat release (Karim et al., 1996). The findings are that there is a rapid variation of temperature, velocity and transport coefficients at the entrance. The increase in gas velocity was found to decrease syngas selectivity and methane conversion.

The conversion and selectivity of light alkanes is strongly dependent on temperature. Therefore, a detailed description of the energy balance is required in order to understand the reaction. The experimental measurements indicate that there is a significant heat loss, as such, numerical studies that consider a monolith as a single channel should add an external heat loss term at the outer boundary of the channel wall (Deutschmann et al., 2001). It is based on this that Deutschmann et al. (2001) developed a 3D model that investigates the natural gas conversion on rhodium coated monoliths. In their work these researches assumed that every channel behaves the same way, thus the radial temperature gradients were neglected, and the entire monolith was modelled as a single channel. The 3D Navier-Stokes equations were coupled with a detailed chemistry and heat balance. The simulations were based on CFD code FLUENT and this was coupled with the external subroutine for surface and gas phase chemistry (DETCHEM). The findings from their study reveal that there is a close agreement between the model and experimental results. The computational expense is reduced significantly in the case of a single channel.

A numerical study that investigates the mass transfer in catalytically reacting channel flows was undertaken by Mladenov et al. (2010). The various models that describe mass transfer in a single channel catalytic converter were compared. The 2D boundary layer and Navier-Stokes, 3D Navier-Stokes and 1D plug flow equations were employed to describe the model and the model results were validated against experimental data. Their findings on the computational time revealed that plug flow models result in a CPU time of a few seconds. On the other hand, the 3D Navier-Stokes models that are coupled with the detailed wash-coat model were found to result in CPU time of a couple of days. The authors concluded that the 2D and 3D Navier-Stokes models show the species profiles that are in close agreement and as a result the 2D models can be used given that they are less computationally demanding compared to the 3D models.

In an effort to elucidate the mechanisms and the roles of electrochemical promotion in partial oxidation of methane over self-sustained electrochemical promotion (SSEP) catalyst, Huang et al. (2016) developed a multi-physical CFD model coupled with detailed chemistry. The description of reaction rates in the model is twofold; the description of the reaction rate by the kinetic model for partial oxidation of methane on Ni based catalyst and the description of the reaction rate by the SSEP effect. Their results demonstrated that the SSEP catalyst results in higher conversion of methane into syngas over a temperature range of 350-650 ^{o}C, and that this is in agreement with the results from a commercial Pt catalyst under the same operating conditions. Additionally, the model allows for a mechanistic relation between the electrochemical properties of the SSEP catalyst, operating conditions and the performance of partial oxidation of methane. The model can be employed in studies that are aimed at quantifying the enhancement of partial oxidation of methane due to SSEP effect.

The performance of catalytic partial oxidation of methane is affected by many process parameters such as geometric configuration, feedstock compositions, type of catalyst, catalyst loading, heat and mass transfer processes. It is based on this realization that Chen et al. (2010) undertook a study on the characteristics of partial oxidation of methane with/without heat recovery. Their study constitutes a numerical simulation which investigates the reaction characteristics in a swiss-roll reactor. They used ANSYS FLUENT v12 to solve the governing equations and boundary conditions. The

results from their study reveal that pre-heating the reactants leads to an enhanced hydrogen and carbon-monoxide selectivity as well as improved methane conversion. Furthermore, their results suggest that the increased number of turns in the reactor and the lower gas hourly space velocity (GHSV) lead to improved process performance. Despite the enhanced process performance, more work is still to be done to overcome the challenges encountered in a large-scale production.

The steady-state CFD simulations are computationally efficient in comparison to the dynamic CFD simulations. However, for simulations of complex geometries, the steady-state simulations become computationally demanding due to a large number of variables (Quiceno et al., 2006). As a result, there have been a number of studies aimed at reducing the computational expense in steady-state CFD simulations by reducing the number of species and reactions in the microkinetic models (Deshmukh and Vlachos, 2007; Stefanidis and Vlachos, 2009). The models based on a reduced mechanism result in a reduced compuitional expense, however, their results can be inacurrate when compared to the full microkinetic models. In view of this, Rebughini et al. (2017) used a cell agglomeration algorithm to help reduce the computational expense in a model that couples CFD with a detailed microkinetic model.

The method works by grouping together the cells of the same thermo-chemical properties. In their work, it was proposed that since there is no transport term in the governing equations of the adsorbed species, the cells in the computational domain can be considered isolated. In this case, the cell agglomeration algorithm is able to reduce the number of adsorbed species that need to be evaluated. The results from their work showed a considerable reduction in computing time in comparison to a case where such a grouping is not applied.

2.5. Optimization of the washcoat thickness

An optimization study on the wash-coat thickness of a monolith reactor for syngas production was undertaken by Stutz and Poulikakos (2008). The study was motivated by a realisation that the wash-coat is impregnated with the precious metals, whose amount needs to be reduced for economic considerations. These researchers modelled the wash-coat as a porous layer, which was approximated as a granular medium with an active catalytic surface. The study constitutes an investigation of two

models; zero wash-coat thickness and a finite wash-coat thickness. The former model comprises the flow channel and the thermal conductive wall (Figure 6); the latter model comprises the flow channel, the wash-coat and the thermal conductive wall (Figure 7). The optimum wash-coat thickness of 70 μm was found under the conditions of constant amount of catalyst per wash-coat and constant feed flowrate.

They further reported that for a thinner wash-coat, all active sites are accessible; however, this comes at a cost of the amount not being sufficient to process the reactants . This results in low conversion of reactants because the small amount of catalyst is limiting. On the other hand, for a thicker wash-coat, they reported that the active sites are sufficient to process the reactants; but this is usually not achieved due to a reduced residence time. In this case, the limiting effect is the residence time which is a result of a constraint on constant flow rate, rather than the increased diffusion resistance (Stutz and Poulikakos, 2008). Therefore, the conversion of the reactants is inevitably low in this case as well. In partial oxidation, oxygen gets fully consumed within the first few millimetres of the catalyst bed, as such, a non-uniform distribution of a catalytic material has to be adopted. This will lead to economic use of the precious metals. The mole fraction profiles from the work of Maffei et al. (2014) in Figure 8, show that oxygen gets fully consumed within the first few millimetres of the catalyst bed.
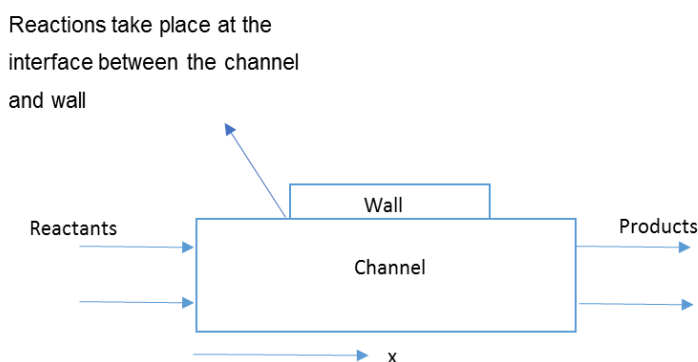
Figure 6: A computational domain for a zero wash-coat thickness (Stutz and Poulikakos, 2008)
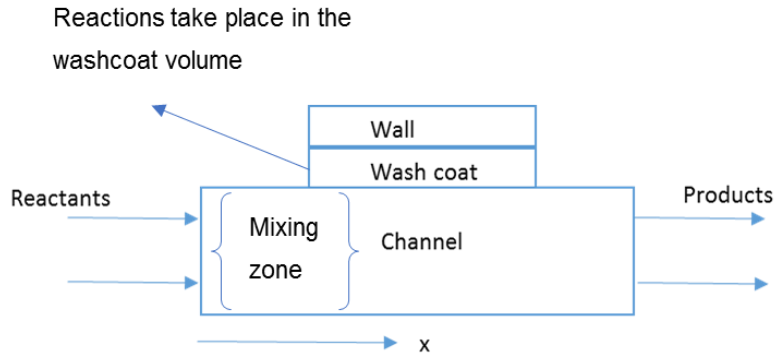
Figure 7: A computational domain for a finite wash-coat thickness (Stutz and Poulikakos, 2008)
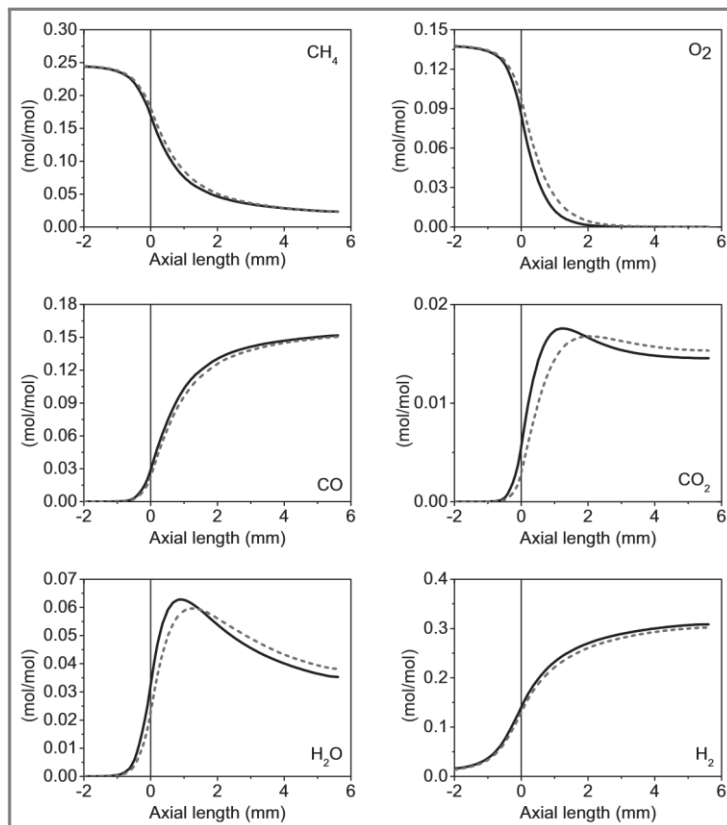
Figure 8: Mole fraction profiles for two duct geometries.Full line: circular duct; dotted line;square (Maffei et al., 2014)

2.6. Numerical studies based on improving catalytic partial oxidation of methane

The catalytic partial oxidation of methane to syngas is characterised by severe conditions such as high temperatures and gas hourly space velocity, complex fluid patterns and mass transfer limitations (Horn et al., 2007). A typical example is the high surface temperatures (800-1100°C) which can result in catalyst deactivation (Tavazzi et al., 2007). Because of these challenges, Maffei et al.(2014) perfomed the CFD analysis of the channel shape effect in monolith catalysts for partial oxidation of

methane on Rh. Their detailed multiscale analysis of monoliths with square and circular ducts revealed that the effect of geometry on local temperature is significant. It was reported that the hot spot temperature is higher in the case of the circular duct (Figure 9). The formation of local hot spot is also evident from the work of Navalho et al. (2013) as demonstrated in Figure 10. However, Maffei et al.(2014) found out that the outlet temperature and composition are not significantly affected by the two geometries they employed in their study. Based on the findings from their work, it is evident that the reactor configuration can be designed to minimize the formation of temperature hot spot.
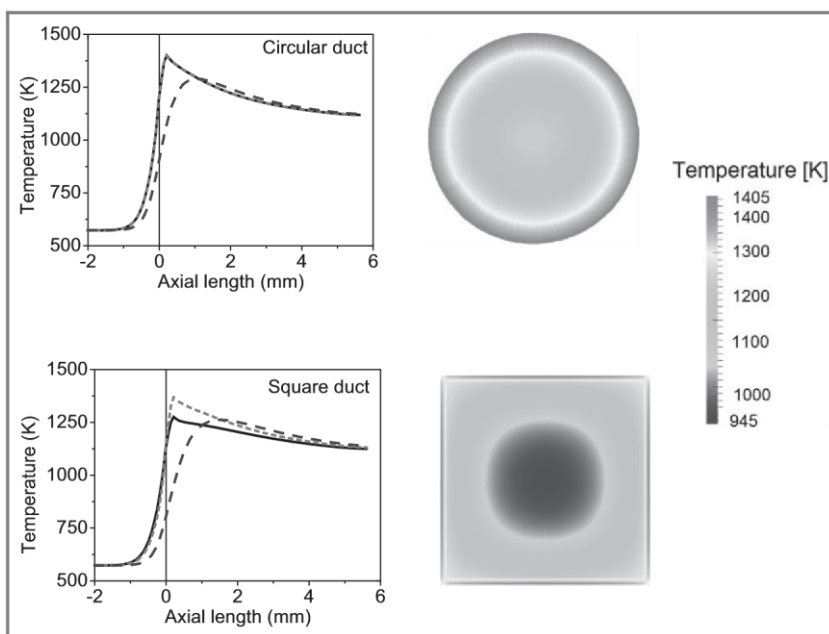
Figure 9: Temperature profiles for two duct geometries.Full line: Temperature at the corners, dotted line; Temperature at edges, dashed line: gas-phase temperature (Maffei et al., 2014)

Navalho et al. (2013) performed an experimental and numerical investigation on the catalytic partial oxidation of methane to syngas. To address the often-encountered hot spot formation on the catalyst bed which eventually leads to thermal deactivation (e.g. sintering), they developed a 1-D heterogeneous model that considers the radiative heat losses. The radiative heat loss from the catalyst bed to the surrounding results in lower surface temperatures, thus the formation of local hot spot is reduced. The developed heterogeneous model was for a single channel and the coupling between transport phenomena and surface chemistry was considered. They concluded that the non-adiabatic reactor configuration operating at low fuel flow rates and high air to fuel ratios allows for a significant decrease in maximum catalyst temperature as compared to an adiabatic reactor configuration. This is demonstrated in Figure 10.
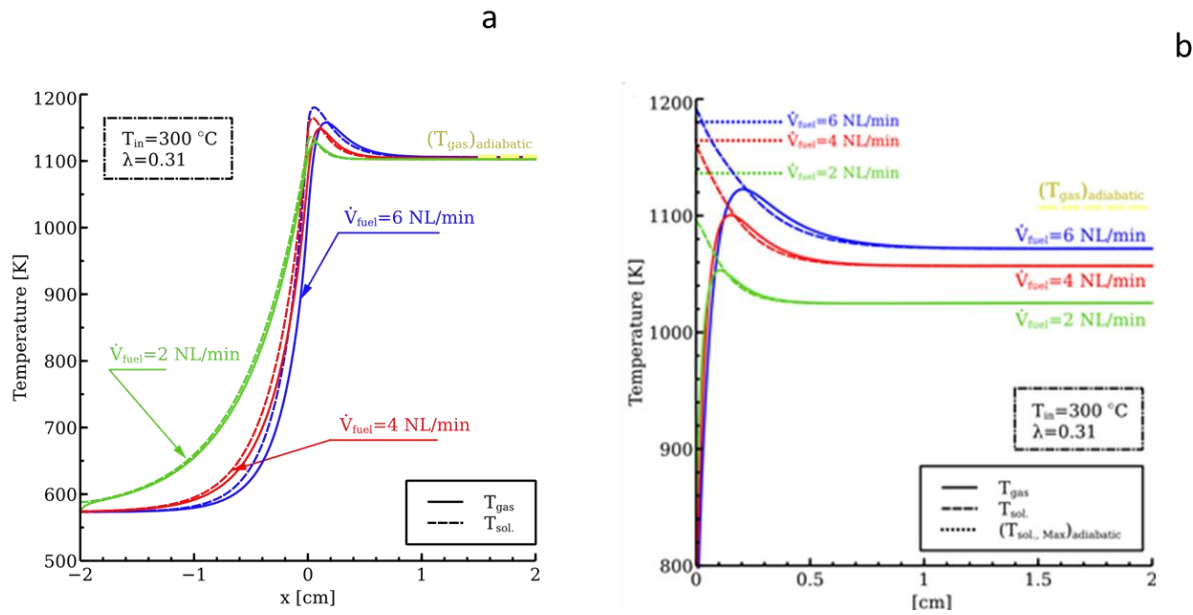
Figure 10: Thermal profiles of adiabatic (a) and non-adiabatic (b) reactor configurations for different air to fuel ratios (Navalho et al., 2013)

The use of simpler models such as boundary-layer and plug flow models addresses the high computational expense in the solution of Navier-Stokes equations for chemically reacting flows (Schlichting and Gersten, 1999; Raja et al., 2000). The boundary-layer approach was used by Schwiedernoch et al. (2003) for a numerical study on partial oxidation of methane in a catalytic monolith. On the numerical study, 2-D and 3-D simulations that predict temperature distribution of the entire monolith were adopted. This approach was coupled with a 2-D laminar reactive flow field simulation that served as a representation of several single monolith channels. The species concentration, temperature fields, gaseous velocity and surface coverage of the adsorbed species were predicted from the 2-D laminar reactive flow simulation based on a multi-step heterogeneous mechanism. The gas phase and surface reactions were modelled using the reaction kinetics of DETCHEM computer package. In their findings they drew the following conclusions,

- There exists a strong competition between partial oxidation, total oxidation and steam reforming reactions in the reactor.
- At ignition, only total oxidation of methane takes place and carbon monoxide and hydrogen selectivity slowly increases with increasing temperature.

27

Based on the conclusions drawn from their work, there needs to be some work done to address the competition between total and partial oxidation and this includes investigating the influence of fuel to air ratio to allow for enhanced syngas selectivity.

The expensive pilot plant work in the design and scale-up of processes can be saved by the use of simulations based on efficient mathematical models (Rostrup-nielsen, 2000). An efficient mathematical model was developed by Bizzi et al. (2004) to conduct numerical investigations on the partial oxidation of methane in a fixed bed reactor with detailed chemistry. They developed a transient, 1-D model with consideration of separate energy balances for the gas phase and solid phases, transport phenomena, internal radiation with the fixed bed, longitudinal gas-phase dispersion, and detailed surface kinetics. Because of the low pressure drop across the catalyst bed, the momentum conservation equation was not considered. Furthermore, the model used the plug flow assumptions to simplify the mass conservation equations. On microkinetic reactivity, the simplifications were made by considering the catalyst to be extremely active and the reaction rate to be faster than the transport of reactants to the surface.

The influence of temperature and feedstock ratio on the reactant conversion and syngas selectivity and reactor performance was studied. The findings were that the low inert context of the feedstock permits high reactant conversion and syngas selectivity. Owing to high prices of pure oxygen, they found an optimal O_2/C ratio of around 0.56 as a trade-off. The results on the effect of space velocity and reactor blowout indicate that at low GHSV, the increase in space velocity results in enhancement of the reactor performance due to better mass transfer. At higher GHSV reactor blowout occurs. On the reactor geometry, their sensitivity analysis on length to diameter at constant volume reveal that deep reactor configurations result in excellent performance.

Schneider et al. (2006) carried out numerical simulations to investigate the catalytic partial oxidation of methane in a short contact time reactor. The short contact time means a short residence time and compact designs. In these systems, high throughputs are achieved at low capital and energy costs and the use of a small amount of a catalyst (Deutschmann and Schmidt, 1999). The developed reactor model constituted a steady, 2-D, elliptic numerical code with the detailed chemistry and

transport phenomena. The reactor was modelled as a single monolith channel operated at a pressure of 5 bar. The findings from their study as observed in Figure 11 revealed that the surface temperature is above the adiabatic equilibrium temperature by 200 K. This was attributed to short residence times and the multiple reaction pathways that constitute steam reforming, water gas shift and methane oxidation. The inadequacy of the heat transfer mechanism in controlling the surface temperatures was reported, and as a result more robust approaches are needed for the thermal management.
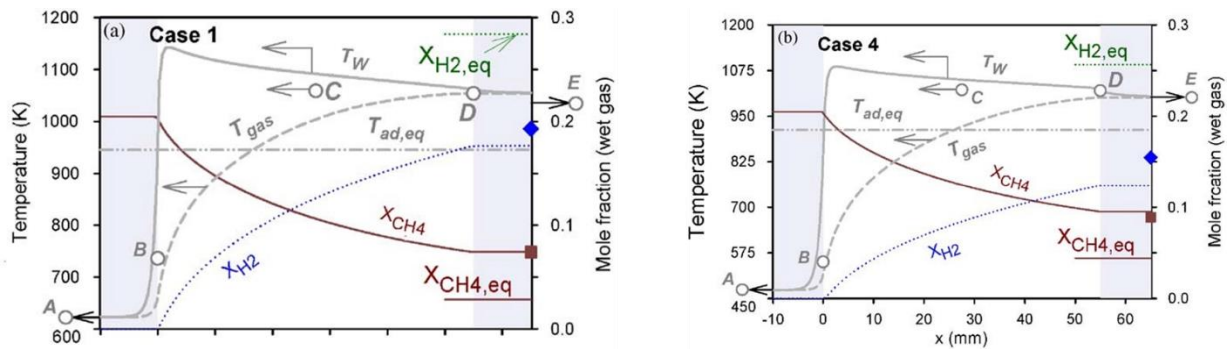
Figure 11: Temperature and species axial profiles for case 1 and case 4 predictions (Schneider et al., 2006)

The simulations of reactive monoliths based on unsteady-state 1D models often do not consider the dynamics of the catalyst surface (Hickman and Schmidt, 1993; Park and Vlachos, 2000). The unsteady-state model that takes into account the dynamics of the catalyst surface was used by (Veser and Frauhammer, 2000). However, their model neglected the heat and mass transfer limitations in the boundary layer near the surface. A more robust approach was adopted by Vernikovskaya et al. (2007) who developed a dynamic one-dimensional, two phase reactor model with considerations of both transport limitation in the boundary layer of the fluid near the catalyst surface coupled with detailed transient kinetic model for reactions on the catalyst surface. The influence of dynamic parameters such as thermal conductivity of the monolith, equivalent diameter of the triangular channel and linear velocity on the partial oxidation of methane was investigated. Their findings indicated that the increase in linear velocity and equivalent diameter, and a decrease in axial conductivity of the solid phase favours decreasing a time delay in syngas production in the Pt/Ce-Zr-La/α-Al_2O_2 honeycomb monolith.

In the catalytic oxidation of methane to syngas, there are many challenges that need to be addressed, these include; catalyst poisoning by sulphur or halogen-containing compounds and solid carbon adsorption or deposition that normally affect catalyst surface performance. In addition, the activation of the catalyst sites is achieved by heating at high temperatures. The mentioned challenges are normally addressed by non-conventional technologies such as plasma. In an attempt to overcome the stated challenges, Luche et al. (2009) performed both experimental and numerical investigations of methane conversion to syngas in a plasma reactor. The reactor model computed chemical transformation using a PSR code and CHEMKIN computer package. The PSR code is a Fortran computer program that is used to predict the steady-state species composition and temperature in a perfectly stirred tank reactor (Glarborg et al., 1986). The findings from their study are that high methane conversion and the maximum hydrogen production are obtained at low flow rates and methane concentration in the feedstock.

Kostenko et al. (2014) performed numerical simulations to investigate methane conversion by partial oxidation in a porous medium reactor with admixing steam. They developed a two-temperature (gas/solid) 1-D model that considers the heterophase reactions. The model was developed for an adiabatic process with the consideration of energy balance equations for the porous medium and the gas phase. The porous solid and gas phase was each described by its own temperature and accounted for as the interpenetrating continuous media. Owing to the reactions that take place on the catalyst surface, the model also considers the carbon deposits. The conclusions drawn from the findings were that the maximum temperature in the combustion wave is influenced by the composition of feedstock and is mildly influenced by the inlet gas velocity. Additionally, the established combustion temperature was such that the steam reforming is low, and the partial conversion of steam was attributed to the reaction of steam with adsorbed carbon on the porous medium.

A numerical model that investigates the spatially resolved data of catalytic partial oxidation of methane on Rh foam catalyst was developed by Nogare et al. (2011). The spatially resolved data which constitute species concentration and temperature, were measured over a wide range of conditions and compared with the micro-kinetic model simulations in order to elucidate the influence of transport on catalytic partial

oxidation of methane on Rh foam catalyst. The simulations are based on a 1D model that describes heat and mass transfer axially, and this transport model is coupled with micro-kinetics. The momentum balance was not taken into consideration as the pressure drop was considered negligible. The results from their work revealed that for different inlet C/O stoichiometries, both the partial oxidation (CO and H_2) and total oxidation (H_2O and CO_2) products are observed. Depending on the feed conditions or the position on the reactor axial coordinate, the consumption of reactants can be either under chemical or mass transfer regime. These researchers found out that for lean mixtures, the consumption of both methane and oxygen is under chemical regime. On the other hand, for rich mixtures, the consumption of methane is under transport regime and the surface is characterised by lower temperatures. Their findings demonstrated that for high ratios of C/O, there is a high presence of carbon atoms that results in an increase of C* and CO*.

Korup et al. (2013) developed a pseudo-2D heterogeneous reactor model with mass and heat transport consideration and the model was coupled with a micro-kinetic model. The system comprised of 3 phases; a bulk gas phase, a boundary layer phase and a chemically reactive surface. Mass and energy balance equations were described for each phase as the computational domain was divided into the 3 distinct phases. However, in the simulations, the energy balance on the boundary layer and surface were not solved for. The underlying reason was that the temperature of the gas in the boundary layer equilibrates with the surface temperature.

Their simulation results based on the mechanism developed by Zerkle et al. (2000) indicated that the oxygen mole fraction profiles are in a close agreement with experimental data. However, the product profiles revealed a significant difference between experimental and model results. On the other hand, the simulation results based on the mechanism by Mhadeshwar and Vlachos (2007) gave a better agreement with experiments eventhough the water gas-shift reaction rates are underpredicted. The two mechanisms do not include carbon growth and this could explain the differences between the model and measured profiles.

The plasma-assisted fuel reforming is one of the promising technologies for the production of syngas and generation of hydrogen for fuel cell vehicles. Given the importance of this technology in the production of syngas, Starik et al. (2015) carried

out a theoretical study on partial oxidation of methane by a non-equilibrium oxygen plasma. The study was aimed at producing hydrogen rich syngas by activation of oxygen through specially arranged electric discharge. The numerical method entails a 1D Euler equations for reacting gas flow. The 1D model was coupled with the energy balance equations and kinetic rate balance equations for atoms, molecules and atoms. The electric discharge leads to the production of highly reactive atoms and radicals which allow for chain mechanism of hydrocarbon oxidation and, thus the conversion of hydrocarbons to syngas ensues.

Their findings reveal that the high yield of syngas is achieved at the CH_4/O_2 ratio of 3.0 which translates to a yield as high as 89%. On the other hand, the hydrogen rich syngas is obtained at the CH_4/O_2 ratio of 4 and in this case the yield of syngas is lower compared to the former case (~69-76%). Depending on the downstream process, the ratio of H_2 to CO in the feedstock differs, as such, the findings from these researchers make it possible to produce syngas that meets the specifications of different downstream processes. Although the model provides the above-mentioned benefits, it includes 138 elementary reaction steps, and this could lead to a high computation costs if the strongly coupled equations are solved for all the steps. A sensitivity analysis can be done to determine how the kinetic, transport and thermodynamic properties of each process affect the overall process performance. The processes which do not have a significant influence can be neglected from the model equations, thus the computational speed can be increased.

It is difficult to carry out experimental investigations of the steps of the reaction mechanism in catalytic partial of methane to syngas (Hickman and Schmidt, 1992). This is because of the fast chemistry and high temperature conditions. Simulations have to be used for a detailed investigation of the reaction behaviour and the explanation of the underlying mechamism. Veser and Frauhammer (2000) investigated the importance of homogeneous side reactions, individual reaction steps and reactor parameters by means of a one-dimensional two-phase reactor model. The detailed chemistry and the elementary reaction mechanism are considered. In the model development the underlying assumptions made were that there are no mass transfer limitations and the homogeneous reactions were neglected. It was found that the reaction pathway is predominantly via a direct oxidation of methane to syngas on

a platinum surface. The reactor parameters that were found to be important are temperature and gas flow rate.

The addition of steam and CO_2 affects the ratio of H_2/CO in the effluent. Adding steam increases the ratio of H_2/CO, while the addition of CO_2 decreases methane conversion and the ratio of H_2/CO (De Groote and Froment, 1996). Given the importance of these factors, a study was undertaken by Hoang et al. (2005) to simulate an oxygen permeable membrane reactor for POM with steam addition. The model constituted a 2D unsteady heterogeneous model that takes into account kinetics and transport phenomena. The study was motivated by a realization that for conventional POM processes, there is a low concentration of hydrogen and high energy loss from heating large amounts of nitrogen. A 2D model was used to describe the behaviour of the gas in the reactor because the oxidation products and oxygen is transported from the vicinity of the membrane to the centre. The conclusions drawn from their study are that increasing the inlet gas temperature is favourable to partial oxidation of methane in an oxygen permeable membrane reactor (Figure 12). In addition, it was found that POM in permeable membrane reactor results in higher hydrogen concentration in the product in comparison to a conventional reactor, thus it can be used for practical applications.
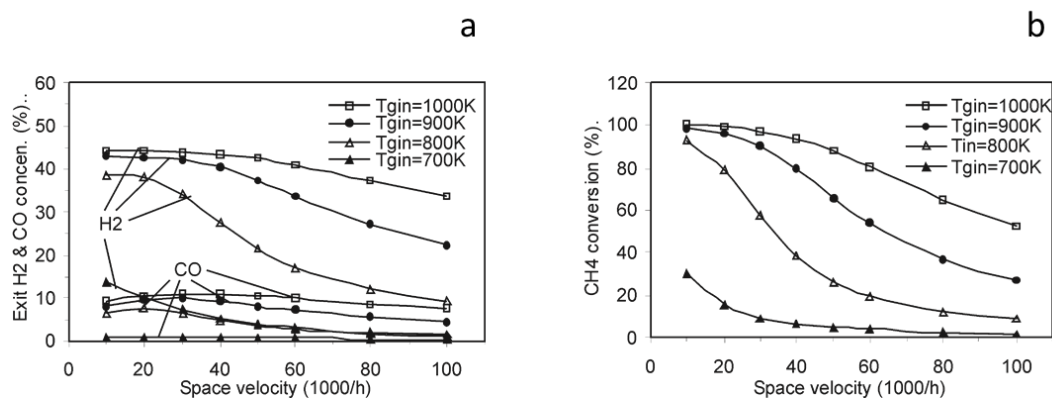
Figure 12: CH_4 conversion (b), exit H_2 and CO concentrations (a) versus gas space velocity at different gas temperatures (Hoang et al., 2005)

A one dimensional mathematical model aimed at describing the influence of process parameters on H_2/CO ratio was developed by Fernandes et al. (2006). The model considered an isothermal membrane reactor at steady state conditions and compared its performance with a conventional reactor. Their study revealed that temperature has

a pronounced effect on the ratio of H_2/CO. They indicated that while the effect of temperature on the ratio of H_2/CO is complex, the generally observed trend is a decrease in the ratio with an increasing temperature. Furthermore, it was demonstrated that the conversion of methane can be enhanced by recycling carbon-dioxide and steam and to the reactor entrance. There are multiple factors that influence the ratio of H_2/CO and in another analysis, Amin and Yaw (2007) demonstrated that by manipulating the ratio of methane, carbon dioxide and oxygen, a desirable ratio of H_2/CO can be achieved. These authors perfomed their analysis on a combined carbon dioxide reforming with partial oxidation.

A study to examine the production of syngas by partial oxidation of methane over Pt and Pt-Rh was undertaken by Hickman and Schmidt (1992). The study was carried out under short contact times (10^{-4} and 10^{-2} sec) and this allowed for the independent analysis of direct oxidation. The method of direct oxidation of methane which is represented by Equation 1.2 was employed. The methods that were used prior to the work of these researchers included a combination of oxidation and reforming reactions to produce syngas from O_2 and CH_4 (Blanks et al., 1990; Vernon et al., 1990; Dissanayake et al., 1991). The objective of the work of Hickman and Schmidt (1992) was to investigate a faster and efficient route of syngas production where H_2 and CO are the primary products of methane oxidation. However, such an approach is compounded by the reactions represented by Equations 2.13 and 2.14 which are faster compared to methane activation which is slow especially at low temperatures.

$$H_2 + \frac{1}{2}O_2 \rightarrow 2H_2O \tag{2.13}$$

$$CO + \frac{1}{2}O_2 \rightarrow CO_2 \tag{2.14}$$

Their study investigated the effect of mass transport, catalyst geometry and temperature on conversion and selectivity. The increase in linear velocity of gases was found to enhance the selectivity of syngas. Given that the direct methane oxidation was applied, and it is fast in nature, the mass transfer rate needs to be higher to minimize chances of H_2 and CO reacting with O_2. Furthermore, it was demonstrated that the catalyst geometry must be such that a thin boundary layer exists as this leads to reduced concentration of partial oxidation products near the surface.

Various mathematical models such as a transient 2D two-phase dispersion and steady-state 2D detailed flow have been used for monoliths, packed-bed reactors and membrane fuel cell systems (Deutschmann and Schmidt, 1998a; Bizzi et al., 2002; Bizzi et al., 2004). However, these methods did not include the effect of plasm on partial oxidation reactors using 2D heterogeneous models. Ra et al. (2012) undertook a numerical investigation of catalytic partial oxidation of methane to syngas using a plasma-assisted gliding arc reactor. Their numerical study entails a 2D heterogeneous plug flow model that considers radial dispersion, rate equations and transport for both gas and solid phase. The heterogeneous plug flow model was employed to relax the oversimplifications that a pure plug flow model makes regarding heat and mass transfer. The model included the main global reactions for catalytic partial oxidation of methane which are constrained to total oxidation, steam reforming, dry reforming and water gas shift reaction. A close agreement between experimental and model results was found. The influence of process parameters on the process performance was investigated.

The findings reveal that an increase in GHSV results in a decrease in the mole fraction of CH_4, O_2, H_2O and CO_2. Additionally, high GHSV results in lower H_2 and CO mole fractions and reactants conversion. The influence of feed composition was also investigated, and the findings revealed that an increase in O_2/CH_4 molar ratio results in an increase in reactor temperature and methane conversion. Furthermore, the H_2O and CO_2 mole fractions increased with the increase in O_2/CH_4 molar ratio, while the H_2 and CO mole fractions decreased.

Chaniotis and Poulikakos (2005) carried out a numerical investigation for a micro-reformer used in catalytic oxidation of methane for hydrogen production. The reactor model consists of a surface perfectly stirred reactor which is a simplified model. The simplied model was validated against the comprehensive models that involve Navier-Stokes equations. Their approach considers a single channel with no axial conduction as the channel walls are assumed to be thermally thin. In addition, the channel walls were considered to be adiabatic. However, axial conduction and radiation may change the system performance and must be considered. This is because the hydrogen yield and methane conversion are strongly dependent on surface temperature, hence conduction through the walls should be included. The underlying assumptions made

by the surface perfectly stirred reactor model are that the conversion of reactants to products is determined by the chemical reaction rates rather than by diffusion, convection or other transport processes. In addition, the authors state that due to short contact times and flow residence time in the channel, the outlet composition is not in thermodynamic equilibrium. However, for longer residence times, the outlet composition agrees with thermodynamic equilibrium.

The validity of this simplified method was determined to check whether it captures all the features manifested in 3D models that take into account both transport and chemistry. Their findings indicate that their simplified model agrees more satisfactorily with the models that solve the full Navier-Stokes Equations. Given the simplifications employed in their model, it was found that it is possible to perform thousands of simulations over a space of 3 hours on a 3.0 GHz Intel Xeon workstation, thus leading to a considerable reduction in computational expense. Such a fast simulator is important in that can be applied in geometric optimization and thus help alleviate pressure drop, hot spot formation and reduce manufacturing costs (economic analysis) in catalytic partial oxidation of methane.

2.7. Economic considerations

The chemicals industry has over many years dedicated its work to the development of technologies that ensure elimination of environmentally hazardous substances, sustainable development and maximize productivity at lower production costs (Kapteijn et al., 2001; Tomas, 2006). To achieve this goal, catalysts are often used as they allow for significant energy savings and reduce the production of by-products which could result in increased separation costs. Among the processes that have received substantial attention is the catalytic partial oxidation of methane to syngas on precious metal catalysts. This process has been shown to present many advantages over conventional processes such as steam reforming due low capital costs, low energy costs, low pressure drop and faster reactions which lead to short-contact times, hence compact reactor designs (Recupero et al., 1998; Welaya et al., 2012; Sengodan et al., 2018).

In the past, partial oxidation on a commercial scale was carried out by non-catalytic processes. This comes at a cost since higher temperatures (1250 -1500 ^{o}C) were

used. Recently, the development of highly active catalysts allowed for the operation at lower temperatures. The findings from the work of Chang and Heinemann (1993) indicated that partial oxidation of methane can be initiated at 400 ^{o}C if the Co/MgO catalysts with high Co loading (>28 wt%) are used. The CoO-Yb$_2$O$_3$ catalysts showed high selectivity and activity in the conversion of methane to syngas at temperatures below 700 ^{o}C (Choudhary et al., 1992). However, the precious metals used in the development of catalysts are expensive. Therefore, the design of the reactor and the catalyst should be such that the capital and operating costs are minimised. Campbell et al. (1994) asserts that the economics of partial oxidation dictates that the process be operated at a high pressure. This is because the gas volume doubles during the reaction process and there is need to compress the gas.

The catalytic partial oxidation of methane to syngas is carried out on precious metal catalysts such as platinum and rhodium. Given the high cost of the precious metals, the catalytic partial oxidation process has to be designed to allow for high profitability. The fast solvers for conversion, selectivity and other process parameters can help to facilitate the economic analysis. A fast solver allows for an investigation of a range of reactor configuration and operating conditions, thus the optimum operating conditions can be found. The catalytic partial oxidation of methane is characterised by the first few millimetres of the catalyst bed dominated by partial oxidation, and down the catalytic bed by the endothermic steam reforming and water gas shift reactions (Prettre et al., 1946; Hawk et al., 1932; Anderson and Boudart, 1983). Owing to the reactions reaching completion within a few millimetres of the catalyst entrance, it is possible to reduce the cost of catalyst fabrication.

The savings on capital cost in the production of syngas can be increased by combining oxygen separation from air with steam reforming and methane oxidation into a single unit. This is achieved through the application of oxygen transfer membranes (Mazanec et al., 2001). The economic analysis of the oxygen transfer membrane for syngas production revealed that the economic advantage is greater than 35% compared to the conventional processes. However, problems such as element fabrication, stress on ceramics and ceramic to metal seals have to be addressed for the process to be commercialised.

Carolan et al. (2001) performed the economic evaluation for the ceramic Ion Transport Membrane (ITM) technology for production of syngas from natural gas. This technology fabricates the membranes from non-porous, metallic oxides that operate at high temperatures and have high O_2 flux and selectivity. The high temperature syngas generation process and air seperation are combined into a single membrane reactor, and this results in significant cost reductions. The savings on capital cost were found to be greater than 33% when compared to a conventinal O_2-blown ATR/ASU technology for syngas production.

The non-uniform distribution of the active catalytic material on the monolithic walls can help reduce the cost of fabrication. Several studies on non-uniform catalyst distribution have been performed. Becker and Wei (1977) studied the durabilities of uniform and non-uniform catalyst distribution towards poisoning. The methodology that integrates an optimum reactor size with non-uniform catalyst and catalyst deactivation was developed by Hwang and Smith (2008). The researchers concluded that non-uniform catalysts reveal higher activity, selectivity and are resistant to poison in comparison to uniform catalysts. The superiority of non-uniform catalysts over uniform catalysts has been reported by several authors (Kasaoka and Sakata, 1968; Mars and Gorgels, 1964; Michalko, 1966; Michalko, 1966b). In the context of monolith reactors, in addition to the mentioned advantages of using the non-uniform catalysts, the economic benefits of employing such configurations are possible. Wu and Hammerle (1983) reported that a three-way catalyst which consists of Pd catalyst as the inlet half and Pt and Rh as the outlet half results in the reduction of precious metal cost when compared to an equal volume three way catalyst.

2.8. Experimental work on the catalytic partial oxidation of methane

Over the past years, there has been a substantial effort both experimentally and numerically to investigate the catalytic partial oxidation of methane to syngas. This section will focus on the work reported for the experimental investigation of catalytic partial oxidation of methane and identify some areas requiring further investigation for the improvement of the process.

Bizzi et al. (2002) performed theoretical and experimental investigations on the short contact time partial oxidation of methane on rhodium coated alumina spheres. On the

experimental part, the experimental set-up was split into four distinct sections; mixing section, reactor section, gas cooling section and gas analysis section. In their study a fixed bed reactor was used, and its choice was premised on the notion that fixed bed reactors offer a good performance particularly when it comes to stability and operation. They reported that methane conversion increases with increasing space velocity. Additionally, the catalyst surface temperature, selectivity of syngas and the gas-phase outlet temperature also increase with increasing space velocity. However, there are some inconsistencies in the literature on the effluence of space velocity as some authors report a decrease in methane conversion with increasing space velocity (Smith and Shekhawat, 2011). This is expected as an increase in space velocity results in decreased residence time.

Pino et al. (2002) investigated the use of partial oxidation of methane to produce hydrogen for polymer electrolyte fuel cells. The study was motivated by the many advantages partial oxidation of methane presents which include low cost, less energy intensive, compact designs and fast start-up (Recupero et al., 1998). However, to achieve the functionality, a catalyst that is active, resistant to carbon formation, offers little sintering and poisoning is desired. In their study, these researchers investigated the partial oxidation of methane with undiluted air on a ceria-supported Platinum (Pt/CeO_2) catalyst. The catalyst preparation was carried out by a novel solution-combustion method with varying metal loading. Their findings indicate that an excellent catalyst activity towards partial oxidation of methane is manifested at 2% Pt/CeO_2. Methane conversion was found to increase with both temperature and Pt content in the catalyst as shown in Figure 13. For example, at 0.5, 1 and 2% Pt/CeO_2, methane conversion (at 900 ℃, O_2:CH_4=0.5 and GHSV= 80000 h^{-1}) was found to be 82, 88 and 95% respectively. Additionally, they showed that there are no carbon deposits formed even after 100 h of reaction time under the operating conditions as required in hydrogen production for fuel cell electric vehicles. Given the advantages partial oxidation of methane presents in hydrogen production for fuel cells, an extensive research is needed to allow for a large-scale application of the process.
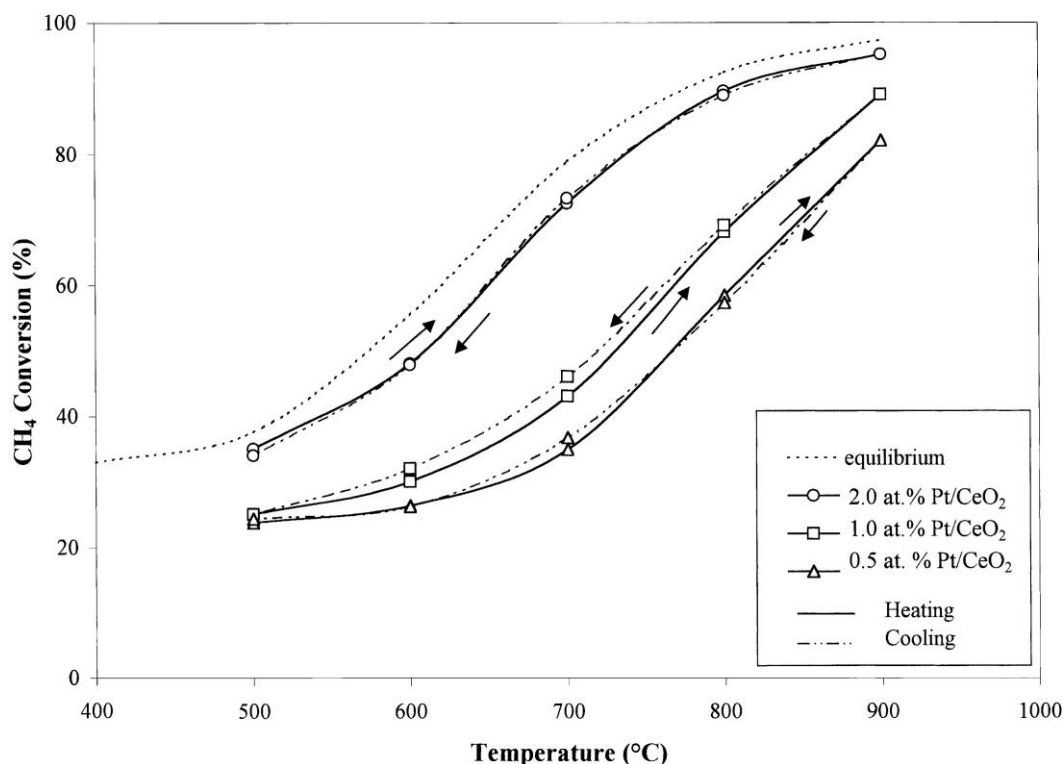
Figure 13: Effect of reaction temperature on CH_4 conversion over Pt/CeO_2 with different amounts of platinum (Pino et al., 2002)

The findings from the work of Pino et al. (2002) agrees with the work on methane partial oxidation over Pt/CeO_2 by Pantu and Gavalas (2002). These authors found that methane conversion increases with increasing temperature. Furthermore, the Pt/CeO_2 catalyst was found to maintain high conversion and selectivity when the feed ratio (CH_4:O_2) was changed from 1.7 to 2.3.

Space velocity affects the selectivity of syngas for the partial oxidation of methane. To investigate the extend of this influence under different support geometries, Hohn and Schmidt (2001) carried out a study using Rh-coated spheres. The catalytic support geometries used are alumina monoliths and non-porous alumina spheres. The method of preparation of both the support geometries was the same. The findings from their study reveal that the use of spheres as supports for partial oxidation of methane results in higher selectivity at all space velocities. However, the use of alumina monoliths as catalytic supports results in poor syngas selectivity at space velocities above $4x10^5$ h$^-$^{1}. The difference in the performance of the two support geometries at varying space velocities is attributed to the differences in heat transfer phenomena in the two geometries. Their heat transfer model revealed that higher rates of convection in

monoliths give rise to lower front temperatures as compared to spheres. The lower front temperatures lead to blowout and lower syngas selectivity.

A comparison on the performance of Rh and Pt catalysts for partial oxidation of methane was performed by Horn et al. *(2007)*. The analysis was done with respect to selectivity and yield in the oxidation zone, mass transport limitations, percentage contribution of partial oxidation and steam reforming to the yield of syngas. Both Rh and Pt catalysts were prepared by impregnating α-Al_2O_3 foam supports with aqueous $Rh(NO_3)_3$ and H_2PtCl_6 precursor solutions. Their findings reveal that both H_2 and CO are formed in larger amounts in the oxidation zone for a Rh catalyst compared to Pt.

In a similar manner to the oxidation zone, in the reforming zone, Rh was found to result in higher methane conversion than Pt. The length of the oxidation zone was found to be longer in Pt (2.33 mm) compared to Rh (1.33 mm) and the Pt catalyst was found to operate at a higher temperature. Both catalysts revealed that the methane partial oxidation is oxygen transport limited. These researchers concluded from the high-resolution spatial profiles that catalytic partial oxidation of methane is a combination of both partial oxidation and steam reforming. Additionally, the yield of H_2 was found to be higher in H_2 than Pt and this was attributed to the following reasons:

1. Rh allows for effective activation of CH_4 in the presence of O_2 than Pt
2. Rh forms H_2 more selectively in the presence of O_2 than Pt
3. Compared to Pt, Rh is evidently a more active steam-reforming catalyst.

According to Neagoe et al. (2015), the thermodynamic analysis reveal that the best operating conditions for partial oxidation of methane are ambient pressure and high temperatures (<900 ^oC). These authors state that the catalytic partial oxidation of methane is more efficient at low pressures as high pressures make it difficult to convert methane (to H_2 and CO) selectively. However, there have been studies that focus on high pressure methane catalytic partial oxidation (Lotti and Sliepcevich, 1967; Vernon et al., 1992; Lyubovsky et al., 2005; Kobayashi et al., 2011). One of the first authors to report some findings on methane oxidation at elevated pressures are Newitt and Haffner (1931).

The findings on methane partial oxidation at elevated pressures indicate that the concentrations water and carbon-dioxide increase with increasing pressure. However,

the effect of high pressure can be compensated by operating at high temperatures. This is evident from the work of Dissanayake et al. (1991), who reported that at 1173 K and 10 bar (Figure 14), methane conversion is higher than 80% while carbon-monoxide selectivity is higher than 90 %. The conclusion drawn from their study is that the production of syngas from methane is may be feasible at elevated pressures.
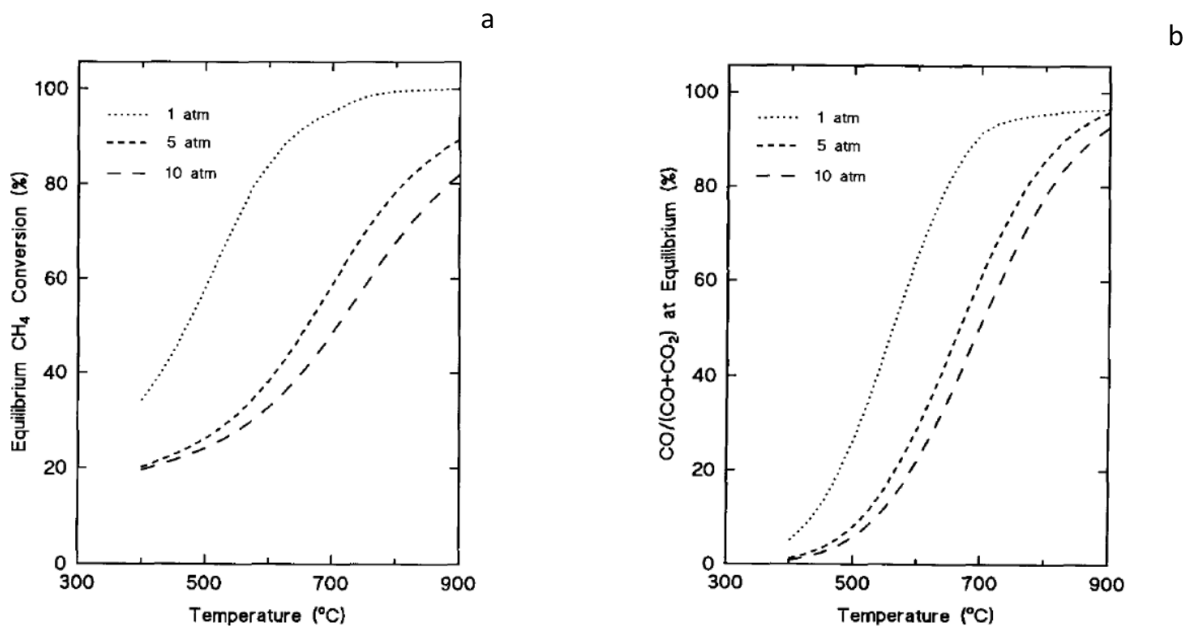
Figure 14: The effect of pressure and temperature on CH_4 equilibrium conversion (a) and equilibrium CO selectivity (b) at $CH_4/O_2=1.78$ (Dissanayake et al., 1991)

The investigations on the influence of pressure on the catalytic partial oxidation of methane in monolith reactors should be done at a constant inlet mass flow instead of a constant space time to avoid exaggerating the negative influence of pressure increase (Sari, 2017)

2.9. Summary

There have been some substantial developments in the modelling of catalytic partial oxidation of methane to syngas due to the many advantages it presents over the conventional methods such as steam reforming. Despite some intensive research work, catalytic partial oxidation has not replaced steam reforming on an industrial level. This is largely due to the formation of hot spots that ultimately leads to catalyst deactivation. Additionally, the complex interplay of total and partial oxidation results in the low yield of syngas and the slow technological progress of the process. Research into simulated heat transfer across multiple tubes appears to be limited due to the high

computational expense. Researchers that have considered heat transfer in multiple tubes have not included the homogeneous and heterogeneous reactions (Flytzani-Stephanopoulos et al., 1986; Cybulski and Moulijn, 1994), and those that included reactions have assumed that the surface and gas-phase reactions have one-step chemistry (James et al., 2003). To facilitate the design and optimization of the process and the scale-up for industrial applications, fast solvers are needed to allow for an investigation of a range of reactor configurations and operating conditions. The solutions to the described challenges can be found by the application of fast and robust methods.

Chapter 3. Research Objectives

Optimisation of monolith reactor systems is complicated by spatial distributions in heat and mass even momentum transfer. It is required that a simulation used for optimisation of the geometry be both fast-solving and exhibit a high level of accuracy. To facilitate geometric and economic optimisation, this programme aims to hybridise analytical solutions with effectiveness factor approaches to develop algebraic models that accurately represent the PDEs that describe monolith reactors. The hybrid model constitutes a cylindrical model that approximates the behaviour of a bundle of channels acting as axial heat sources.

The abovementioned hybridization is facilitated through the coupling of the modified plug flow model for a single channel monolith with the analytical solutions for heat transfer across the neighbouring channels. By their model construction, plug flow models neglect momentum, heat and mass transfer gradients. As a result of this, CFD models or lumped models that take into account the transport phenomena are often used (Nogare et al., 2011). The present work concerns an attempt to account for transport limitations by adopting an effectiveness factor approach for integration into a plug flow model. The simplifications made by the plug flow model on momentum, heat and mass transfer are relaxed through the application of effectiveness factor.

The model will help facilitate geometric optimization with the view of reducing manufacturing costs (by using less catalyst), and alleviating pressure drop and hot spot formation that deactivates the catalyst. In addition, the study concerns the use the hybrid model in the economic analysis of methane partial oxidation to gauge operating conditions and process parameters that maximize profitability

3.1. Hypothesis

The complex behaviour in monolith reactor modelling can be solved by coupling a two-scale model through a linear combination of two analytical solutions.

Objectives of the study

- Predict temperature, selectivity, surface coverage and concentration.
- Perform economic analysis to determine the operating conditions and parameters that maximize the process profitability.
- Perform sensitivity analysis to gauge the systems response to changes in feedstock ratio, channel diameter and kinetic data.
- Use CFD as a numerical experiment and benchmark to validate the hybrid model and the modified plug flow model.
- Compare the computational expense of the CFD multichannel model and the hybrid model.
- Determine the channel size and operating conditions that minimize the formation of local hot spot and ultimately prevent catalyst deactivation.
- Attempt to account for wall mass transfer by adapting an effectiveness factor approach for integration in a plug flow model.
- Determine whether the distribution of the catalytic material on the monolith walls can improve the economics of methane partial oxidation.

3.2. Key Questions

- Can the coupling of analytical solutions to single channel mass and momentum transfer with heat transfer across the single-shell extra- multi- channel space capture the same features observed from solving a detailed CFD multichannel model? Is there an equivalent homogeneous cylindrical model that approximates the behaviour of a bundle of channels acting as axial heat sources?
- Are the effectiveness factor approaches able to accurately correct the wall mass transfer?
- Can the reactor configuration be optimized to reduce the formation of local hot spot?
- Can the non-uniform distribution of the catalytic material on the monolithic walls improve the process economics of methane partial oxidation?

Chapter 4. Model Development

In heterogeneous catalysis, it is normally the case that the surface species may be large in number and this leads to numerous mass balance equations particularly in a case where a micro-kinetic modelling approach is adopted. In a case of a micro-kinetic model, where there is no assumption made regarding the rate limiting step, the full mass balance equation is solved for each component. The use of the micro-kinetic model in CFD simulations is required because the reduced mechanisms can result in significant deviations from experimental results (Partopour and Dixon, 2017). Therefore, the computational expense becomes high due to a large number of species, stiff and non-linear equations. The simulations of heterogeneous catalytic reactions in multi-channel monoliths is limited due to the high computational expense. To address this, the current study will develop a computationally efficient way of solving the governing equations in this multi-channel system by adopting a pseudo homogeneous approach.

The source terms from the balance equations often result in a stiff set of equations that increase the computational time in the solving of the catalytic reacting flows. There have been numerous approaches over the years that were developed to reduce computational expense in these systems (James et al., 2003; Goldin et al., 2009; Rebughini et al., 2017). Rebughini et al. (2017) used a cell agglomeration algorithm to help reduce the computational expense in a model that couples CFD with micro-kinetics to surface reactivity. The method works by grouping together the cells of the same thermo-chemical properties before calling the reaction step integrator. As a result, this leads to a significant reduction in the number of chemistry integrations. In the work of modelling heterogeneous catalytic systems in CFD, the computational cells are taken as independent batch reactors, as such, the method used by these researchers groups the cells on that basis. In such a grouping, the results from their work showed a considerable reduction in computing time in comparison to a case where such a grouping is not applied. Given that the computational expense is proportional to the number of lumped zones instead of the number of cells, the extension of this method to multichannel monoliths can address the high computational cost.

A simple multichannel model that investigates the effect of spatial coupling of channels was developed by James et al. (2003). The model approximates the convection term by linearization and includes heat transfer between channels. The underlying assumptions are that the heterogeneous and homogeneous reactions are a simple one step chemistry and diffusion is negligible. However, the design of monoliths for practical applications requires the use of more detailed approaches.

4.1. A numerical description of heterogeneous catalytic reacting flows

The numerical approach to describing the catalytic reacting flows constitute a system of conservation equations. The mathematical equations that describe flow processes are non-linear partial differential equations. The solution to these equations yields a distribution of concentration, temperature and velocity vector fields. The current study investigates catalytic partial oxidation of methane in monolith reactors. Both the single and multichannel monolith simulations are performed. The system is considered to be laminar and operated at atmospheric pressure. Pressure drop is considered to be negligible and both the uniform and non-uniform gas distribution in the channels is investigated. Furthermore, the distribution of the catalyst activity is taken to be uniform.

Given that the system under consideration is heterogeneous, there needs to be a mathematical description of both the gas and the solid phases. The description of reaction rates requires a chemical reaction mechanism that describes the reaction pathway. The DETCHEM reaction mechanism (Table 2) for partial oxidation of methane on platinum was employed (Quiceno et al., 2006). The micro-kinetic modelling is adopted, and in this approach no prior knowledge of the rate limiting step is needed as all the elementary reaction steps are considered.

Analytical solutions to these conservation equations are difficult to find, as such, numerical solutions are often adopted. A numerical solution should predict chemical reaction rates, transport and thermodynamic properties. The equations that describe fluid flow are the Navier-Stokes equations and are usually solved using CFD codes. For flow through tubes with homogeneous and heterogeneous reactions, the CFD codes are coupled with microkinetic solvers.

The equations that are used to describe the local reaction rate on the surface are expressed as a function of mean molar concentration are as shown in Equation 4.1.

The mean field approximation was employed, and the fractional surface coverage is described as shown in Equation 4.3. The Mean Field Approximation makes the assumption that the local state of the active surface can be represented by mean values of the species coverage (Kunz et al., 2011). In this case the reaction rate is represented as a function of the species molar concentration and surface and coverage. In the evaluation of chemical reaction rates, for a series of elementary steps, the most crucial rate is the intrinsic rate of the reaction which comprises rate of desorption, chemisorption and surface reaction. The kinetic data for evaluating these rates are obtained experimentally in the absence of heat and mass transfer limitations. The reason for using the intrinsic rate in this case is to avoid the double inclusion of the diffusion terms, as the diffusion terms are included in the overall reactor model (Hagen, 2006).

$$r_i{}^{het} = \sum_{k=1}^{k_s} v_{ik} k_{f_k} \prod_{j=1}^{N_g + N_s} [X]^{v'_{jk}} \qquad , \ i = 1, 2, \ldots, N_g + N_s \qquad (4.1)$$

Where $r_i{}^{het}$ is the formation rate of species i, X is the surface species molar concentration, K_s is is the number of elementary surface reactions, N_s is the number of adsorbed species and v'_{ik} are the stoichiometric coefficients.

The rate coefficients depend on temperature and are described by Equation 4.2,

$$k_{f_k} = A_k T^{\beta_k} \exp\left[\frac{-E_{a_k}}{RT}\right] \prod_{i=1}^{N_s} \theta_i{}^{\mu_{i_k}} \exp\left[\frac{\varepsilon_{i_k} \theta_i}{RT}\right] \qquad (4.2)$$

Where A_k is the preexponential factor, θ_i is the species surface coverage, E_{ak} is the activation energy, β_k is the temperature coefficient and R is the gas constant. The species surface coverage is calculated from Equation 4.3.

$$\sigma_{cat} \frac{\partial \theta_i}{\partial t} = r_i{}^{het} \qquad (4.3)$$

4.2.Modelling of a monolith

The modelling challenges in monoliths are twofold. The monolith consists of many thousands of channels, each with spatial distribution of heat and mass transfer even momentum transfer. Yet the systems sub-model needs to be relatively simpler.

A faster way of predicting state variables in a multichannel monolith would be adopting a pseudo homogeneous approach. The method treats a monolith bundle of channels as a single cylindrical channel, but with the same overall dimensions from a multi-channel case. Figure 15 is a representation of a full-scale monolith (a) and a monolith viewd using a pseudo homogeneous approach (b).
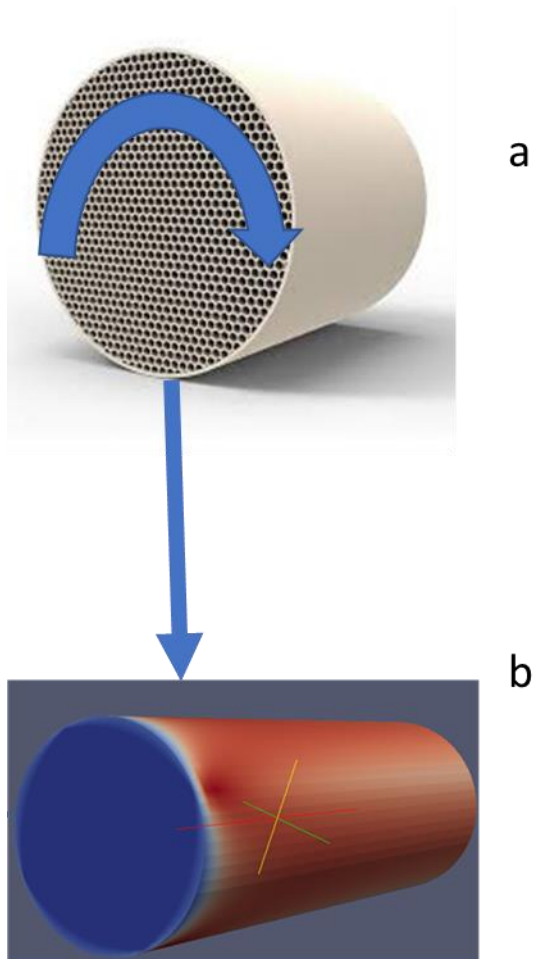
Figure 15: A schematic of a full-scale monolith reactor (a) and a pseudo -homogeneous model adopted in modelling a monolith reactor (b)

4.3. Scale and scope of modelling

Monolith reactor modelling can be classified in two scales, namely the micro and macro scales. The micro scale typically refers to the single channel with low to moderate computational time. On the other hand, macro scale refers to the bundle of channels (normally in the thousands) across which conduction results in strong coupling of fluid properties and hence the transport and kinetic characteristics in each channel. This coupling at the macroscale is the primary cause of the high computational expense of these systems. The schematic in Figure 16 illustrates the described notion.

Although the gas flow is in the channels, the local reaction temperature within a tube depends not only on the axial position but the radial position of the tube within the bundle. Chen et al. (1988) investigated the importance of radial heat loss and non-uniform flow distribution in monolithic catalytic converters. The findings from their study indicate that radial heat loss and non-uniform flow distribution lead to thermal gradients. This is illustrated in Figure 17 where radial heat loss and flow maldistribution result in severe thermal gradients. Therefore, the radial conduction of heat across the "bundle" of channels should be considered in monolith modelling. The first step in developing a fast solving model requires a high-speed simulation of the heat and mass transfer within a single channel. Integrating such a model into a multichannel monolith simulation, will make the overall simulation speed significantly higher.

The modified plug flow model, proposed herein, falls under the category of micro scale modelling since it treats a monolith as a single channel (Figure 16) and does not take into account the interaction of channels through heat transfer. The dispersed plug flow model coupled with effectiveness factor approaches can only be used to describe the chemical and physical phenomena in a single channel monolith. On the other hand, the second approach which utilizes the hybrid model falls under the macroscale modelling as the monolith is modelled as a bundle of thousands of channels.
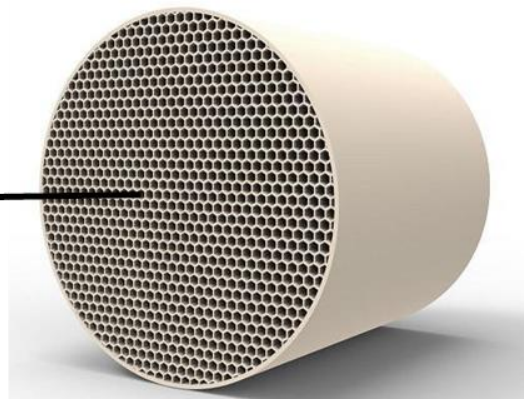
Figure 16: A schematic of a monolith reactor (IndiaMART, 2009)
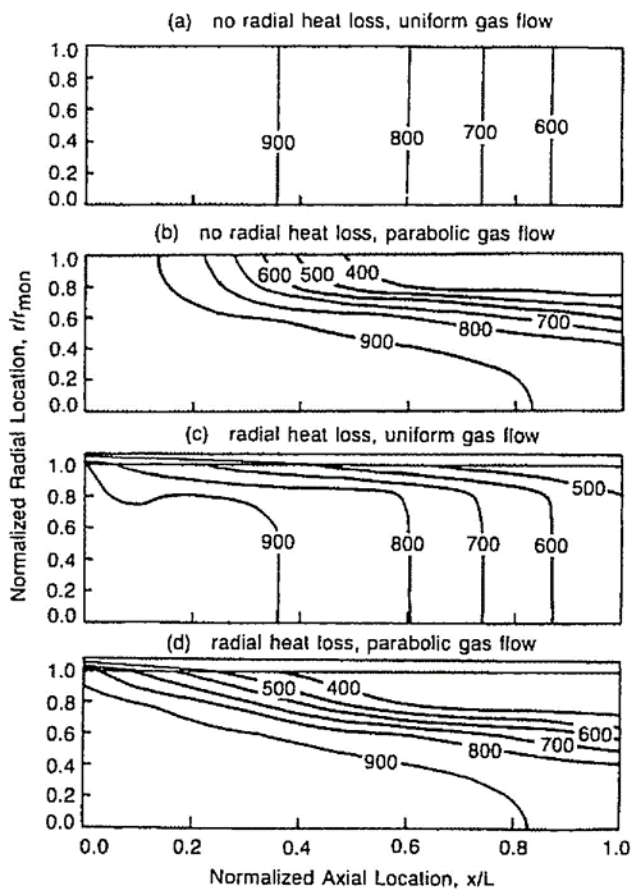
Figure 17: Temperature contours (Chen et al., 1988)

4.4. OpenFOAM

OpenFOAM was used in the modelling of partial oxidation of methane. OpenFOAM is a free computational mechanics tool that solves the Navier-Stokes equations numerically and makes use of C++ object-oriented libraries. The transport and reaction terms in conjunction with continuity and momentum equations were solved by the use

of OpenFOAM CFD code with the integration of an OpenFOAM solver named catalyticFOAM that performs CFD simulations with the micro-kinetics of surface chemistry. CatalyticFOAM is a microkinetics solver that allows for multiscale simulations for general geometries and is based on first-principles approach to heterogeneous and homogeneous reactions (Maestri and Cuoci, 2013). The solver consists of two kinetic libraries to manage the gas-phase chemistry and surface microkinetics. It employs the operator-splitting methods to split the governing equations into sub-equations and applies the best numerical methods for each sub-equation. As a result, this approach avoids the costly matrix operations which are often encountered in fully coupled algorithms.

The solution procedure in CFD comprises a 3-step process which involves pre-processing, solving and post processing.

4.5. Pre-processing

The pre-processing step entails the meshing and discretization of the flow domain. The discretization process involves the separation of the flow domain into a computational mesh which consist of cells (Maric et al., 2014). The collective of all the cells is the computational grid. The discretization which is done both temporally and spatially is carried out through the finite volume method. The grid independent solution is achieved by increasing the mesh resolution in the areas of the domain where larger gradients occur.

4.6. Finite Volume Method

The Finite Volume Method is a technique that is used to transform the partial differential equations that represent conservation laws into discrete algebraic equations (Moukalled and Mangani, 2016). Prior to discretising the governing equations, the solution domain is divided into a finite number of computation cells. A typical finite volume grid is as shown in

Figure **18**. The method employs the integration of the governing equations over a finite control volume to obtain the discretised transport equations. For example, a generic transport equation shown in Equation 4.4 is discretised as observed in equation 4.5.

$$\frac{\partial(\rho\phi)}{\partial t} + \nabla.(\rho U\phi) = \nabla.(\Gamma_\phi \nabla\phi) + S_\phi \qquad (4.4)$$

$$\int_t^{t+\Delta t} \left\{ \int_V \frac{\partial(\rho\phi)}{\partial t} dv + \int_S \rho U(\phi).ndS = \int \Gamma_\phi \nabla\phi.ndS + \int_V S_\phi dV \right\} dt \qquad (4.5)$$

In Equation 4.5, the variable *V* represents the volume of a computation cell, while *S* represents the surface of a computation cell. For a steady state operation, the first term of Equation 4.5 and the outer integral over time will vanish and the resulting equation is as follows,

$$\int_S \rho U(\phi).ndS = \int \Gamma_\phi \nabla\phi.ndS + \int_V S_\phi dV \qquad (4.6)$$

Where the first term is the net convective flux of scalar quantity ϕ, the second term is the net diffusive flux and the fourth term represents the source or sink. The integration of Equation 4.6 on a computational cell requires two levels of approximation. The first level entails the approximation of the surface or volume integrals in terms of variable values on the cell face within the control volume (Ranade, 2001). At the second level, the approximation of variable values is done in terms of the values of the computational nodes (cell centres).
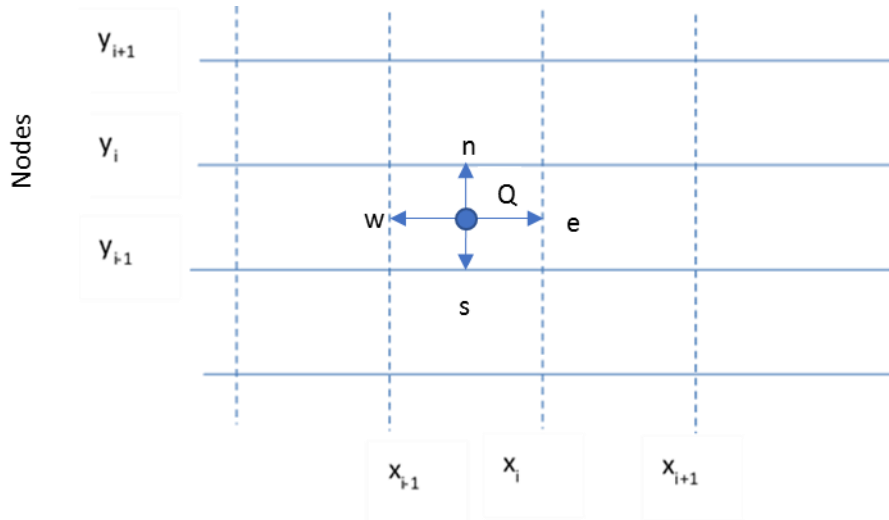
Figure 18: A finite volume control volume for a cartesian grid

The first level approximation for a control volume centered on node Q in

Figure 18 is done by a second-order approximation to replace the volume or surface integrals. The flux through the control volume boundary can be calculated as follows,

$$F_e = \int_{S_e} f ds \qquad (4.7)$$

Where *f* represents the component of the diffusive of convection vector which is normal

to face S_e and e in the area of face e. The second-order approximation of Equation 4.7 results in Equation 4.8.

$$F_e = f_e S_e \tag{4.8}$$

Where f_e represents the value of the integrand at the centre of face e.

4.7. Operator splitting schemes

The micro-kinetics solver developed by Maestri and Cuoci (2013) solves the transport reaction equations by employing the operator splitting schemes. The operator splitting becomes an effective approach because in solving these equations it separates the reaction and transport terms. Ren & Pope (2008) applied the strang splitting schemes on the form of the time-dependent reaction-transport system shown in Equation 4.9.

$$\frac{dr}{dt} = S(r, u(r)) + M(r, u(r), t) \tag{4.9}$$

In Equation 4.9, S represents the rate of change of the primary variables due to chemical reactions, M denotes the change of primary variables resulting from transport processes, r denotes the dependant primary variables and u denotes the secondary variables which are known functions of r. These researchers described the different splitting schemes in a threefold process.

The first step entails the integration of the reaction terms over a time interval $\Delta t/2$. This is done by solving Equation 4.10.

$$\frac{dr^a}{dt} = S(r^a, u(r^a)) \tag{4.10}$$

In this process, the initial condition which is denoted by $r^a(0)$ becomes the final state r from the previous time step. The solution from Equation 4.10 is represented by $r^a(\Delta t/2)$. The second step involves the integration of the transport terms over the time step Δt by solving Equation 4.11.

$$\frac{dr^b}{dt} = M(r^b, u(r^b), t) \tag{4.11}$$

In this case the initial condition which is denoted by $r^b(0)$ becomes the final state from step 1, $r^a(\Delta t/2)$, and the solution of Equation 4.11 is represented by $r^b(\Delta t)$. The final step is similar to the first time and it consists in taking the final state of step 2, $r^b(\Delta t)$, as the initial condition. The final state of the system is represented by the solution $r^b(\Delta t/2)$ and this solution is used as the initial condition in the next time step.

The operator splitting is second order accurate in time and space (Khan and Liu, 1995). The spatial accuracy is achieved when the time step is close to the stability limit. A converged and stable solution can be achieved by mesh refinement.

Chapter 5. Modelling of a single channel monolith

5.1. Governing Equations

In the first step toward developing a fast-solving hybrid simulation, a detailed CFD simulation was used to obtain the unsteady state, spatial temperature and concentration profiles for a range of input conditions. The single channel monolith CFD simulation was then accepted as a benchmark to which the modified plug flow model was measured against to be considered as viable. The single channel simulations were performed on the cylindrical monolith depicted in Figure 19. The species mass fractions and temperature profiles from the modified plug flow model were validated against the single channel channel CFD results. Upon validation, the modified plug flow model was embedded into the multichannel simulation for the fast solving hybrid model.

The governing equations for modelling a single channel monolith are presented in Equations 4.3, 4.12 to 4.16 and are applicable to both surface and gas phase reactions. The law of conservation of mass describes the increase of mass in a fluid element as equivalent to the net flow rate of mass into the fluid element. The conservation of total mass for a Newtonian fluid is as shown in Equation 4.12.

Mass and energy balances are represented by Equations 4.14 , 4.15 and 4.16 respectively. The energy of a fluid element is described as the sum of gravitational potential energy, internal and kinetic energy. The first law of thermodynamics describes the rate of change of energy of a fluid element as equal to the rate of heat addition to the fluid element and the rate of work done on the fluid element (Versteeg and Malalasekera, 2007). The energy Equation is represented by Equation 4.15 and 4.16. The right-hand side of Equation 4.14 describes the reaction rate and the transport by diffusion.

Momentum transfer is represented by Equation 4.13 and its right-hand side describes pressure gradient, viscosity and other body forces. The rate of change of momentum is defined by the Newton's second law as the sum of forces on the fluid particle. The application of the operator splitting schemes makes an assumption that the chemical reaction terms are stiff while the transport terms are non-stiff (Ren and Pope, 2008; Maestri and Cuoci, 2013). The non-linearity of the set of equations is in the source

terms which are non-linear in both temperature and concentration. The spatial and temporal scales are long due to the numerous species to account for and this results in significant computational expense of the simulation.

The governing equations represented by Equations 4.3, 4.12 to 4.16, the resultant boundary conditions (inlet boundaries,outlet boundaries and catalytic walls) and surface chemistry form a complete theoretical framework to describe the entire flow domain in terms of T, p, x and u. Where T is temperature, p is pressure, x is the species mass fraction and u is the velocity profile respectively.

$$\frac{\partial \rho}{\partial t} + \nabla.(\rho u) = 0 \tag{4.12}$$

$$\frac{\partial}{\partial t}(\rho u) + \nabla.(\rho u u) = -\nabla p + \nabla.[\mu(\nabla u + \nabla u^T) - \frac{2}{3}\mu(\nabla u)I] + \rho g \tag{4.13}$$

$$\frac{\partial}{\partial t}(\rho x_k) + \nabla.(\rho x_k u) = -\nabla.(\rho x_k U_k) + r_k^{\text{hom}} \tag{4.14}$$

$$\rho \hat{C}_p \frac{\partial T}{\partial t} + \rho \hat{C}_p u \nabla T = \nabla.(\lambda \nabla T) - \rho \sum_{k=1}^{N} C_p x_k U_k - \sum_{k=1}^{N} \hat{H}^{\text{hom}} r_k^{\text{hom}} \tag{4.15}$$

$$\rho \hat{C}_p \frac{\partial T}{\partial t} = \nabla.(\lambda_{solid}\nabla T) + Q^{het} \tag{4.16}$$
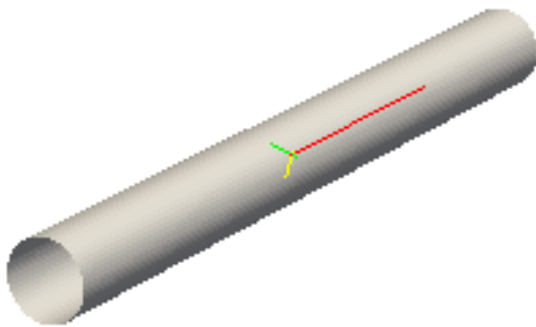
Figure 19: A cylindrical monolith

The coupling of surface micro-kinetics and the resultant transport properties was achieved by making use of a reaction mechanism for catalytic partial oxidation of methane over Pt gauze developed by Quiceno et al. (2006). The total number of species from the reaction mechanism is 16 which consists of 6 gas phase species and 10 adsorbed species. The reaction mechanism is presented in Table 2 and mechanism with the associated kinetic data is shown in Table 15.

5.2. Initial and boundary conditions

The solution of a set of governing model equations demands that initial and boundary conditions to be specified. The boundary conditions are used to determine the influence of the surrounding environment on the flow processes. Ranade et al. (2002) stated that the solution domain, coordinate system employed in formulating the model equations and the characteristics of the model equations are used to determine the boundary conditions requirements.

The commonly used boundary conditions are the Dirichlet and Neumann boundary conditions. The Danckwerts-type boundary conditions for are represented by Equations 4.19 and 4.20 (the Danckwerts-type were used for a cylindrical channel and Dirichlet for a square channnel). In Equation 4.19, u is the velocity vector, x_k is the mass fraction, ρ is density and D_k is the diffusion coefficient. The left-hand side of Equation 4.19 represents mass flux due to both diffusion and convection. By employing the analogy between heat and mass transfer, and equivalent inlet condition for temperature is as shown in Equation 4.20. The heat and mass flux at the outlet boundaries are assumed to be zero as shown in Equations 4.21, 4.22 and 4.23. The boundary conditions at the reacting catalytic walls are represented by Equations 4.24 and 4.25. In these two Equations, A_{cat}/A represents the ratio of the effective catalytic area (active sites per m^2) to the total geometric area. The Equations show the heat flux due to the exothermic reactions at the catalytic walls and the mass flux due to the species reactions at the walls. The no-slip boundary condition was imposed for velocity at the walls and for pressure a fixed value at the inlet was specified and a zero gradient at the outlet and reactor walls.

5.2.1. Inlet boundary conditions

In this boundary, velocity, temperature and the composition of the feed stock is assumed to be known. The velocity boundary condition is represented by Equation 4.17, where the velocity at the inlet has the known value U_{set}. The total mass flux for each gas phase species and the gas phase temperature is specified using the Danckwerts' conditions in Equation 4.19 and 4.20.

$$U_{in} = U_{set} \tag{4.17}$$

$$\nabla T_{solid}|_0 = 0 \tag{4.18}$$

$$\rho u x_k |_{inlet} - \rho D_k \nabla x_k |_{inlet} = \rho u x_k |_0 \tag{4.19}$$

$$\rho u \hat{H}_k |_{inlet} - \lambda \nabla T |_{inlet} = \rho u \hat{H}_k |_0 \tag{4.20}$$

5.2.2. Outlet boundary conditions

At the outlet boundary, the heat flux and the mass flux are assumed to be equal to zero as shown in Equation 4.21, 4.22 and 4.23.

$$\nabla x_k|_{outlet} = 0 \tag{4.21}$$

$$\nabla T|_{outlet} = 0 \tag{4.22}$$

$$\nabla T_{solid}|_{outlet} = 0 \tag{4.23}$$

5.2.3. Catalytic Walls

At the catalytic walls, a no slip boundary condition is imposed for velocity. For the scalar properties such as temperature and species concentration, the boundary condition is represented by Equations 4.24 and 4.25.

$$\rho D_{k, mix}(\nabla x_k)|_{solid} = \frac{A_{cat}}{A} r_k^{het} \tag{4.24}$$

$$\lambda_{gas} \nabla T|_{gas} = (\lambda_{solid} \nabla T)|_{solid} \tag{4.25}$$

5.3. Solving

Solution development begins with the choice of appropriate solvers to approximate the solution. The nature of the mesh (geometry and topology) and the underlying mathematical model dictate the time spend to obtain the solution. The geometry and meshing were performed in OpenFOAM blockMesh utility and are shown in Figure 20 and Figure 21. The governing Equations were solved by catalyticFOAM, a CFD micro-kinetic solver for heterogeneous catalysis developed by Maestri and Cuoci (2013). These authors validated catalyticFOAM against experimental data and Ansys FLUENT for a fuel-rich H_2 combustion in an annular isothermal reactor. A close agreement with a maximum relative error of less than 1% was found.

The Equations 4.1 and 4.3 represent a set of stiff equations and for their solution, the BzzOde numerical libraries were used due to their best performance in handling stiff equations (Ferraris and Manca, 1998) .The homogeneous reactions were not taken into account as low pressure was considered. Numerical stability, convergence and consistency are the properties of the numerical method that should be achieved by any solution approach adopted. The solution is taken to have converged if the numerical solution and the exact solution are in close agreement as the grid spacing tends to zero. To ensure that a solution is consistent, a mesh sensitivity analysis is carried out until a grid independent solution is found. When the truncation error is zero, a solution is taken to be consistent.

In the current study a grid size corresponding to 600 axial cells and 15 radial cells was found to be an optimum grid at which the results of the predicted state variables are resolution independent. The mesh sensitivity results are presented in Figure 22. In this case, the mass fraction profiles along the reactor axial coordinate reveal that the profiles are resolution independent from 600 axial cells and 15 radial cells.
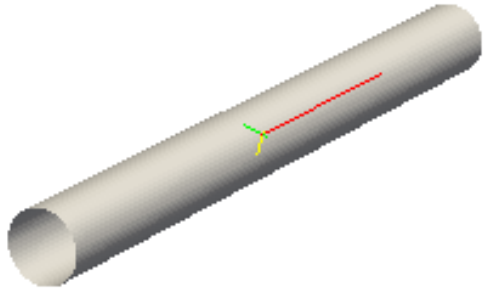
Figure 20: A single channel monolith
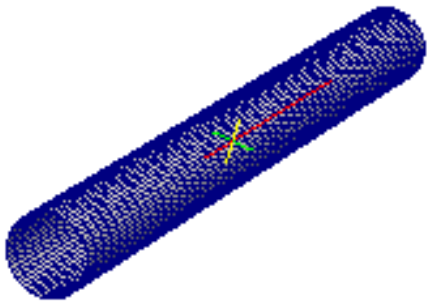
Figure 21: A depiction of mesh generation for a single channel monolith
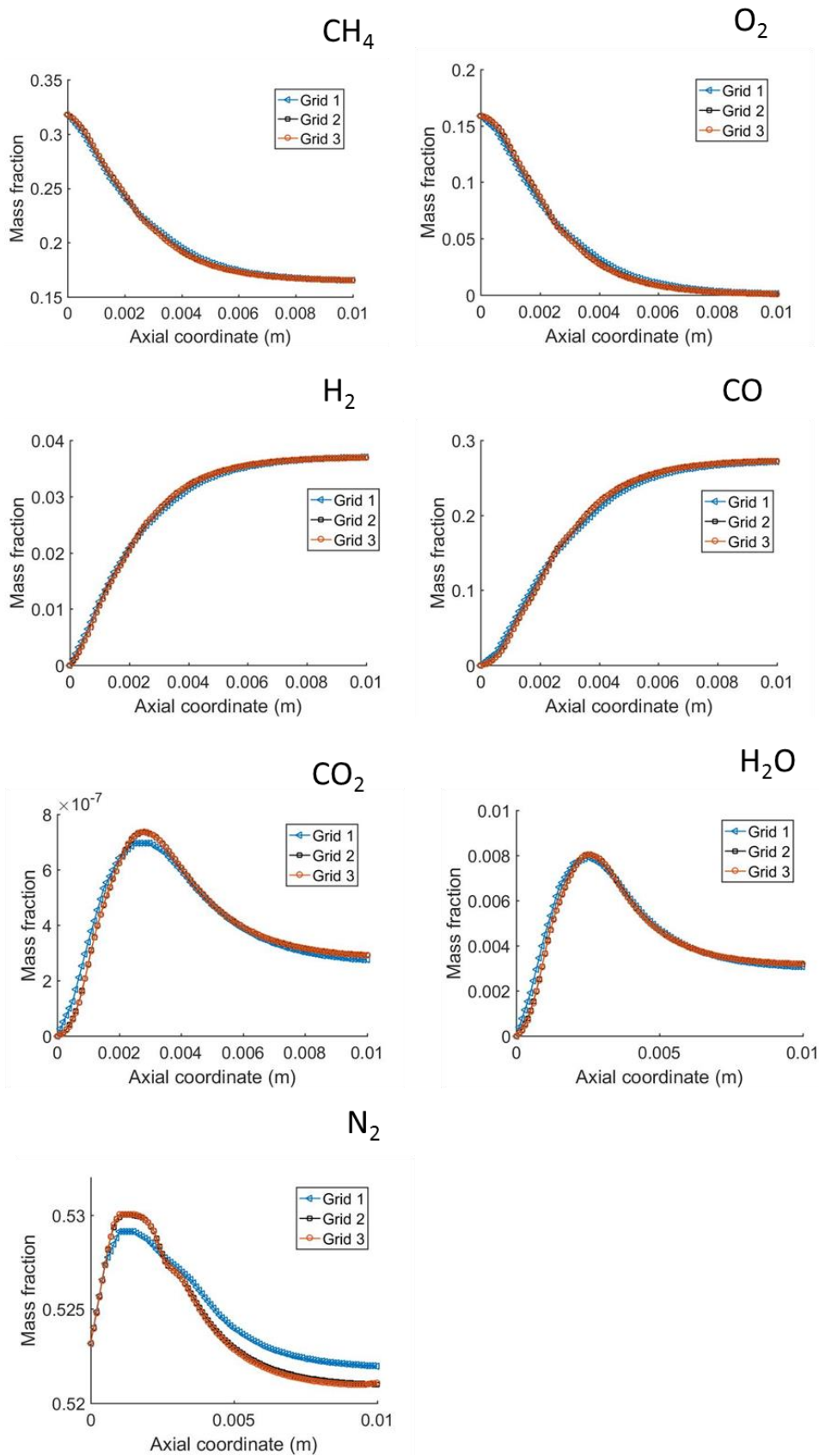
Figure 22: Grid dependence in the prediction of mass fraction profiles in a monolith (300 axial cells and 15 radial cells(Grid 1), 600 axial cells and 15 radial cells (Grid 2) and 1200 axial cells and 15 radial cells (Grid 3))

The temperatures of the gas and the catalyst at the three different grids were compared and are shown in Figure 23. As in the case of mass fraction profiles, the optimum grid size was found to be 600 axial cells and 15 radial cells.
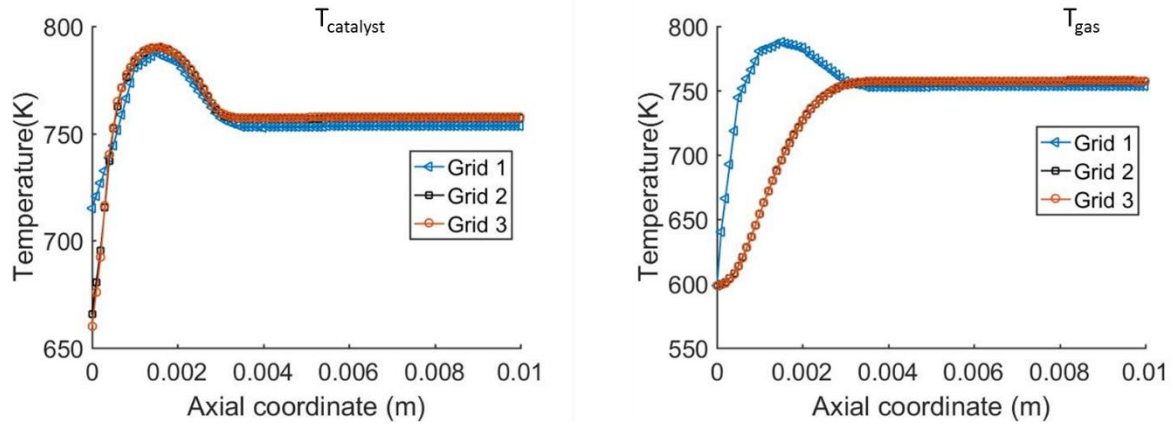
Figure 23: Grid dependence in the prediction of temperature profiles in a monolith (300 axial cells and 15 radial cells(Grid 1), 600 axial cells and 15 radial cells (Grid 2) and 1200 axial cells and 15 radial cells (Grid 3))

A grid convergence index method for mesh refinement studies in CFD by Roache (1994) was used to provide the order of convergence accuracy and the error band on the grid convergence of the numerical solution. This method is based on Richardson extrapoloation and the grid convergence index is calculated as shown in Equation 4.23,

$$GCI = \frac{F_s |\varepsilon| r^p}{(r^p - 1)}$$ (4.23)

Where F_s is the safety factor, p is the order of accuracy, ε is the relative error and r is the grid refinement ratio. In the current study, the value of F_s is taken to be 1.25 because three different grids are compared and the value of r is 2. The order of accuracy is expressed as follows,

$$p = Ln\left(\frac{f3 - f2}{f2 - f1} \middle/ Ln(r)\right)$$ (4.24)

Where f represents the solutions from grids 1, 2 and 3. The mass fractions for CO, H_2, CO_2 and H_2O at 5.5 mm from the inlet are presented in Table 3. The corresponding order of convergence accuracy and grid convergence index are also shown. The species mass fractions at zero grid spacing is calculated from Equation 4.25,

$$f_{exact} \cong f_1 + \frac{f_1 - f_2}{r^p - 1} \qquad\qquad (4.25)$$

Where f_1 and f_2 are the discrete solutions from the two finest grids.

Table 3: Species mass fraction at different grids (calculated at 5.5 mm from the channel inlet)

Species	Grid 1	Grid 2	Grid 3	Zero grid spacing
CO_2	6.966E-07	7.295E-07	7.32E-07	7.3198E-07
H_2O	4.274E-03	4.253E-03	0.00425	4.2502E-03
CO	2.466E-01	2.510E-01	0.251265	2.5129E-01
H_2	3.474E-02	3.503E-02	0.035054	3.5055E-02

Table 4: Mesh refinement analysis using Richardson extrapolation

Species	p	ε_{12}	GCI_{12} (%)	ε_{23}	GCI_{23}(%)	GCI_{12}/GCI_{23}	r^p
CO_2	3.81	4.72E-02	0.453	3.22E-03	0.031	14.67	14.01
H_2O	3.34	5.07E-03	0.069	5.03E-04	0.007	10.07	10.12
CO	3.83	1.78E-02	0.169	1.23E-03	0.012	14.46	14.21
H_2	3.85	8.38E-03	0.078	5.77E-04	0.005	14.54	14.42

The results in Table 4 indicate that the asymptotic range is achieved because $GCI_{12}/GCI_{23} \approx r^p$. The order of convergence accuracy for all the species is less than 3.9 and the mass fractions have an uncertainty of less than 0.5%. The species mass fractions at zero grid spacing (Table 3) have an error band less than 0.03%.

5.4. Post processing

 Post processing entails the analysis of the results which include temperature, concentration, pressure and velocity vector fields. In OpenFOAM, where parallel computing is performed to solve the computationally expensive problems on high resolution, this step involves reconstruction of the decomposed domain and generating the plots of interest. In domain decomposition, the mesh and associated fields are broken into various processors for numerical solution. For post processing, the mesh and the field data were reconstructed to generate the complete domain.

5.5.Summary of CFD modelling of a single channel monolith

The temperature and mass fraction profiles for a laminar flow (Re=16.8) in a single cylindrical monolith channel simulation are as observed in Figure 24 and Figure 25. The simulations were perfomed at the initial temperature of 598.15 K and the species mass fractions were 0.318 (CH_4), 0.159 (O_2) and 0.523 (N_2). The summation of species mass fractions in Figure 24 was confirmed to be unity.The 3D plots indicate that there exist radial gradients up to 0.005 m axial coordinate, beyond this point the radial gradients disappear. The competition between total and partial oxidation is evident as there are steep radial gradients of total oxidation products (CO_2 and H_2O) in the few millimetres from the entrance. At this region, there is a high concentration of O_2 and this results in the formation of total oxidation products. The surface coverage results in Figure 26 reveal that carbon coverage increases to the channel exit and this agrees with experimental observations (Deutschmann and Schmidt, 1998b).The temperature profiles in Figure 25 indicate that there is a formation of local hot spot and this is a common challenge in catalytic partial oxidation of methane.
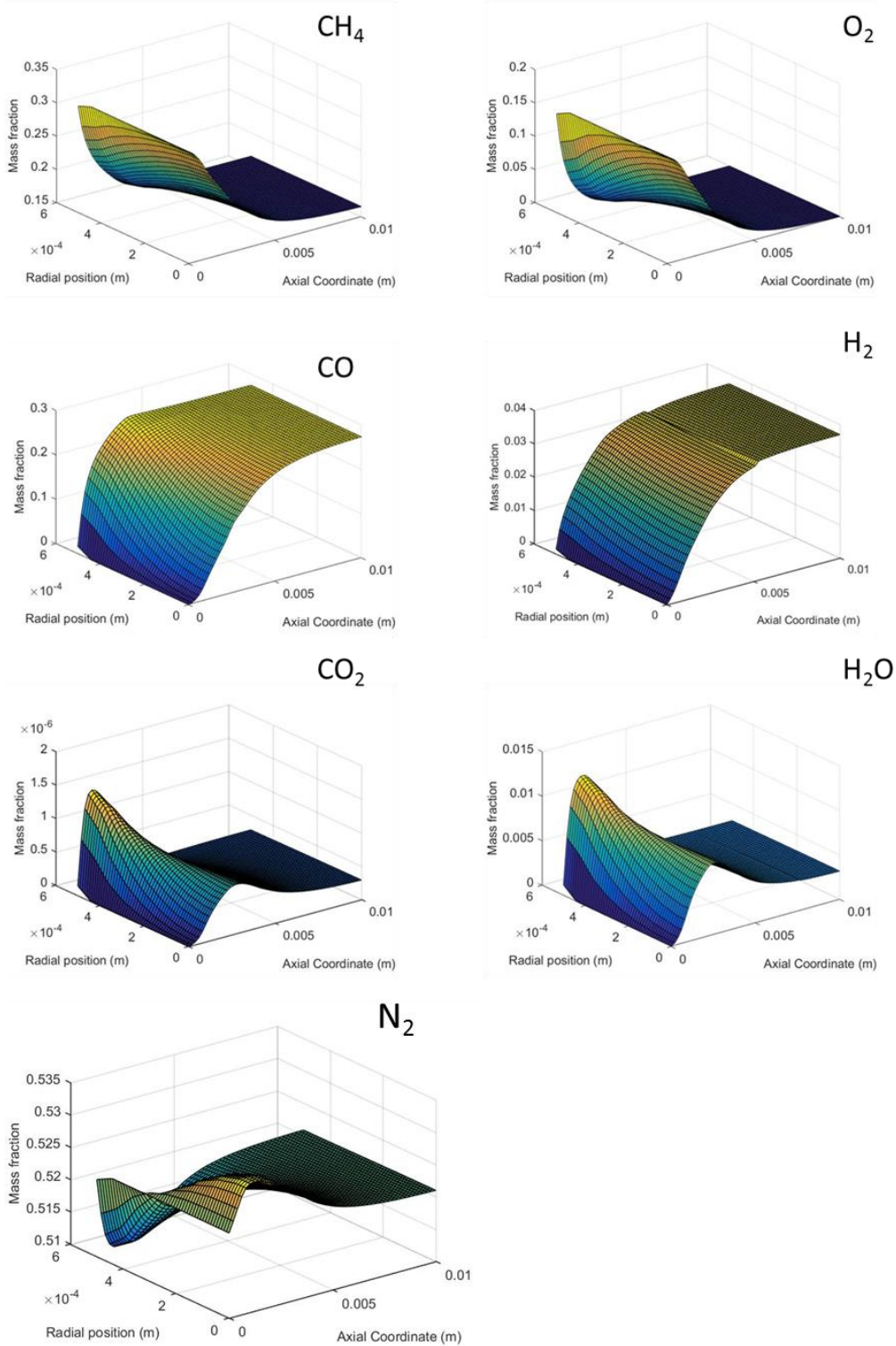
Figure 24: 3D mass fraction profiles along the reactor radial and axial coordinate (a monolith with 10 mm in length and 1.0 mm diameter)
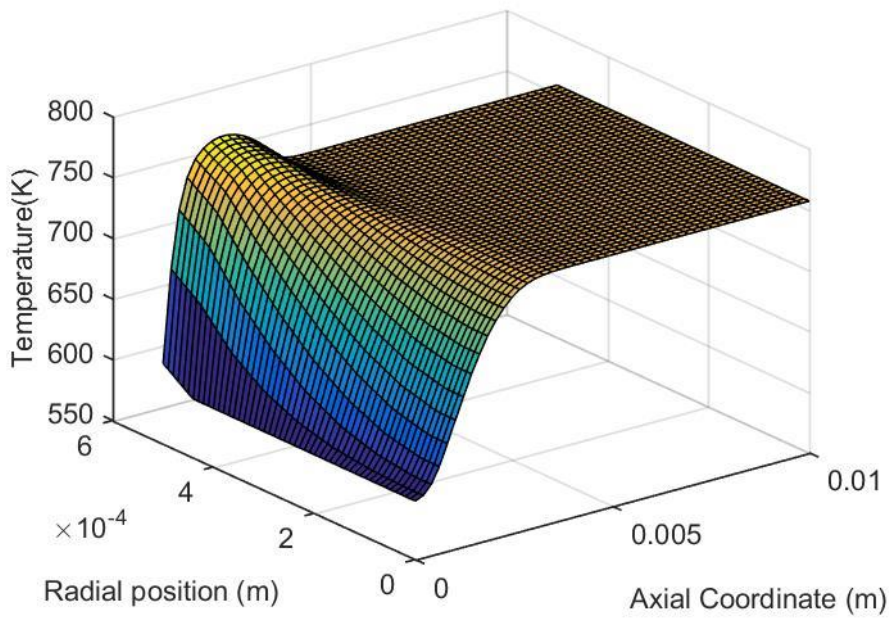
Figure 25: 3D temperature profiles along the reactor radial and axial coordinate (a monolith with 10 mm in length and 1.0 mm diameter)
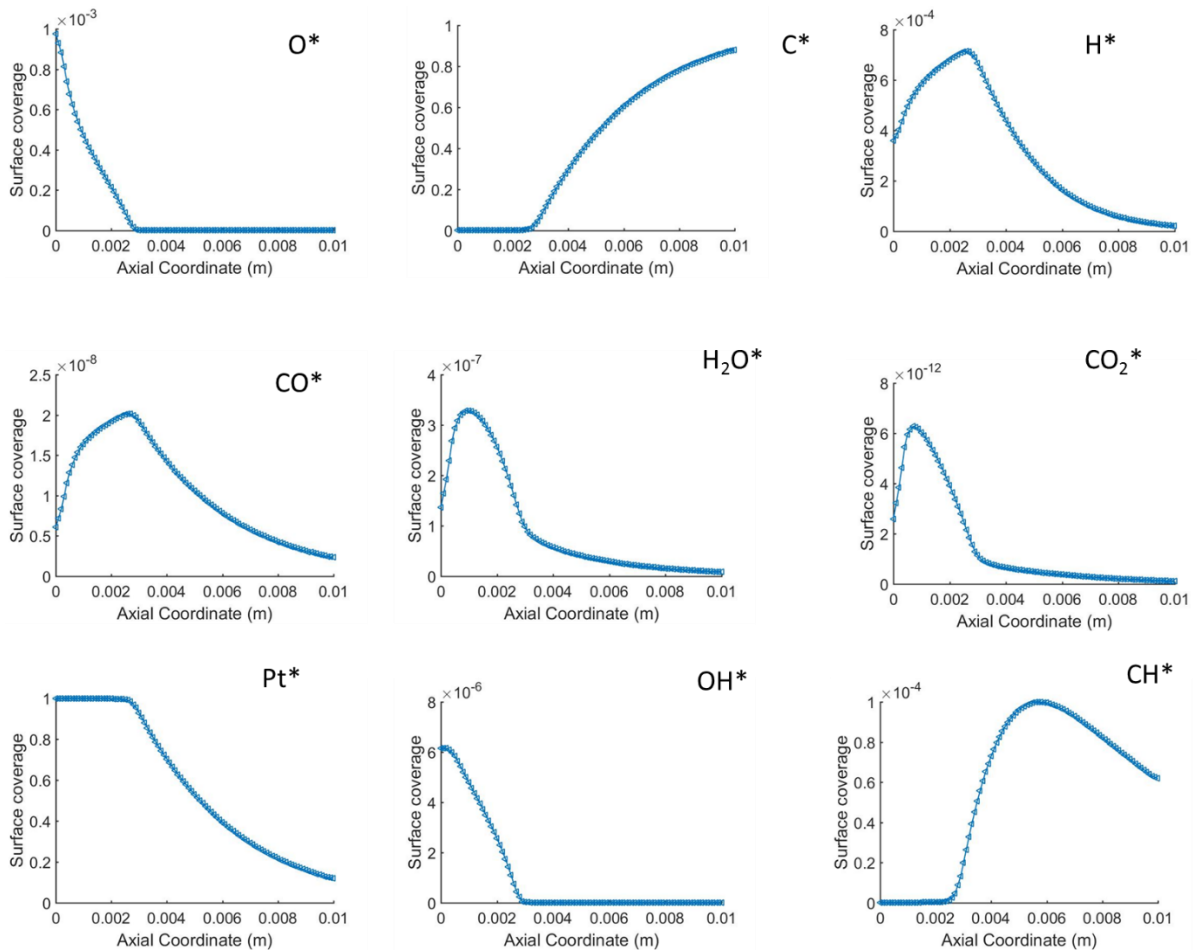
Figure 26: Species surface coverage along the axial coordinate (a monolith with 10 mm in length and 1.0 mm diameter)

5.6. A dispersed plug flow approach for a single channel monolith

A dispersed plug flow model was used to model a single channel monolith instead of an ideal plug flow because the axial dispersion considered is sufficient to capture the complex transport patterns and the radial and axial flow in a monolith (Dudukovic and Felder, 1983). The applicability of the dispersion model is dependent on the value of Peclet number (can only be used for Peclet numbers greater than 20). Given that not the entire reactor wall is covered with the active element   to gauge the reaction rates, the ratio of the impregnated catalytic area to the geometric area was identified as a key adjustable variable in Equations 4.33, 4.34 and 4.35. Although the flow is laminar, the reaction rates are strongly non-linear. It was determined that the dispersion model that approximates the laminar flow was the best approach to modelling this problem.

A dispersed plug flow model is represented by Equation 4.33. The gradients considered in this case are only longitudinal. The simplifications made by the plug flow model with regards to heat and mass transfer result in different reaction rates observed in the CFD model and the Plug Flow model. In particular, the dispersion model assumes homogeneous reaction, whereas the CFD model models the real-world situation of surface reaction. It should be noted that the equivalent homogeneous reaction rate was determined by translation between reaction volume and catalytic specific surface area as shown in Equation (4.26). Where the left-hand side represents the area-based rate (r'') and the right-hand side the volumetric reaction rate (r). The underlying assumption in the development of the simplified general flow equations is that the fluid is incompressible.

$$r'' A = rV \tag{4.26}$$

An effectiveness factor approach was adopted to account for these differences. The effectiveness factor approach is an attempt to account for the presence of mass transfer limitations. This correction allows for accurate estimates of species concentrations and thereby more accurate estimates of the real reaction rate. The isothermal and non-isothermal cases were considered in the use of the effectiveness factor (η) as a correction factor. For an isothermal case, the effectiveness factor for larger values of Thiele modulus is described by Fogler (2006) as presented in Equation 4.27. In the non-isothermal simulations, the effectiveness factor (Equation 4.29) was

estimated using parameters β and γ Fogler (2006). For effectiveness factor greater than unity, Equation 4.29 is used to approximate the values of effectiveness factor (Herz, 1975). The non-isothermal effectiveness factor a range of ($\beta\gamma$) values was proposed by Liu (1969) and is as shown in Equation 4.28 .The parameters β and γ are estimated as observed in Equation 4.30 and 4.31, where γ (Arrhenius number) is the dimensionless activation energy and β (maximum temperature difference) is the dimensionless heat of reaction.

$$\eta = \left(\frac{2}{n+1}\right)^{\frac{1}{2}} \frac{3}{r} \sqrt{\frac{D^{n-1}}{k}} \tag{4.27}$$

$$\eta = \frac{1}{\phi} \exp\left[\frac{\beta\gamma}{5}\right] \tag{4.28}$$

$$\eta = \left(\frac{2}{n+1}\right)^{\frac{1}{2}} \frac{3}{r} \sqrt{\frac{DC^{n-1}}{k}} \exp(\frac{\beta\gamma}{5}) \tag{4.29}$$

$$\gamma = \frac{E}{RT_s} \tag{4.30}$$

$$\beta = \frac{T_{max} - T_s}{T_s} \tag{4.31}$$

The effectiveness factor is used to correct the wall mass transfer as shown by Equations 4.32.

$$r'' = \frac{A_{cat}}{A} \eta \, r_s'' \tag{4.32}$$

The reaction rate from Equation 4.32 is used in Equation 4.33 and 4.35, thus in this case the concentration used is equal in magnitude with the concentration used in the reaction rate terms in a channel model. A reaction mechanism for catalytic partial oxidation of methane over Pt gauze developed by Quiceno et al. (2006) was used. The total number of species from the reaction mechanism is 16 which consists of 6 gas phase species and 10 adsorbed species. The boundary conditions at the inlet and outlet are demonstrated in Equations 4.36 through 4.37 respectively.

$$\rho \frac{d(x_k u)}{dz} = \frac{A_{cat}}{A} r_k - \rho D \frac{d^2 x_k}{dz^2} \quad \text{k=1, 2..., NG} \tag{4.33}$$

Where x is the species mass fraction, MW is the molecular weight, NG is the total number of gas phase species, r_k is the reaction rate, A_{cat}/A represents the ratio of the catalytic area to the total geometric area, and D is the diffusion coefficient. The variation of species site fraction is described by Equation 4.34,

$$\sigma_{cat}\frac{\partial \theta_i}{\partial t} = \frac{A_{cat}}{A} r_i^{het} \qquad \text{i=1, 2,..., NS} \qquad (4.34)$$

Where NS is the total number of surface species, r_i^{het} is the heterogeneous reaction rate and σ_{cat} is the site density. The energy balance is described by Equation 4.35,

$$\rho \hat{C}_p u\nabla T = \nabla.(\lambda \nabla T) - \frac{A_{cat}}{A} \sum_{k=1}^{N} \hat{H} r_k \qquad (4.35)$$

Where H is the mass specific enthalpy, r_k is the reaction rate and C_p is the specific heat.

$$x_{(z=0)} = x_{in} \qquad (4.36)$$

$$\frac{dx}{dz_{(z=L)}} = 0 \qquad (4.37)$$

The species mass fraction and temperature profiles predicted by the modified plug flow model are shown in Figure 27 and Figure 28 . The simulations were performed at 598.15 K as the initial temperature and a feed composition (mass fractions) of 0.318 (CH_4), 0.159 (O_2) and 0.523 (N_2). The modified plug flow model with effectiveness factor if validated against a CFD model can render the simulation of monolith catalysed systems computationally efficient. However, in the case of a multi-channel monolith, the modified plug flow model cannot be applied as it does not take into account heat transfer across the neighbouring channels. In this case, a 3D CFD multichannel model is used as a numerical experiment and benchmark in validating the pseudo homogeneous model.
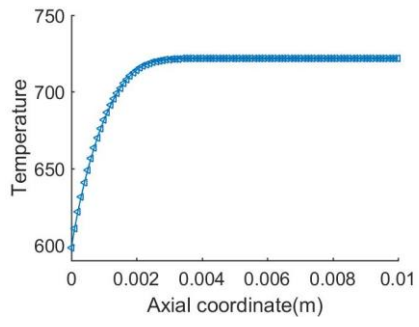
Figure 27: Temperature profile predicted from a modified plug flow model
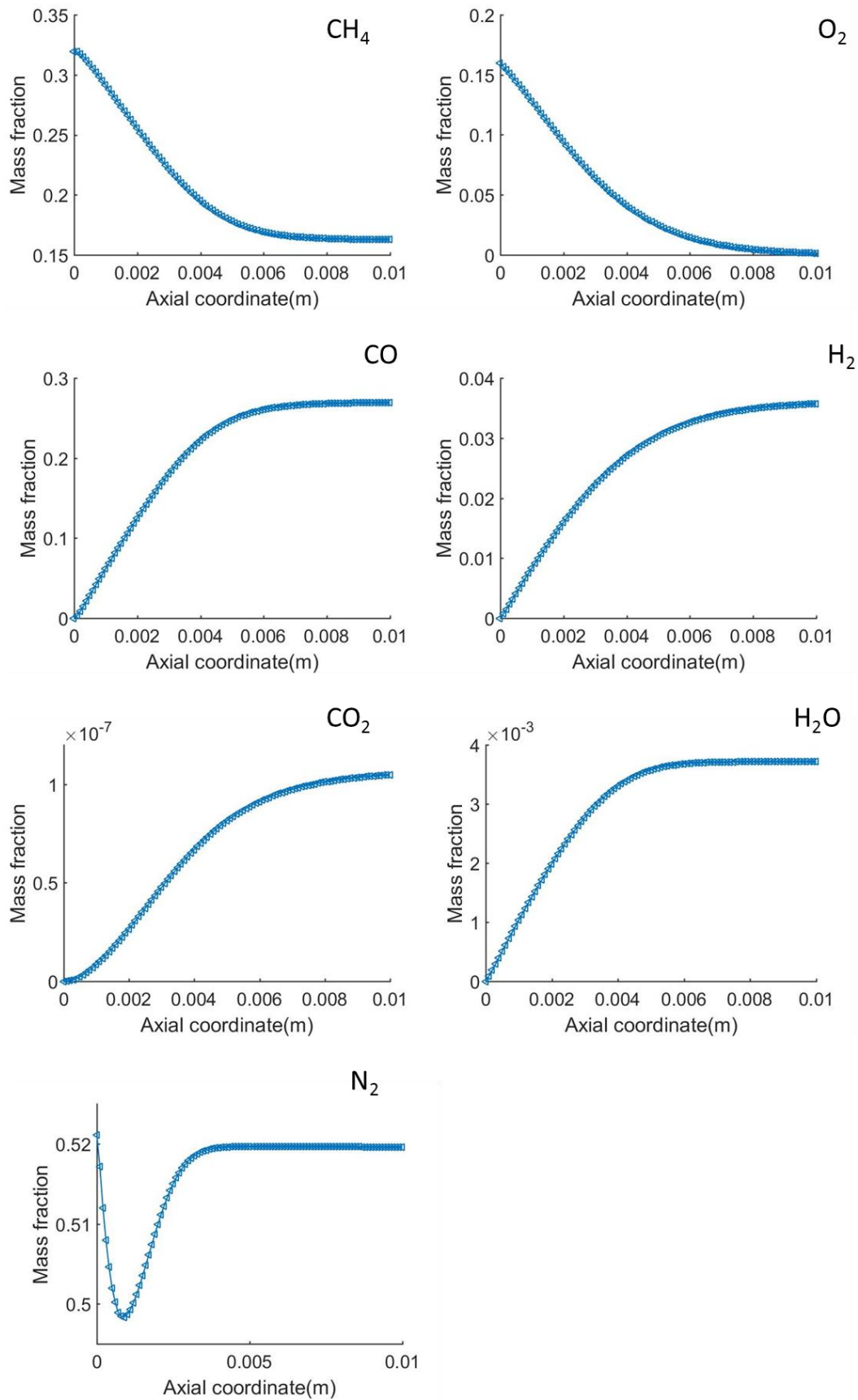
Figure 28: Mass fraction profiles predicted from a modified plug flow model

Chapter 6. CFD model for a multichannel monolith

The multichannel monolith reactor is depicted in Figure 29. Due to the non-porous nature of the walls, the only transfer possible between channels is conductive heat transfer as there is no mass transfer between channels. The conductive heat transfer is a significant influencer of the reaction rate in the channels and must be accounted for in developing an accurate simulation.
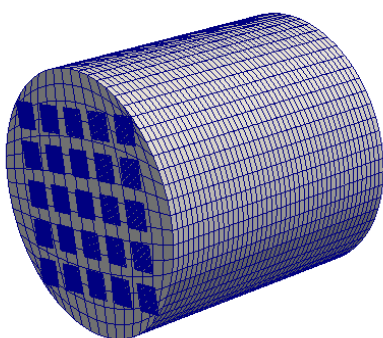
Figure 29: A schematic of a 25 channels monolith reactor

The CFD modelling of a multichannel monolith catalysed system is performed by a numerical solution procedure that couples the Navier-Stokes equations with micro-kinetics of surface reactivity. The underlying equations for both the gas phase and catalytic walls are expressed in Equations 4.3, 4.12 to 4.16. The current study made use of a CFD solver for micro-kinetics named catalyticFOAM developed by Maestri and Cuoci (2013).

The micro-channel simulation does not consider the conductive heat transfer between the neighbouring channels. To account for this transfer, the current work modelled the walls that separate the channels as a fluid and imposed a zero-velocity boundary condition for the velocity at the entrance. The walls that separate the monolith channels are as observed in Figure 30. Additionally, the thermal conductivity of a ceramic monolith was assigned to this region that is modelled as an unmoving fluid. The respective channels behave as heat sources given that there is heat released from the exothermic catalytic reactions. The temperature gradient exists between the respective channels, and the conductive heat transfer is calculated as shown in Equation 4.25. Due to a large number of channels, the computational expense is

significant. A depiction of a bundle that consists of 25 channels is as observed in Figure 30
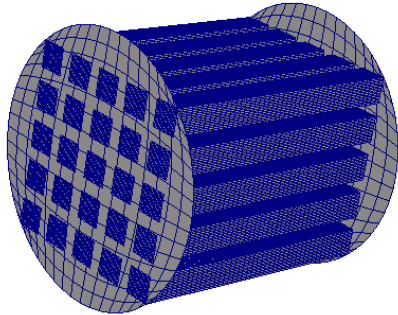
Figure 30: A schematic of tube bundle that consist of 25 channels

The initial and boundary conditions are same as the one employed for a single channel in Equations 4.17 to 4.25.

6.1. Numerical solution

The geometry under consideration constitutes a 25 square channels monolith, with the generation of the geometry and mesh being performed in the OpenFOAM blockMesh utility. Although a low number of channels is used during the development phase, if the method works for this low number, it can be extended to greater numbers of channels. The mesh is shown in Figure 31 and 34. The coupling of chemistry and the resultant transport processes was done through the use of catalyticFOAM, a CFD micro-kinetic solver for heterogeneous catalysis developed by Maestri and Cuoci (2013). The numerical solution has been discussed in detail in section 4.10

The mesh sensitivity analysis was carried out to determine the optimum grid size that yields the resolution independent results. The grid size corresponding to 10530 axial cells and 390 radial cells was found to be an optimum grid at which the results of the predicted parameters are resolution independent.
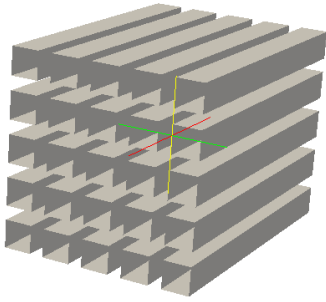
Figure 31: A schematic of square channels employed the current work
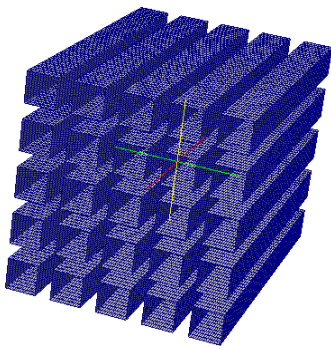
Figure 32: A depiction of the mesh for the 25-channel bundle.

6.2. Summary

Although a 3D CFD simulation for a 25-channel monolith was achieved through modelling the walls that separate channels as a fluid and imposing zero velocity boundary condition, when simulating a real-life scenario which involves thousands of channels, such an exercise becomes impractical. In this work, by demonstrating the efficiency and accuracy with which the proposed hybrid model can predict the system at this small scale, it becomes possible to model and predict the larger scale systems.

6.3. Hybrid model

In a monolith reactor, the radial and axial thermal gradients result in heat transfer across thousands of channels. The individual channels behave as axial line heat sources due to the exothermic reactions upon the monolith walls. To accurately predict the temperature distribution, the radial and axial heat transfer in each channel must be included in a numerical model. In particular, the axial and radial temperature distribution affects the reaction rates in the channels. Therefore, the solution of heat,

mass and momentum transfer in respective channels requires significant computational expense.

A computationally efficient way of solving the governing equations in this multi-channel system would be to adopt a pseudo homogeneous approach. In this approach the multi-tube monolith is modelled as a single cylindrical tube (Figure 33) with the radius equivalent to the multi-channel monolith. Radial conduction axial convection are all preserved in this model. Since heat and mass transfer in a single cylinder (even for the case of non-uniform distributions) is well studied, analytical solutions are available (Elazhary and Soliman, 2009; Han et al., 1996). To facilitate geometric and economic optimisation, these analytical solutions are hybridized with effectiveness factor approaches to develop algebraic models that accurately represent the PDEs that describe monolith reactors.

The hybrid model is based on the principle that, due to the high density of channels in a monolith, there will exist an equivalent homogeneous cylindrical model that approximates the behaviour of a bundle of channels acting as axial heat sources. A cylindrical model which is based on the flow of a virtual fluid whose attributes (conductivity, viscosity) are such that the channel bundle behaviour can be approximated would solve at sufficiently low computational expense that it becomes suitable for optimisation applications.

The simulation and computation of multi-tubular monoliths benefits from the hybrid model given that a monolith, when described with the stiff and non-linear equations inherent to fundamental momentum mass and heat transfer, results in long temporal and spatial scales. In addition, the kinetics are complex, and transport and chemistry are strongly coupled. Therefore, the simulation of the entire monolith system is then computationally expensive exercise when approached by traditional means
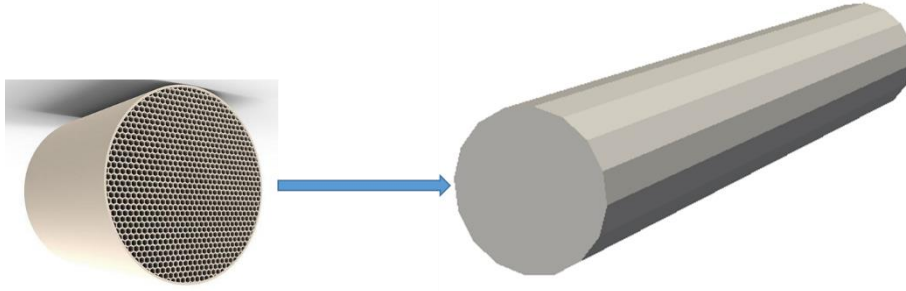
Figure 33: A multi-channel monolith and the corresponding pseudo-homogeneous representation

6.4. Analytical solutions for the radial and axial heat transfer

The dispersed plug flow model was validated against a single channel CFD results. However, in the case of multichannel simulations, this approach could not be applied given that it does not consider the interaction of channels through heat transfer. The fast-modified plug flow model is embedded into the multichannel case by the coupling with a linear combination of the two analytical solutions for the energy balance. Since there is no mass transfer between channels, the mass balance equations used in the hybrid model are the same as those employed in the modified plug flow model for a single channel. With the hybrid model, the prediction of temperature distribution in each channel is performed efficiently by solving the model equation (Equation 4.38).

The monolith reactor (Figure 23) constitutes two regions; namely the free-flow and the zero flow. The free-flow represents a region where the fluid flows through the channel, while zero-flow refers to the monolith wall where there is no mass flow. The zero-flow and free-flow regions were modelled separately, and a linear combination imposed for coupling with the modified plug flow model (hybrid model). There exist analytical solutions for energy balance in these two regions. To describe the axial and radial temperature distribution, a linear combination of the two analytical solutions was employed. The linear combination of the heat fields was performed using the area weighting and is as shown in Equation 4.38,

$$T(r, z,t) = (1 - \beta)T_z(z, t) + \beta T_r(r)) \tag{4.38}$$

Where β represents the ratio of the wall area to the channel area, T_z is the axial temperature and T_r is the radial temperature.

The advection-diffusion reaction equation is represented by Equation 4.39 and the corresponding analytical solution in the free-flow region is as shown in Equation 4.40. The analytical solution for the advection-conduction reaction (in the free-flow region) is obtained by applying the heat and mass transfer analogy and is shown in Equation 4.41. The conductive heat transfer through the zero-flow region has its analytical solution expressed in Equation 4.42 and the linear combination of the two analytical solutions (Equation 4.38) allows for an axial and radial description of the temperature profiles.

$$\frac{\partial C}{\partial t} = -U\frac{\partial C}{\partial x} + D\frac{\partial^2 C}{\partial^2 x} - \lambda C \tag{4.39}$$

$$C(x,t) = C_i + (C_0 - C_i)\frac{1}{2}\left[erfc(\frac{x-Ut}{2\sqrt{Dt}}) + \exp\left(\frac{Ux}{D}\right)erfc\left(\frac{x+Ut}{2\sqrt{Dt}}\right)\right] \tag{4.40}$$

$$T_z(x,t) = \frac{T_0}{2}\left[erfc\left(\frac{x-Ut}{2\sqrt{\alpha t}}\right) + \exp\left(\frac{Ux}{\alpha}\right)erfc\left(\frac{x+Ut}{2\sqrt{\alpha t}}\right)\right] \tag{4.41}$$

$$T_r(r) = T_r(r_0) + \frac{qR}{k}\ln\frac{r_0}{r} \tag{4.42}$$
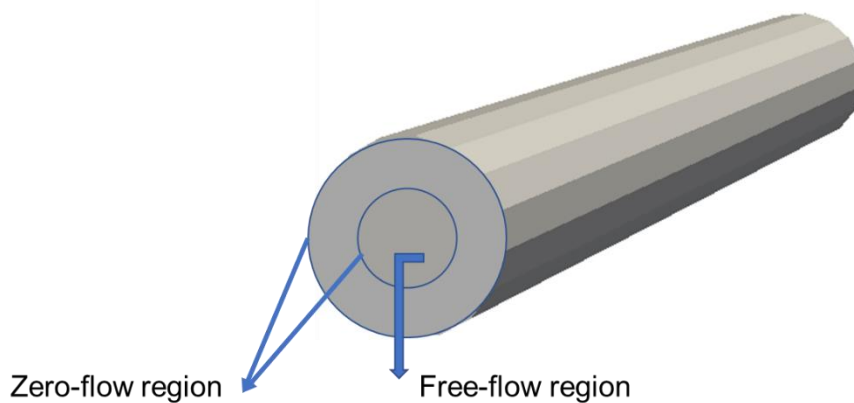
Figure 34: A free-flow and zero-flow region in a monolith

6.5. Analytical solution to advection-dispersion equation (free flow region)

The advection-reaction-dispersion phenomenon in the free-flow region is described by Equation 4.43 and there exists a corresponding analytical solution.

$$\frac{\partial C}{\partial t} = -U\frac{\partial C}{\partial x} + D\frac{\partial^2 C}{\partial^2 x} - \lambda C \tag{4.43}$$

Where C is concentration, D is the hydrodynamic dispersion coefficient, λ is first order rate coefficient, U is flow velocity and x is the axial coordinate. The initial and boundary conditions employed are given by Equations 4.44 to 4.46.

$$C(x,0) = 0, \text{ for } x \geq 0 \tag{4.44}$$

$$C(0,t) = C_0, \text{ for } t \geq 0 \tag{4.45}$$

$$C(\infty,t) = 0, \text{ for } t \geq 0 \tag{4.46}$$

Where C_0 is the initial concentration. The analytical solution proposed by Lapidus and Amtjndson (1952) is as shown by Equation 4.47.

$$C(x,t) = C_i + (C_0 - C_i)\frac{1}{2}\left[erfc(\frac{x-Ut}{2\sqrt{Dt}}) + \exp\left(\frac{Ux}{D}\right)erfc\left(\frac{x+Ut}{2\sqrt{Dt}}\right)\right] \tag{4.47}$$

Equation 4.47 by Lapidus and Amtjndson (1952) describes the analytical solution for mass transfer and given the analogy that exists between heat and mass transfer, an equivalent analytical solution for heat transfer can be obtained. The heat transfer phenomena as described by Equation 4.48 has an analytical solution of the form expressed in Equation 4.49,

$$\rho C_p \frac{\partial T}{\partial t} = -U\frac{\partial T}{\partial x} + k\frac{\partial^2 T}{\partial^2 x} \tag{4.48}$$

$$T_z(x,t) = \frac{T_0}{2}\left[erfc\left(\frac{x-Ut}{2\sqrt{\alpha t}}\right) + \exp\left(\frac{Ux}{\alpha}\right)erfc\left(\frac{x+Ut}{2\sqrt{\alpha t}}\right)\right] \tag{4.49}$$

Where $\alpha = k/\rho C_p$

The analytical solution in Equation 4.50 can be expressed in the form of dimensionless numbers.

$$\frac{T_z}{T_0} = \frac{1}{2}\left[erfc\left(\frac{1-T_R}{2\sqrt{Foh}}\right) + \exp(FohT_R)erfc\left(\frac{1+T_R}{2\sqrt{Foh}}\right)\right]$$ (4.50)

Where the dimensionless numbers used are $Fo=\alpha t/x^2$ and $T_R=U_t/x$. Fo is the Fourier number.

6.6. Heat transfer through a rod (a zero-flow region)

The conductive steady state heat transfer phenomenon through a rod is represented by Equation 4.51.

$$\frac{d}{dr}(r\frac{dTr}{dr}) = 0$$ (4.51)

Equation 4.51 can be integrated twice to yield the form expressed in Equation (4.52).

$$T_r(r) = A\ln(r) + B$$ (4.52)

The integration constants A and B are from the boundary and initial conditions.
At $r=R$, the boundary condition is expressed by Equation (4.53).

$$q = -k\frac{dTr}{dr}$$ (4.53)

The constant A is therefore derived from Equation 4.43 and has a form that is depicted in Equation 4.54.

$$A = -\frac{qR}{k}$$ (4.54)

At $r=r_0$, $T=T(r_o)$ and the constant B is expressed as shown in Equation 4.55.

$$B = T(ro) + \frac{qR}{k}\ln(ro)$$ (4.55)

The description of the constants A and B lead to a final form of Equation 4.52.

$$T_r(r) = T_r(r0) + \frac{qR}{k}\ln\frac{r0}{r}$$ (4.56)

$$q = \frac{A_{cat}}{A}\sum_{i=1}^{NG}Hir''i$$ (4.57)

The two analytical solutions were combined to solve the heat transfer phenomena that takes into account both radial and longitudinal conduction. The combination of the two cases yields the final form depicted in Equation 4.58.

$$T = \frac{1}{2}\text{erfc}(\frac{1-T_R}{2\sqrt{F_o}}) + \exp(F_o T_R)\text{erfc}(\frac{1+T_R}{2\sqrt{F_o}}) * T(r_0) + \frac{qR}{k}\ln\frac{r_1}{r} \qquad (4.58)$$

A linear combination of the two solutions as illustrated in Equation 4.59 was employed to capture the important features of heat transfer in an advection-diffusion-reaction system.

$$T(r, z, t) = (1 - \beta)T_z(z, t) + \beta T_r(r) \qquad (4.59)$$

Where $T_z(z,t)$ represents the solution in Equation 4.49 and $T_r(r)$ the solution in Equation 4.56. The coefficient β represents the ratio of the wall area to the channel area. If the wall thickness approaches zero, the mode of heat transfer is by convection and dispersion as the last term in Equation 4.59 is negligible. On the other hand, if the diameter of the channel approaches zero, the mode of heat transfer is by conduction as the first term of Equation 4.59 would be negligible.

The temperature described by Equation 4.59 is integrated into the dispersed plug flow model by introducing the last term on the right hand of Equation 4.60. The introduction of this term considers the interaction of channels through heat transfer.

$$\rho \hat{C}_p u\nabla T = \nabla.(\lambda\nabla T) - \sum_{k=1}^{N} H_{r_k}{}^{ii} H + UA(T_w - T) \qquad (4.60)$$

The overall heat transfer coefficient (U) was determined from Equation (4.61),

$$U = \frac{1}{\frac{1}{h_{air}} + \frac{\Delta y}{k} + \frac{A_{air}}{A_{gas}h_{gas}}} \qquad (4.61)$$

Where h is the heat transfer coefficient, Δy the wall thickness and A area. The heat transfer coefficient is calculated as shown in Equation 4.62.

$$h = Nu\frac{k}{D_h} \qquad (4.62)$$

The dimensionless number (Nusselt number) is calculated from Equation 4.63.

$$Nu = 8.233(1 - \frac{1.883}{\alpha}) + \frac{3.767}{\alpha^2} - \frac{5.814}{\alpha^3} + \frac{5.361}{\alpha^4} - \frac{2}{\alpha^5}$$ (4.63)

In Equation 4.63, α refers to the aspect ratio for the geometry of interest.

The above equations describe the hybrid model framework and were used to predict the state variables for catalytic partial oxidation of methane to syngas. To gauge the accuracy of results from the energy balance in Equation 4.60, a comparison between the wall temperature calculated from the analytical solution and the temperature predicted from CFD was performed. The wall temperature profiles predicted from CFD and the analytical solution are as presented in Figure 35 and Figure 36. As observed, there is a close agreement between the temperatures predicted from both cases. The comparison between the centre-line and the wall temperature is shown in Figure 37 and as observed, thermal equilibrium is achieved within a space time of 1.0 milli-second.
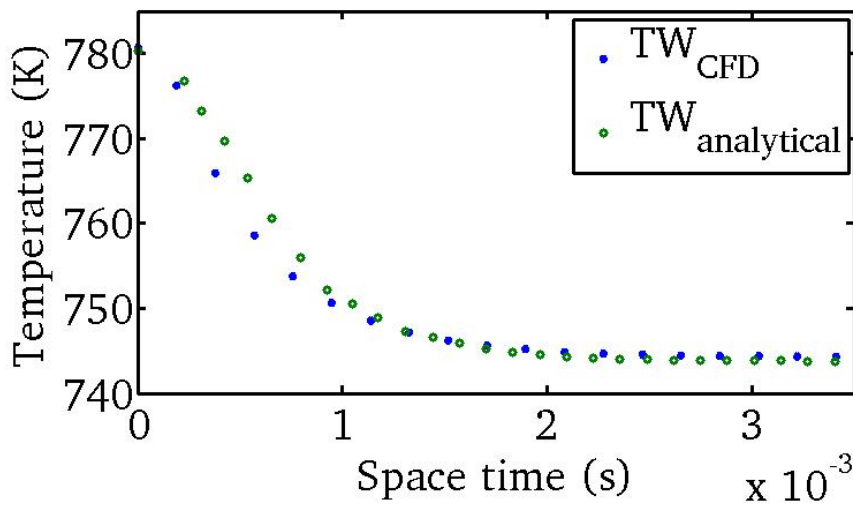
Figure 35: Comparison between an analytical solution for the wall temperature and the wall temperature predicted from CFD (r=0.53R)
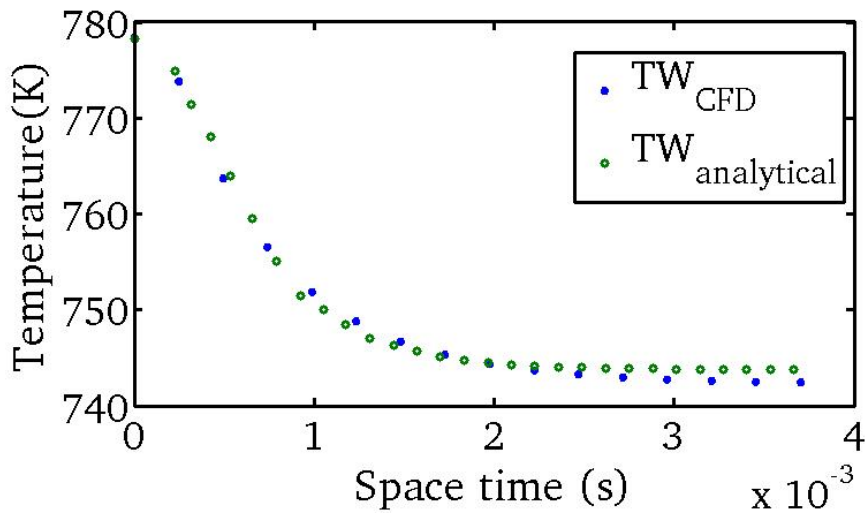
Figure 36: Comparison between an analytical solution for the wall temperature and the wall temperature predicted from CFD (r=0.60R)
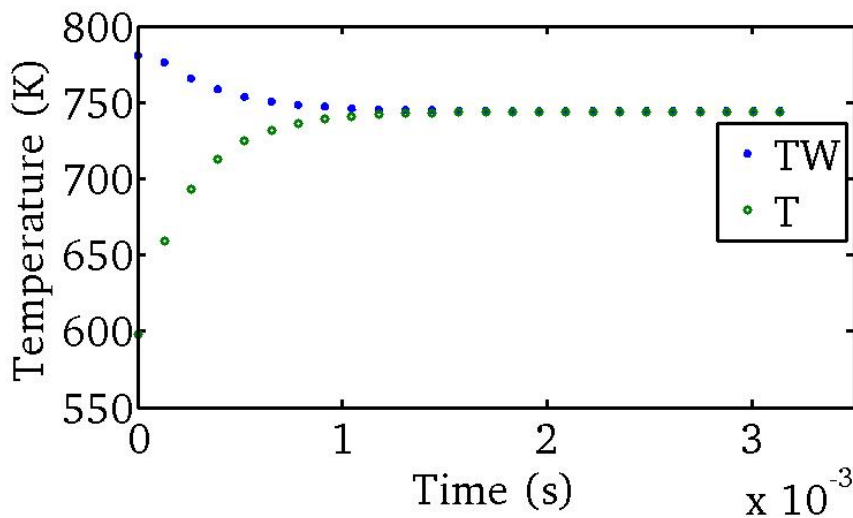
Figure 37: Area averaged temperature profiles and Wall temperature (r=R)

The temperature profiles predicted from the CFD model and the analytical solution for the energy balance are in a close agreement as observed. Therefore, the analytical solutions can be hybridized with the effectiveness factor approaches for the computationally efficient modelling of monolith reactors

6.7. Convergence and stability

The accuracy of the parameters predicted by a numerical method is dependent on many factors that include convergence and stability. In CFD studies, a grid independent solution is found by changing the grid resolution until the solution does

no longer change with grid size. An optimum grid size was obtained by varying the grid size and observing the temperature predicted at each grid size and the point where the temperature became constant was chosen as the optimum point.

6.8. Size range and meshing

The grid dependence in the prediction of outlet temperature in a monolith reactor was investigated and the optimum grid size was found to be composed of 10530 axial cells as observed in Figure 38. The findings in Figure 38 are for the temperature at the reactor outlet. In the current work, only surface reactions were taken into account, the gas phase reactions were neglected, as such, the mesh was refined at the regions where reactions are taking place to capture the system behaviour correctly. The determination of the optimum grid size is important as it ensures that the ultra-fine mesh that increases computational expense is not used.
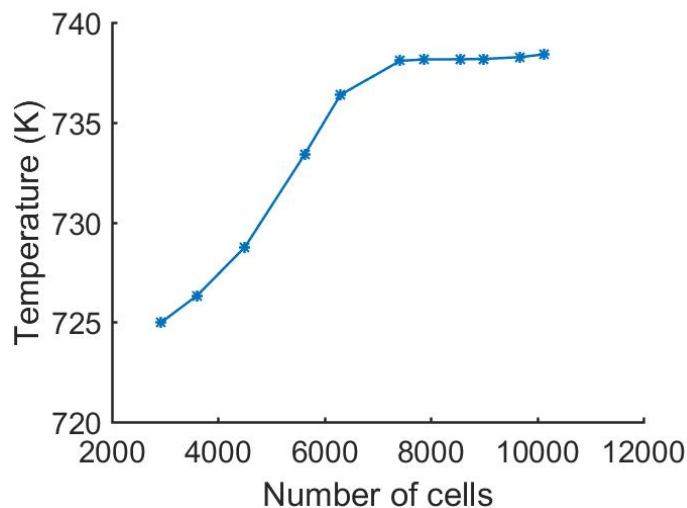
Figure 38: Grid dependence in the prediction of outlet temperature in a monolith

Upon finding the resolution independent results, the model results were then validated against a 3D CFD model. Three models have been discussed namely the hybrid model, modified plug flow model and CFD. A summary on the major characteristic features is provided in Table 5.

Table 5: A summary on the major characteristic features of the hybrid model,CFD and modified plug flow model

Model	Major characteristic Features
Modified Plug flow	A single channel model that makes use of effectiveness factor to correct for wall mass transfer. A computationally efficient method for modelling a single channel monolith but cannot be applied in a case of multi-channel monoliths.
Hybrid Model	A homogeneous cylindrical model that approximates the behaviour of a bundle of channels acting as axial line heat sources. A computationally efficient method when modelling a multi-channel monolith.
CFD	A 3D model that solves that transport equations coupled with micro-kinetics in each of the thousands of channels. Computationally expensive when modelling a multi-channel monolith.

Chapter 7. Model Validation

Model validation was conducted by comparing both the hybrid model and modified plug flow model results with CFD (numerical experiment and benchmark) results for multi-channel monolith. The model consistency tests on mass and energy balances were carried out to ensure that the model descriptions are viable. The inlet conditions employed are those typical of methane partial oxidation and are as observed in Table 6.

Table 6: The inlet conditions for catalytic partial oxidation of methane to syngas in a monolith reactor

Temperature (K)	473.15
CH_4 (Mole fraction)	0.456
O_2 (Mole fraction)	0.114
N_2 (Mole fraction)	0.430
Velocity (m/s)	2.0
Catalyst loading (mg/m^3)	1.45

The validation for the modified plug flow model and the hybrid model was carried out under the scenarios and conditions shown in Table 7 and Table 8.

Table 7: Scenarios and conditions for validation of a hybrid model

Initial temperature (K)	598.15
catalyst loading (mg/m^3)	0.41
catalyst loading (mg/m^3)	1.1
catalyst loading (mg/m^3)	2.08

Table 8: conditions for validation of the modified plug flow model

Initial temperature (K)	573.15	600.15	673.15	773.15

7.1. Model consistency test

The model consistency tests were performed in the analysis of the results from the simulations. The mass and energy balance were used in the testing of the model consistency and the results are as observed in Table 9 and Table 10. In both cases, the relative error is less than 1.0 % and this demonstrates consistency in the model. The mass flowrate profiles in Figure 39 show in absolute terms a constant value from

the reactor inlet to the outlet. The relative error is as observed in Table 9 and Table 10 is less than the relative tolerance set for the solver which is 2.0e-1, as such, this translates to accuracy of the results. The element mass fractions are shown in Figure 40 and their sum was calculated and found to be unity as illustrated in Figure 41.The consistency checks were employed for a wide range of operating conditions to investigate the model reliability and generality.

Table 9: Comparison between the total mass flowrate at the reactor inlet and outlet

Total mass flow rate in (kg/s)	Total mass flow rate out (kg/s)	Relative error (%)
4.715E-07	4.706E-07	0.19

Table 10: Comparison between total heat source and total net energy rate in a monolith reactor

Total heat source (W)	Total net energy rate (W)	Relative error (%)
-1013100	-1011570	0.15
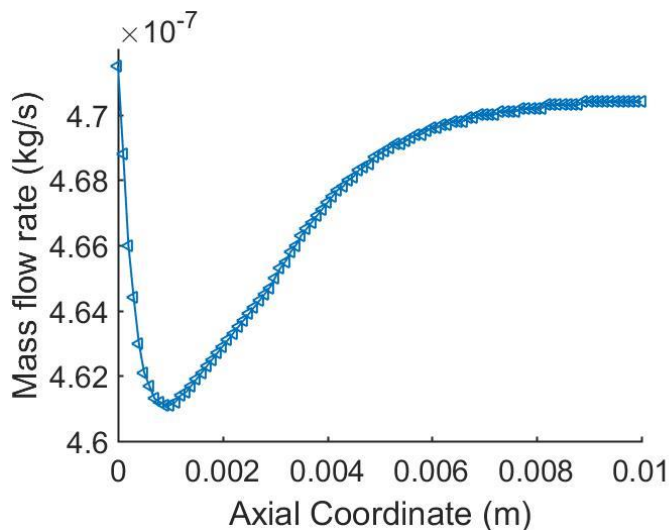
Figure 39: Mass flowrate along the reactor axial coordinate
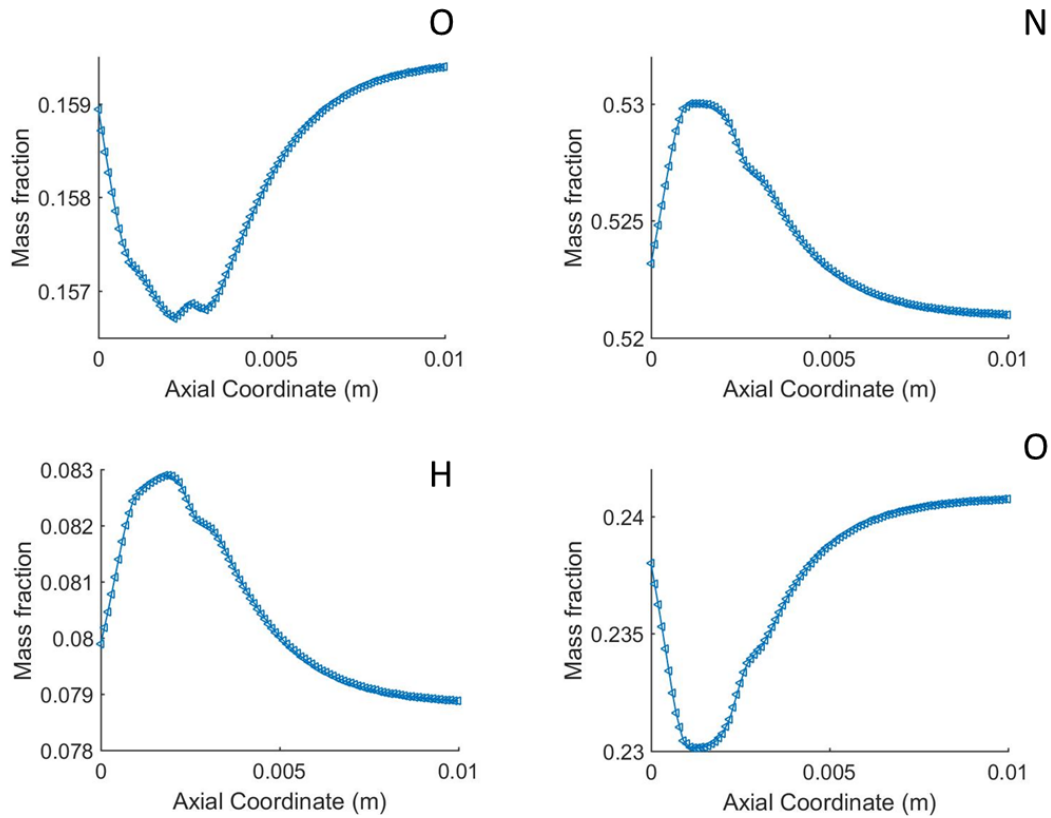
Figure 40: Element mass fraction profiles along the axial coordinate
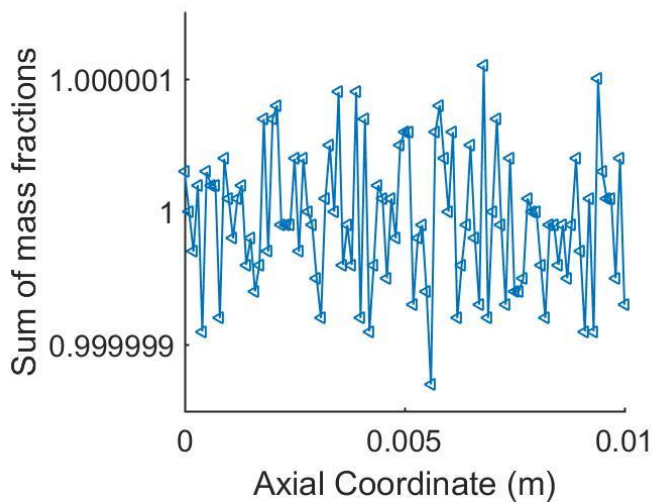
Figure 41: The sum of element mass fractions along the axial coordinate

7.2. Validation of the plug flow model with effectiveness factor

The single channel CFD simulations were used as a numerical experiment and the comparison with the plug flow approach without the effectiveness approach is shown in Figure 42 and Figure 43. In this case, there is a significant discrepancy between CFD and plug flow results and this is attributable to the absence of radial and axial

gradients in the plug flow model. This preliminary check confirms that radial transfer gradients are significant and cannot be ignored in any attempt at model development.

In the CFD model, the reactions only take place at the catalytic walls since that is where the catalyst is embedded. On the other hand, the equivalent reaction rate in the homogenous gas phase must be simulated in the plug flow model as the homogeneous gas phase reactions were neglected, as such, for a plug flow model to fully mimic the CFD model, the concentration employed in the plug flow model must be equivalent to the surface concentration in CFD. An area averaging approach was employed for the CFD results prior to comparison with the 1D dispersed plug flow model results. This approach was taken because the heat and mass transfer limitations lead to 3D variance in the predicted state variables, the averaging was done as shown in Equation 5.1 (the same approach was adopted for area averaged temperature profiles).

$$\overline{C(z)} = \frac{1}{Ac} \iint C(x, y, z)dxdy \qquad (5.1)$$
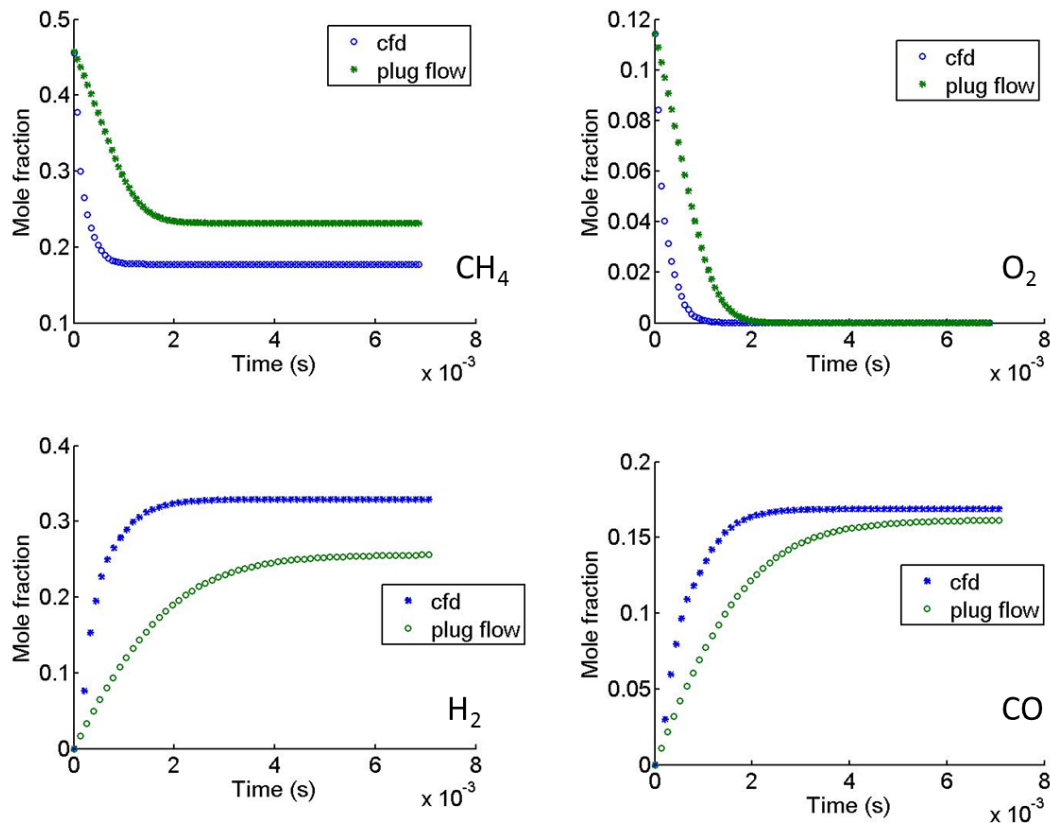
Figure 42: The comparison between CFD and the plug flow model mole fraction profiles in a single channel monolith (a 100 mm length and 1.0 mm diameter monolith)
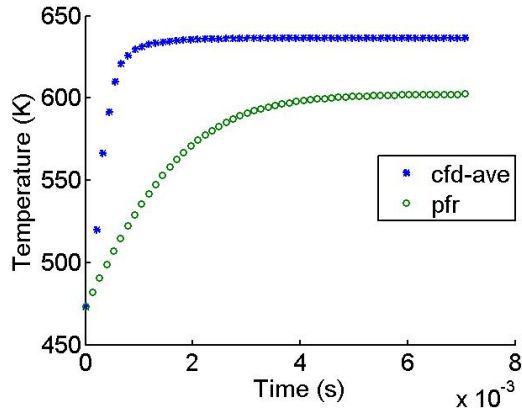
Figure 43: The comparison between CFD and the plug flow temperature profiles in a single channel monolith (a 100 mm length and 1.0 mm diameter monolith)

7.2.1. The application of effectiveness factor to correct the wall concentration

Upon the application of the effectiveness factor to the species concentrations as shown in Equation 4.32, a close agreement between CFD and plug flow model is achieved as observed in Figure 45. The inlet concentrations used are the same as those reported on Table 6. The translation from mass fraction to mole fraction was done as shown in Equation 5.2. The use of the effectiveness factor was further exploited in the non-isothermal case to determine its generality. The effectiveness factor for the respective species in non-isothermal simulations is shown in Figure 44. As observed, the effectiveness factor is greater than unity for all the species and this agrees with general observations in for non-isothermal effectiveness factors. The species concentration profiles in Figure 45 and Figure 46 show a close agreement between CFD and the plug flow model, thus the applicability of this approach can be realized in non-isothermal cases. On the energy balance, the temperature profiles were compared for different inlet temperatures as observed in Figure 47 and it is evident that a dispersed plug flow model with an effectiveness factor is able to capture all the important features of a CFD model at varied inlet temperatures.

$$y_i = x_i \frac{MW_{mix}}{MW_i} \tag{5.2}$$

Where y_i is the mole fraction of species i, x_i is the mass fraction of species i, MW_{mix} is the molecular weight of the mixture and MW_i is the molecular weight of species i.

The results as observed in Figure 45 to 49 reveal that catalytic partial oxidation of methane takes place within milliseconds, facilitating simple and compact designs of the reactor. The reactor dynamic response is increased as a result of the compactness (Donazzi et al., 2008). Additionally, these short residence times that are required (or contact times) mean that the catalytic partial oxidation of methane is ideal for small to medium scale production of syngas or hydrogen.

The short residence times therefore imply that the catalytic partial oxidation reactions are dominant within the first few millimetres of the catalytic bed. It is therefore not necessary to impregnate the channel beyond a few millimetres. A non-uniform catalytic distribution of the active element on the support can therefore be employed for economic considerations. The reaction rate terms in CFD are area based, therefore the plug flow reaction rates which are volume based were multiplied by the ratio of volume to area (Equation 4.26) to allow for a sound comparison.
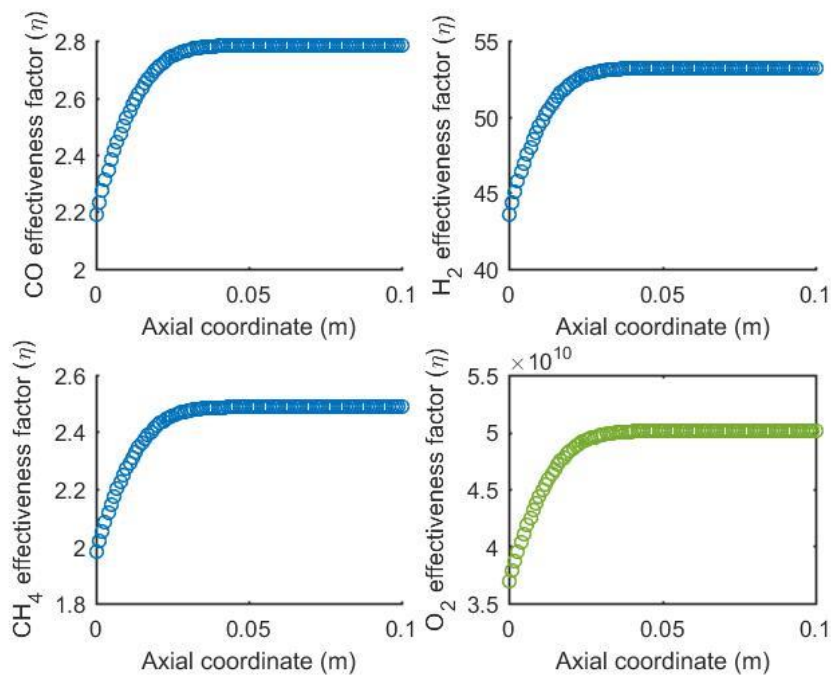
Figure 44: The effectiveness factors for a non-isothermal catalytic partial oxidation reaction
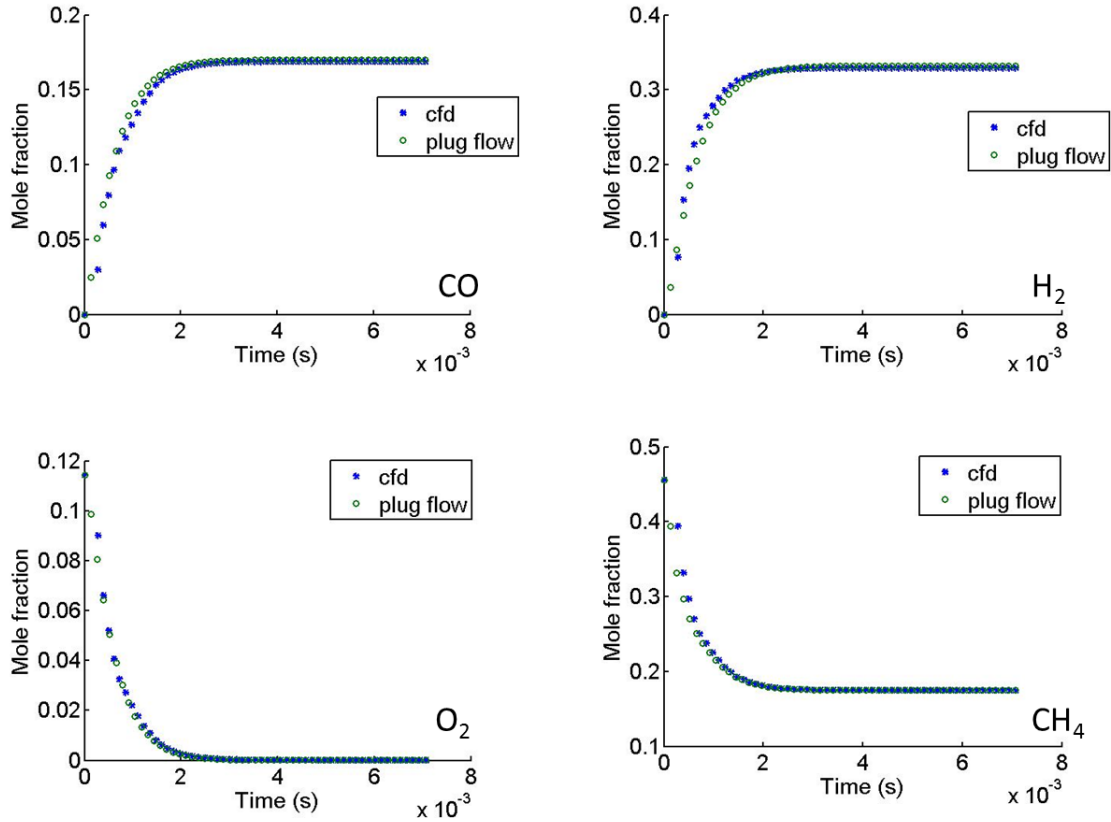
Figure 45:The comparison between CFD and the modified plug flow model mole profiles in a single channel monolith (a 100 mm length and 1.0 mm diameter monolith) at T_O=473.15 K
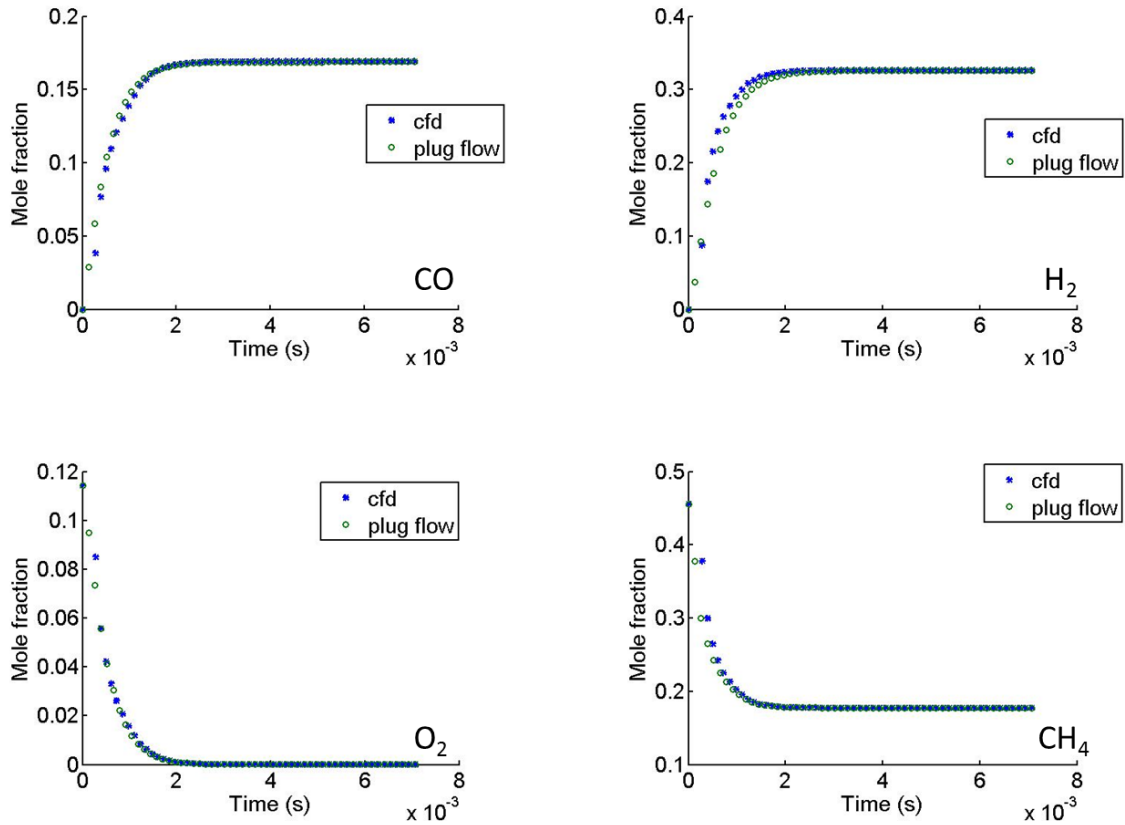
Figure 46: The comparison between CFD and the modified plug flow model mole profiles in a single channel monolith (a 100 mm length and 1.0 mm diameter monolith) at T_O=573.15 K
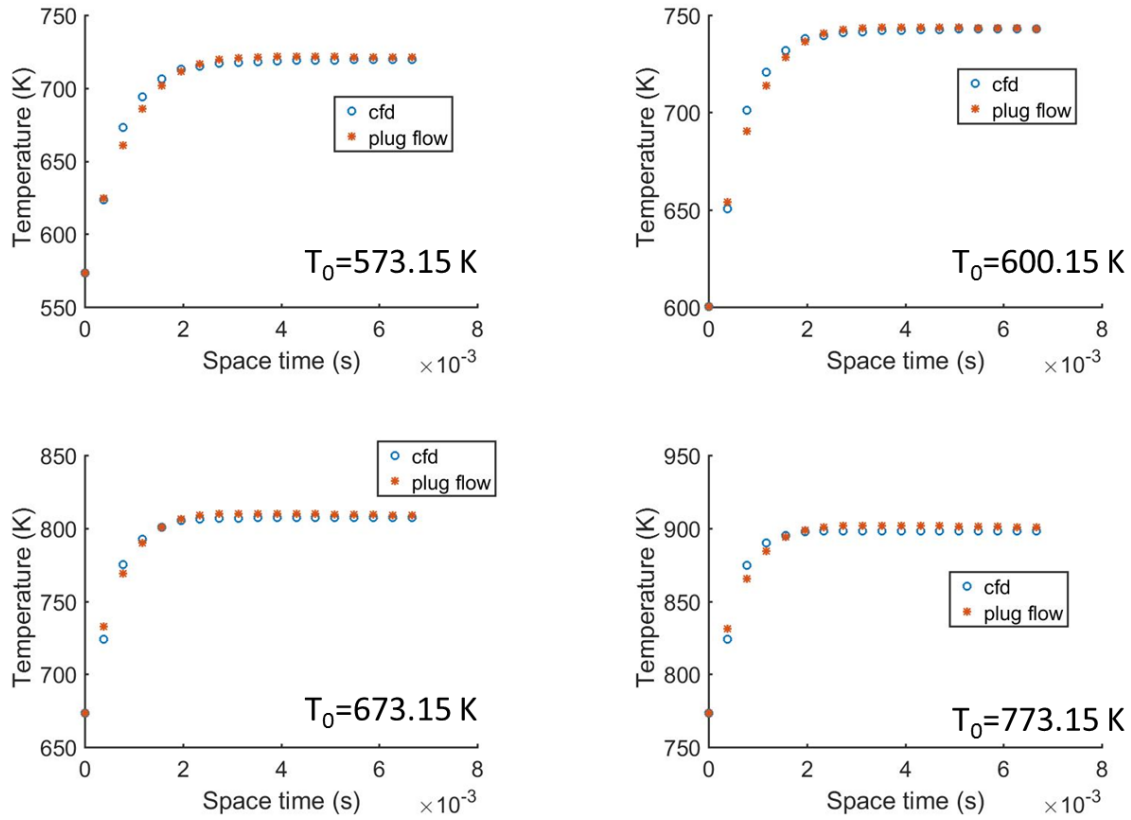
Figure 47:The comparison between CFD and the modified plug flow model temperature profiles in a single channel monolith (a 100 mm length and 1.0 mm diameter monolith)

7.2.2. The influence of a non-uniform velocity profile on temperature and species concentration

A comparison between the mole fraction profiles for a uniform and non-uniform velocity was undertaken. The simulations were performed under laminar flow regime (Re=36.4). The non-uniform velocity is calculated from Equation 5.3. As observed in Figure 48, there is a close agreement between the H_2 and CO mole fraction profiles predicted at non-uniform and uniform velocity.

$$u = u_{max}(1-(\frac{r}{R})^2)$$ (5.3)
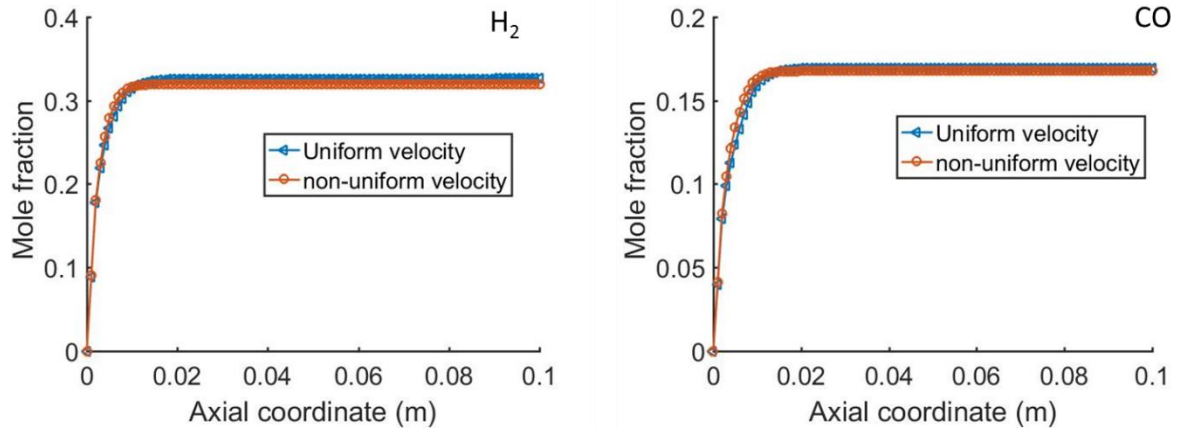
Figure 48: Comparison between mole profiles for a non-uniform and uniform velocity at the inlet in a single channel monolith (a 100 mm length and 1.0 mm diameter monolith)

The accuracy and generality of the modified plug flow model was gauged by comparing the temperature profiles for a non-uniform velocity with the CFD model. As observed in Figure 49, there is a close agreement between the modified plug flow and the CFD model at non-uniform velocity conditions.
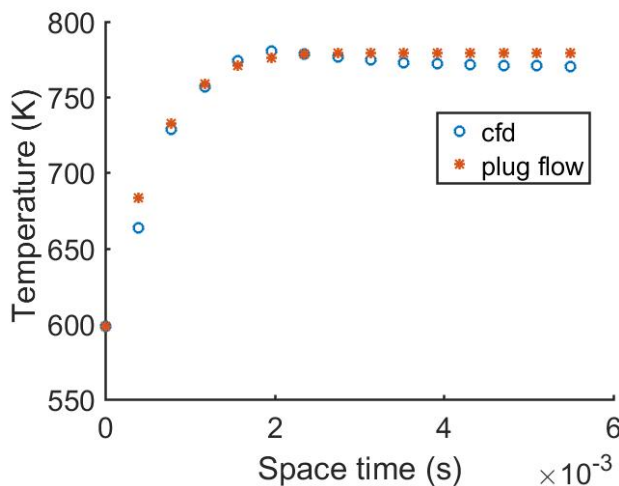
Figure 49: Temperature profiles for a uniform and non-uniform velocity (comparison between CFD and plug flow model) in a single channel monolith

The influence of geometry on the distribution of temperature and concentration was investigated. The temperature and mole fraction profiles in a cylindrical and square channel for a non-uniform velocity are as observed in Figure 50 and 39. To allow for a sound comparison, the diameter of the cylindrical channel and the hydraulic diameter of the rectangular channel was taken to be the same (0.001 m). It is evident from Figure 50 and 53 that axial profiles for species mole fraction are the same for the two geometries. This can be ascribed to equal rates of mass transfer given that the same

94

diameter was used. On the other hand, the relative difference between the temperatures in the two geometries is 0.36 %.
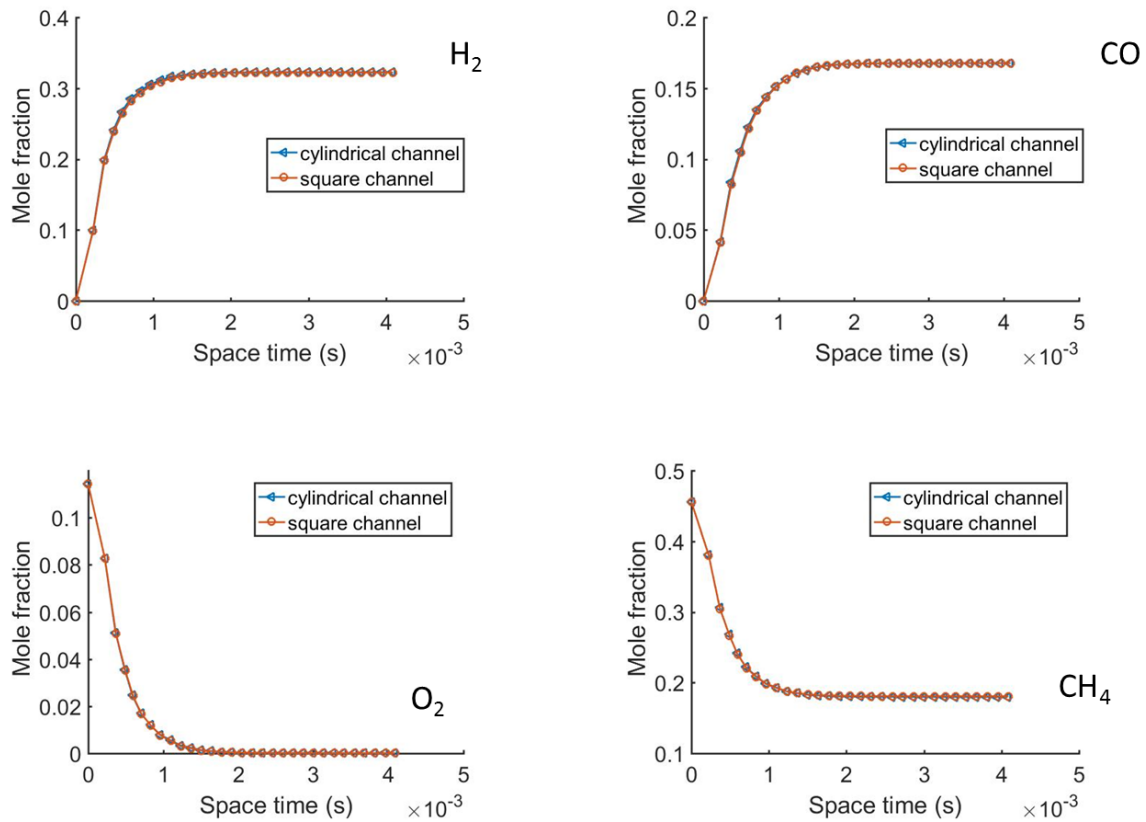
Figure 50: Comparison between mole fraction profiles for a non-uniform velocity in a cylindrical and square single channel monolith (a 100 mm length and 1.0 mm diameter monolith)
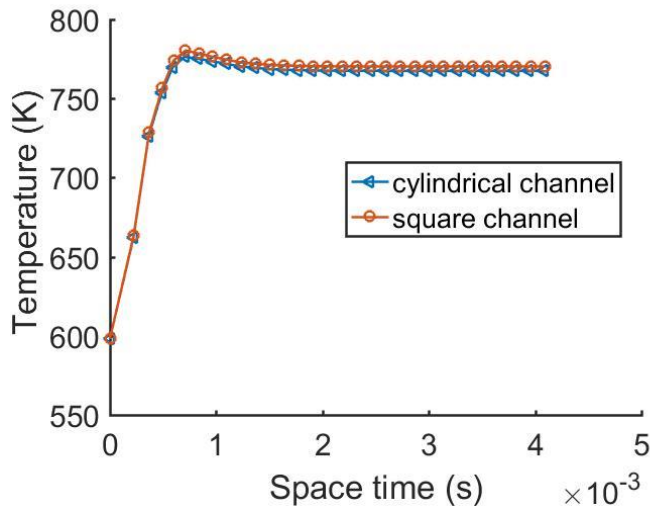
Figure 51: Temperature profiles for a non-uniform velocity in a cylindrical and square single channel monolith (a 100 mm length and 1.0 mm diameter monolith)

7.2.3. Simulation performance

As described so far, the quality of the dispersion model with effectiveness factor was validated against the single channel CFD model and was found to be accurate. To

95

benchmark the performance of this model, a comparison between the two models (CFD and dispersion) was performed with regards to time needed to find a converged solution.

The clock time for a single channel CFD simulation was compared with the clock time for a 1D steady state dispersed plug flow model. It was found that a CFD simulation run in parallel on four threads and two cores of an Intel(R) Core(TM) i5-5300U CPU @ 2.30GHz workstation resulted in 1.3 hours clock time. On the other hand, the dispersed plug flow model equations solved in MATLAB® resulted in 0.53 seconds of clock time which is a considerable reduction in computational expense. This reduction can be ascribed to the dispersion model as a simplified model since steady state and 1D conditions were applied. We therefore consider the corrected dispersion model as suitable substitution in developing a faster solving monolith reactor model.

7.2.4. Conclusions

Three types of reactor models were investigated namely the dispersed plug flow with and without the effectiveness factor and the 3D CFD for a single channel. There is a significant discrepancy between the plug flow model and the CFD model due to the simplifications the plug flow model makes with regards to mass and heat transfer. The relative error between the plug flow and CFD temperature profiles is 23.7 %. On the species mole fraction profiles, the relative error between CFD and plug flow model is 34.6 % H_2 and 20.8 % CO. However, upon using a modified plug flow model to correct the wall mass transfer, there is a close agreement between CFD and the modified plug flow. Both temperature and species mole fraction profiles predicted from the dispersed plug flow model with effectiveness factor gave accurate results with the relative error of 0.59% for temperature, 0.76% for CO and 0.52% for H_2 mole fraction. The modified plug flow model captures the important features of the 3D CFD model at moderate computational expense. The clock time for the modified plug flow is 0.53 seconds in comparison to 1.3 hours for the CFD model. Therefore, the dispersed plug flow model with effectiveness factor is a fast simulator of monolith reactors for a single channel case. Due to its fast nature and speed, the modified plug flow model can be embedded in the multichannel monolith modelling to help reduce the computational costs.

7.3. Validation of the hybrid model

The hybrid model was validated against the multi-channel 3D CFD model. The operating conditions employed are those typical for partial oxidation reactions and are presented in Tables 11 and 12.

Table 11: The feed conditions for catalytic partial oxidation of methane to syngas in a monolith reactor

Temperature (K)	598.15
CH_4 (mass fraction)	0.318
O_2 (mass fraction)	0.159
N_2 (mass fraction)	0.523
Velocity (m/s)	2.50
Catalyst loading (mg/m^3)	1.45

Table 12: The monolith reactor size

Channel length (mm)	100
Channel diameter (mm)	1.00

The temperature profiles across the tube bundle in a 25 channels monolith were predicted from CFD and are presented in Figure 52. A uniform velocity of 2.5 m/s was employed at the inlet of all the channels. As observed, before thermal equilibrium is achieved, the channel which corresponds to r=0.0 mm is characterised by a higher temperature and the temperature decreases outwards and is lower at the outer channels which correspond to r=R. This difference is attributable to the temperature of the outer channels being different from the temperature of the surrounding environment, thus creating a gradient. The thermal equilibrium is achieved as a result of the conductive heat transfer between the channels. The spacing between the channels is also thin enough to facilitate effective heat transfer.
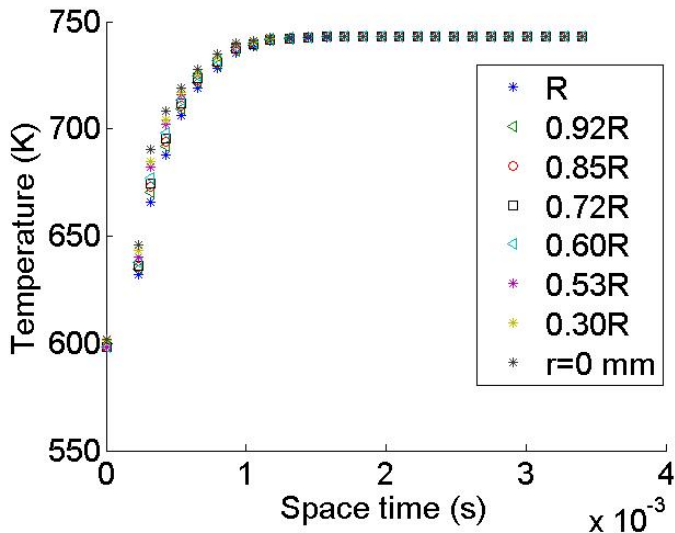
Figure 52: Temperature profiles at various radial positions for z

The species mole fraction profiles for CO, H_2, CH_4 and O_2 are presented in Figure 53. The local temperature distribution differs across the channels, as such, it is expected that the local concentration profiles will differ across the channels due to different reaction rates. In the catalytic partial oxidation reactions, there is an interplay of water gas shift, steam reforming, dry reforming, partial oxidation and total oxidation reactions. The ratio of H_2 to CO is an important factor as some downstream applications require a certain value. The feedstock ratio, inlet temperature and flowrate dictate what ratio of H_2 to CO is achieved at the reactor outlet. The water gas shift reactions favour lower temperatures, and it is expected that at these temperatures the CO produced from partial oxidation and reforming reactions will be converted to H_2. This phenomenon is observed in Figure 53 where the mole fraction of H_2 at the reactor outlet is greater at r=R in comparison to r=0.0 mm.

The local consumption of O_2 is found to be higher at r=0.0 mm and decreases to r=R and this is observed in the stepper gradient for the O_2 mole fraction profile at the centre of the tube bundle. This can be explained by the enhanced reaction rate at that position due to higher temperatures. Methane conversion was found to be 83% and this can be increased by optimizing the geometry to increase mass transfer of reactants from the gas phase to the catalytic walls.
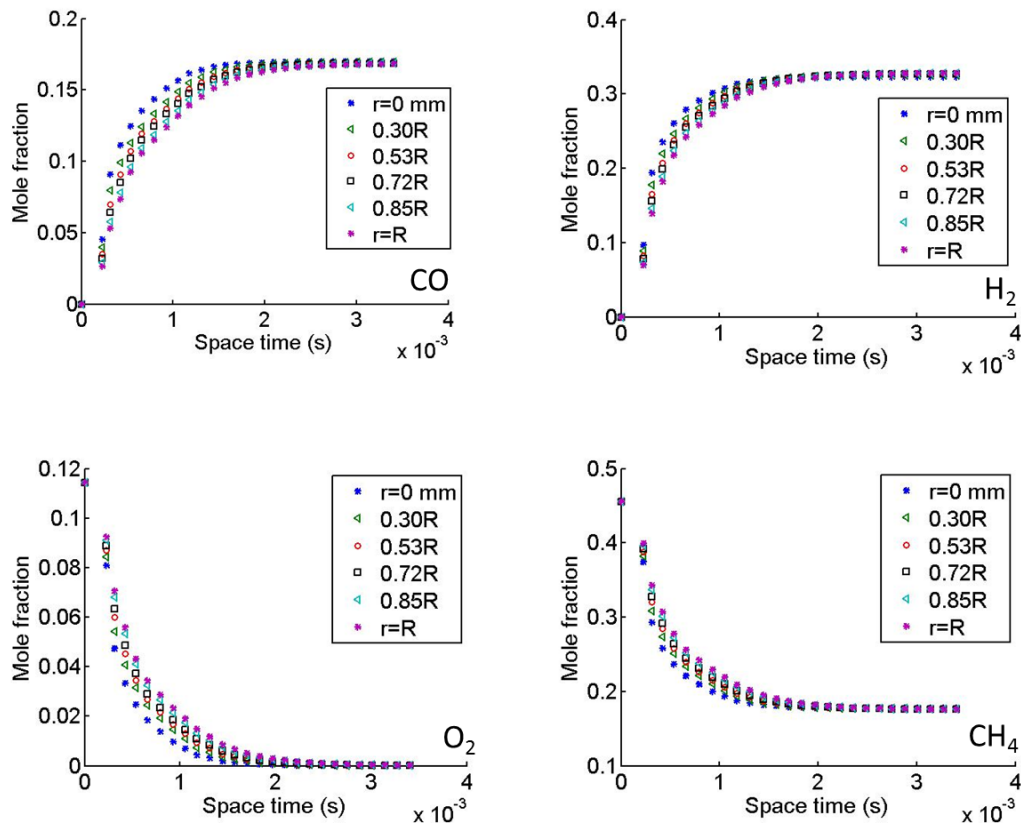
Figure 53: Mole fraction profiles at various radial positions for all z (axial coordinate)

The comparison between the CFD multichannel simulations and the hybrid model results was undertaken as shown in Figure 54. In the hybrid model, the ratio of the area of the zero flow to free flow (β) that corresponds to the dimensions of the geometry used in CFD simulations was used. It was discovered that upon applying ratio (0.09) there is a significant discrepancy between CFD results and the hybrid model results. The new ratio of 0.81 was found by fitting the hybrid model results to CFD results and value was applied across all radial positions in the hybrid model. The application of the new ratio (at a fixed shell diameter) results with the monolith channel size of 0.1 mm and 310464 as the total number of channels.

Upon using the new ratio, it can be observed that a close agreement between the hybrid model and the CFD multichannel simulations is achieved. The comparison was undertaken for r=0.0 mm to r=R and in each case a close agreement was achieved. For each radial position chosen in the hybrid model, Equation 4.49 was used to describe the wall temperature that corresponds to the wall temperature observed in the CFD multichannel model, thus taking into account interaction that takes place in a multichannel case. The comparison between the wall temperature predicted by the

hybrid model and CFD is shown in Figure 36, and as observed, there is a close agreement between the results predicted by the two models. The higher wall temperatures at the reactor entrance is attributed to the exothermic partial oxidation reactions. These partial oxidation reactions reach completion within the few millimetres of the catalyst bed, and towards the reactor outlet, there is thermal equilibrium reached between the wall temperature and the gas phase temperature.
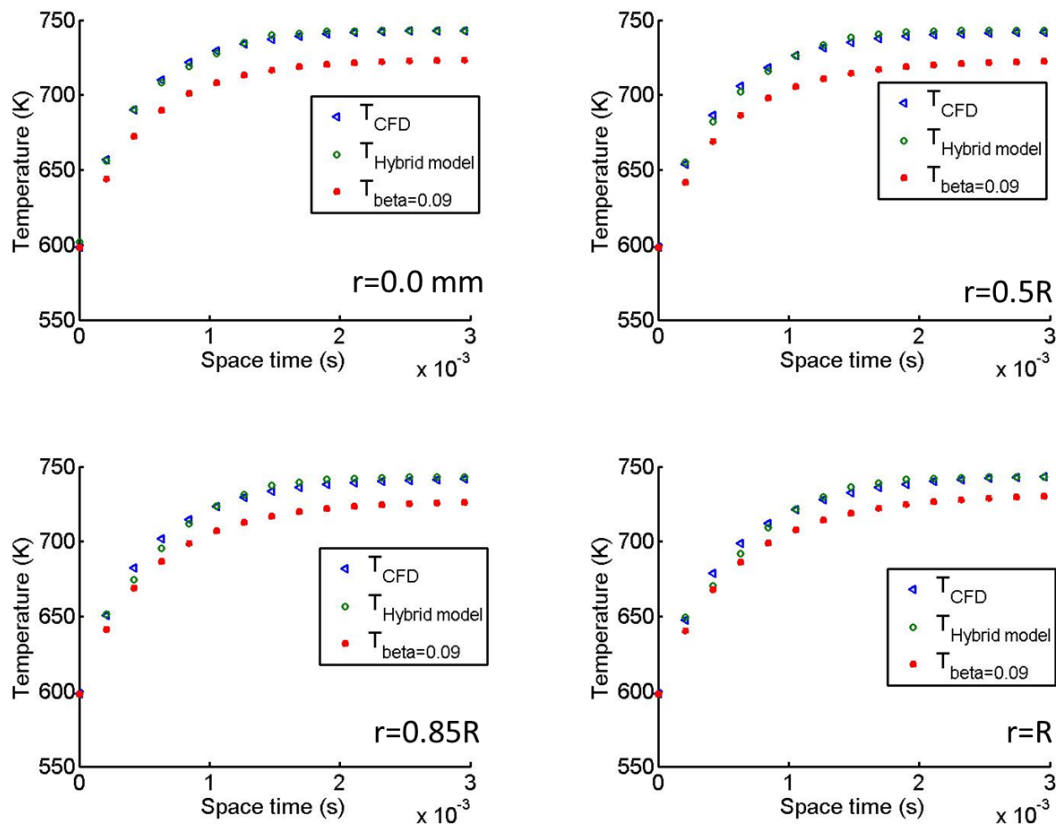
Figure 54: Comparison between a Hybrid and CFD temperature profiles predicted from CFD (r=R)

The species mole fraction profiles predicted from CFD and the Hybrid model at r=0.0 mm and r=R are presented in Figure 55. For both r=0.0 mm and r=R, a close agreement between the CFD and Hybrid model results was found for the gas phase species (CH_4, O_2, CO, H_2). The ratio of methane to oxygen in the reactor inlet was taken to be 4.0 and this resulted in oxygen being fully consumed while methane conversion was found to be 83 %. The use of rich mixtures as employed in this study can help reduce the formation of total oxidation products (H_2 and CO_2) which are favoured in the case of lean mixtures at the feedstock.
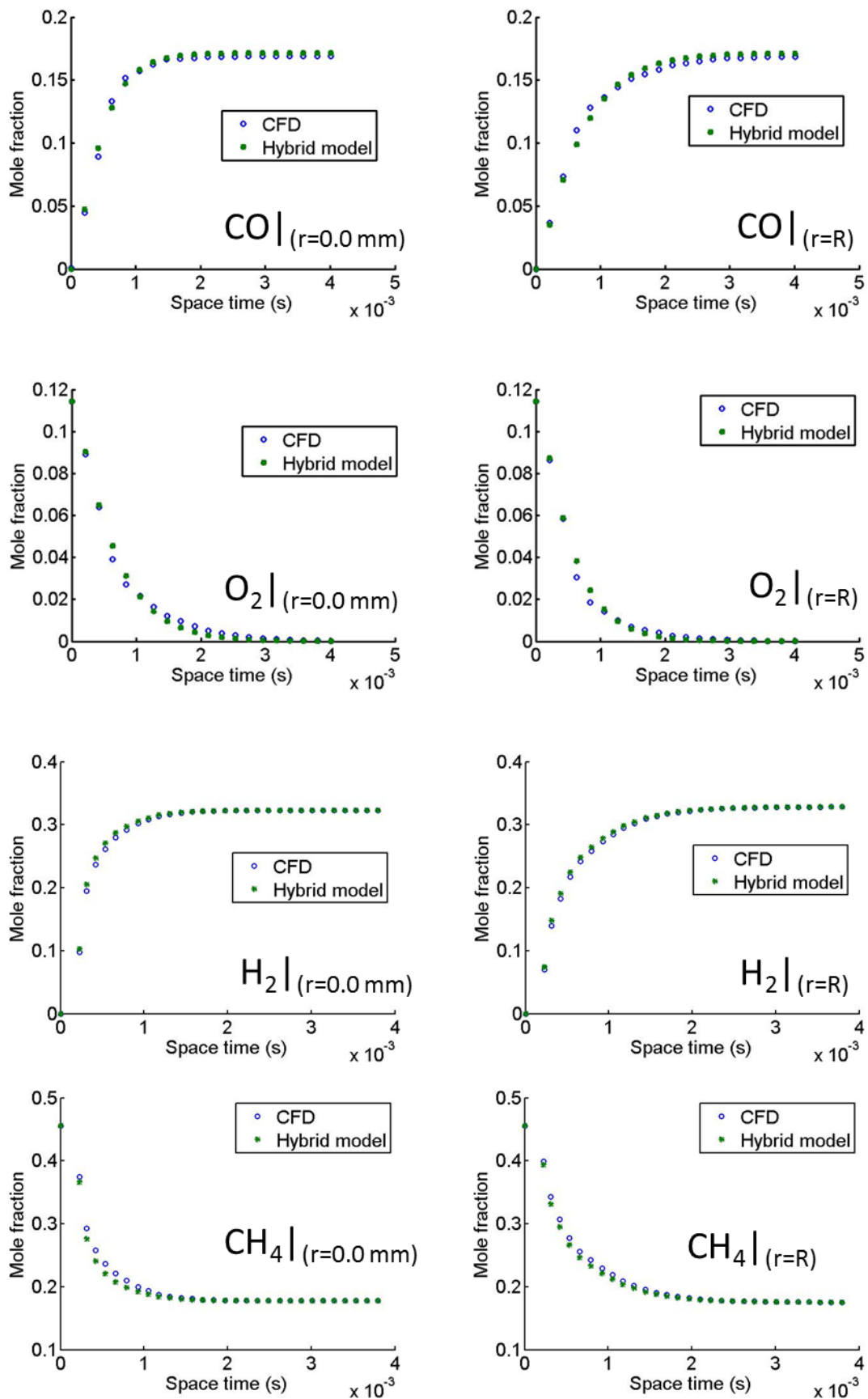
Figure 55: Comparison between a hybrid model CO mole fraction and the mole fraction predicted from CFD (r=0.0 mm and r=R)

The comparison between the hybrid and CFD model for two different catalyst loading (1.1 and 2.08 mg/m^3) is shown in Figure 56 and Figure 57. The length of the monolith channel used in this case is 10 mm. In both cases there is a close agreement between the mass fraction profiles predicted from CFD and the hybrid model. The temperature profiles were also found to in close agreement and this is demonstrated in Figure 58.
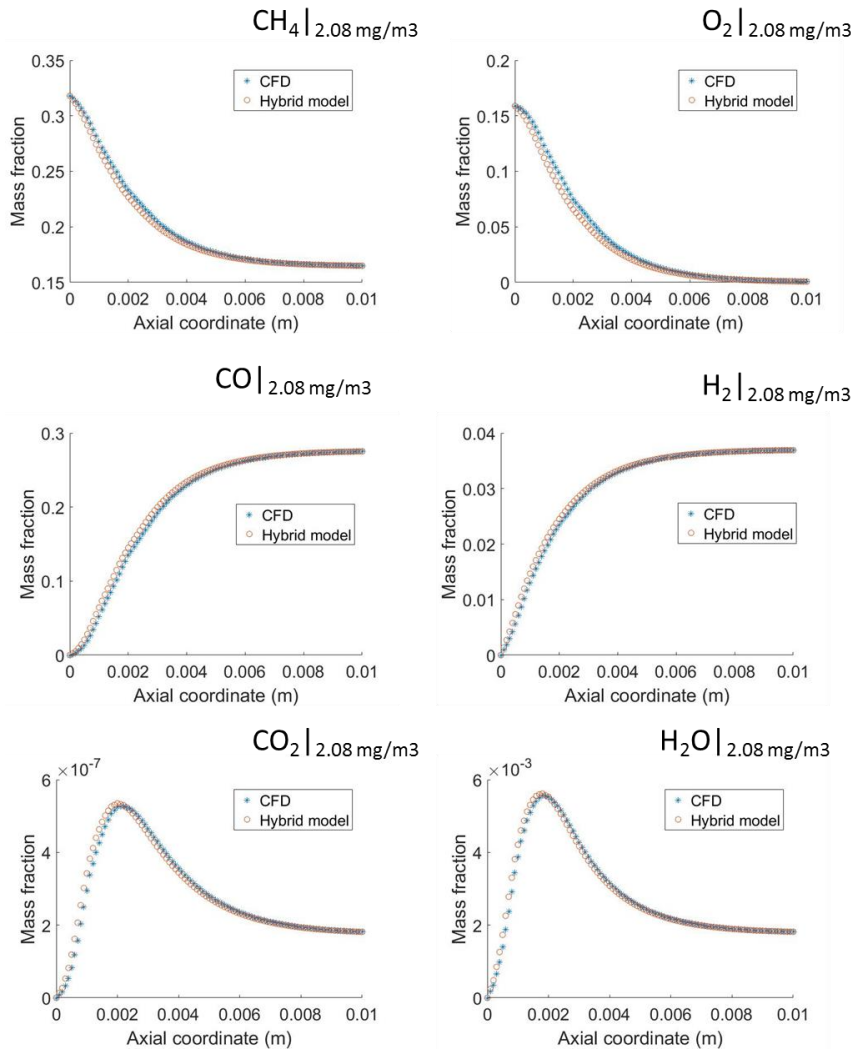
Figure 56: Comparison between a hybrid model mass fraction and the mass fraction predicted from CFD (r=0.0 mm)
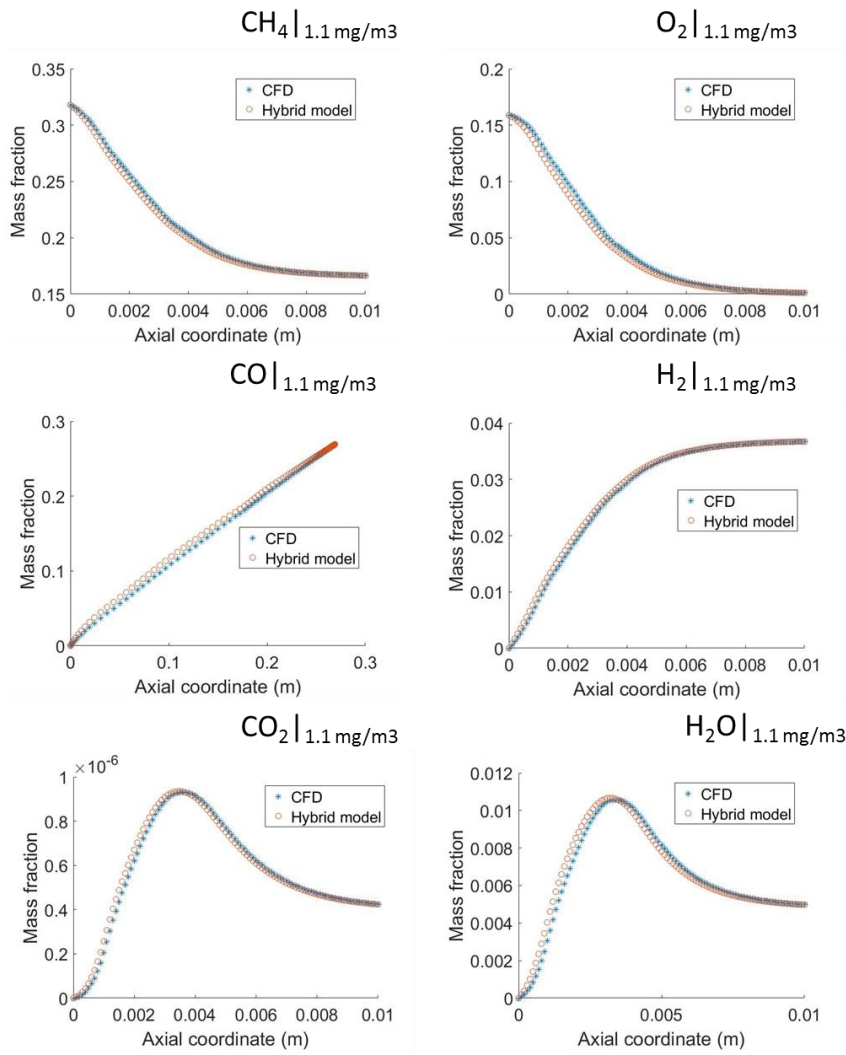
Figure 57: Comparison between a hybrid model mass fraction and the mass fraction predicted from CFD (r=0.0 mm)
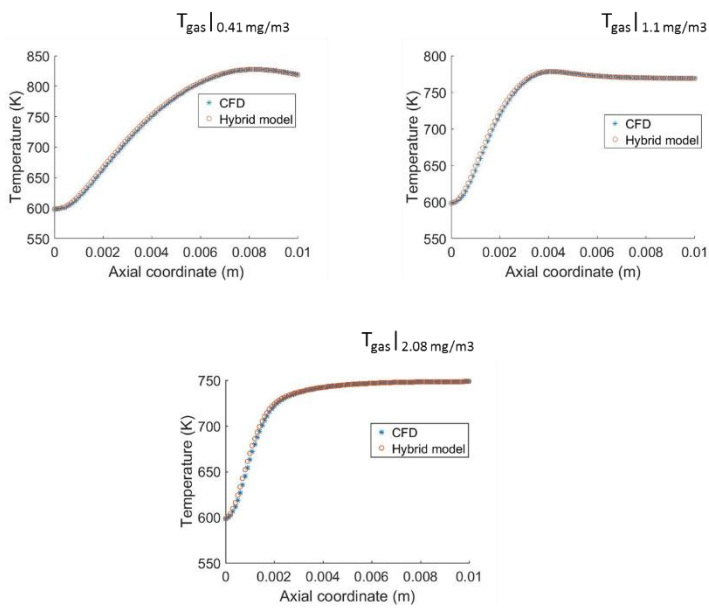
Figure 58: : Comparison between a hybrid model temperature profiles and the temperature predicted from CFD (r=0.0 mm)

7.3.1. Summary

The hybrid model is able to predict the state variables (temperature and concentration) at the same level of accuracy observed in the 3D CFD multichannel model for catalytic partial oxidation of methane. In addition to its accuracy, the hybrid model presents a high-speed way of modelling heterogeneous catalytic processes in a monolith reactor.

7.3.2. Conclusions

A multichannel monolith has been modelled by the hybrid model and the important features of a 3D CFD multichannel model were maintained. The hybrid model is a fast predictor of conversion and with the moderate computational expense it offers, a wide range of reactor configurations can be investigated for design and optimization. This is particularly important in the reduction of hot spot as the reactor configuration plays a significant role in dictating the temperature distribution. Additionally, mass transfer is an important factor to consider in improving methane conversion, and the geometric properties such as channel diameter are key in improving mass transport. The hybrid model allows for hundreds of simulations to be performed within a short space of time, thus the aforementioned can be achieved. Given the fast nature of the hybrid model, the sensitivity analysis can be carried out to establish an understanding of the interrelationships among geometric and operational variables.

Chapter 8. Sensitivity Analysis

A sensitivity analysis is undertaken to investigate how a range of values for a set of independent variables affect the system response. It allows for an enhanced understanding of the system dynamics as the correlation between the system response and a range of operating conditions can be established. The current study used the hybrid model to investigate the influence of feedstock ratio, inlet velocity, channel diameter and inlet temperature on syngas productivity and temperature.

8.1. The fraction of reaction flux at various channel diameters

The model parameters were analysed and their influence on the design of a monolith channel was determined. Depending on the feedstock ratio (rich or lean mixtures), the consumption of oxygen and methane can be governed by either chemical or transport regime (Nogare et al., 2011). Geometry plays a significant role in the consumption of oxygen. For instance, in the case of larger diameters, the mass transfer coefficient decreases resulting in lower consumption of oxygen. In the design of a monolith channel for partial oxidation of methane, a significant amount of time should be devoted to channel geometry, particularly regarding its influence on oxygen consumption, which eventually affects local temperature.

The fraction of the reaction rate flux for O_2 , CH_4 ,H_2 and CO is shown in Figure 59. The results show that for both CH_4 and O_2 the fraction is less than 0.5 from the entrance to the channel outlet. The results indicate that the reactions are happening under the chemical regime since the fraction of the reaction rate to diffusion flux is always less than 0.5. These results can help inform the optimization of mass transfer by a change in process parameters. The diffusion and reaction rate flux for both O_2 and CH_4 are shown in Figure 60 and Figure 61. The reaction rate fluxes were evaluated at the catalytic walls because that is where the reactions are defined (homogeneous reactions were neglected due to low pressure). It is evident from the figures that the reaction rate flux is always higher than the diffusion flux for both O_2 and CH_4.
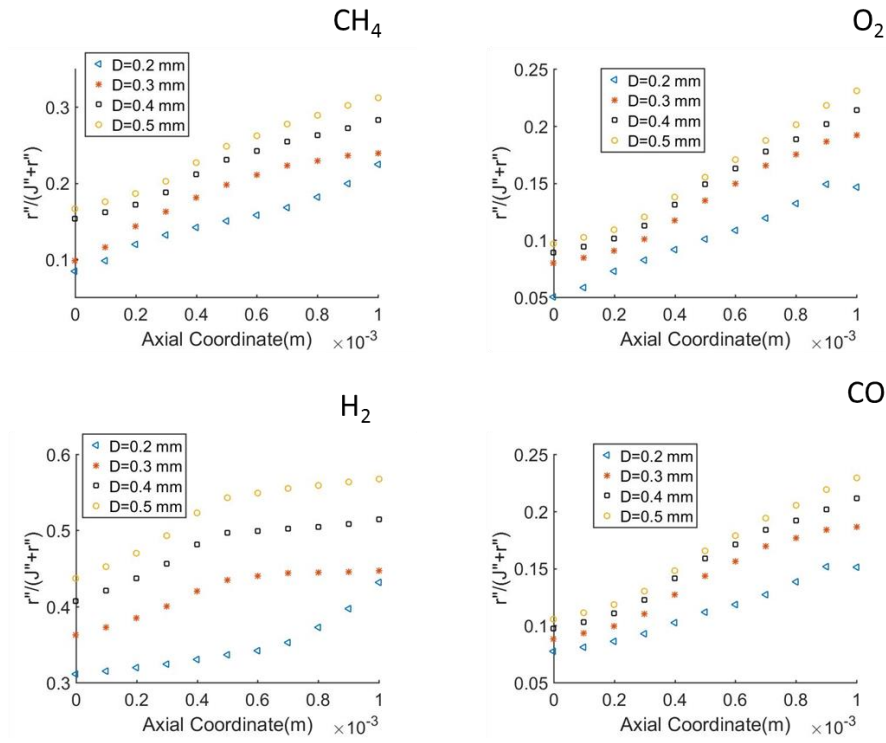
Figure 59: The fraction of reaction rate flux at various channel diameters
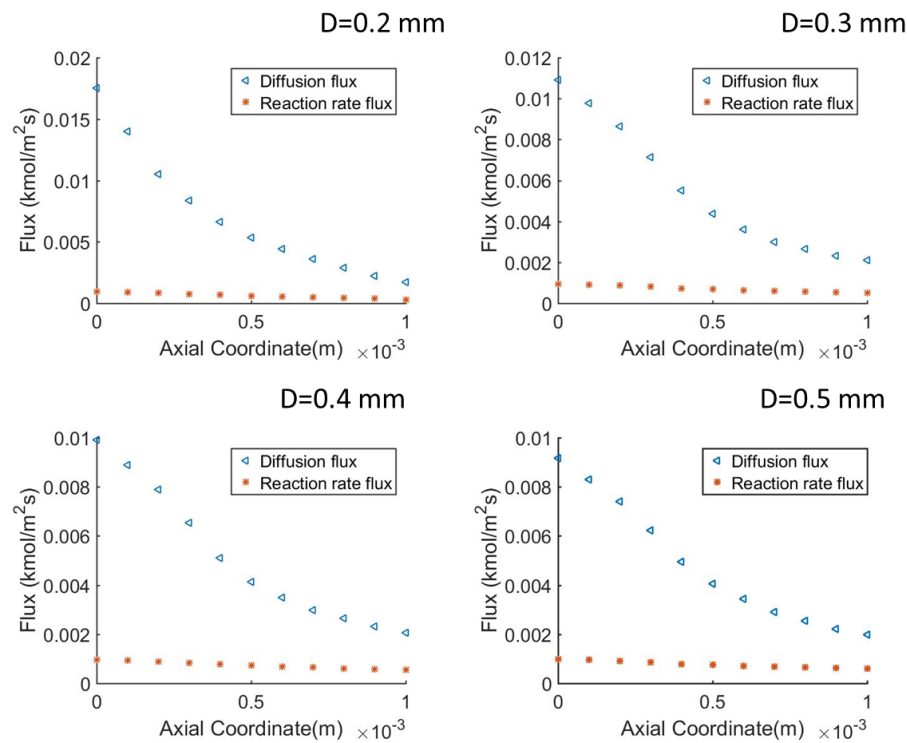
Figure 60: O_2 reaction rate and diffusion flux at various channel diameters
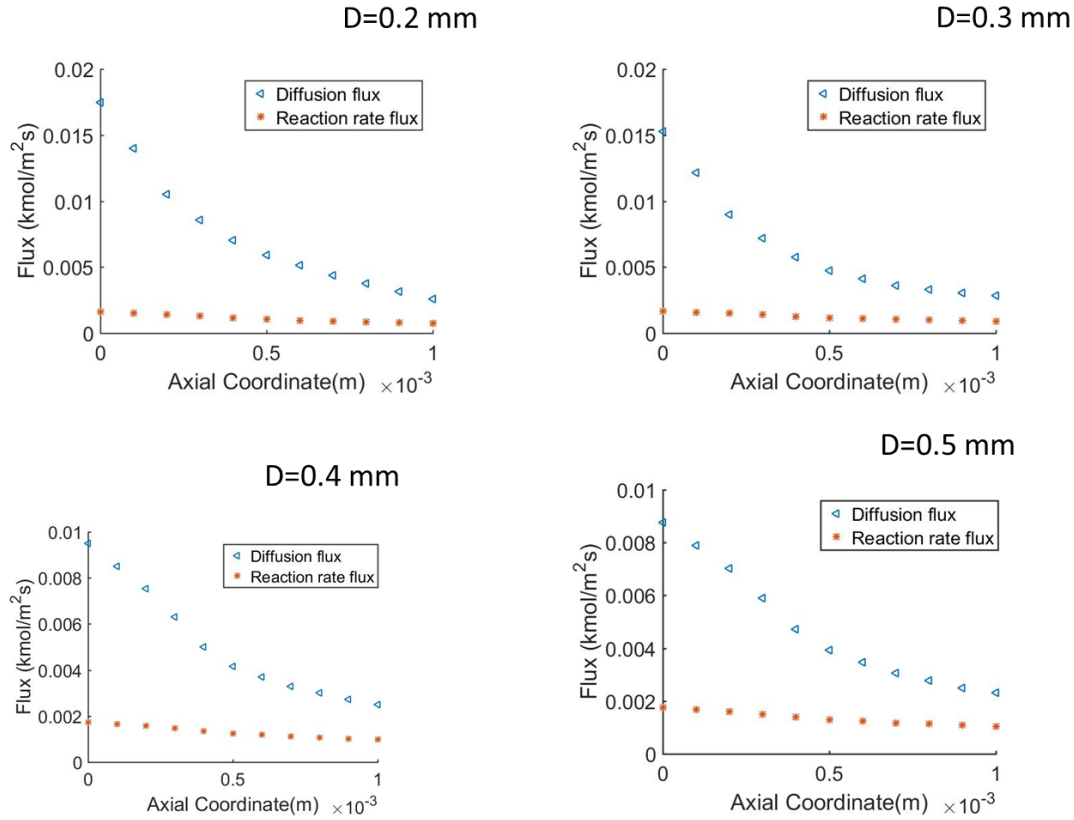
Figure 61: CH$_4$ reaction rate and diffusion flux at various channel diameters

8.2. The effects of diffusion and convection

The analysis on the convection flux and diffusion flux towards overall mass transfer was undertaken by employing the Peclet number. The Peclet number was calculated from the ratio of convection rate to diffusion rate (Equation 6.1). The results in Figure 62 reveal that the convective transport exceed diffusion and contributes significantly towards the overall mass transport. This is attributed to the Peclet number being always greater than unity for all the channel diameters chosen as shown in Figure 62. The channels with bigger diameters reveal larger local Peclet number as observed in Figure 62 and this can be attributed to mass transport by diffusion being greater in smaller diameters as compared to bigger diameters. Under these circumstances, the axial dispersion can be excluded from the model. However, to retain generality as far as possible, axial dispersion was retained in the balance.

$$Pe = \frac{LU}{D}$$
(6.1)
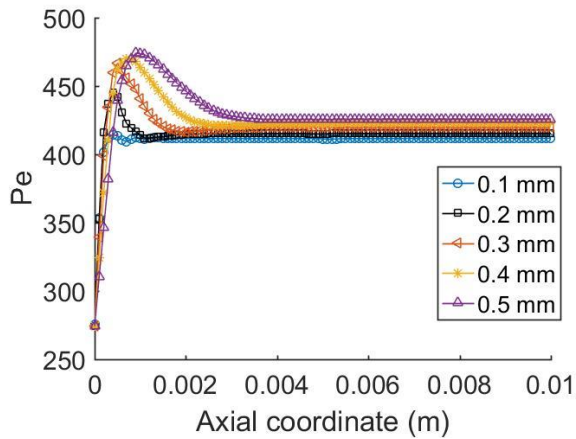
Figure 62: Peclet number at various channel diameters

The analysis on the effects of diffusion and convection is one of the important first steps towards the optimization of monolith reactors for methane oxidation. This is because the catalytic walls might be active enough to effect the desired reaction and conversion, however, the rate of transport of species from the bulk gas phase to the active sites influences the reaction concentration.

8.3. The influence of kinetic parameters on state variables

The sensitivity analysis was carried out by adjusting the kinetic parameters (on Table 15) from the reaction mechanism by a certain percentage and investigating the impact on the predicted state variables.The results from Figure 63 to Figure 67 show a comparison between the temperature and species mass fraction profiles predicted from varying magnitudes of Arrhenius number (A). It is evident from the sensitivity study that the accuracy of the kinetic parameters obtained at micro-scale are key to correctly modelling the heterogeneous systems at macro-scale.
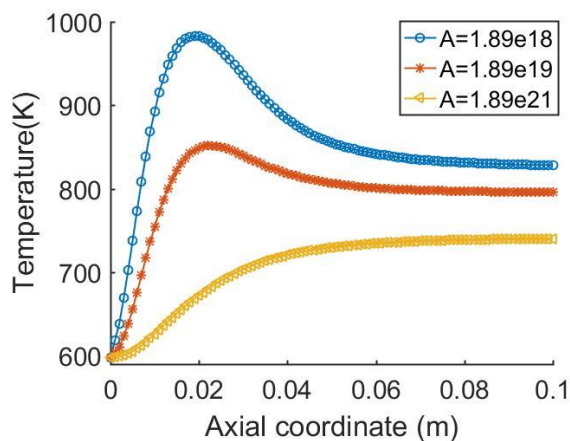
Figure 63: Temperature profiles at various magnitudes of kinetic parameters (a 10 mm length and 0.5 mm diameter monolith, 1.45 mg/m^3 catalyst loading and 2.5 m/s inlet velocity)

Figure 64: CH$_4$ mass fraction profiles at various magnitudes of kinetic (a 10 mm length and 0.5 mm diameter monolith, 1.45 mg/m^3 catalyst loading and 2.5 m/s inlet velocity)
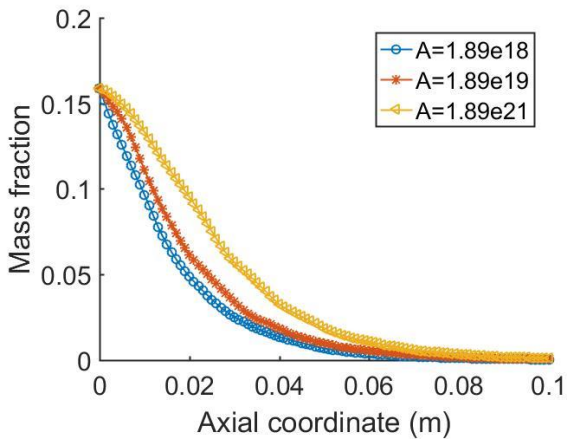
Figure 65: O$_2$ mass fraction profiles at various magnitudes of kinetic parameters (a 10 mm length and 0.5 mm diameter monolith, 1.45 mg/m^3 catalyst loading and 2.5 m/s inlet velocity)
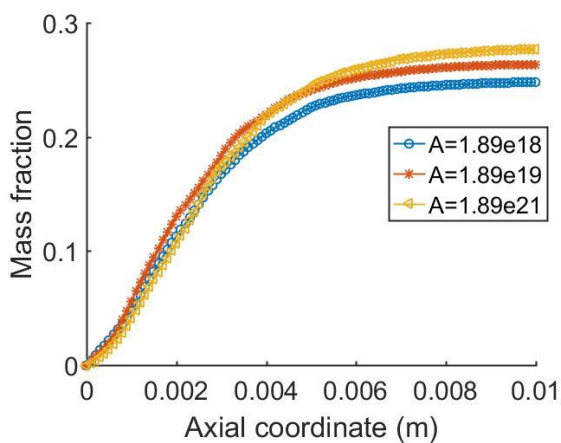
Figure 66: CO mass fraction profiles at various magnitudes of kinetic parameters (a 10 mm length and 0.5 mm diameter monolith, 1.45 mg/m^3 catalyst loading and 2.5 m/s inlet velocity)
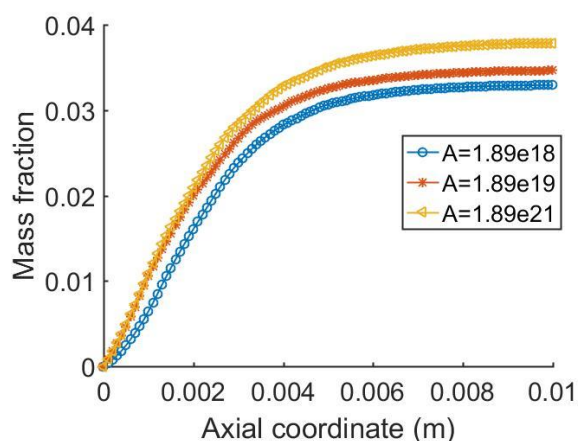
Figure 67: H_2 mass fraction profiles at various magnitudes of kinetic (a 10 mm length and 0.5 mm diameter monolith, 1.45 mg/m^3 catalyst loading and 2.5 m/s inlet velocity)

The inaccurate kinetic parameters result in the propagation of error from micro-scale to macro-scale, and this affects the accuracy of the state variables predicted by the model. Therefore, for accurate determination of state variables, the current study used the reaction mechanism developed by Quiceno et al. (2006) given that it is a robust kinetic scheme for catalytic partial oxidation of methane in high temperatures and short contact times.

8.4. The influence of feedstock ratio on syngas productivity

The ratio of methane to oxygen in the feedstock is an important parameter in catalytic partial oxidation of methane as it dictates the ratio of hydrogen to carbon-monoxide at the reactor outlet. The ratio of hydrogen to carbon-monoxide is important to control as different downstream processes require a specific ratio. The total oxidation products (water and carbon-dioxide) may be present in significant amounts if the stoichiometry in the feedstock is closer to that which favours total oxidation. The findings in Figure 68 and Figure 69 reveal that the mass fractions for both H_2 and CO change with a change in the feedstock ratio.

The ratio of 2.5 (CH_4/O_2) results in the highest mass fractions of both H_2 and CO at the reactor outlet and this translates to the optimum ratio. The findings on the ratio of H_2 to CO as presented in Figure 72 show that at the reactor outlet, this ratio is affected by the ratio of CH_4 to O_2. The ratio of H_2 to CO at the reactor outlet is always close to 2.0 for feedstock ratios of greater than 2.0 and this is suitable for most downstream processes such as Fischer-Tropsch and methanol synthesis (Zhang et al.,2001;

Bhavsar et al.,2014). At the feedstock ratios of less than 2.0, the H_2 to CO ratio at the reactor outlet is less than 2.0 and this can be ascribed to the stoichiometry favouring the formation of total oxidation products.

The increased mass fraction of H_2 and CO in the case of rich mixtures can be attributed to increased selectivity. The mass fraction of total oxidation products is shown to decrease with the use of rich mixtures as observed in Figure 73 and Figure 74 and this translates to enhanced syngas selectivity. In this case, the mass fractions of H_2O and CO_2 (which are total oxidation products) is shown to be greater for lean mixtures. At the ratio of 4.0, the total oxidation products are shown to be less in the product when compared to all other feedstock ratios and this translates to increased syngas selectivity. The H_2 and CO selectivity results in Figure 75 indicate that the selectivity is highest at the identified optimum feedstock ratio (2.5).
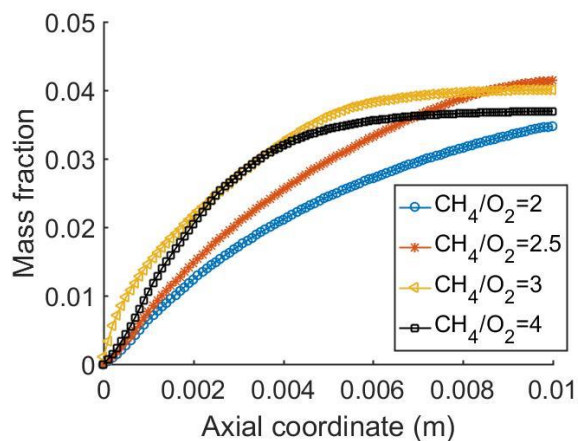
Figure 68: H_2 mass fraction profiles at various feedstock ratios (a 10 mm length and 0.5 mm diameter monolith with 598.15 K inlet temperature and 2.5 m/s inlet velocity)
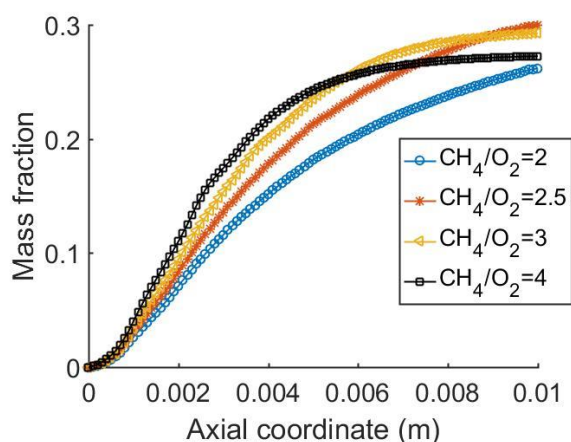
Figure 69: CO mass fraction profiles at various feedstock ratios (a 10 mm length and 0.5 mm diameter monolith with 598.15 K inlet temperature and 2.5 m/s inlet velocity)

111
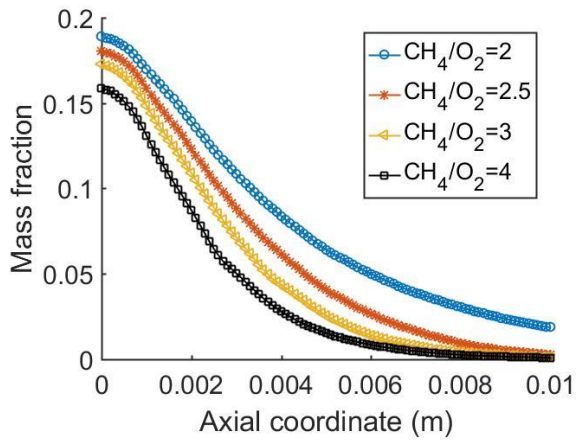
Figure 70: O_2 mass fraction profiles at various feedstock ratios (a 10 mm length and 0.5 mm diameter monolith with 598.15 K inlet temperature and 2.5 m/s inlet velocity)
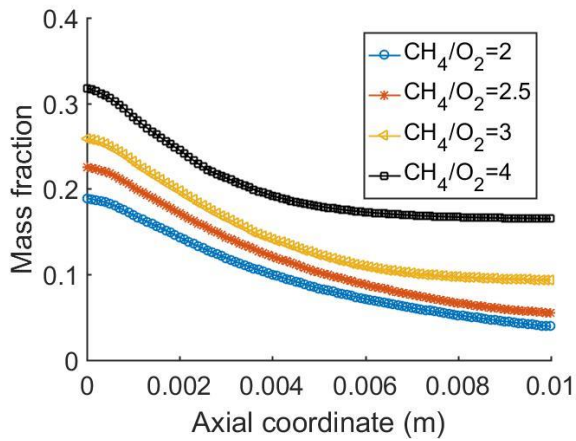
Figure 71: CH_4 mass fraction profiles at various feedstock ratios (a 10 mm length and 0.5 mm diameter monolith with 598.15 K inlet temperature and 2.5 m/s inlet velocity)
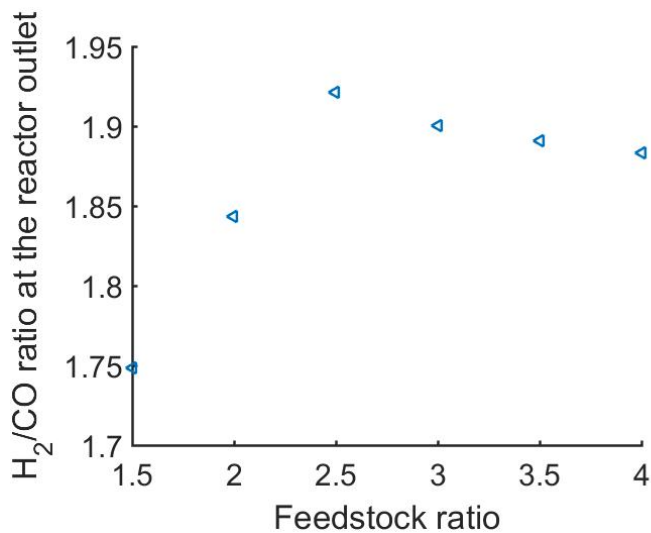
Figure 72: The ratio of H_2 to CO at various feedstock ratios (a 10 mm length and 0.5 mm diameter monolith with 598.15 K inlet temperature and 2.5 m/s inlet velocity)
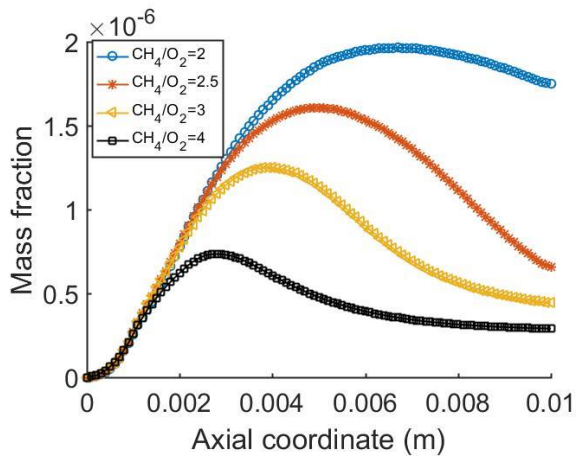
Figure 73: CO_2 mass fraction profiles at various feedstock ratios (a 10 mm length and 0.5 mm diameter monolith with 598.15 K inlet temperature and 2.5 m/s inlet velocity)
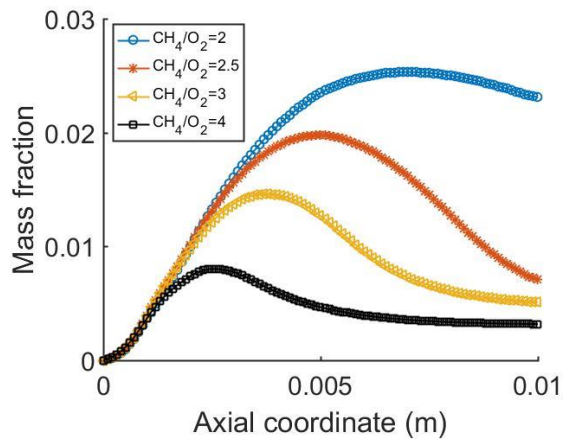
Figure 74: H_2O mass fraction profiles at various feedstock ratios (a 100 mm length and 1.0 mm diameter monolith with 598.15 K inlet temperature and 2.5 m/s inlet velocity)
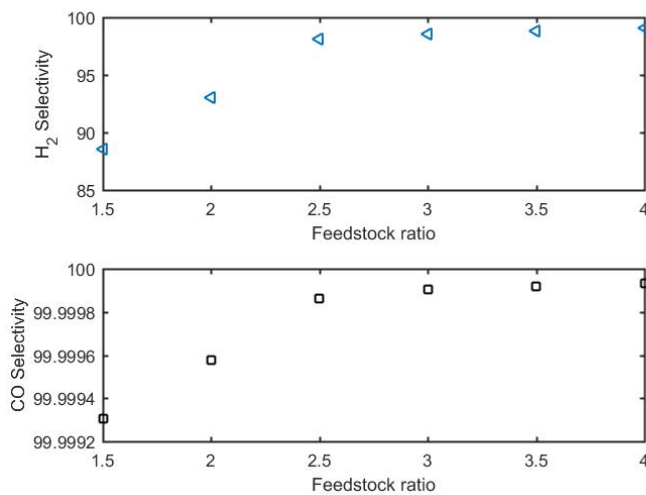
Figure 75: H_2 and CO selectivity at various feedstock ratios (a 100 mm length and 1.0 mm diameter monolith with 598.15 K inlet temperature and 2.5 m/s inlet velocity)

The feedstock ratio influences the product distribution at the reactor outlet as mentioned above. The ratio of 2.5 (CH_4/O_2) was found to be optimum as it resulted in

the highest syngas selectivity. Adding to high selectivity, this fuel to oxygen ratio results in the H_2 to CO ratio close to 2.0 which is suitable for most downstream applications. Therefore, it is desirable to control the feedstock ratio in order to meet the product specifications.

8.5. The influence of feedstock ratio on surface coverage

The influence of feedstock ratio was further investigated on surface coverage. The surface coverage results at various feedstock ratios are presented in Figure 76 to Figure 80. It is evident from the results that for rich mixtures (or oxygen deficient mixtures) the catalyst active sites become deposited with carbon as observed in Figure 77 and this may lead to deactivation. The On the hand, the lean mixture mitigates the carbon deposition as evidenced by the free sites results presented in Figure 76. The empty sites as shown in Figure 76 allow for the adsorption of reactants and a result the reaction proceeds and this is illustrated by the increased syngas produced shown in Figure 68 and Figure 69.

This analysis is desirable as it helps to inform the best operating conditions that will keep the function of the catalyst in its enhanced state. The feedstock ratio of 2.0 was found to be optimum and the surface coverage results indicate that at this ratio there is less carbon deposit as observed in Figure 76 and Figure 77. The species mass fraction profiles indicated that the total oxidation products are favoured by a low ratio of methane to oxygen in the reactor feed and this is explained by the carbon monoxide and hydrogen surface coverage results.

The CO surface coverage results show that in the case of lean mixtures, CO has a higher surface coverage (Figure 125), and this explains the formation of carbon monoxide which is higher in this case compared to rich mixtures. Additionally, hydrogen surface coverage (Figure 127) is higher in lean mixtures and this leads to water formation due to the presence of adsorbed OH. Deutschmann and Lanny D. Schmidt (1998) explained that the more adsorbed CO there is, the more CO_2 is produced. These authors further explained that the adsorbed OH leads to water formation due to the adsorbed hydrogen. The surface coverage results are in agreement with the kinetics of partial oxidation of methane and the reaction mechanism as observed in Table 2. The increasing carbon surface coverage as

observed in Figure 77 is in agreement with the carbon surface coverage at the catalyst exit determined experimentally (Deutschmann and Schmidt, 1998b).
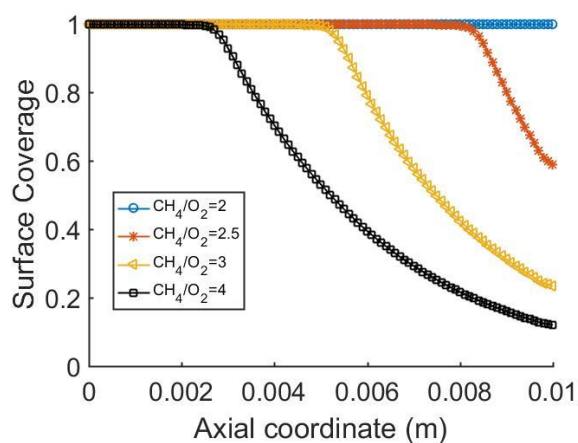
Figure 76: The free sites on the catalyst surface at various feedstock ratios (a 10 mm length and 0.5 mm diameter monolith with 598.15 K inlet temperature and 2.5 m/s inlet velocity)
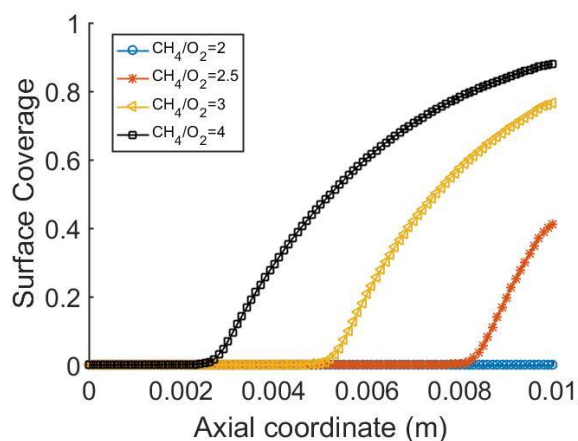
Figure 77: C fractional surface coverage at various feedstock ratios (a 10 mm length and 0.5 mm diameter monolith with 598.15 K inlet temperature and 2.5 m/s inlet velocity)
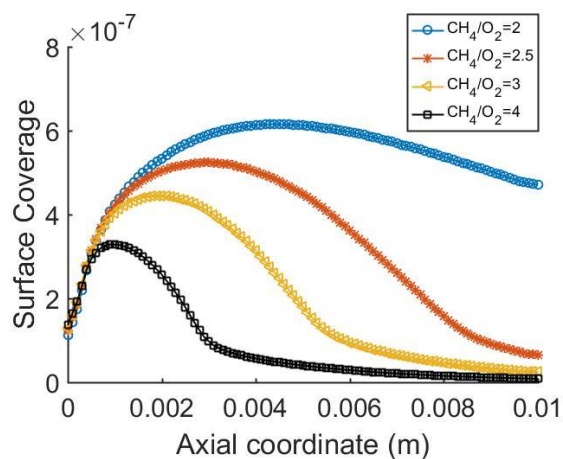
Figure 78: H_2O fractional surface coverage at various feedstock ratios(a 10 mm length and 0.5 mm diameter monolith with 598.15 K inlet temperature and 2.5 m/s inlet velocity)
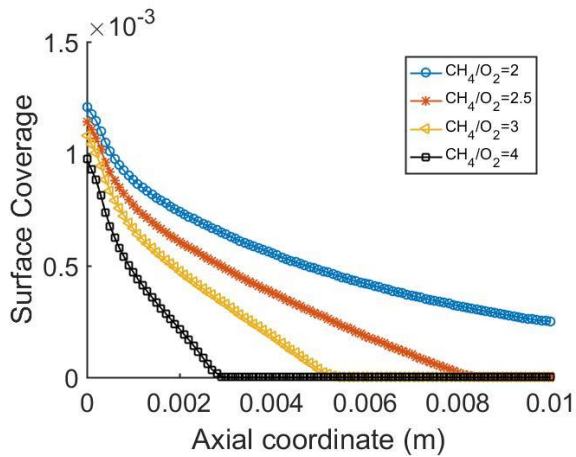
Figure 79: O fractional surface coverage at various feedstock ratios (a 10 mm length and 0.5 mm diameter monolith with 598.15 K inlet temperature and 2.5 m/s inlet velocity)
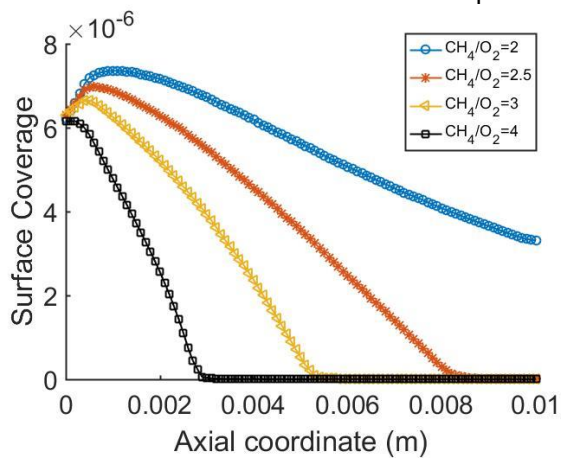
Figure 80: OH fractional surface coverage at various feedstock ratios (a 10 mm length and 0.5 mm diameter monolith with 598.15 K inlet temperature and 2.5 m/s inlet velocity)

The carbon fractional surface coverage was shown to increase from the reactor intlet further downstream in the case of rich mixtures. In Figure 81, it can be observed that there is not enough oxygen to react with the adsorbed carbon, hence the increased carbon surface coverage. The syngas productivity in this case is lower than the case where there is more adsorbed oxygen to react with carbon and produce carbon dioxide.
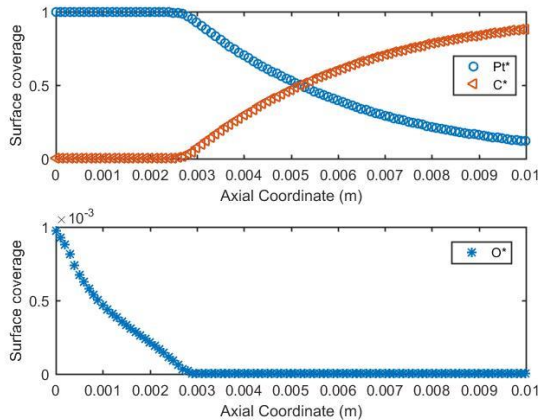
Figure 81: Vacant sites, Oxygen and carbon fractional surface coverage at CH_4/O_2=4.0 (a 10 mm length and 0.5 mm diameter monolith with 598.15 K inlet temperature and 2.5 m/s inlet velocity)

The sensitivity analysis on species surface coverage indicate that the rich mixtures result in carbon deposits in the active sites. The fuel to oxygen ratio of 2.5 was found to be optimum as it resulted in less carbon deposits on the catalyst active sites. Therefore, attention should be paid to the feedstock ratio as this can help reduce the carbon deposits in the active sites.

8.6. The reaction rate profiles at various feedstock ratio

The results shown in Figure 82 to Figure 87 help explain the mass fraction profiles in Figure 68 to Figure 74. In each case, the net formation or consumption of each species at different fuel to oxygen ratio is shown. At high ratios, steam and dry reforming reactions take place in the channel and this is evident from the net reaction rates for both CO_2 and H_2O as shown in Figure 86 and Figure 87. The findings indicate that further downstream, the reaction rate of both H_2O and CO_2 show that they are consumed in the reaction as indicated by reaction rate profiles.
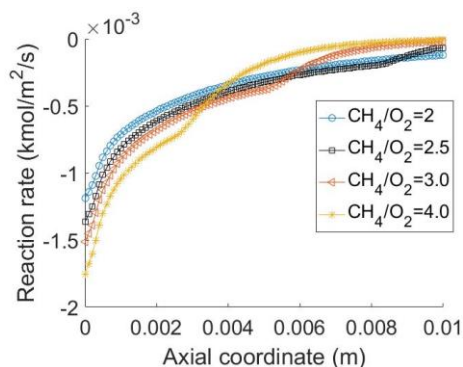
Figure 82: CH_4 reaction rate flux (kmol/m^2/s) (a 10 mm length and 0.5 mm diameter monolith with 598.15 K inlet temperature ,1.45 mg/m^3 catalyst loading and 2.5 m/s inlet velocity)
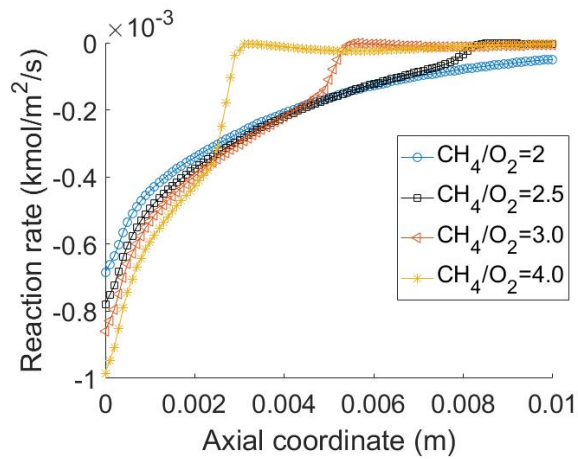
Figure 83: O_2 reaction rate flux (kmol/m^2/s) (a 100 mm length and 1.0 mm diameter monolith with 598.15 K inlet temperature ,1.45 mg/m^3 catalyst loading and 2.5 m/s inlet velocity)
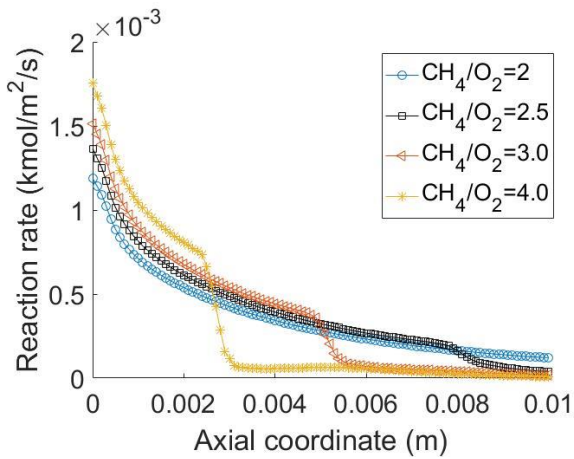
Figure 84: CO reaction rate flux (kmol/m^2/s) (a 10 mm length and 0.5 mm diameter monolith with 598.15 K inlet temperature ,1.45 mg/m^3 catalyst loading and 2.5 m/s inlet velocity))
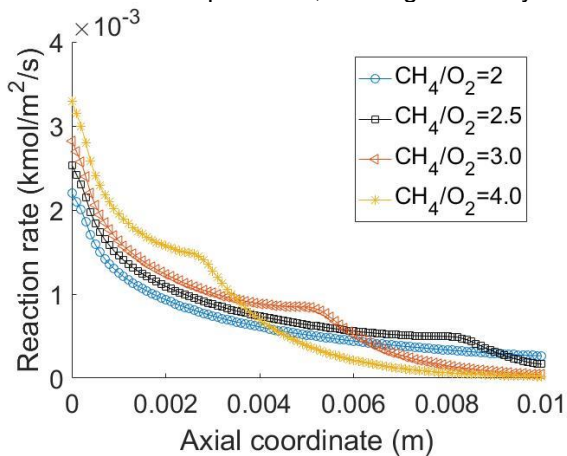
Figure 85: H_2 reaction rate flux (kmol/m^2/s) (a 10 mm length and 0.5 mm diameter monolith with 598.15 K inlet temperature ,1.45 mg/m^3 catalyst loading and 2.5 m/s inlet velocity)
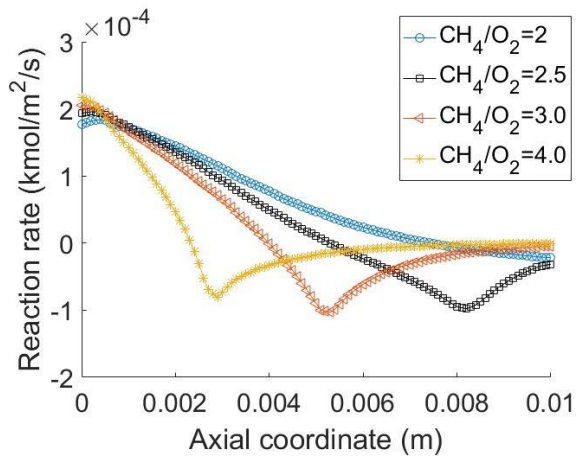
Figure 86: H_2O reaction rate flux ($kmol/m^2/s$) (a 10 mm length and 0.5 mm diameter monolith with 598.15 K inlet temperature ,1.45 mg/m^3 catalyst loading and 2.5 m/s inlet velocity)
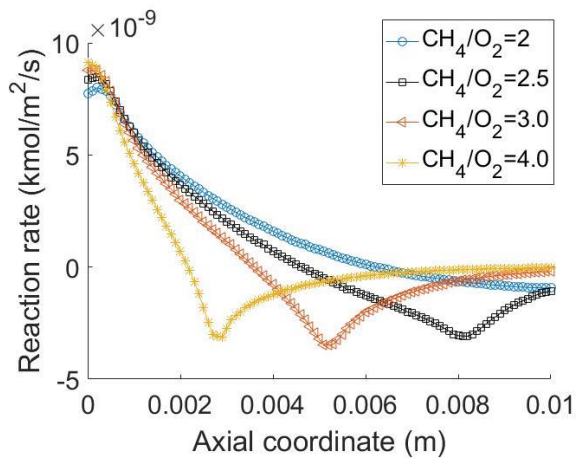
Figure 87: CO_2 reaction rate flux ($kmol/m^2/s$) (a 10 mm length and 0.5 mm diameter monolith with 598.15 K inlet temperature ,1.45 mg/m^3 catalyst loading and 2.5 m/s inlet velocity)

The lean mixtures result in the steam and dry reforming reactions in the monolith channels and this is evident from the net reaction rates for both CO_2 and H_2O. These reactions will influence the ratio of H_2 to CO at the reactor outlet and it is important that the feedstock ratio is controlled to achieve the desired product distribution.

8.7. The influence of channel diameter on syngas productivity

The channel diameter was varied and its influence on the consumption of oxygen was investigated. In all the channel diameters chosen, the space time was kept constant and this was done by keeping the inlet velocity constant in all the diameters. Oxygen consumption in catalytic partial oxidation reactions is explained to be fully external mass transfer limited by Maffei et al. (2014). This is evident from the oxygen mass

fraction profiles presented in Figure 88. It is observed that oxygen consumption is enhanced at smaller diameter channels and this is due to increased mass transfer of reactants from the gas phase to the catalytic walls. Oxygen consumption reaches completion rapidly in small diameters and is characterised by steeper gradients. On the methane, the investigations on channel diameter reveal that larger diameters lead to increased methane conversion as observed in Figure 89.
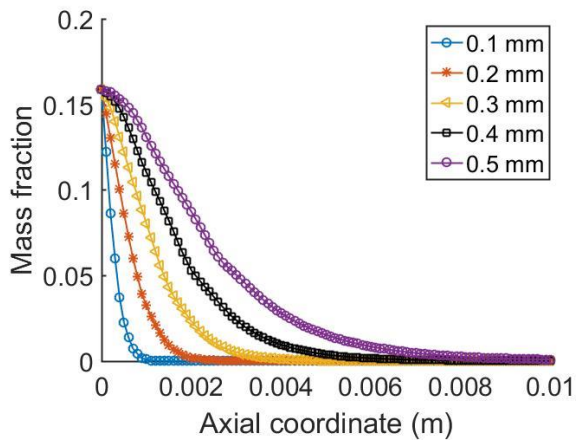
Figure 88: O_2 mass fraction profiles at various channel diameters (a 100 mm length monolith with 598.15 K inlet temperature)
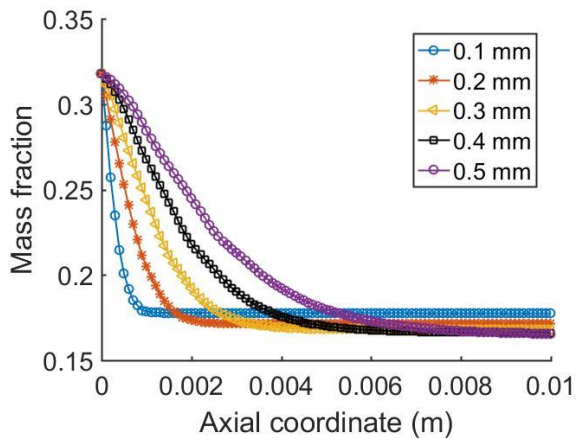
Figure 89: CH_4 mass fraction profiles at various channel diameters (a 10 mm length monolith with 598.15 K inlet temperature)

The amount of hydrogen produced in catalytic partial oxidation is affected by the interplay of partial oxidation, total oxidation, reforming reactions and water gas shift reactions. At lower temperatures, water gas shift reactions are favoured, and carbon monoxide produced from partial oxidation is converted into hydrogen.

The ratio of hydrogen to carbon monoxide is an important factor as the downstream applications require as certain ratio as feedstock. The design of the channel diameter

can therefore be an important factor to consider in controlling the ratio to meet the downstream requirements. The hydrogen mass fraction profiles are observed in Figure 90 and the abovementioned phenomenon can be observed. The influence of channel diameter on carbon-monoxide mass fraction profiles is shown in Figure 91 and the findings reveal that the local mass fraction is higher at smaller diameters and the difference is diminishes at the channel outlet. The differences in the mass fraction profiles at different channel diameters can be attributed to the mass transfer coefficient dependency on the channel diameter. The mass transfer coefficient has an inverse proportion to the channel diameter. In view of this, the channel diameter can be varied to investigate the influence of mass transfer coefficient on the reaction rate, and mass transfer can be optimized to allow for more compact designs.
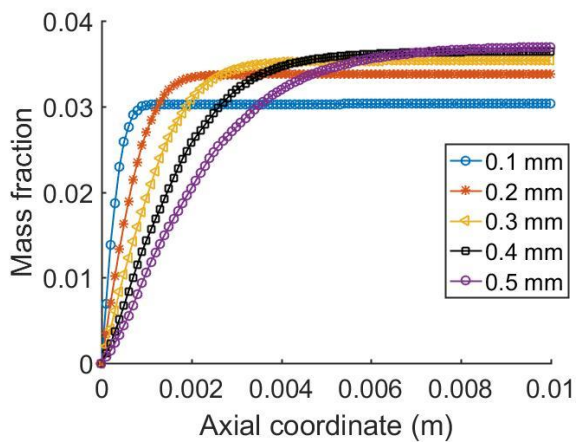
Figure 90: H$_2$ mass fraction profiles at various channel diameters (a 10 mm length monolith with 598.15 K inlet temperature)
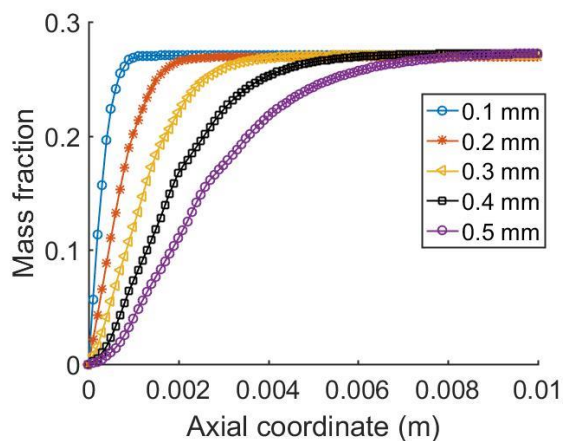
Figure 91: CO mass fraction profiles at various channel diameters (a 10 mm length monolith with 598.15 K inlet temperature)

There is an interplay of partial and total oxidation in the catalytic partial oxidation of methane and this is one of the major challenges and as a result, the production of carbon dioxide and water is expected at the reactor outlet. As with other parameters, the influence of channel diameter on the production of the total oxidation products was investigated. The findings as observed in Figure 92 and Figure 93 indicate that the amount of carbon dioxide and water produced increase with the decrease in channel diameter. The mass fraction profiles for both water of carbon dioxide show an increase at the bed length less than 0.0025 m and a sudden decrease thereafter. This decrease is explained by the dry and steam reforming reactions that take place to produce hydrogen and carbon monoxide. The reaction rate profiles in Figure 94 and Figure 95 explain this observed behaviour in that the produced water and carbon-monoxide start to be consumed in the reforming reactions.
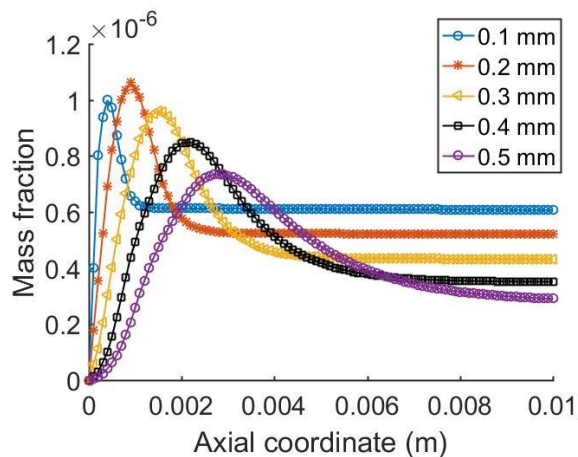
Figure 92: CO_2 mass fraction profiles at various channel diameters (a 10 mm length monolith with 598.15 K inlet temperature)
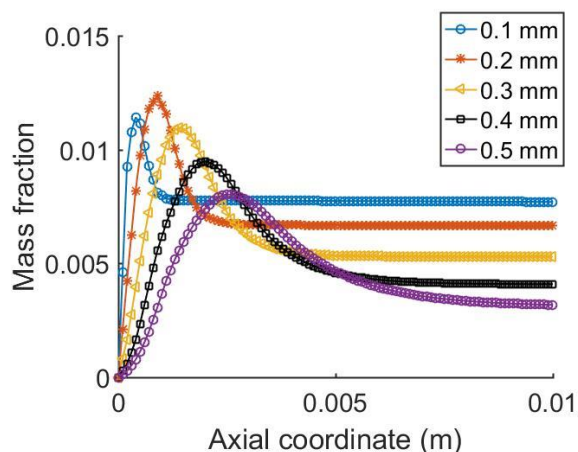
Figure 93: H_2O mass fraction profiles at various channel diameters (a 10 mm length monolith with 598.15 K inlet temperature)
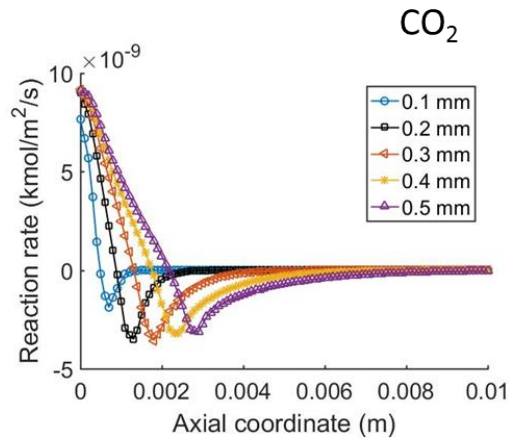
Figure 94: CO_2 reaction rate profiles at various channel diameters (a 10 mm length monolith with 598.15 K inlet temperature)
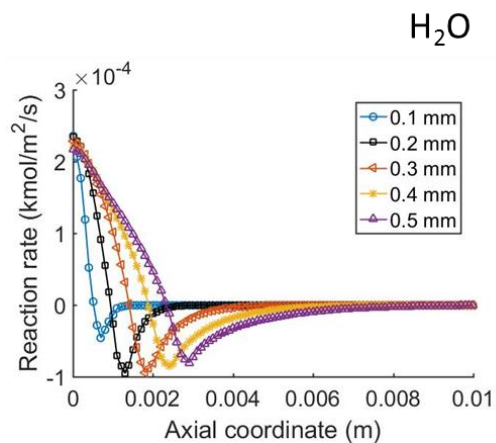
Figure 95: H_2O reaction rate profiles at various channel diameters (a 10 mm length monolith with 598.15 K inlet temperature)

The channel diameter is an important parameter to consider in catalytic partial oxidation of methane as it can help elucidate the interplay among the primary reaction and other reactions such as total oxidation, water gas shift and steam reforming. This is because some reactions are favoured by lower temperatures (water gas shift) and the choice of the appropriate channel diameter can help inhibit such reactions.

8.8. The influence of inlet velocity on syngas productivity

The different inlet velocities result in different hydrodynamics in the reactor and as a result the difference in the temperature and species concentration profiles is expected. The corresponding Reynolds numbers for the range of inlet velocities in Figure 96 are 35.9, 44.8, 53.9, 63.1 and 71.2 . The findings in Figure 96 and Figure 97 show that the higher the inlet velocity (higher Reynolds number), the higher the mass fraction for H_2

and lower mass fraction for CO. This can be attributed to increased mass transfer at higher velocities, which ultimately increases the rate of reactants consumption.
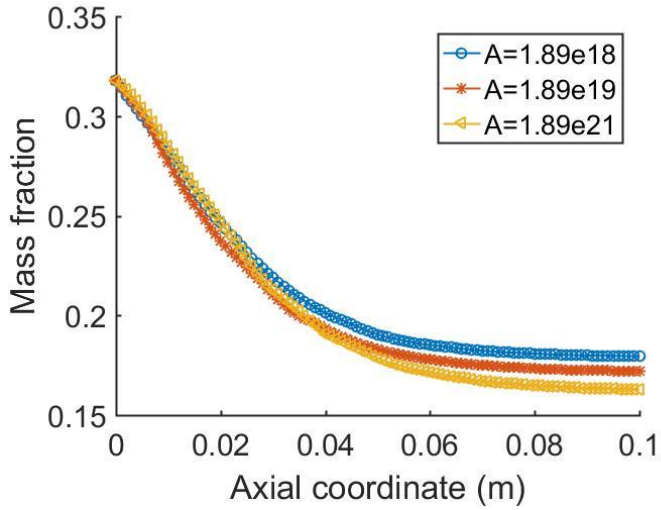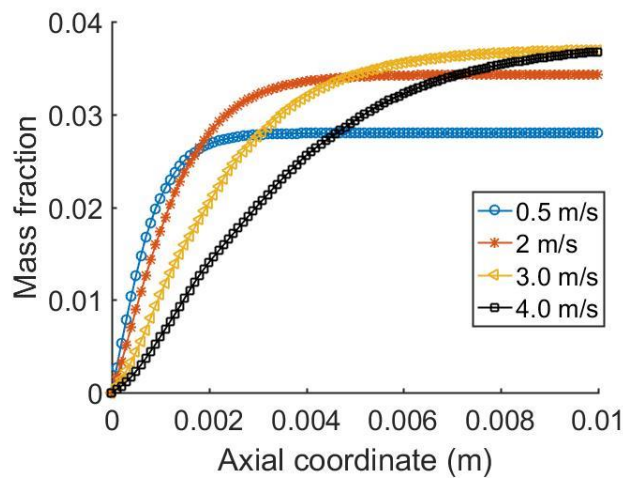

Figure 96: H_2 mass fraction profiles at various inlet velocities (a 10 mm length and 0.5 mm diameter monolith and1.45 mg/m^3 catalyst loading)
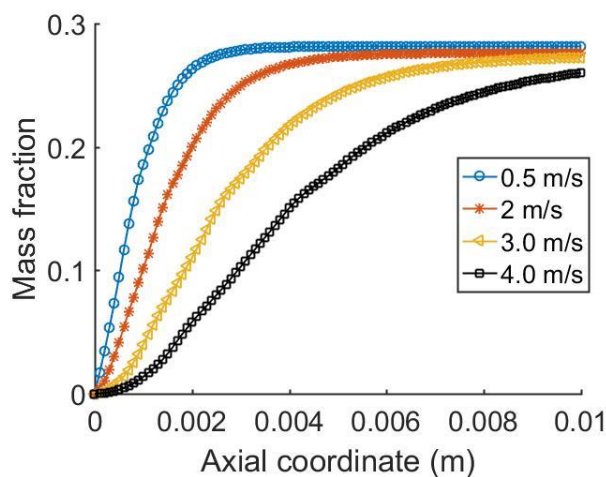
Figure 97: CO mass fraction profiles at various inlet velocities (a 10 mm length and 0.5 mm diameter monolith and 1.45 mg/m^3 catalyst loading)

8.9. The effect of inlet temperature on syngas productivity

The inlet temperature has an influence on methane activation and the product distribution at the reactor outlet. At higher temperatures, methane is easily activated, and it expected that this will result in higher mass fractions of H_2 and CO. The mass fraction profiles in Figure 98 indicate that mass fractions are higher in the case of higher inlet temperatures. However, at the reactor outlet, the mass fractions for H_2 are higher for lower inlet temperatures and this can be attributed to water gas shift reactions that take place and are favoured by lower temperatures. In the case of CO,

the mass fraction at the reactor outlet is higher for higher temperatures and this is because at high temperatures , less CO is converted in the water gas shift reactions. The water gas shift reaction is represented by Equation 6.2.

$$CO + H_2O \rightarrow H_2 + CO_2 \tag{6.2}$$
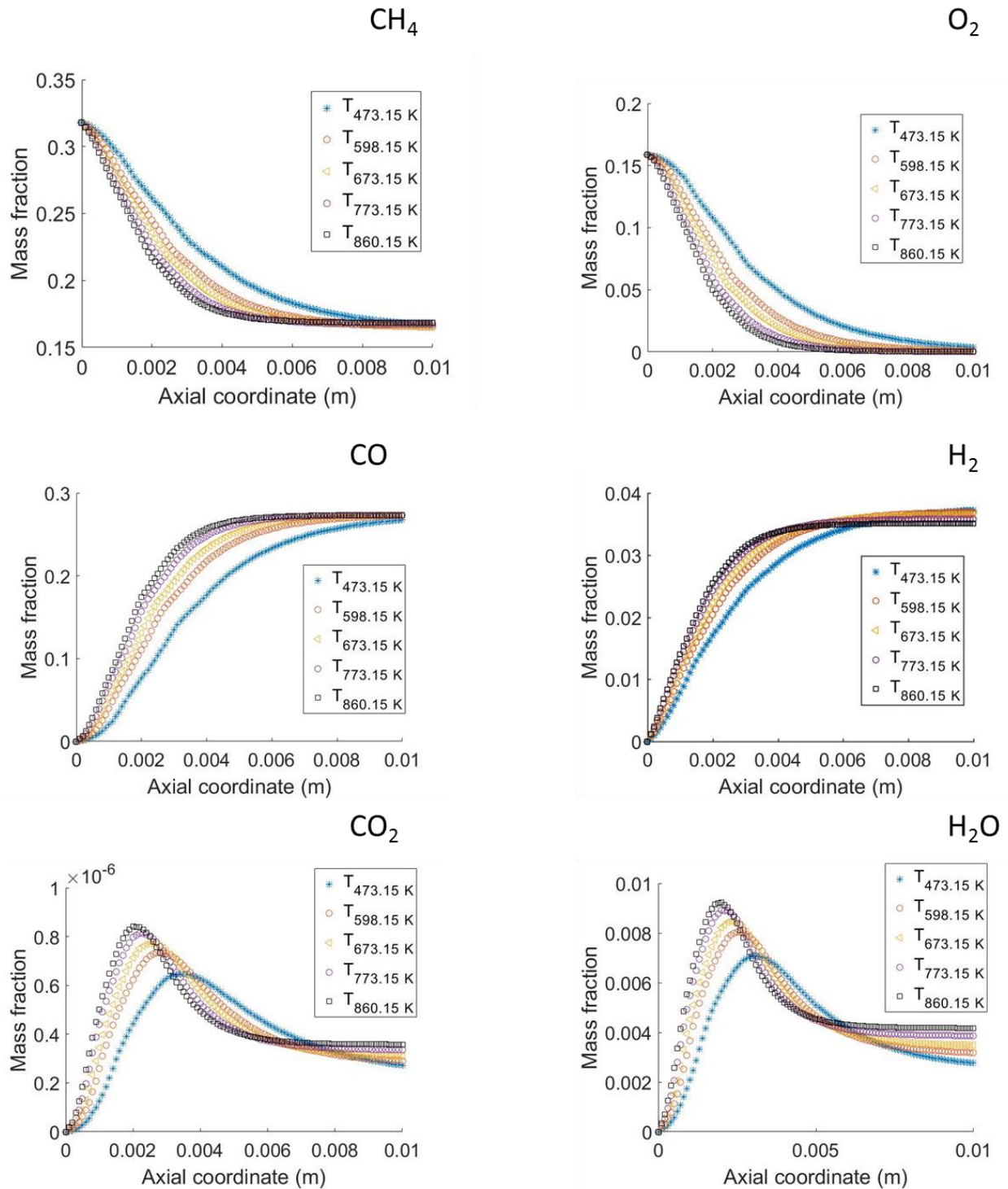
Figure 98: Mass fraction profiles at various inlet Temperatures (a 10 mm length and 0.5 mm diameter monolith, 1.45 mg/m^3 catalyst loading and 2.5 m/s inlet velocity)

The inlet temperature has an influence on the ratio of H_2 to CO at the reactor outlet and this is important to consider in producing syngas as a feedstock to a certain downstream process.

8.10. The effect of feedstock ratio on temperature

The temperature in a monolith channel is influenced by the exothermicity and endothermicity of a reaction. In a case of partial oxidation of CH_4 to syngas, there are multiple reactions taking place, namely; the mildly exothermic partial oxidation, exothermic total oxidation, an endothermic steam reforming, dry reforming and water gas shift reaction. Depending on the ratio of fuel to oxygen chosen in the feedstock, one of the above described reactions will dominate and thus the temperature in the channel will change with the ratio. The gas and catalyst temperature profiles are shown in Figure 99. It is evident from the figures that the highest temperature is encountered at a ratio of fuel to oxygen ($CH_4/O_2=2.0$) and this is attributed to total oxidation being dominant as the stoichiometry is much closer to that required in total oxidation reactions. On the other hand, for higher ratios, in which case the reaction path way favours partial oxidation, the temperature increases on the first few millimetres of the catalyst bed and decreases downstream due to some endothermic reforming reactions. The temperature profiles ultimately reach thermal equilibrium.
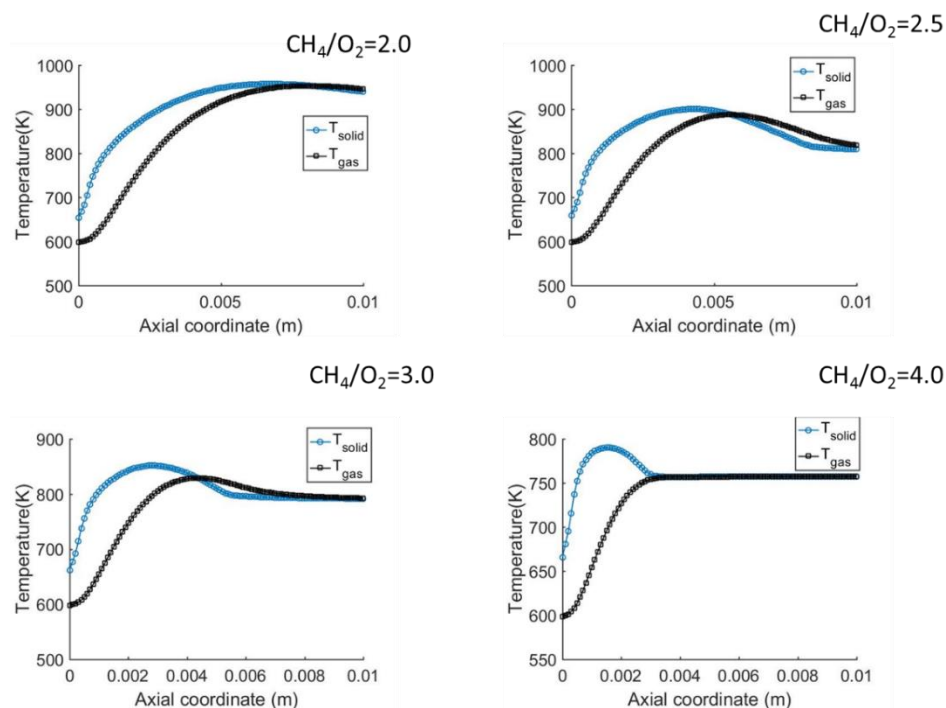
Figure 99: Temperature profiles at various feedstock ratios (a 10 mm length and 0.5 mm diameter monolith, 1.45 mg/m^3 catalyst loading and 2.5 m/s inlet velocity)

The feedstock ratio can be chosen such that the often-encountered formation of local hot spot is reduced. The rich mixtures result in lower temperatures in comparison to lean mixtures.

8.11. The influence of inlet velocity on temperature

The temperature profiles along the channel axial position are shown in Figure 100. The local temperature is higher for lower velocities in the first few millimetres (0.2 mm) of the catalyst bed. The lower inlet velocity (0.5 m/s) results in a high local temperature and this can be attributed to an increased residence time, thus increasing the exothermic consumption of oxygen. However, down the catalyst bed, the temperature profiles for both the higher and lower inlet velocities are the same as observed in Figure 100.

T_{gas}
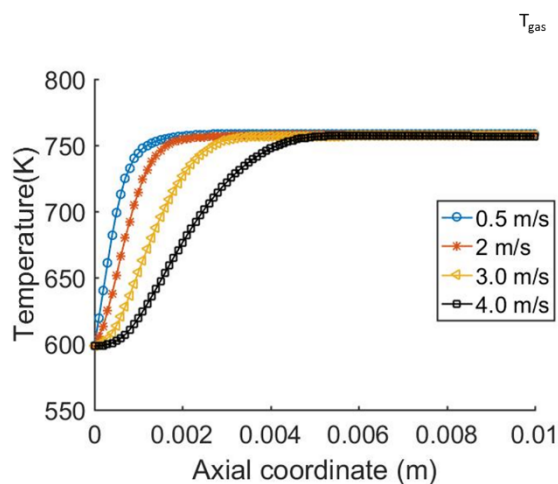
Figure 100: Temperature profiles at various inlet velocities (a 10 mm length and 0.5 mm diameter monolith and1.45 mg/m^3 catalyst loading)

8.12. Conclusion

The reactor configuration has a significant influence on the species concentration and temperature. It is therefore desirable to pay attention to the geometry as it helps in achieving a certain ratio of H_2 to CO in the reactor outlet. Furthermore, the formation of local hot spot which is one of the challenges in the partial oxidation of methane can be addressed by an optimized geometry. The consumption of both CH_4 and O_2 were found to be governed by chemical regime. The analysis based on the Peclet number indicate that convective effects dominate in the determination of overall mass transfer.

Chapter 9. Monolith Geometric Optimization

The current study is aimed at the sensitivity analysis that can be used in optimization studies. Upon performing the sensitivity study on the hybrid model, the information was used in the geometric optimization of a monolith reactor with the view of maximising profit margin, minimizing the fabrication costs and reducing the formation of local hot spot. The non-uniform catalyst distribution can be applied to reduce the catalyst density, hence fabrication costs while maintaining a high syngas productivity.

The channel diameter was varied and its influence on process profitability determined. The channel size influences the local temperature distribution, and this makes the diameter of a channel an important parameter to consider in studies that aim to reduce hot spot formation and the complex interplay among the partial and total oxidation reactions.

9.1. Non-uniform catalyst distribution on the monolithic wall

The active catalytic material is deposited on the monolith walls to result in the desired reaction. The distribution of wash-coat is normally taken to be uniform. However, for catalytic partial oxidation reactions, the partial oxidation reactions happen within the first few millimetres of the catalytic bed and further downstream, the steam reforming, dry reforming and water gas shift reactions take place. Given that the partial oxidation reactions happen within the few first millimetres of the catalyst entrance, a non-uniform distribution of wash-coat can be adopted as this would be a sound economic approach in utilizing the catalyst which is often made of expensive precious metals. The non-uniform distribution can be done as shown in Equation 7.10, and the OpenFOAM solver used allows for the application of this approach and this was done as shown in the sample code in Table 13.

Table 13: A block of code for computing a non-uniform catalytic distribution on the monolithic walls

```
//- Writing mass balances for the adsorbed phase
            for (int i=1; i<=NS; i++)
                    dX[baseCounter+i] =Rsurf[i]/siteDensity;
            //- Adding surface generation term
            double coefficient;
             if (coordinate_ <= 0.001)
                    {
                            coefficient =faceAreas_[edge]*alfaCat_/volume_/rho;
                    }
            else if (coordinate_ > 0.001)
                    {
                            coefficient = faceAreas_[edge]*alfaCat_/volume_/rho*0;
                    }
```

In this case, not all the monolith walls are catalytic, only the axial coordinate less than 0.001 m is deposited with the catalytic material. To account for this phenomenon, a ratio of the effective catalytic area to the total geometric area (α_{cat}) is used in the reaction rate expressions for the adsorbed species. This ratio is calculated as shown in Equation 7.1 and is included in the rate expressions as represented in Equation 7.2.

$$\alpha_{cat} = \frac{A_{cat}}{A} \tag{7.1}$$

$$\rho D_{k,mix}(\nabla x_k) = \frac{A_{cat}}{A} r_k^{het} \tag{7.2}$$

Several researchers have conducted experimental work on monolith reactors and their findings demonstrated that a generally observed trend is the deposition of poisons at the reactor inlet (Becker and Wei, 1977). Based on these findings, a monolith is designed as a two-zone reactor with the upstream monolithic walls not deposited with the catalytic material while the downstream is deposited (Morbidelli et al., 2001). This non-uniform distribution of the catalytic material was in this study applied to allow for optimum catalyst density for economic considerations.

9.1.1. Economic analysis

The economic analysis was performed with respect to payback period, fabrication costs, profit margin and syngas revenue. The analysis is aimed at maximizing these

economic variables with respect to geometric parameters. The revenue generated from syngas is calculated in Equation 7.3,

$$\text{Syngas revenue} = \text{price of syngas} * \text{throughput} \tag{7.3}$$

Where the throughput is calculated in Equation 7.4,

$$throughput = \sum_{i=1}^{n} f_{syngas,i} \tag{7.4}$$

Where n is the total number of channels and $fs_{syngas,i}$ is flowrate of syngas at the reactor outlet of the ith channel. The flowrate is calculated from the hybrid model (from the mass balance equation) and a summation of mass flow rate across all channels is performed to gauge to total flowrate. The channel diameter was varied to investigate its influence on the process economics. In the varying the channel diameter, the shell diameter and the spacing between channels was kept costant. In such an approach, the number of channels decreases with an increase in channel diameter and this is represented by Equation 7.4,

$$n = \frac{D_s + \Delta x}{\Delta x + D_c} \tag{7.4}$$

Where D_s is the shell diameter and D_c is the channel diameter and Δx is the spacing between neigbouring channels.

The cost of feed stock is calculated as shown in Equation 7.5.

$$\text{Cost of feed stock} = \text{cost of O}_2 + \text{cost of natural gas} \tag{7.5}$$

The cost of O_2 and natural gas are estimated from Equations 7.6 and 7.7,

$$\text{Cost of natural gas} = price \sum_{i=1}^{n} f_{naturalgas,i} \tag{7.6}$$

Where n is the number of channels.

$$\text{Cost of O}_2 = price \sum_{i=1}^{n} f_{O_2,i} \tag{7.7}$$

The process payback period can be determined from the syngas revenue and total capital as shown in Equation 7.8.

$$\text{Payback period} = \frac{\text{Total capital}}{\text{Revenue}}$$

(7.8)

In the calculation of total capital, the current study only included the cost of monolith fabrication and cost of raw materials. The costs that include wages, compression costs, maintenance, storage etc. we're not considered. The cost of monolith fabrication was estimated from the cost of a monolith reactor and the total cost of active catalytic material impregnated on the monolithic walls. The cost is as shown in Equation 7.9.

Cost of fabrication = cost of monolith + cost of total active
element deposited on the reactor walls

(7.9)

The total amount of the active catalytic material deposited on the reactor walls is as calculated in Equation 7.10.

Amount deposited on the reactor wall $= \alpha_{cat} MW \, \sigma_{cat} A$

(7.10)

Where α_{cat} is the ratio of the area of the catalytic area to the geometric area, σ_{cat} is the site density and A is the geometric area.

9.2. Economic optimization

The hybrid model which is a faster solver in monolith modelling was employed to determine the process profitability based on the process parameters. Due to the fast nature of the hybrid model, a wide range of reactor configurations can be investigated to determine the optimum configuration that maximizes profitability. Not only the geometry effects can be investigated in relation to their influence on the process profitability but also process parameters such as inlet velocity, pressure and feedstock ratio. The current analysis investigated the process economics based on the cost of feedstock and the fabrication of the monolith reactor and the price of syngas. The other

costs that would be incurred such as labour, maintenance and energy costs were not taken into consideration.

9.2.1. The influence of channel size on the process profitability

The key adjustable parameters in the economic analysis are α_{cat} and β, where α is the geometric parameter and β is operational. The hybrid model facilitates the monolith reactor optimization with the view of maximizing the economic variables (profit margin, return on investment and syngas revenue) with respect to α and β.

The results in Figure 101 reveal that the optimum channel size that maximizes profitablity is 2.5 mm. The monolith shell diameter chosen is 0.1 m and the syngas total throughput is 6.96×10^{-3} m^3/s. The space time was kept constant in all the sizes chosen. However, upong keeping a constant inlet flowrate, thus varying the space time, the results in Figure 102 indicate that the optimum channel diameter that maximizes profitability is 0.8 mm. The difference in the two cases can be described by a higher flow per unit area in some smaller in the case where a constant space time was employed, thus affecting the reaction rate. The highest syngas revenue translates to the highest methane conversion as observed in Figure 103. The highest methane conversion as observed is at 0.8 mm diameter which is also the size at which the highest revenue is generated.

The cost of monolith fabrication for a range of channel sizes is presented in Figure 104. In the case of small diameter channels, the cost is higher due to increased amount of the precious metal used. This increase can be attributed to the high number of channels used in the case of smaller diameter . The choice of a channel size should therefore be dictated by the operating point that maximizes profitability. The productivity of syngas is influenced by the reactor configuration as observed in Figure 101. The highest flowrate of syngas at the reactor outlet is observed at the channel diameter of 0.8 mm and this translates to the highest syngas revenue as observed in Figure 107.
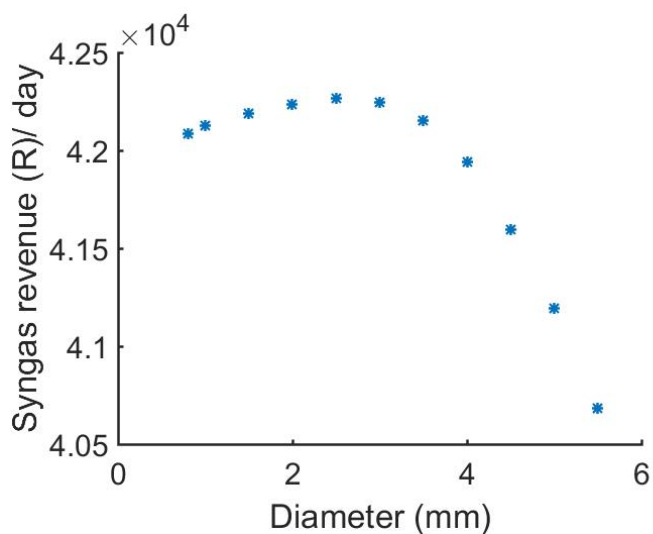
Figure 101: Profitability of the catalytic partial oxidation as a function of channel diameter at constant space time.
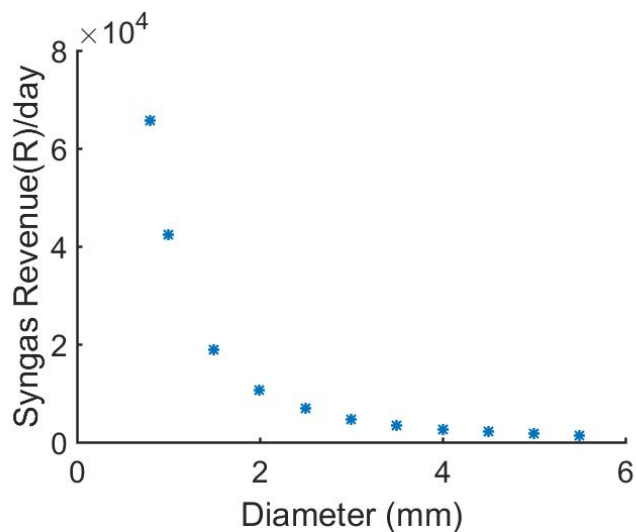
Figure 102: Profitability of the catalytic partial oxidation as a function of channel diameter at varying space time
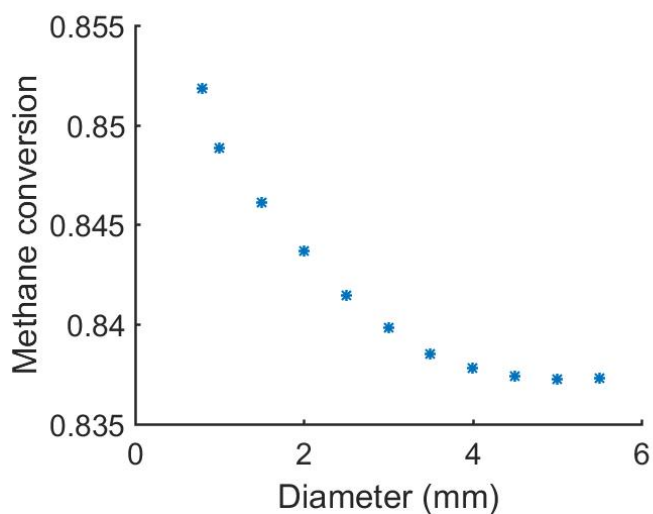
Figure 103: Methane conversion at a range of channel diameters
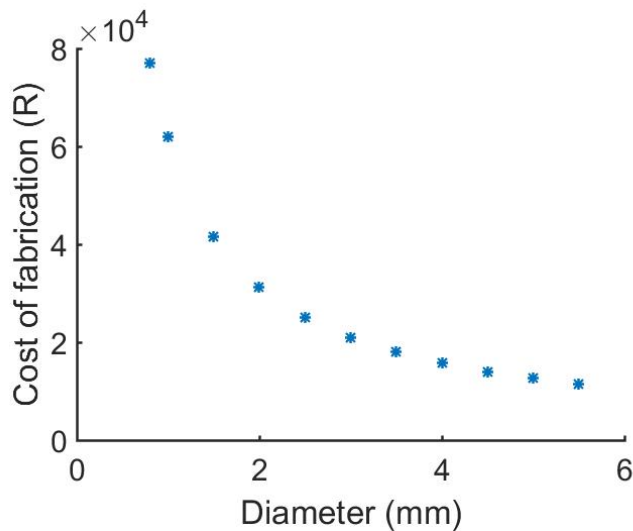
Figure 104: The cost of monolith fabrication at various channel sizes

The reaction rate fields at various channel diameters are presented in Figure 105. As observed, the smaller diameters have higher reaction rates in comparison to bigger diameters and this is attributed to high mass transfer rates in smaller diameters. This also explains the higher syngas revenue in smaller diameter channels as observed in Figure 101. The inlet flow rate and shell diameter were kept constant while changing the channel diameter and this was done to ensure that the higher reaction rates in smaller diameters is not due to higher flow per unit area. From these observations, it is evident that smaller diameter channel result in higher reaction rates and conversion, hence a better performance. Since the inlet flowrate was kept constant, the inlet velocities at each channel size differ and the velocity profile is as observed in Figure 106. With the fixed inlet flowrate, the hydrodynamics in various channel diameters is different and that results in the difference in the observed reactor performance. The syngas throughput from various sizes is presented in Figure 107 and the observations indicate that the smallest (0.8 mm) diameter results in the highest syngas throughput. This is ascribed to the higher number of channels in a smaller diameter case and the higher conversions as observed in Figure 103.
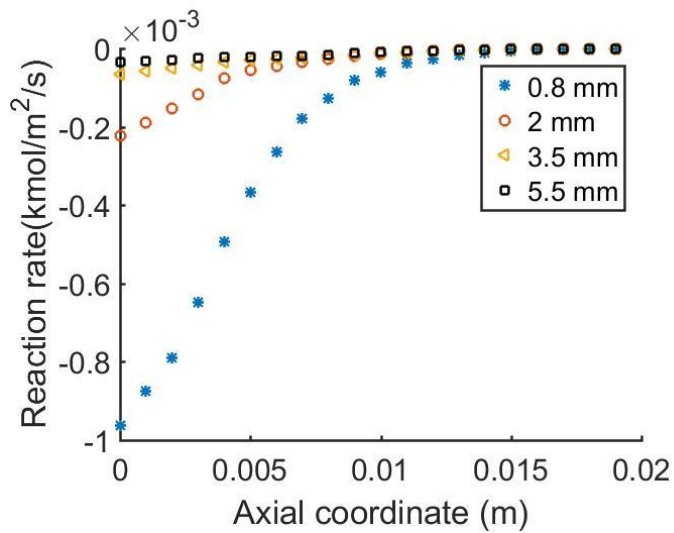
Figure 105: Reaction rate field at various channel diameters
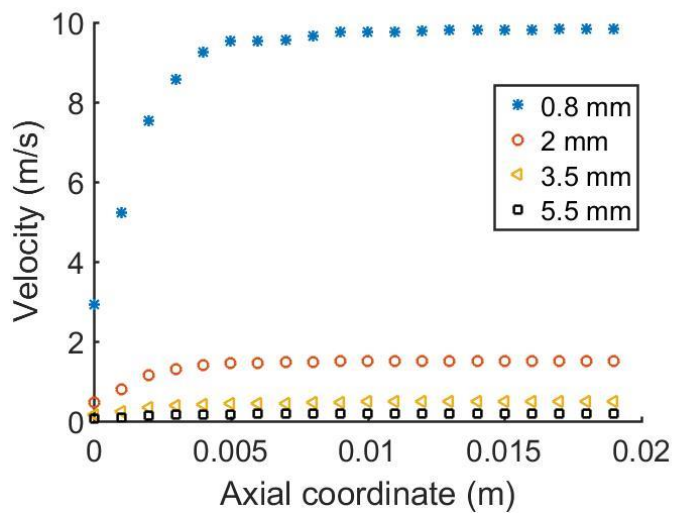
Figure 106: Velocity profile at various channel diameters
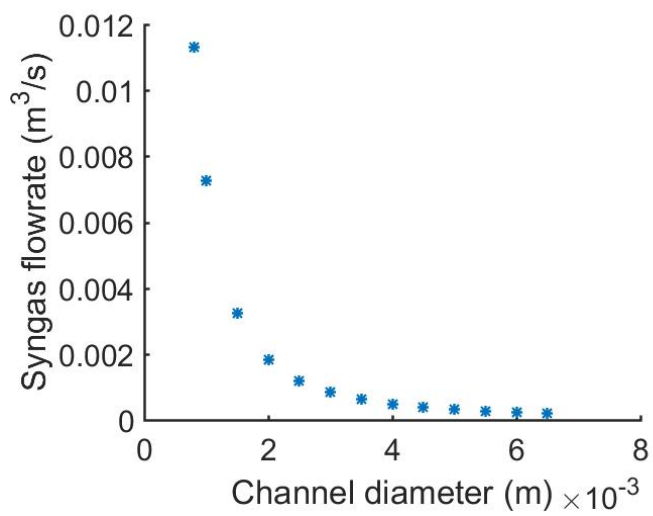
Figure 107: Syngas flowrate at various channel diameters

The influence of channel diameter on profitability at various inlet velocities was investigated and the findings are presented in Figure 108. The results in Figure 108 were obtained from 33 simulations and with a 3D CFD multichannel monolith simulation, this could have resulted in a high computational expense. However, the faster hybrid model performed the simulations at moderate computational expense. As observed, the profitability is maximized at the 2.5 mm diameter and higher inlet velocities. This can be ascribed to the increased CH_4 conversion as revealed in Figure 103. At smaller diameters mass transfer is enhanced as mass transfer coefficient is inversely proportional to the channel diameter and the reaction rate is increased.

The revenue generated from syngas is increased at the maximum conversion of methane and the results in Figure 103 attest to that. A 2D plot that shows the variation of syngas revenue with channel size and inlet velocity is presented in Figure 108. As observed, the revenue is higher at higher velocities and this is due to the increased flowrate. Although smaller diameters would result in higher pressure drop that could increase the pumping costs, in monoliths, pressure drop is minimal, and the use of smaller diameters would still be optimum for the process profitability. The hybrid model can therefore aid the design and optimization of monolith catalysed systems as it allows for an investigation of a wide range of operating conditions and reactor configurations. The process economics can also be undertaken, and feasibility studies done at reasonable timelines.
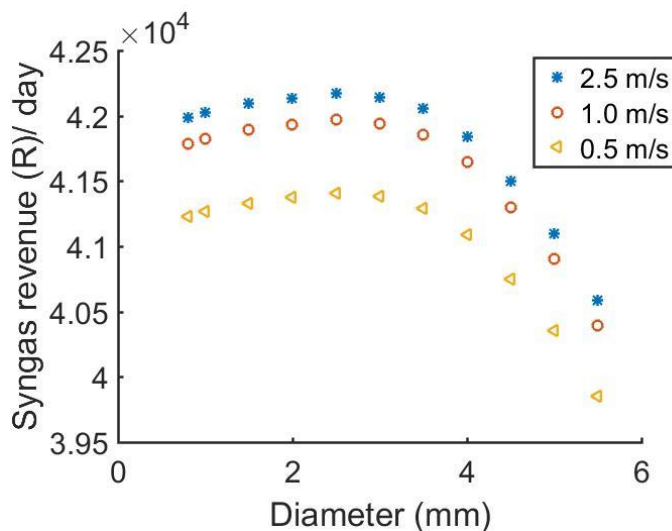
Figure 108: Syngas revenue for various channel sizes at a range of inlet velocities

9.3.Payback period and breakeven analysis

The model can facilitate the fast determination of the payback period and breakeven point for partial oxidation process. The payback period is described as the time taken to recover the fixed capital investment after start-up. Whereas the breakeven point reveals the throughput needed to ensure that revenue exceeds the production cost. The payback period evaluated at different channel diameters is presented in Figure 109. In this case, the shell size was kept constant while changing the channel diameter, and this results in a larger density of the catalyst used in smaller diameter monoliths. The findings reveal that the smaller channels have a longer payback period due to higher capital cost. Although the payback period is longer, this is offset by the higher revenue generated from the use of smaller diameter channels.

The breakeven analysis at various inlet velocities is presented in Figure 110. The findings indicate that the expenditure exceeds revenue significantly at higher flowrates of feedstock. The higher inlet flowrates are therefore the best operating to consider in maximizing the syngas revenue.
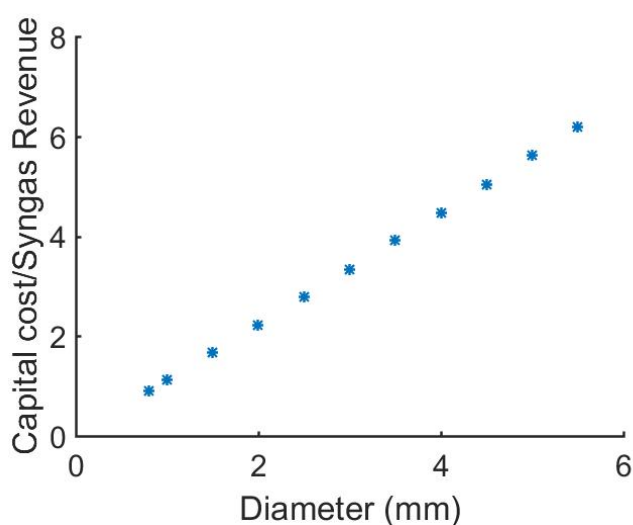
Figure 109: Payback period evaluated at various channel diameters
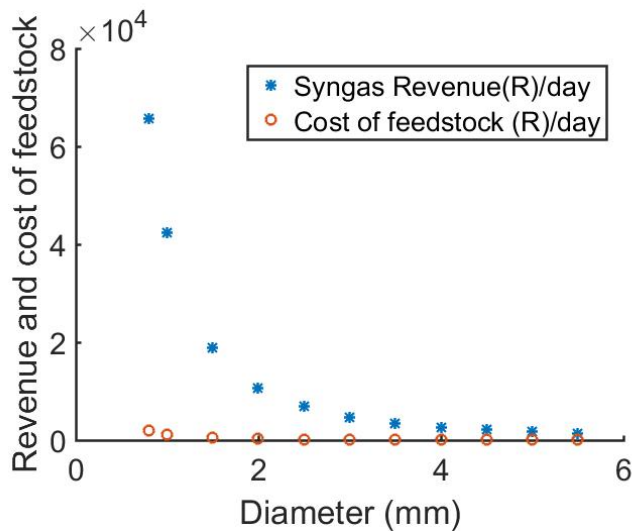
Figure 110: Breakeven point at various channel diameters

9.4. Catalyst distribution on the support

The catalytic material consists of expensive precious metals and for their effective utilization, they are dispersed on large-surface-area supports (Morbidelli et al., 2001). For non-uniform catalyst distribution, the amount of the catalytic material deposited on the support was made to be the same in the first few millimetres of the catalytic wall and was decreased further down the catalytic wall for a non-uniform catalyst distribution. The non-uniform distribution reduces the payback period by an order of magnitude as the amount of active element deposited on the support is reduced.

The hybrid model was validated against the CFD results for different lengths of the catalyst bed. The validation was carried out at 5.0 mm and 10.0 mm catalyst bed length and the results are as observed in Figure 111. The operating conditions are those typical of partial oxidation as presented on Table 6. There is a close agreement between the hybrid model and CFD results, and as a result, the hybrid model was used in geometric optimization of the monolith reactor. The validation of the hybrid model at various catalyst loading was performed in section 5.3.
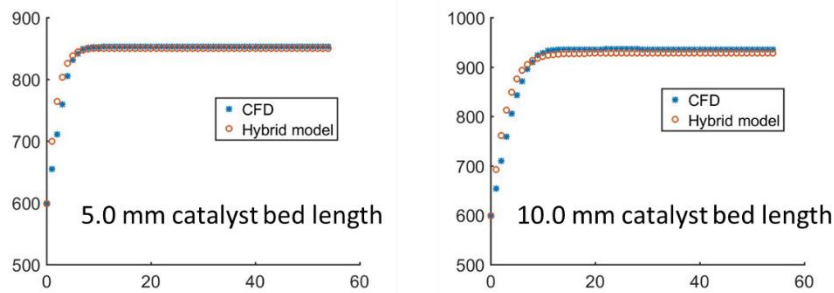
Figure 111: Comparison between temperature profiles for the hybrid model and CFD at 5.0 mm and 10. mm catalyst bed length (100 mm length and 1.0 mm diameter monolith)

The influence of the degree of impregnation on state variables was investigated and the results are as shown in Figure 112 to Figure 114. As observed, methane conversion increases with increasing catalyst loading and the optimum catalyst loading was found to be 1.45 mg/m^3. The catalyst bed temperature was found to increase with the decreasing catalyst loading as shown in Figure 114. Therefore, the determination of the optimum degree of impregnation is desirable as it can help reduce the formation of local hot spot.
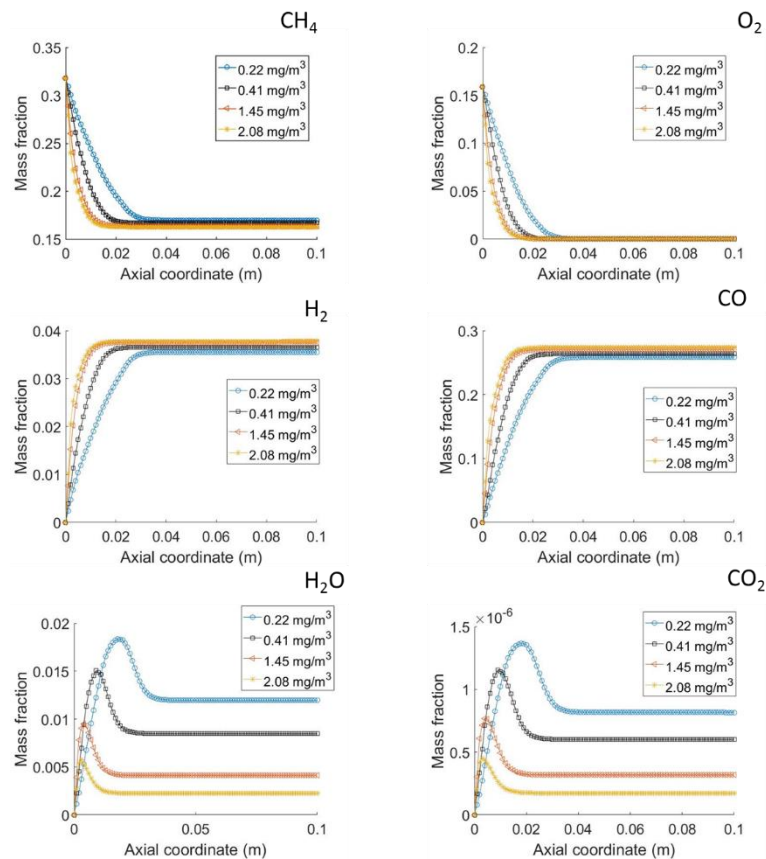
Figure 112: Mass fraction profiles at various catalyst loading (CH_4/O_2=4.0 and the monolith of length 100 mm and 1.0 mm diameter)
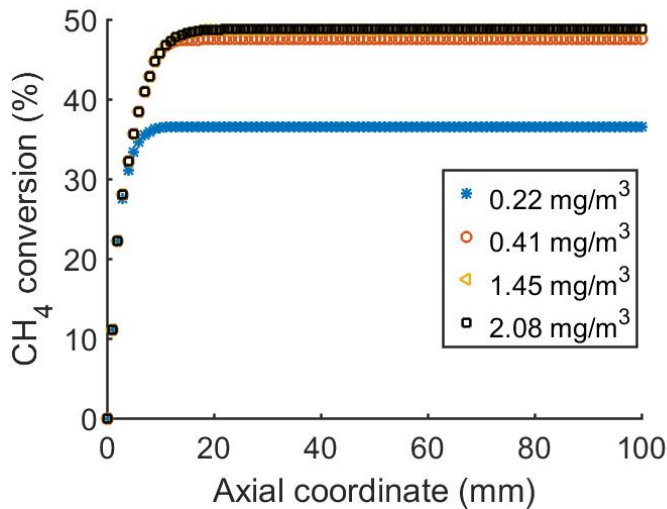
Figure 113: CH$_4$ conversion at various catalyst loading (CH$_4$/O$_2$=4.0 and the monolith of length 100 mm and 1.0 mm diameter)
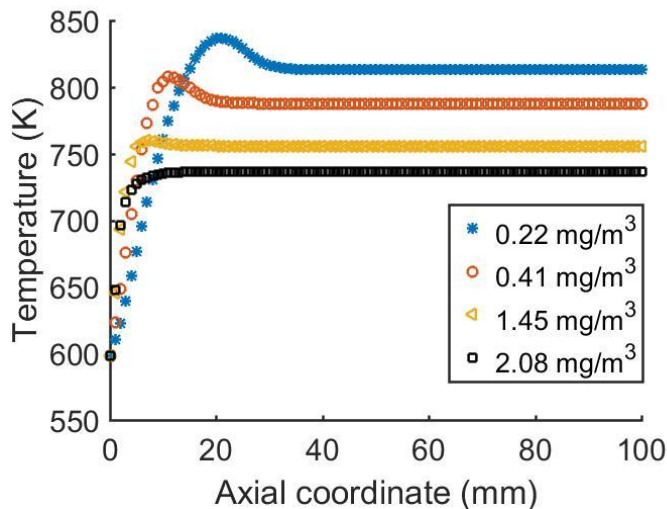
Figure 114: Temperature profiles at various catalyst loading (CH$_4$/O$_2$=4.0 and the monolith of length 100 mm and 1.0 mm diameter)

The results in Figure 115 show the payback period at various channel diameters . The 50 mm catalyst bed length is the optimum value that it results in the shortest payback period as observed in Figure 115. The reduction in the payback period in comparison to a longer catalyst bed length is explained by the differences in the cost of fabrication between the two cases. As observed in Figure 116, the cost of monolith fabrication is less for a shorter length of the catalyst bed. The distribution of the active element was implemented in the hybrid model by the introduction of the term (α_{cat}) shown in Equation 7.11. Where α_{cat} is a dimensionless number that represents the ratio of the catalytic area to the total geometric area. The reaction rate terms in the mass and energy balance equations (Equation 4.14, 415 and 4.16) were multiplied by this

variable. In a case of uniform distribution, the value of α_{cat} is constant along the reactor axial coordinate, while is it varied in the non-uniform distribution. This dimensionless number is used to multiple the reaction rate terms for surface reactions.

The length of the catalyst bed can also help reduce the formation of local hot spot as observed in Figure 119 . The temperature profile for a shorter catalyst bed length is flat in comparison to the longer bed length. The reduction of local hot spot helps to prevent the catalyst deactivation, and this can lead to some savings in production costs. Despite a shorter length of the catalyst bed, methane conversion is shown to be over 80 % at catalyst bed length of 20 mm. In these simulations, the ratio of CH_4 to O_2 in the feedstock is 2.0 and this explains the higher conversion of methane due to sufficient oxygen. A high throughput of syngas can be achieved in this lower percentage impregnation, thus high syngas revenue can be maintained.
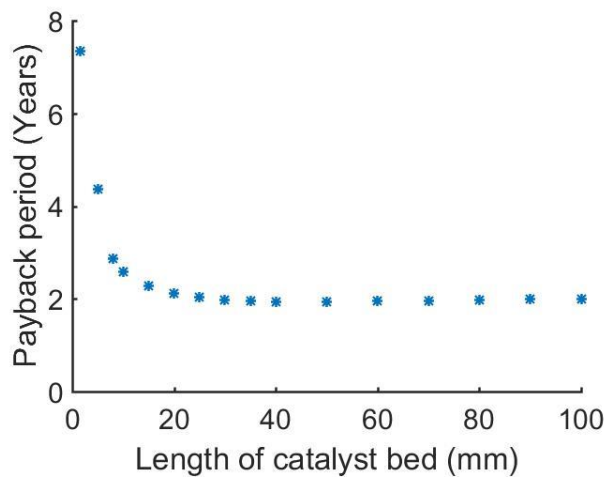
Figure 115: Payback period evaluated at various lengths of the catalyst bed
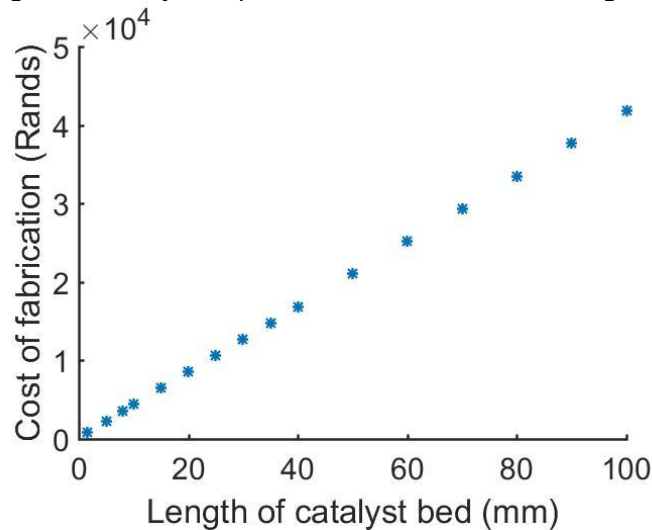
Figure 116: The cost of monolith fabrication at various at various catalyst bed lengths (CH_4/O_2=2.0 and the monolith of length 100 mm and 1.0 mm diameter)

$$\alpha_{cat} = \frac{amount\ of\ active\ element\ deposited\ on\ the\ support}{Mw\ x\ site\ density\ x\ geometric\ area} \qquad (7.11)$$
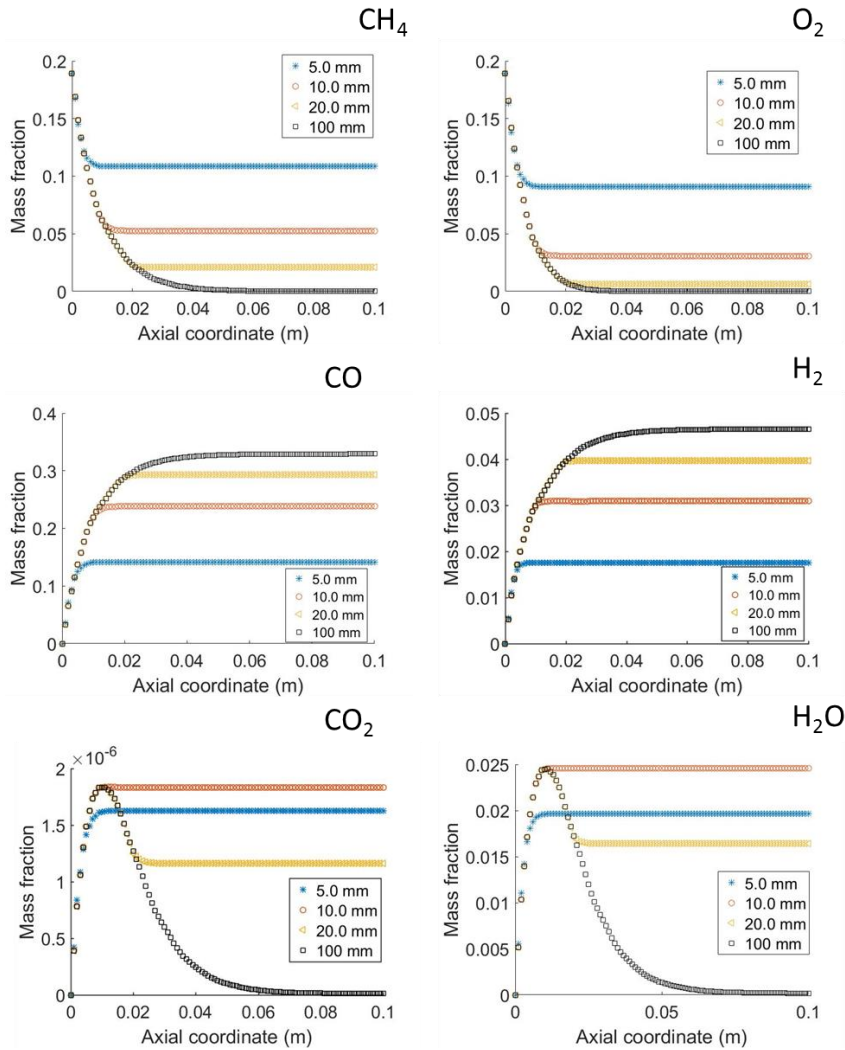
Figure 117: Mass fraction profiles at various catalyst bed lengths (CH_4/O_2=2.0 and the monolith of length 100 mm and 1.0 mm diameter)
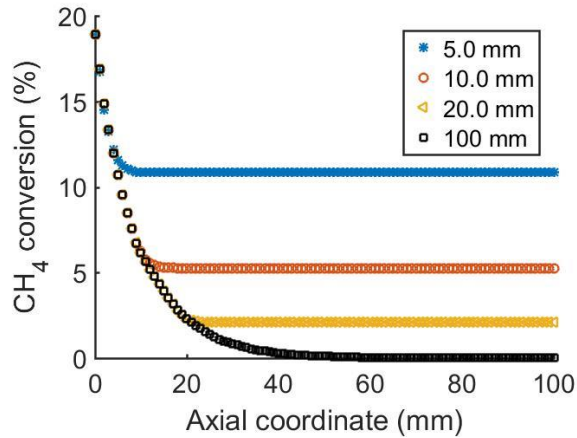
Figure 118: CH_4 conversion profiles at various catalyst bed lengths (CH_4/O_2=2.0 and the monolith of length 100 mm and 1.0 mm diameter)

The temperature profiles in Figure 119 show a decrease in temperature after 15 mm of the reactor entrance, and this can be attributed to the endothermic steam reforming reactions that dominate from this region as the partial oxidation kinetics predict. The H_2O mass fraction profiles are presented in Figure 117 to help elucidate this phenomenon. As observed, at 20 mm and 100 mm catalyst bed length, the mass fraction profiles show H_2O consumed in the reaction (steam reforming) and this endothermic reaction leads to the decrease in temperature as observed in Figure 119. The steam reforming reaction is represented by Equation 7.12. The heat of reaction at various catalyst bed lengths are shown in Figure 120. The findings indicate that at a longer catalyst beed length, further downstream the endothermic reactions dominate as evidenced by the results on the product of the heat of reaction and reaction rate in Figure 121. This higher reaction rate can also be explained by higher temperatures observed in the case of a longer catalyst bed length as observed in Figure 119.

$$CH_4 + H_2O \rightarrow CO + 3H_2 \qquad \Delta_rH = +206 \ KJmol^{-1} \qquad (7.12)$$
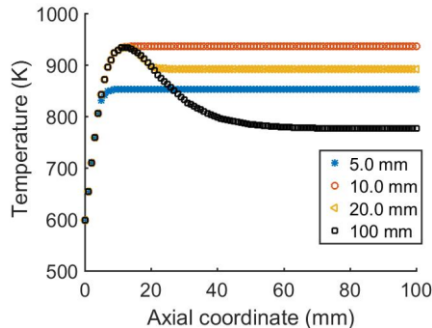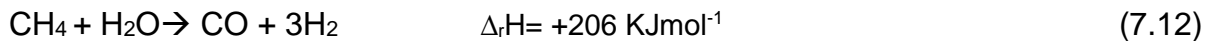
Figure 119: Temperature profiles at various catalyst bed lengths (CH_4/O_2=2.0 and the monolith of length 100 mm and 1.0 mm diameter)
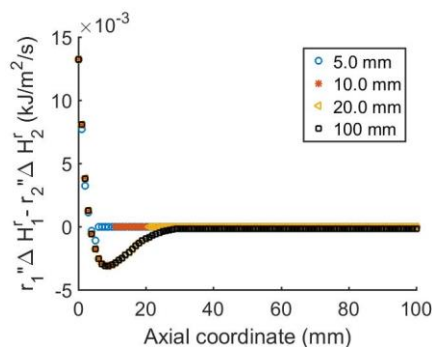
Figure 120: The difference between a product of the reaction rate and heat of reaction($r_1H^r_1$-$r_2H^r_2$) for

143

exothermic and endothermic reactions (CH_4/O_2=2.0 and the monolith of length 100 mm and 1.0 mm diameter)
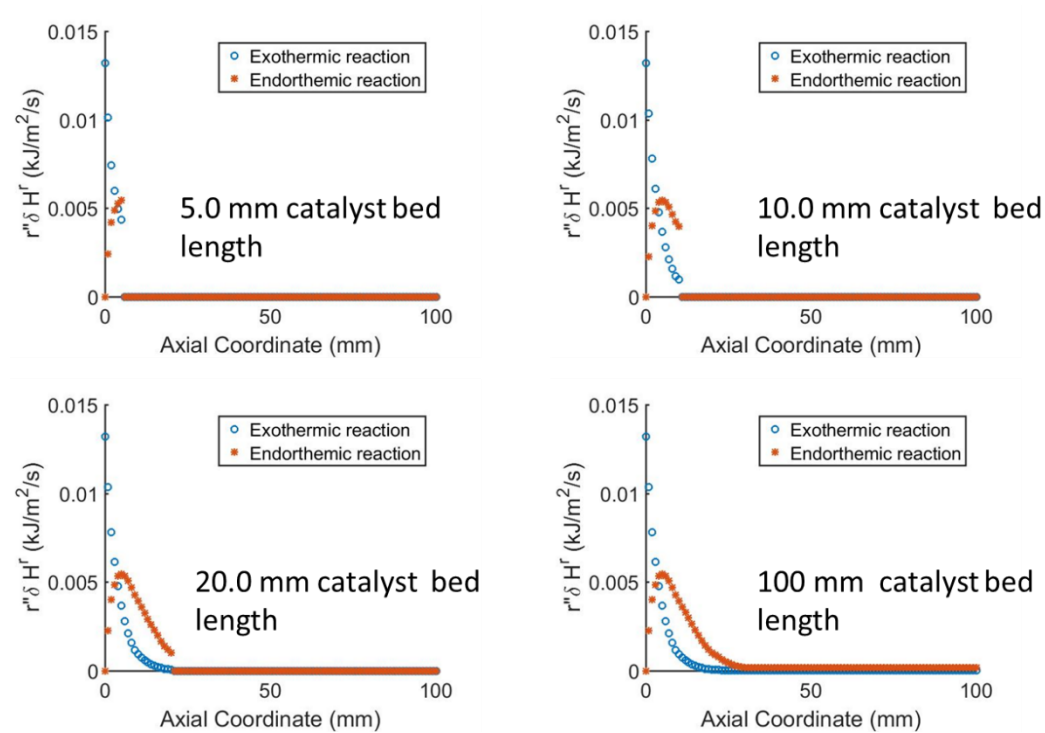
Figure 121: The product of heat of reaction and reaction rate at various catalyst bed length (CH_4/O_2=2.0 and the monolith of length 100 mm and 1.0 mm diameter)

Upon changing the feedstock ratio (CH_4/O_2= 4.0), methane conversion decreases as observed in Figure 122. The highest conversion is 49 % which is found at 20 mm and 100 mm catalyst bed lengths. The lower conversion is attributed to insufficient O_2 in the feedstock. The corresponding mass fraction profiles are presented in Figure 123.
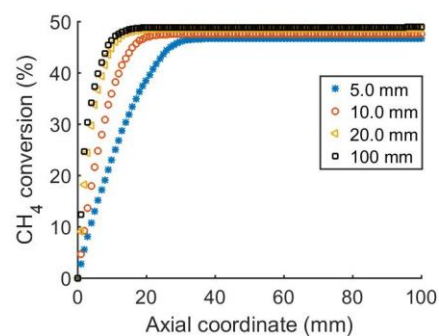
Figure 122: CH_4 conversion profiles at various at various catalyst bed lengths (CH_4/O_2=4.0 and the monolith of length 100 mm and 1.0 mm diameter)
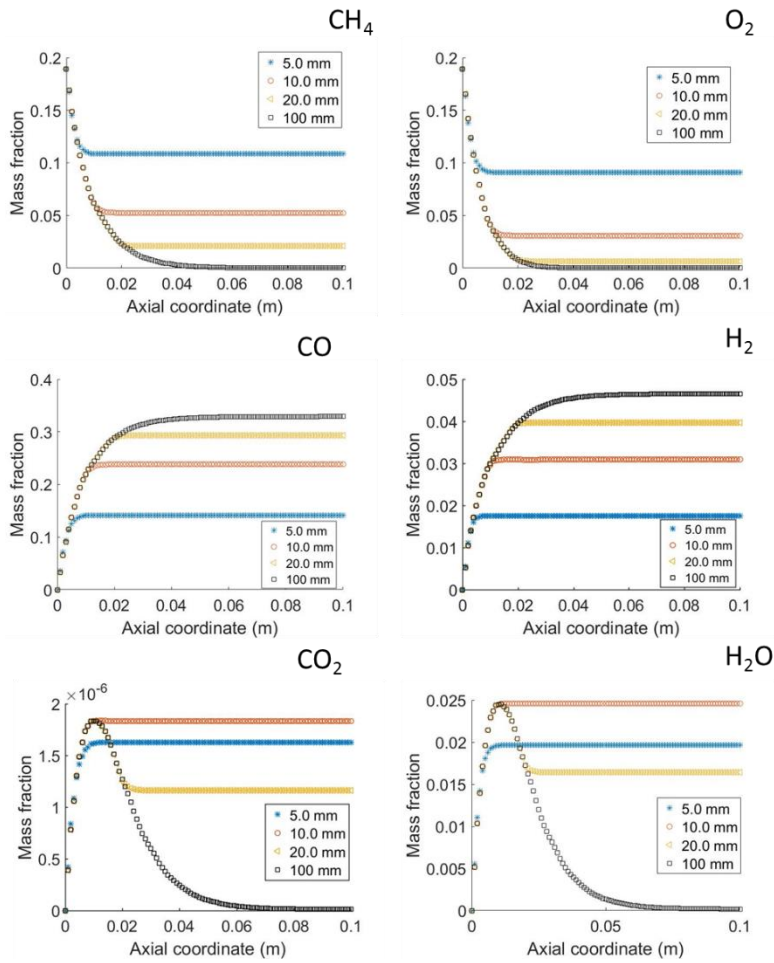
Figure 123: Mass fraction profiles at various catalyst bed lengths (CH_4/O_2=4.0 and the monolith of length 100 mm and 1.0 mm diameter)

The non-uniform distribution of the catalytic material has been shown to present many advantages as mentioned. The profit margin at various catalyst bed lengths is presented in Figure 124. As observed, the highest profit margin is achieved at the catalyst bed length of 50 mm. Therefore, the design of a monolith should allow for the optimum percentage impregnation as this is economically viable and results in the reduction of hot spot formation. It should be noted that the profit margin could be lower than the one presented in Figure 124 if costs such as labour, maintenance and utility are considered.
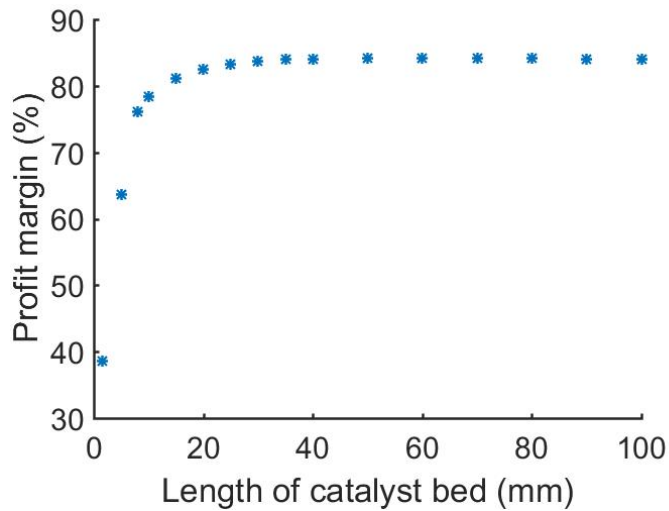
Figure 124: Profit margin at various catalyst bed length

The non-uniform catalyst distribution on the monolith walls has been shown to reduce the hot spot formation and achieve a higher syngas productivity (from 50 % impregnation). The superiority of non-uniform catalysts over uniform catalysts as reported by several authors (Kasaoka and Sakata, 1968; Mars and Gorgels, 1964; Michalko, 1966; Michalko, 1966b) has been demonstrated.

Chapter 10. Conclusions

For the simulation of a single channel monolith, three types of reactor models were investigated namely the dispersed plug flow with and without the effectiveness factor and the 3D CFD. There is a significant discrepancy between the plug flow model and the CFD model due to the simplifications the plug flow model makes with regards to mass and heat transfer. The relative error between the plug flow and CFD temperature profiles is 23.7 %. On the species mole fraction profiles, the relative error between CFD and plug flow model is 34.6 % H_2 and 20.8 % CO. Given this significant discrepancy between the plug flow model and the CFD model, the plug flow model with effectiveness factor which gives accurate results was developed.

Upon using a modified plug flow model to correct the wall mass transfer, there is a close agreement between CFD and the modified plug flow. Both temperature and species mole fraction profiles predicted from the dispersed plug flow model with effectiveness factor gave accurate results with relative error of 0.59% for temperature, 0.76% for CO and 0.52% for H_2 mole fraction. The modified plug flow model captures the important features of the 3D CFD single channel model at moderate computational expense.

The clock time for the modified plug flow is 0.53 seconds in comparison to 1.3 hours for the CFD model. Therefore, the dispersed plug flow model with effectiveness factor is a fast simulator of monolith reactors for a single channel case. For the geometry employed in this study, the effectiveness factor gives the accurate descriptions observed in a single channel CFD model even when conditions are changed. However, upon employing a different geometry there is need for re-parameterisation of the effectiveness factor. Due to its fast nature and speed, the modified plug flow model can be embedded in the multichannel monolith modelling to help reduce the computational costs.

The efficient modelling and simulation of a single channel was illustrated through the application of a modified plug flow model as described. The extension to the multichannel case, however, was not achieved by simple repeated application of this model since the temperature distribution which ultimately affects the reaction rates is

different in multichannel and a single channel scenario. The monolith is described with the stiff and non-linear equations inherent to fundamental momentum mass and heat transfer, and this results in long temporal and spatial scales. Therefore, the simulation of the entire monolith system is then computationally expensive exercise when approached by traditional means.

Due to the high density of channels in a monolith, an equivalent homogeneous cylindrical model (hybrid model) was developed to approximate the behaviour of a bundle of channels acting as axial heat sources. In this approach, the analytical solutions were hybridized with the effectiveness factor approach to develop algebraic models that accurately represent the PDEs that describe monolith reactors. Therefore, the hybrid model solves at sufficiently low computational expense and it is suitable for optimisation applications.

The axial temperature and species concentration profiles at various radial positions from the hybrid model were found to be in a close agreement with CFD simulations. The maximum relative error on temperature was found to be 0.35 %. The clock time on an Intel(R) Core(TM) i5-5300U CPU @ 2.30GHz workstation is 0.53 seconds which is a significant reduction in computational costs. On the other hand, for a CFD multi-channel simulation, an average of 38 hours is needed to obtain a converged solution. The hybrid model allows for hundreds of simulations to be performed within a short space of time, thus some optimization studies such as economic optimization of catalytic partial oxidation can be carried out. The model can help to determine the operating conditions that minimize the formation of local hot spot and increase the yield of syngas that is often affected by the complex interplay between total and partial oxidation.

The sensitivity analysis indicate that the channel size has a significant influence on local temperature distribution in a monolith reactor. It was concluded that smaller channel diameters result in higher local temperatures which could lead to formation of local hot spot, hence deactivation of the catalyst. The feedstock stoichiometry (CH_4 and O_2) dictates the ratio of H_2 to CO in the reactor outlet. Therefore, depending on the syngas downstream application, a different stoichiometry at the reactor inlet can be used. In addition, the feedstock ratio influences the species surface coverage. The sensitivity study on the influence of feedstock ratio on surface coverage revealed that

rich mixtures result in the deposition of carbon in the catalyst active sites. This is attributed to rich mixtures not having enough oxygen to react with the adsorbed carbon, hence the increased carbon surface coverage.

The hybrid-model was developed to facilitate geometric optimization with the view of reducing hot spot formation, alleviating pressure drop and manufacturing costs. This is because monolith reactors applied in catalytic partial oxidation of methane are coated with precious metal catalysts, significantly contributing to capital costs. By isolating regions of high catalytic activity, it was possible to reduce the amount of precious metal coating required to achieve high conversion.

Due to the low computational expense of the hybrid model, it was possible to investigate a wide range of design geometry and operating condition . It was shown that, for methane oxidation over a Platinum gauze catalyst, the channel diameter could be optimised to the 0.8 mm level resulting in the highest syngas revenue (R 65754.14 /day). The distribution of the catalytic material on the monolithic walls was found to influence the reactor performance hence the process profitability. The method that optimizes design and operation of catalytic monolith reactors through the application of fast-solving hybrid models was developed and validated. The hybrid model can be used in other geometries other than the cylindrical monoliths. The key adjustable parameters are α_{cat} and β.

10.1.   Recommendations

The modified plug flow model predicts surface coverage, temperature and concentration of species in a single channel monolith. On the other hand, the hybrid model predicts the described state variables in a multichannel model at moderate computational expense. The modified plug flow model was embedded into a hybrid model to achieve a reduced computational time. Given the fast nature of the hybrid model, it can be employed in the full-scale process design and economic analysis of the methane partial oxidation. In addition, the economic performance of employing different catalytic materials can be gauged by using the hybrid model. Although the model was employed in partial oxidation of methane to syngas, its application can be extended to total oxidation of methane in pollution control and to other heterogeneous processes. Since the method works well in simulating the complex behaviour in monolith reactors, it is recommended that this approach of hybridisation be adopted

for simulations involving complex geometries. In addition, the model can be used in the modelling of highly exothermic reactions such as selective oxidations. The monolith can be modelled more efficiently by considering only the first few millimetres (less than 20 mm) where the reactions take place.

Chapter 11. References

Abbasi, R., Wu, L., Wanke, S.E., Hayes, R.E., 2012. Kinetics of methane combustion over Pt and Pt-Pd catalysts. Chem. Eng. Res. Des. 90, 1930–1942.

Amin, N.A.., Yaw, T.., 2007. Thermodynamic equilibrium analysis of combined carbon dioxide reforming with partial oxidation of methane to syngas. Int. J. Hydrogen Energy 32, 1789–1798.

Anderson, J.R., Boudart, M., 1983. Catalysis-Science and Technology, 1st ed. New York.

Arutyunov, V.S., Krylov, O. V, 2007. Oxidative conversion of methane. Russ. Chem. Rev. 74, 1111–1137.

Aschroft, A.T., Cheetham, A.K., Green, M.L.., Vernon, P.D.., 1991. Partial oxidation of methane to synthesis gas using carbon dioxide. Lett. to Nat. 352, 225–226.

Balachandran, U., Dusek, J.., Mieville, R.., Poeppel, R.., Kleefisch, M.., Pei, S., Kobylinski, T.., Udovich, C.., Bose, A.., 1995. Dense ceramic membranes for partial oxidation of methane to syngas. Appl. Catal. A Gen. 133, 19–29.

Becker, E.R., Wei, J., 1977. Nonuniform Distribution of Catalysts on Supports. J. Catal. 381, 372–381.

Bhavsar, S., Najera, M., More, A., Veser, G., 2014. Chemical-looping processes for fuel-flexible combustion and fuel production. In: Reactor and Process Design in Sustainable Energy Technology. Reactor and Process Design in Sustainable Energy Technology, Pittsburgh, pp. 233–273.

Bizzi, M., Basini, L., Saracco, G., Specchia, V., 2002. Short contact time catalytic partial oxidation of methane: Analysis of transport phenomena effects. Chem. Eng. J. 90, 97–106.

Bizzi, M., Saracco, G., Schwiedernoch, R., Deutschmann, O., 2004. Modeling the partial oxidation of methane in a fixed bed with detailed chemistry. AIChE J. 50, 1289–1299.

Blanks, R.., Wittrig, T.., Peterson, D.., 1990. Bidirectional Adiabatic Synthesis Gas Generator. Chem. Eng. Res. Des. 45, 2407–2413.

Campbell, C., Ertl, G., Kuipers, H., Segner, J., 1980. A molecular beam study of the catalytic oxidation of CO on a Pt (111) surface. J. Chem. 73, 5862.

Campbell, C., Ertl, G., Kuipers, H., Segner, J., 1981. A molecular beam investigation

of the interactions of CO with a Pt (111) surface. Surf. Sci. 107, 207–219.

Campbell, I., Foulds, G.A., Lapszewicz, J.A., 1994. Process Optimisation of the Catalytic Partial Oxidation of Methane to Synthesis Gas. Stud. Surf. Sci. Catal. 81, 329–331.

Campbell, K.D., Zhang, H., Lunsford, J.H., 1988. Methane Activation by the Lanthanide Oxides. J. Phys. Chem. 92, 750–753.

Carolan, M.., Dyer, P.., Minford, E., Barton, T.., Peterson.D.R, Sammells, A.., Butt, D.., Cutler, R.., Taylor, D.., 2001. Development of the High Pressure ITM Syngas Process. In: Studies in Surface Science and Catalysis. Elsevier B.V., pp. 39–44.

Chang, Y.F., Heinemann, H., 1993. Partial oxidation of methane to syngas over Co / MgO catalysts . Is it low temperature ? Catal. Ind. 21, 215–224.

Chaniotis, A.K., Poulikakos, D., 2005. Modeling and optimization of catalytic partial oxidation methane reforming for fuel cells. J. Power Sources 142, 184–193.

Chen, D.K.., Bissett, E.J., Ostrom, D.L.., 1988. A Three-Dimensional Model for the Analysis of Transient Thermal and Conversion Characteristics of Monolithic Catalytic Converters. SAE Trans. 97, 177–189.

Chen, J., Gao, X., Yan, L., Xu, D., 2018. Computational fluid dynamics modeling of the millisecond methane steam reforming in microchannel reactors for hydrogen production. R. Soc. Chem. 8, 25183–25200.

Chen, W., Chiu, T., Hung, C., 2010. Enhancement effect of heat recovery on hydrogen production from catalytic partial oxidation of methane. Int. J. Hydrogen Energy 35, 7427–7440.

Chevalier, C., Pitz, J.., Warnatz, J., Westbrook, C.., Melenk, H., 1992. Hydrocarbon Ignition: Automatic Generation of Reaction Mechanisms and Applications to Modelling of Engen Knock. Combust. Inst. 24, 93–101.

Chisti, Y., 2007. Biodiesel from microalgae. Biotechnol. Adv. 25, 294–306.

Choudhary, V.R., Rajput, A.M., Rane, V.H., 1992. Low temperature oxidative conversion of methane to synthesis gas over Co/rare earth oxide catalysts. Catal. Ind. 16, 269–272.

Cimino, S., Di, A., Pirone, R., Russo, G., 2001. Transient behaviour of perovskite-based monolithic reactors in the catalytic combustion of methane. Catal. Today 69, 95–103.

Cimino, S., Lisi, L., Mancino, G., Musiani, M., Vázquez-Gómez, L., Verlato, E., 2012.

Catalytic partial oxidation of CH4-H2 mixtures over Ni foams modified with Rh and Pt. Int. J. Hydrogen Energy 37, 17040–17051.

Corbo, P., Migliardini, F., 2007. Hydrogen production by catalytic partial oxidation of methane and propane on Ni and Pt catalysts. Int. J. Hydrogen Energy 32, 55–66.

Cui, X., Kær, S.K., 2018. Two-dimensional thermal analysis of radial heat transfer of monoliths in small-scale steam methane reforming. Int. J. Hydrogen Energy 43, 11952–11968.

Cybulski, A., Moulijn, J.., 1994. Modeling of Heat Transfer in Metallic Monoliths Consisting of Sinusoidal Cells. Chem. Eng. Sci. 49, 19–27.

Cybulski, A., Moulijn, J.., 2005. Structured Catalysts and Reactors, 2nd ed. CRC Press, Taylor and Francis Group, London.

Davis, M.E., Davis, R.J., 1993. Microkinetic Analysis of Catalytic Reactions, Fundamentals of Chemical Reaction Engineering. McGraw-Hill Higher Education, New York.

De Groote, A.., Froment, G.F., 1996. Simulation of the catalytic partial oxidation of methane to synthesis gas. Appl. Catal. A Gen. 138, 245–264.

de Smet, C.R.., de Croon, M.H.J.., Berger, R, J., Marin, G, B., Schouten, J, C., 2000. Kinetics for the partial oxidation of methane on a Pt gauze at low conversions. AIChE J. 46, 1837–1849.

Deshmukh, S.R., Vlachos, D.G., 2007. A reduced mechanism for methane and one-step rate expressions for fuel-lean catalytic combustion of small alkanes on noble metals. Combust. Flame 149, 366–383.

Deutschmann, O., Schmidt, L.., 1999. Detailed modelling of short-contact-time. In: Chemical Thermodynamics, Kinetics, Catalysis, Chemical Reaction Engineering, Method for Scalling up and Down. Second European Congress of Chemical Engineering, Montpellier, pp. 1–8.

Deutschmann, O., Schmidt, L.D., 1998a. Modeling the partial oxidation of methane in a short-contact-time reactor. AIChE J. 44, 2465–2477.

Deutschmann, O., Schmidt, L.D., 1998b. Two-dimensional modeling of partial oxidation of methane on rhodium in a short contact time reactor. Symp. Combust. 27, 2283–2291.

Deutschmann, O., Schwiedemoch, R., Maier, L.I., Chatterjee, D., 2001. Natural Gas Conversion in Monolithic Catalysts: Interaction of Chemical Reactions and

Transport Phenomena. Stud. Surf. Sci. Catal. 136, 251–258.

Dissanayake, D., Rosynek, M., Kharas, K.C.., Lunsford, J.., 1991. Partial Oxidation of Methane to Carbon Monoxide and Hydrogen over a Ni/Al203 Catalyst. J. Catal. 127, 117–127.

Donazzi, A., Beretta, A., Groppi, G., Forzatti, P., 2008. Catalytic partial oxidation of methane over a 4% Rh/α-Al2O3 catalyst. Part I: Kinetic study in annular reactor. J. Catal. 255, 241–258.

Dudukovic, M.., Felder, R.., 1983. Mixing Effects in Chemical Reactors - III- Dispersion Model. AIChE 4, 39–49.

Elazhary, A., Soliman, H.M., 2009. Analytical solutions of fluid flow and heat transfer in parallel-plate micro-channels at high zeta-potentials. Int. J. Heat Mass Transf. 52, 4449–4458.

Elg, A.P., Eisert, F., Rosén, A., 1997. The temperature dependence of the initial sticking probability of oxygen on Pt(111) probed with second harmonic generation. Surf. Sci. 382, 57–66.

Elnashaie, S.S.E.., Elshishini, S.., 1993. Modelling,Simulation and Optimization of Industrial fixed bed catalytic reactors, 7th ed. Gordon and Breach Science Publishers S.A, Amsterdam.

Fan, M., Abdullah, A.., Bhatia, S., 2010. Utilization of greenhouse gases through carbon dioxide reforming of methane over Ni–Co/MgO–ZrO2: Preparation, characterization and activity studies. Appl. Catal. B Environ. 100, 365–377.

Feio, L.S.F., Hori, C.E., Mattos, L. V, Zanchet, D., Noronha, F.B., Bueno, J.M.C., 2008. General Partial oxidation and autothermal reforming of methane on Pd /CeO2 – Al2O3 catalysts. Appl. Catal. A Gen. 348, 183–192.

Fernandes, F.A.., Souza, C.., Sousa, J.., 2006. Modeling of partial oxidation of methane in a membrane reactor. Therm. Eng. 5, 40–45.

Ferraris, G.B., Manca, D., 1998. BzzOde: a new C++ class for the solution of stiff and non-stiff ordinary differential equation systems. Comput. Chem. Eng. 22, 1595–1621.

Flytzani-Stephanopoulos, M., Voecks, G.., Charng, T., 1986. Modelling of heat transfer in non-adiabatic monolith reactors and experimental comparisons of metal monoliths with packed beds. Chem. Eng. Sci. 41, 1203–1212.

Fogler, H.S., 2006. Elements of Reaction Engineering, 4th ed, Pearson Education. Massachusetts.

Gannouni, A., Albela, B., Zina, M.S., Bonneviot, L., 2013. Metal dispersion, accessibility and catalytic activity in methane oxidation of mesoporous templated aluminosilica supported palladium. Appl. Catal. A Gen. 464–465, 116–127.

Glarborg, P., Kee, R.J., Grcar, J.F., Miller, J.A., 1986. PSE : a Fortran program for modeling well-stirred reactors. Albuquerque.

Goldin, G.., Ren, Z., Zahirovic, S., 2009. A cell agglomeration algorithm for accelerating detailed chemistry in CFD. Combust. Theory Model. 13, 721–739.

GXLJ, 2014. 200 Mesh Industrial Honeycomb Ceramic Substrate Ceramic Honeycomb Monolith Catalyst [WWW Document]. Guangxi Huihuang Langjie Environ. Tech Co., Ltd. URL https://huihuangcatalytic.en.made-in-china.com/ (accessed 4.18.19).

Hagen, J., 2006. Industrial Catalysis, 2nd ed. Wiley-VCH, Weinheim.

Han, R.J., Moss, O.R., Wong, B.A., 1996. Derivation and application of an analytical solution of the mass transfer equation to the case of forced convective flow around a cylindrical and a spherical particle with fluid surface properties. J. Aerosol Sci. 27, 235–247.

Hawk, C.O., Golden, P.L., Storch, H.H., Fieldner, A.C., 1932. Conversion of Methane to Carbon Monoxide and Hydrogen. Ind. Eng. Chem. 24, 23–27.

Hayes, R.E., Mukadi, L.S., Votsmeier, M., Gieshoff, J., 2004. Three-Way Catalytic Converter Modelling with Detailed Kinetics and Washcoat Diffusion. Top. Catal. 30/31, 411–415.

Hickman, D.A., Schmidt, L.D., 1992. Synthesis Gas Formation by Direct Oxidation of Methane over Pt Monoliths. J. Catal. 138, 267–282.

Hickman, D.A., Schmidt, L.D., 1993. Steps in CH4 oxidation on Pt and Rh surfaces: High-temperature reactor simulations. AIChE J. 39, 1164–1177.

Hoang, D.L., Chan, S.H., Ding, O.L., 2005. Kinetic Modelling of Partial Oxidation of Methane in an Oxygen Permeable Membrane Reactor. Chem. Eng. Res. Des. 83, 177–186.

Hohn, K.L., Schmidt, L.D., 2001. Partial oxidation of methane to syngas at high space velocities over Rh-coated spheres. Appl. Catal. A Gen. 211, 53–68.

Horn, R., Williams, K.A., Degenstein, N.J., Nogare, D.D., Tupy, S.A., Schmidt, L.D., 2007. Methane catalytic partial oxidation on autothermal Rh and Pt foam catalysts : Oxidation and reforming zones , transport effects , and approach to thermodynamic equilibrium. J. Catal. 249, 380–393.

Huang, H., Zhou, X., Liu, H., 2016. A CFD model for partial oxidation of methane over self-sustained electrochemical promotion catalyst. Int. J. Hydrogen Energy 41, 208–218.

Hwang, S., Smith, R., 2008. Heterogeneous Catalytic Reactor Design with Non-Uniform Catalyst Considering Shell-Progressive Poisoning Behavior. Chem.Eng.Technol 31, 384–397.

Inbamrung, P., Sornchamni, T., Prapainainar, C., Tungkamani, S., Narataruksa, P., Jovanovic, G.N., 2018. Modeling of a square channel monolith reactor for methane steam reforming. Energy 152, 383–400.

IndiaMART, 2009. Ceramic Honeycomb, Usage: Industrial Use [WWW Document]. URL https://www.indiamart.com/proddetail/ceramic-honeycomb-4159790573.html (accessed 8.2.18).

Irani, M., Alizadehdakhel, A., Pour, A.N., Hoseini, N., Adinehnia, M., 2011. CFD modeling of hydrogen production using steam reforming of methane in monolith reactors: Surface or volume-base reaction model? Int. J. Hydrogen Energy 36, 15602–15610.

Iwaniszyn, M., Piątek, M., Gancarczyk, A., Jodłowski, P.J., Łojewska, J., Kołodziej, A., 2017. Flow resistance and heat transfer in short channels of metallic monoliths: Experiments versus CFD. Int. J. Heat Mass Transf. 109, 778–785.

Jahn, R., Kubiček, M., Marek, M., Snita, D., 1997. 3-D modeling of monolith reactors. Catal. Today 38, 39–46.

James, A., Brindley, J., Mcintosh, A.., 2003. Multi-channel monolith reactors as dynamical systems. Combust. Flame 134, 193–205.

James, A., Brindley, J., Mcintosh, A.C., 2002. Stability of Multiple Steady States of Catalytic Combustion. Combust. Flame 130, 137–146.

Kapteijn, F., Nijhuis, T.A., Heiszwolf, J.J., Moulijn, J.A., 2001. New non-traditional multiphase catalytic reactors based on monolithic structures. Catal. Today 66 66, 133–144.

Karim, H., Pfefferle, L.., Smooke, M.., Markatou, P., Xu, Y., 1996. Combustion Science and Technology Computational Comparison Between an Elliptic and a Boundary Layer Formulation for Methane / Air Combustion Above a Heated Non-Catalytic Surface. Combust. Sci. Technol. 119, 107–130.

Kasaoka, S., Sakata, Y., 1968. Effectiveness factors for non-uniform catalyst pellets. J. Chem. Eng. Japan 1, 138–142.

Kee, R.J., Coltrin, M.E., Glarborg, P., Zhu, H., 2003. Chemically Reacting Flow: Theory, Modeling, and Simulation, 2nd ed. John Wiley & Sons, Inc, Hoboken.

Kee, R.J., Rupley, F.M., Miller, J.A., Coltrin, M.E., Grcar, J.F., Meeks, E., Moffat, H.K., Lutz, A.E., 2000. A software package for the evaluation of gas-phase, multicomponent transport properties. San Diego.

Khan, L.A., Liu, P.L., 1995. An operator splitting algorithm for coupled one-dimensional equations. Comput. Methods Appl. Mech. Eng. 127, 181–201.

Khan, M.M., Somorjai, G.A., 1985. A Kinetic Study of Partial Oxidation of Methane with Nitrous on a Molybdena-Silica Catalyst. J. Catal. 271, 263–271.

Kobayashi, Y., Horiguchi, J., Kobayashi, S., Yamazaki, Y., Omata, K., 2011. Effect of NiO content in mesoporous NiO – Al2O3 catalysts for high pressure partial oxidation of methane to syngas. Appl. Catal. A, Gen. 395, 129–137.

Kolaczkowski, S.T., Chao, R., Awdry, S., Smith, A., 2007. Application of a CFD Code (FLUENT) to Formulate Models of Catalytic Gas Phase Reactions in Porous Catalyst Pellets. Chem. Eng. Res. Des. 85, 1539–1552.

Korup, O., Goldsmith, C.F., Weinberg, G., Geske, M., Kandemir, T., Schlögl, R., Horn, R., 2013. Catalytic partial oxidation of methane on platinum investigated by spatial reactor profiles, spatially resolved spectroscopy, and microkinetic modeling. J. Catal. 297, 1–16.

Kostenko, S.S., Ivanova, A.N., Karnaukh, A.A., Polianczyk, E. V., 2014. Simulation of the methane conversion by partial oxidation in a porous medium reactor. Chem. Eng. J. 238, 100–110.

Kunz, L., Maier, L., Tischer, S., Deutschmann, O., 2011. Modeling the Rate of Heterogeneous Reactions. In: Modeling and Simulation of Heterogeneous Catalytic Reactions. Wiley-VCH, Weinheim, pp. 113–148.

Lapidus, L., Amtjndson, R., 1952. Mathematics of Adsorption in Beds. VI. The Effect of Longitudinal Diffusion in Ion Exchange and Chromatographic Columns. J. Phys. Chem. 56, 984–988.

Liu, H., Zhao, J., Li, C., Ji, S., 2005. Conceptual design and CFD simulation of a novel metal-based monolith reactor with enhanced mass transfer. Catal. Today 105, 401–406.

Liu, S.L., 1969. Difference Approximations to Parabolic Partial Differential Equations. AIChE J. 15, 334–338.

Liu, W., 2007. Multi-scale catalyst design. Chem. Eng. Sci. 62, 3502–3512.

Lotti, L., Sliepcevich, C.M., 1967. Partial oxidation of methane at high pressures. I&EC Process Des. Dev. 6, 67–74.

Luche, J., Aubry, O., Khacef, A., Cormier, J.-M., 2009. Syngas production from methane oxidation using a non-thermal plasma: Experiments and kinetic modeling. Chem. Eng. J. 149, 35–41.

Lyubovsky, M., Roychoudhury, S., LaPierre, R., 2005. Catalytic partial "oxidation of methane to syngas" at elevated pressures. Catal. Letters 99, 113–117.

Maestri, M., Cuoci, A., 2013. Coupling CFD with detailed microkinetic modeling in heterogeneous catalysis. Chem. Eng. Sci. 96, 106–117.

Maestri, M., Vlachos, D.., Beretta, A., Forzatti, P., Groppi, G., Tronconi, E., 2009. Dominant Reaction Pathways in the Catalytic Partial Oxidation of CH4 on Rh. Top Catal 52, 1983–1988.

Maffei, T., Rebughini, S., Gentile, G., Lipp, S., Cuoci, A., Maestri, M., 2014. CFD analysis of the channel shape effect in monolith catalysts for the CH4 partial oxidation on Rh. Chemie-Ingenieur-Technik 86, 1099–1106.

Maghrebi, R., Yaghobi, N., Seyednejadian, S., Tabatabaei, M.H., 2013. CFD modeling of catalyst pellet for oxidative coupling of methane : Heat transfer and reaction. Particuology 11, 506–513.

Maric, T., Hopken, J., Mooney, K., 2014. The OpenFOAM Technology Primer, 1st ed. sourceflux, Darmstadt.

Mars, P., Gorgels, M., 1964. Hydrogenation of acetylene – a theory of selectivity. In: Chemical Reaction Engineering: Proceedings of the Third European Symposium, Supplement to Chem. Eng. Sci. Pergamon Press, Oxford, pp. 55–65.

Mazanec, T.J., Prasad, R., Odegard, R., Steyn, C., Robinson, E.T., 2001. Oxygen Transport Membranes for Syngas Production. In: Studies in Surface Science and Catalysis. Elsevier B.V., pp. 147–152.

McCabe, R.W., Schmidt, L.D., 1977. binding states of CO and H2 on clean and oxidized (111)Pt. Surf. Sci. 65, 189–209.

Meng, F., Chen, G., Wang, Y., Liu, Y., 2010. Metallic Ni monolith – Ni / MgAl 2 O 4 dual bed catalysts for the autothermal partial oxidation of methane to synthesis gas. Int. J. Hydrogen Energy 35, 8182–8190.

Mhadeshwar, A.B., Vlachos, D.G., 2007. A Catalytic Reaction Mechanism for Methane Partial Oxidation at Short Contact Times, Reforming, and Combustion,

and for Oxygenate Decomposition and Oxidation on Platinum. Ind. Eng. Chem. Res. 46, 5310–5324.

Michalko, E., 1966a. Method for oxidizing gaseous combustible waste products. U.S. Patent 3,259,454.

Michalko, E., 1966b. Preparation of catalyst for the treatment of combustible waste products. U.S. Patent 3,259,589.

Mladenov, N., Koop, J., Tischer, S., Deutschmann, O., 2010. Modeling of transport and chemistry in channel flows of automotive catalytic converters. Chem. Eng. Sci. 65, 812–826.

Morbidelli, M., Gavriilidis, A., Varma, A., 2001. Catalyst Design: Optimal Distribution of Catalyst in Pellets,Reactors, and Membranes, 1st ed. Cambridge University Press, New York.

Mosayebi, Z., Rezaei, M., Ravandi, A.B., Hadian, N., 2012. Autothermal reforming of methane over nickel catalysts supported on nanocrystalline MgAl2O4 with high surface area. Int. J. Hydrogen Energy 37, 1236–1242.

Moukalled, F., Mangani, L., 2016. The Finite Volume Method in Computational Fluid Dynamics, 1st ed. Springer, Heidelberg.

Navalho, J.E.P., Frenzel, I., Loukou, A., Pereira, J.M.C., Trimis, D., Pereira, J.C.F., 2013. Catalytic partial oxidation of methane rich mixtures in non-adiabatic monolith reactors. Int. J. Hydrogen Energy 38, 6989–7006.

Neagoe, C., Boffito, D.C., Ma, Z., Trevisanut, C., Patience, G.S., 2015. Pt on Fecralloy catalyses methane partial oxidation to syngas at high pressure. Catal. Today 270, 1–8.

Neumann, D., Veser, G., 2005. Catalytic partial oxidation of methane in a high-temperature reverse-flow reactor. AIChE J. 51, 210–223.

Newitt, D.M., Haffner, A.E., 1931. The Formation of Methyl Alcohol and Formaldehyde in the Slow Combustion of Methane at High Pressures. Proc. Roy.Soc 134, 591–604.

Nogare, D.D., Degenstein, N.J., Horn, R., Canu, P., Schmidt, L.D., 2011. Modeling spatially resolved data of methane catalytic partial oxidation on Rh foam catalyst at different inlet compositions and flowrates. J. Catal. 277, 134–148.

Pantu, P., Gavalas, G.R., 2002. Methane partial oxidation on Pt /CeO2 and Pt/Al2O3 catalysts. Appl. Catal. A, Gen. 223, 253–260.

Park, Y.K., Vlachos, D.G., 2000. Partial Oxidation of Light Alkanes in Short Contact

Time Microreactors. Catalysis 15, 98–137.

Partopour, B., Dixon, A.G., 2017. Resolved-Particle Fixed Bed CFD with Microkinetics for Ethylene Oxidation. AIChE 63.

Pawlowski, S., Nayak, N., Meireles, M., Velizarov, S., Crespo, J.G., 2018. CFD modelling of flow patterns , tortuosity and residence time distribution in monolithic porous columns reconstructed from X-ray tomography data. Chem. Eng. J. 350, 757–766.

Pino, L., Recupero, V., Beninati, S., Shukla, A.K., Hegde, M.S., Bera, P., 2002. Catalytic partial-oxidation of methane on a ceria-supported platinum catalyst for application in fuel cell electric vehicles. Appl. Catal. A Gen. 225, 63–75.

Prettre, M., Eichner, C., Perrin, M., 1946. The catalytic oxidation of methane to carbon monoxide and hydrogen. Trans. Faraday Soc. 42, 335–339.

Quiceno, R., Pérez-Ramírez, J., Warnatz, J., Deutschmann, O., 2006. Modeling the high-temperature catalytic partial oxidation of methane over platinum gauze: Detailed gas-phase and surface chemistries coupled with 3D flow field simulations. Appl. Catal. A Gen. 303, 166–176.

Ra, M.H., Jakobsen, H.A., Hustad, J.E., 2012. Modeling and simulation of catalytic partial oxidation of methane to synthesis gas by using a plasma-assisted gliding arc reactor. Fuel Process. Technol. 101, 44–57.

Raja, L.L., Kee, R.J., Deutschmann, O., 2000. A critical evaluation of Navier – Stokes , boundary-layer , and plug-flow models of the flow and chemistry in a catalytic-combustion monolith. Catal. Today 59, 47–60.

Ranade, V., 2001. Computational Flow Modeling for Chemical Reactor Engineering, 5th ed. Academic Press, Cambridge.

Rebughini, S., Cuoci, A., Dixon, A.G., Maestri, M., 2017. Cell agglomeration algorithm for coupling microkinetic modeling and steady-state CFD simulations of catalytic reactors. Comput. Chem. Eng. 97, 175–182.

Rebughini, S., Maestri, M., 2016. Review on modelling of spatially resolved transport and reaction in gas-solid chemical reactors. Milano.

Recupero, V., Pino, L., Leonardo, R. Di, Lagana, M., Maggio, G., 1998. Hydrogen generator , via catalytic partial oxidation of methane for fuel cells. J. Power Sources 71, 208–214.

Ren, Z., Pope, S.B., 2008. Second-order splitting schemes for a class of reactive systems. J. Comput. Phys. 227, 8165–8176.

Rezaei, M., Meshkani, F., Ravandi, A.B., Nematollahi, B., Ranjbar, A., Hadian, N., Mosayebi, Z., 2011. Autothermal reforming of methane over Ni catalysts supported on nanocrystalline MgO with high surface area and plated-like shape. Int. J. Hydrogen Energy 36, 11712–11717.

Roache, P.J., 1994. Perspective : A Method for Uniform Reporting of Grid Refinement Studies. J. Fluids Eng. 116, 404–413.

Rostrup-nielsen, J., 2000. Reaction kinetics and scale-up of catalytic processes. J. Mol. Catal. A Chem. 163, 157–162.

Sadeghi, F., Tirandazi, B., Khalili-Garakani, A., Nasseri, S., Nabizadeh Nodehi, R., Mostoufi, N., 2017. Investigating the effect of channel geometry on selective catalytic reduction of NOx in monolith reactors. Chem. Eng. Res. Des. 118, 21–30.

Sari, A., 2017. Chemical Engineering Research and Design A theoretical study on high pressure partial oxidation of methane in Rh-washcoated monoliths. Chem. Eng. Res. Des. 121, 134–148.

Schlichting, H., Gersten, K., 1999. Boundary-Layer Theory, 8th ed. Springer, Heidelberg.

Schneider, A., Mantzaras, J., Jansohn, P., 2006. Experimental and numerical investigation of the catalytic partial oxidation of CH4/O2 mixtures diluted with H2O and CO2 in a short contact time reactor. Chem. Eng. Sci. 61, 4634–4649.

Schwiedernoch, R., Tischer, S., Correa, C., Deutschmann, O., 2003. Experimental and numerical study on the transient behavior of partial oxidation of methane in a catalytic monolith. Chem. Eng. Sci. 58, 633–642.

Sengodan, S., Lan, R., Humphreys, J., Du, D., Xu, W., Wang, H., 2018. Advances in reforming and partial oxidation of hydrocarbons for hydrogen production and fuel cell applications. Renew. Sustain. Energy Rev. 82, 761–780.

Smith, M.W., Shekhawat, D., 2011. Fuel Cells:Technologies for Fuel Cell Processing. In: Shekhawat, D., Spivey, J.., Berry, D.. (Eds.), Catalytic Partial Oxidation. Morgantown, pp. 74–122.

Soick, M., Buyevskaya, O., Hohenberger, M., Wolf, D., 1996. Partial oxidation of methane to synthesis gas over Pt/MgO - Kinetics of surface processes. Catal. Today 32, 163–169.

Spence, A., Worth, D.., Kolaczkowski, S.., Crumpton, P.., 1993. Modelling catalytic combustion in a monolith reactor: A numerical algorithm for varying solid phase

peclet numbers. Comput. Chem. Eng. 17, 1057–1066.

Srinivasan, R., Hsing, I., Berger, P.E., Jensen, K.F., Firebaugh, S.L., Schmidt, M.A., Harold, M.P., Lerou, J.J., Ryley, J.F., 1997. Micromachined Reactors for Catalytic Partial Oxidation Reactions. AIChE J. 43, 3059–3069.

Stampfl, C., Ganduglia-pirovano, M. V, Reuter, K., Scheffler, M., 2002. Catalysis and corrosion : the theoretical surface-science context. Surf. Sci. 500, 368–394.

Starik, A.M., Kuleshov, P.S., Loukhovitski, B.I., Titova, N.S., 2015. Theoretical study of partial oxidation of methane by non-equilibrium oxygen plasma to produce hydrogen rich syngas. Int. J. Hydrogen Energy 40, 1–13.

Stefanidis, G.D., Vlachos, D.G., 2009. Controlling Homogeneous Chemistry in Homogeneous - Heterogeneous Reactors : Application to Propane Combustion. Ind. Eng. Chem. Res. 48, 5962–5968.

Stoller, R.E., Golubov, S.I., Domain, C., Becquart, C.S., 2008. Mean field rate theory and object kinetic Monte Carlo : A comparison of kinetic models. J. Nucl. Mater. 382, 77–90.

Stutz, M.J., Poulikakos, D., 2008. Optimum washcoat thickness of a monolith reactor for syngas production by partial oxidation of methane. Chem. Eng. Sci. 63, 1761–1770.

Tavazzi, I., Beretta, A., Groppi, G., Maestri, M., Tronconi, E., Forzatti, P., 2007. Experimental and modeling analysis of the effect of catalyst aging on the performance of a short contact time adiabatic CH 4 -CPO reactor. Catal. Today 129, 372–379.

Tomas, V., Franjo, J., 2006. State-of-the-art in the monolithic catalysts / reactors. Appl. Catal. A Gen. 311, 112–121.

Vernikovskaya, N. V., Bobrova, L.N., Pinaeva, L.G., Sadykov, V.A., Zolotarskii, I.A., Sobyanin, V.A., Buyakou, I., Kalinin, V., Zhdanok, S., 2007. Transient behavior of the methane partial oxidation in a short contact time reactor: Modeling on the base of catalyst detailed chemistry. Chem. Eng. J. 134, 180–189.

Vernon, P.D.. ., Green, M.L.., Cheetham, A.., Ashcroft, A.., 1990. Partial Oxidation of Methane to Synthesis Gas. Catal. Letters 6, 181–186.

Vernon, P.D.., Green, M.L.H., Cheetham, A.., Ashcroft, A.T., 1992. Partial oxidation of methane to synthesis gas, and carbon dioxide as an oxidisig agent for methane conversion. Catal. Today 13, 417–426.

Versteeg, K.H., Malalasekera, W., 2007. An Introduction to Computational Fluid

Dynamics.

Veser, G., Frauhammer, J., 2000. Modelling steady state and ignition during catalytic methane oxidation in a monolith reactor. Chem. Eng. Sci. 55, 2271–2286.

Welaya, Y.M.., Gohary, M.M.., Ammar, N.R., 2012. Steam and partial oxidation reforming options for hydrogen production from fossil fuels for PEM fuel cells. Alexandria Eng. J. 51, 69–75.

Witt, P.M., Schmidt, L.D., 1996. Effect of Flow Rate on the Partial Oxidation of Methane and Ethane 1. J. Catal. 475, 465–475.

Worth, D.J., Spence, A., Crumpton, P.I., 1996. Radiative exchange between square parallel channels in a concentric monolith structure. Int. J. Heat Mass Transf. 39, 1463–1474.

Wu, C., Hammerle, R.H., 1983. Development of a Low Cost , Thermally Stable , Monolithic Three-way Catalyst System. Ind. Eng. Chem. Prod. Res. Dev. 22, 559–565.

Zerkle, D.K., Allendorf, M.D., Wolf, M., Deutschmann, O., 2000. Understanding Homogeneous and Heterogeneous Contributions to the Platinum-Catalyzed Partial Oxidation of Ethane in a Short-Contact-Time Reactor. J. Catal. 39, 18–39.

Zhang, Y., Xiong, G., Yang, W., Sheng, S., 2001. Partial Oxidation of Methane to Syngas over NiO/y-Al203 Catalysts Prepared by the Sol-Gel Method. In: Spivey, J.., Iglesia, E., Fleisch, T.. (Eds.), . Studies in Surface Science and Catalysis, pp. 21–26.

Table 14: Sum of species mass fractions along the reactor axial

Axial coordinate	xCH_4	xCO	xH_2	xH_2O	xN_2	xO_2	x_{total}
0.000000	0.317881	0.000000	0.000000	0.000000	0.523179	0.158940	1.000000
0.001000	0.301625	0.020896	0.004933	0.002273	0.526025	0.144248	1.000000
0.002000	0.285369	0.041792	0.009866	0.004546	0.528870	0.129556	0.999999
0.003000	0.269616	0.067021	0.014130	0.006029	0.529806	0.113398	0.999999
0.004000	0.254007	0.093487	0.018202	0.007286	0.530197	0.096821	1.000000
0.005000	0.241669	0.115176	0.021343	0.007953	0.530255	0.083603	0.999999
0.006000	0.231948	0.133043	0.023738	0.008150	0.530047	0.073072	0.999998
0.007000	0.223020	0.149590	0.025926	0.008175	0.529811	0.063476	0.999999
0.008000	0.215677	0.163496	0.027700	0.007857	0.529518	0.055751	0.999999
0.009000	0.208458	0.177223	0.029429	0.007516	0.529206	0.048167	1.000000
0.010000	0.202224	0.189522	0.030807	0.006987	0.528738	0.041722	1.000000
0.011000	0.195990	0.201822	0.032185	0.006458	0.528269	0.035276	1.000000
0.012000	0.190676	0.212723	0.033237	0.005940	0.527674	0.029749	1.000000
0.013000	0.185477	0.223449	0.034248	0.005424	0.527064	0.024338	1.000000
0.014000	0.181411	0.231880	0.035014	0.005012	0.526553	0.020129	0.999999
0.015000	0.177912	0.239165	0.035658	0.004651	0.526093	0.016521	1.000000
0.016000	0.174965	0.245293	0.036197	0.004347	0.525703	0.013495	1.000000
0.017000	0.172708	0.249975	0.036605	0.004115	0.525400	0.011196	0.999999
0.018000	0.170625	0.254293	0.036981	0.003902	0.525122	0.009077	1.000000
0.019000	0.169151	0.257334	0.037247	0.003753	0.524926	0.007589	1.000000
0.020000	0.167677	0.260374	0.037513	0.003603	0.524731	0.006101	0.999999
0.021000	0.166729	0.262328	0.037682	0.003509	0.524604	0.005148	1.000000
0.022000	0.165782	0.264281	0.037851	0.003414	0.524477	0.004195	1.000000
0.023000	0.165096	0.265694	0.037973	0.003346	0.524384	0.003507	1.000000
0.024000	0.164485	0.266952	0.038081	0.003286	0.524302	0.002894	1.000000
0.025000	0.163994	0.267961	0.038168	0.003238	0.524236	0.002403	0.999999
0.026000	0.163599	0.268772	0.038238	0.003199	0.524183	0.002008	0.999999
0.027000	0.163252	0.269486	0.038299	0.003165	0.524136	0.001661	0.999999
0.028000	0.162999	0.270006	0.038344	0.003141	0.524102	0.001408	1.000000
0.029000	0.162756	0.270505	0.038386	0.003117	0.524069	0.001166	0.999999
0.030000	0.162595	0.270837	0.038415	0.003102	0.524047	0.001004	1.000000
0.031000	0.162434	0.271168	0.038443	0.003086	0.524025	0.000843	0.999999
0.032000	0.162324	0.271394	0.038462	0.003075	0.524010	0.000733	0.999999
0.033000	0.162221	0.271607	0.038481	0.003065	0.523996	0.000630	1.000000
0.034000	0.162142	0.271769	0.038494	0.003058	0.523986	0.000551	1.000000
0.035000	0.162075	0.271906	0.038506	0.003051	0.523977	0.000484	1.000000
0.036000	0.162019	0.272021	0.038516	0.003046	0.523969	0.000429	0.999999
0.037000	0.161976	0.272109	0.038523	0.003042	0.523963	0.000386	0.999999
0.038000	0.161937	0.272190	0.038530	0.003038	0.523958	0.000347	1.000000
0.039000	0.161910	0.272246	0.038535	0.003035	0.523954	0.000320	1.000000
0.040000	0.161883	0.272302	0.038540	0.003033	0.523951	0.000292	1.000001
0.041000	0.161865	0.272338	0.038543	0.003031	0.523949	0.000275	1.000001
0.042000	0.161847	0.272374	0.038546	0.003029	0.523946	0.000257	1.000000
0.043000	0.161835	0.272399	0.038548	0.003028	0.523945	0.000245	1.000000
0.044000	0.161823	0.272422	0.038550	0.003027	0.523943	0.000234	0.999999
0.045000	0.161814	0.272441	0.038552	0.003026	0.523942	0.000224	0.999999
0.046000	0.161806	0.272457	0.038554	0.003025	0.523941	0.000217	1.000000
0.047000	0.161799	0.272470	0.038555	0.003024	0.523940	0.000210	0.999998
0.048000	0.161794	0.272481	0.038556	0.003024	0.523940	0.000205	1.000000
0.049000	0.161789	0.272491	0.038557	0.003023	0.523939	0.000200	1.000000
0.050000	0.161785	0.272498	0.038558	0.003023	0.523939	0.000197	0.999999
0.051000	0.161781	0.272506	0.038558	0.003022	0.523938	0.000193	0.999999
0.052000	0.161778	0.272512	0.038559	0.003022	0.523938	0.000190	1.000000
0.053000	0.161776	0.272517	0.038560	0.003022	0.523938	0.000188	1.000001
0.054000	0.161773	0.272522	0.038560	0.003022	0.523938	0.000185	1.000000
0.055000	0.161770	0.272527	0.038561	0.003021	0.523937	0.000183	0.999999
0.056000	0.161768	0.272531	0.038562	0.003021	0.523937	0.000181	0.999999
0.057000	0.161765	0.272536	0.038562	0.003021	0.523937	0.000179	1.000000
0.058000	0.161763	0.272540	0.038563	0.003021	0.523937	0.000177	1.000000
0.059000	0.161762	0.272543	0.038563	0.003021	0.523937	0.000175	1.000001
0.060000	0.161760	0.272545	0.038563	0.003020	0.523937	0.000174	1.000000
0.061000	0.161758	0.272548	0.038564	0.003020	0.523937	0.000173	1.000000
0.062000	0.161757	0.272550	0.038564	0.003020	0.523937	0.000171	1.000000
0.063000	0.161755	0.272553	0.038565	0.003020	0.523937	0.000170	1.000000
0.064000	0.161753	0.272557	0.038565	0.003020	0.523937	0.000168	1.000000
0.065000	0.161752	0.272559	0.038566	0.003020	0.523937	0.000167	1.000000
0.066000	0.161750	0.272561	0.038566	0.003020	0.523937	0.000166	0.999999
0.067000	0.161749	0.272563	0.038566	0.003019	0.523937	0.000165	1.000000
0.068000	0.161748	0.272565	0.038567	0.003019	0.523937	0.000164	1.000000
0.069000	0.161747	0.272566	0.038567	0.003019	0.523937	0.000163	1.000000
0.070000	0.161745	0.272569	0.038567	0.003019	0.523937	0.000162	1.000000
0.071000	0.161744	0.272571	0.038568	0.003019	0.523937	0.000161	1.000000
0.072000	0.161742	0.272574	0.038568	0.003019	0.523937	0.000160	1.000000
0.073000	0.161740	0.272576	0.038569	0.003019	0.523937	0.000158	0.999999
0.074000	0.161739	0.272579	0.038569	0.003018	0.523937	0.000157	0.999999
0.075000	0.161738	0.272581	0.038569	0.003018	0.523938	0.000156	1.000001
0.076000	0.161736	0.272583	0.038570	0.003018	0.523938	0.000155	1.000000
0.077000	0.161735	0.272585	0.038570	0.003018	0.523938	0.000154	1.000000
0.078000	0.161734	0.272587	0.038570	0.003018	0.523938	0.000153	1.000000
0.079000	0.161732	0.272589	0.038571	0.003018	0.523938	0.000152	1.000000
0.080000	0.161731	0.272591	0.038571	0.003018	0.523938	0.000151	1.000000
0.081000	0.161729	0.272593	0.038571	0.003017	0.523938	0.000150	0.999999
0.082000	0.161728	0.272595	0.038572	0.003017	0.523939	0.000149	1.000000
0.083000	0.161726	0.272597	0.038572	0.003017	0.523939	0.000148	0.999999
0.084000	0.161725	0.272600	0.038573	0.003017	0.523939	0.000147	1.000001
0.085000	0.161723	0.272602	0.038573	0.003017	0.523939	0.000146	1.000000
0.086000	0.161721	0.272604	0.038574	0.003017	0.523939	0.000145	0.999999
0.087000	0.161720	0.272606	0.038574	0.003016	0.523940	0.000144	1.000000
0.088000	0.161718	0.272609	0.038575	0.003016	0.523940	0.000143	1.000000
0.089000	0.161716	0.272611	0.038575	0.003016	0.523940	0.000142	0.999999
0.090000	0.161714	0.272614	0.038576	0.003016	0.523940	0.000140	1.000000
0.091000	0.161712	0.272616	0.038576	0.003016	0.523940	0.000139	0.999999
0.092000	0.161711	0.272618	0.038577	0.003015	0.523941	0.000138	1.000000
0.093000	0.161709	0.272621	0.038577	0.003015	0.523941	0.000137	1.000000
0.094000	0.161707	0.272623	0.038578	0.003015	0.523941	0.000136	0.999999
0.095000	0.161705	0.272626	0.038578	0.003015	0.523941	0.000134	0.999999
0.096000	0.161702	0.272630	0.038579	0.003014	0.523942	0.000133	1.000000
0.097000	0.161699	0.272633	0.038580	0.003014	0.523943	0.000131	1.000000
0.098000	0.161696	0.272637	0.038581	0.003014	0.523943	0.000129	1.000000
0.099000	0.161695	0.272638	0.038581	0.003014	0.523944	0.000128	1.000000
0.100000	0.161693	0.272640	0.038582	0.003014	0.523945	0.000127	1.000001

The surface coverage results for CH_4, CH_2, CH, CO, CO_2 and H_2 at various feedstock ratios are presented in Figure 127 to 132.
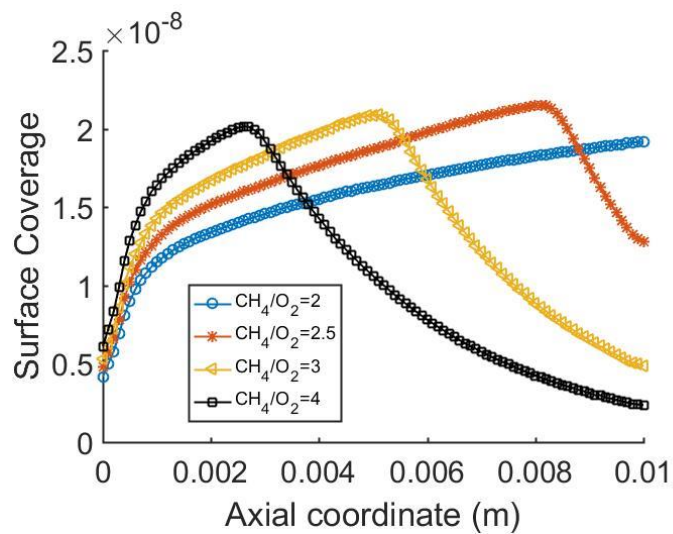
Figure 125: CO surface coverage at various feedstock ratios(a 10 mm length and 0.5 mm diameter monolith with 598.15 K inlet temperature and 2.5 m/s inlet velocity)
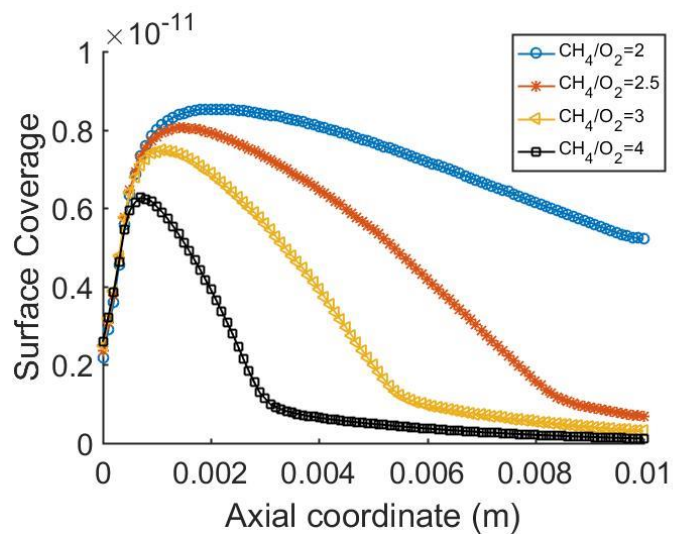
Figure 126: CO_2 surface coverage at various feedstock ratios (a 10 mm length and 0.5 mm diameter monolith with 598.15 K inlet temperature and 2.5 m/s inlet velocity)
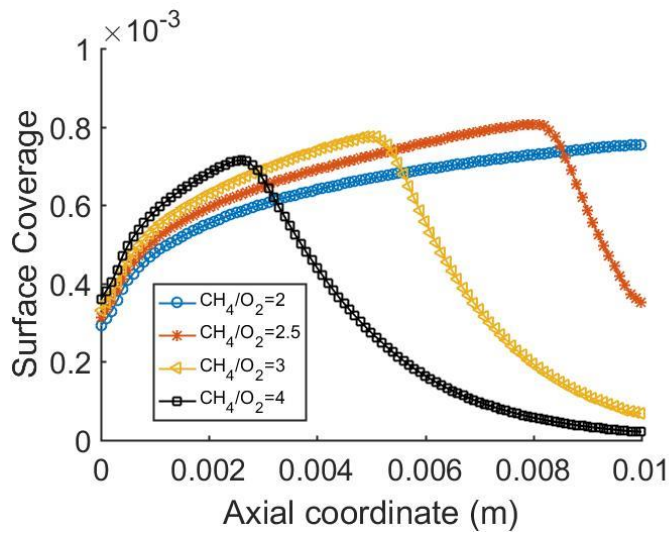
Figure 127: H surface coverage at various feedstock ratios (a 100 mm length and 1.0 mm diameter monolith with 598.15 K inlet temperature and 2.5 m/s inlet velocity)

Figure 128: CH surface coverage at various feedstock ratios (a 100 mm length and 1.0 mm diameter monolith with 598.15 K inlet temperature and 2.5 m/s inlet velocity)

Figure 129: CH_2 surface coverage at various feedstock ratios (a 100 mm length and 1.0 mm diameter monolith with 598.15 K inlet temperature and 2.5 m/s inlet velocity)

Figure 130: CH$_3$ surface coverage at various feedstock ratios (a 100 mm length and 1.0 mm diameter monolith with 598.15 K inlet temperature and 2.5 m/s inlet velocity)

Appendix C

A sample code used in geometry generation

```python
#!/usr/bin/env python
import os
from math import *
#import numpy
from string import split

def write_blockmesh(case,d_outer,l,rows,cols,grid_th=80,grid_l=100,exp_w=1.2,foam_version="2.0"):
    #start writing blockMeshDict file
    f = file(os.path.join(case,"constant","polyMesh","blockMeshDict"),"w")
    f.write("""FoamFile
{
    version """+foam_version+""";
    format  ascii;
    class   dictionary;
    object  blockMeshDict;
}
convertToMeters 1.0;

vertices
(
""")

    block_A = (0,1,2,3,4,5,6,7)

    points = [(0,0),
              (d_outer,0),
              (0,d_outer),
              (d_outer,d_outer)]

    for y in range(rows):
        yoff = d_outer*(y+0.5)
        for x in range(cols):
            xoff = d_outer*(x+0.5)
            for z in [0.0,l]:
                for k in range(len(points)):
                    f.write("\t("+str(points[k][0]+xoff)+" "+str(points[k][1]+yoff)+" "+str(z)+")\n")
    f.write(");\n")

    #write edges
    #f.write("""
#edges
#(
#""")
    # write blocks
    f.write("""
blocks
(
""")

    for y in range(rows):
        for x in range(cols):
            for block in [block_A]:
                f.write("\thex (")
                pointoff = 2*(y*cols+x)*len(points)
                for v in block:
                    f.write(" "+str(v+pointoff)+" ")
                f.write(")\n")
                f.write("\t("+str(grid_th/4)+" "+str(grid_th/4)+" "+str(grid_l)+")\n")
                f.write("\tsimpleGrading (1 1 1)\n")
    f.write(");\n")

    #patches
    f.write("""
patches
(
""")

    f.write("""
    type reactingwall
    (
""")
    for y in range(rows):
        for x in range(cols):
            pointoff = 2*(y*cols+x)*len(points)
            f.write("\t\t\t("+str(1+pointoff)+" "+str(1+pointoff+len(points))+" "+str(2+pointoff+len(points))+" "+str(7+pointoff)+")\n")
            f.write("\t\t\t("+str(0+pointoff)+" "+str(pointoff+len(points)-1)+" "+str(pointoff+len(points)-2)+" "+str(1+pointoff)+")\n")
            f.write("\t\t\t("+str(0+pointoff)+" "+str(pointoff+len(points)-3)+" "+str(1+pointoff+len(points))+" "+str(4+pointoff)+")\n")
            f.write("\t\t\t("+str(3+pointoff)+" "+str(3+pointoff+len(points))+" "+str(2+pointoff+len(points))+" "+str(2+pointoff)+")\n")
    f.write("""
    )
""")

    f.write("""
    patch inlet
    (
""")
    for y in range(rows):
        for x in range(cols):
            pointoff = 2*(y*cols+x)*len(points)
            f.write("\t\t\t("+str(0+pointoff)+" "+str(4+pointoff)+" "+str(7+pointoff)+" "+str(3+pointoff)+")\n")
    f.write("""
    )
""")
    f.write("""
    patch outlet
    (
""")
    for y in range(rows):
        for x in range(cols):
            pointoff = (2*(y*cols+x)+1)*len(points)
            f.write("\t\t\t("+str(pointoff-3)+" "+str(pointoff-2)+" "+str(2+pointoff)+" "+str(1+pointoff)+")\n")
    f.write("""
    )
""")
    f.write(");\n")
    f.write("""
    mergePatchPairs
    (
""")
    f.write(");\n")
    f.close()

case = "/home/khana/OpenFOAM/tubebundle_blockmesh"
r = 2
c = 2
d_o = 0.5
length = 4.0
write_blockmesh(case,d_o,length,r,c,grid_th=80,exp_w=1.2,foam_version="2.0")
```

Appendix D

```
/*************************************************************************
 *    catalyticFOAM                                                      *
 *                                                                       *
 *    Copyright (C) 2011 by Alberto Cuoci and Matteo Maestri             *
 *                                                                       *
 *    Authors                                                            *
 *    alberto.cuoci@polimi.it                                            *
 *    matteo.maestri@polimi.it                                           *
 *    sandro.goisis@mail.polimi.it                                       *
 *    alessandra.osio@mail.polimi.it                                     *
 *                                                                       *
 *    Last modified: 05/30/2012                                          *
 *************************************************************************/

class OneEdgePolicy
{
        protected:
                static const int nEdges_ = 1;
};

class TwoEdgePolicy
{
        protected:
                static const int nEdges_ = 2;
};

class ThreeEdgePolicy
{
        protected:
                static const int nEdges_ = 3;
};

class FourEdgePolicy
{
        protected:
                static const int nEdges_ = 4;
};

//- Class definition for chemical reactions
template<typename EdgePolicy>
class ODESystem_BatchReactor_Heterogeneous : public EdgePolicy
{
    private:

        OpenSMOKE_ReactingGasMixture *gas_mixture;
        OpenSMOKE_ReactingSurface *surface_chemistry;
        OpenSMOKE::OpenSMOKEVectorDouble cgas;
        //OpenSMOKE::OpenSMOKEVectorDouble Djk;
        //OpenSMOKE::OpenSMOKEVectorDouble lambda;
        //OpenSMOKE::OpenSMOKEVectorDouble Dmix;
        // OpenSMOKE::OpenSMOKEVectorDouble Rsurf;
        OpenSMOKE::OpenSMOKEVectorDouble Rbulk;
        OpenSMOKE::OpenSMOKEVectorDouble massFractions;
        OpenSMOKE::OpenSMOKEVectorDouble molarFractions;
        OpenSMOKE::OpenSMOKEVectorDouble Rhom;
        OpenSMOKE::OpenSMOKEVectorDouble theta;
        OpenSMOKE::OpenSMOKEVectorDouble Hi;

        double T;
        double Q;
        double MW;
        double cTot;
        double rho;
        double lambdaMix;
        double lambdaWall;
        double DeMix;
        double cpMix;
        double siteDensity;
        double Htot;
        double Hidomega;

        int NC;
        int NS;
        int NEQ_;
        int indexT;
public:
        OpenSMOKE::OpenSMOKEVectorDouble   Rgas_;
        OpenSMOKE::OpenSMOKEVectorDouble Rsurf;
        double        coordinate_;

private:

        double        p_;
                bool          energyEquation_;
        double        alfaCat_;
                double        volume_;
                double        QReaction_;
                double            boundaryConditionsGM;
        double        dmtot_;
        //double        coordinate_;

        //OpenSMOKE::OpenSMOKEVectorDouble    Rgas_;
        OpenSMOKE::OpenSMOKEVectorDouble    bulk_;
        OpenSMOKE::OpenSMOKEVectorDouble    faceAreas_;

    public:

        //- Access functions
        inline void SetPressure(const double pressure)                                 { p_=pressure; }
        inline void SetEnergyEquation(const bool flag)                                 { energyEquation_=flag; }
        inline void SetAlfaCatalyst(const double alfa)                                 { alfaCat_=alfa; }
        inline void SetVolume(const double volume)                                     { volume_=volume; }
        inline void SetCoordinate(const double coordinate)                                  { coordinate_=coordinate; }
        inline void SetFaceAreas(const OpenSMOKE::OpenSMOKEVectorDouble& faceAreas)   { faceAreas_=faceAreas; }

        inline double QReaction() const               { return QReaction_; }
```

```cpp
            inline double BoundaryConditions() const                          { return boundaryConditionsGM; }
            inline OpenSMOKE::OpenSMOKEVectorDouble& Rgas()        { return Rgas_; }
            inline int NEQ() const                              { return NEQ_; }

            double x_coordinate_Celli;
            //- Constructor:
            void Setup(OpenSMOKE_ReactingGasMixture *gas_mixtureOUT, OpenSMOKE_ReactingSurface *surface_chemistryOUT);

            //- Destructor:
            virtual ~ODESystem_BatchReactor_Heterogeneous() {};

            //- Functions:
            int GetSystemFunctions(const double t, OpenSMOKE::OpenSMOKEVector<double, OpenSMOKE::OneIndexPolicy> &y, OpenSMOKE::OpenSMOKEVector<double, OpenSMOKE::OneIndexPolicy> &f);

public: // pseudo

            OpenSMOKE::OpenSMOKEVectorDouble y;
            OpenSMOKE::OpenSMOKEVectorDouble f;

            #if BZZMATH_SUPPORT == 1
                    BzzVector Y0;
                    BzzVector YF;
                    BzzVector YMin;
                    BzzVector YMax;
            #else
                    double* Y0;
            #endif
};

template<typename EdgePolicy>
void ODESystem_BatchReactor_Heterogeneous<EdgePolicy>::Setup(OpenSMOKE_ReactingGasMixture *gas_mixtureOUT, OpenSMOKE_ReactingSurface *surface_chemistryOUT)
{
            gas_mixture = gas_mixtureOUT;
            surface_chemistry = surface_chemistryOUT;

            NC      = gas_mixture->NumberOfSpecies();
            NS      = surface_chemistry->NumberSiteSpecies();
            NEQ_    = NC+1+NS*this->nEdges_;
            indexT = NC+1;

            ChangeDimensions(NC, &cgas, true);
            ChangeDimensions(NC, &Rgas_, true);
            //ChangeDimensions(NC, &Djk, true);
            //ChangeDimensions(NC, &Dmix, true);
            //ChangeDimensions(NC, &lambda, true);
            ChangeDimensions(NC, &molarFractions, true);
            ChangeDimensions(NC, &massFractions, true);
            ChangeDimensions(NC, &Rhom, true);
            ChangeDimensions(NC, &Hi, true);
            ChangeDimensions(NS, &theta, true);
            ChangeDimensions(NS, &Rsurf, true);
            ChangeDimensions(NS, &Rbulk, true);
            ChangeDimensions(NS, &bulk_, true);

            ChangeDimensions(NEQ_, &y, false);
            ChangeDimensions(NEQ_, &f, false);

            T           = 0.0;
            Q           = 0.0;
            MW          = 0.0;
            cTot        = 0.0;
            rho         = 0.0;
            cpMix       = 0.0;
            siteDensity = 0.0;

            #if BZZMATH_SUPPORT == 1
                    ChangeDimensions(NEQ_, &Y0);
                    ChangeDimensions(NEQ_, &YF);
                    ChangeDimensions(NEQ_, &YMin);
                    ChangeDimensions(NEQ_, &YMax);
                    YMin = 0.;       YMin[indexT] = 200.;
                    YMax = 1.;       YMax[indexT] = 4000.;
            #else
                    Y0 = new double[NEQ_];
            #endif
}

template<typename EdgePolicy>
int ODESystem_BatchReactor_Heterogeneous<EdgePolicy>::GetSystemFunctions(const double t, OpenSMOKE::OpenSMOKEVector<double, OpenSMOKE::OneIndexPolicy> &X, OpenSMOKE::OpenSMOKEVector<double,
OpenSMOKE::OneIndexPolicy> &dX)
{
            //- Allocating massive fractions
            #if CHECK_MASSFRACTIONS_HOMOGENEOUS == 1
            for(int i=1;i<=NC;i++)
                    massFractions[i] = max(X[i], 1.e-64);
            #else
            for(int i=1;i<=NC;i++)
                    massFractions[i] = X[i];
            #endif

            //- Allocating temperature
            T =X[indexT];

            //- Evaluate molar fractions, overall concentration and density
            gas_mixture->GetMWAndMoleFractionsFromMassFractions(MW, molarFractions, massFractions);
            cTot = p_/(OpenSMOKE_Constants::R_J_kmol*T);
            rho = cTot*MW;

            //- Evaluate homogeneous reaction rates
            Product(cTot, molarFractions, &cgas);
            gas_mixture->kinetics()->KineticParameters(T, p_);
            gas_mixture->kinetics()->ComputeFromConcentrations(T, cgas, cTot, &Rhom, Q);
            ElementByElementProduct(Rhom, gas_mixture->M(), &Rhom);

            //- Writing mass balances for the gas phase
            for(int i=1;i<=NC;i++)
                    dX[i] =Rhom[i]/rho;
```

```cpp
        //- Writing temperature equation
        dX[indexT] = 0.;
        if (energyEquation_ == true)
        {
                cpMix = gas_mixture->thermodynamics()->GetMeanMixConstantPressureSpecificHeatFromMassFractions(T, massFractions);
                dX[indexT] = Q/(rho*cpMix);
    // std::cout << "Q " << Q << std::endl;
        }

        //- Surface solution
        for(int edge=1; edge<=this->nEdges_;edge++)
        {
                int baseCounter = NC+1+NS*(edge-1);

                //- Allocating site fractions
                #if CHECK_MASSFRACTIONS_HETEROGENEOUS == 1
                for(int i=1;i<=NS;i++)
                        theta[i] = max(X[baseCounter+i], 1.e-64);
                #else
                for(int i=1;i<=NS;i++)
                        theta[i] = X[baseCounter+i];
                #endif

                //- Evaluating site density and heterogeneous reaction rates
                Product(cTot, molarFractions, &cgas);
                surface_chemistry->material()[1].ReactionRates(T, cgas, theta, bulk_, Rgas_, Rsurf, Rbulk, QReaction_);
                siteDensity = surface_chemistry->material()[1].sites()[1].density();



                //- Total mass variation
                dmtot_ = Dot(Rgas_, gas_mixture->M());

                //- TODO Condizioni al contorno nuove. Th MAESTRI

                double boundaryConditionsGM_temp = 0.;
                gas_mixture->thermodynamics()->GetMixAveragedEnthalpy_Mass(T, Hi);
                for (int i = 1; i<= NC; i++)
                        {
                        boundaryConditionsGM_temp = boundaryConditionsGM_temp + Hi[i]*Rgas_[i];
                        }
                        boundaryConditionsGM = boundaryConditionsGM_temp;


                //- Writing mass balaces for the adsorbed phase
                for(int i=1;i<=NS;i++)
                        dX[baseCounter+i] =Rsurf[i]/siteDensity;

                //- Adding surface generation term
                double coefficient;
    // A non-uniform distribution of the catalytic material on the support
                 if (coordinate_ <= 0.09)
                        {
                                coefficient =faceAreas_[edge]*alfaCat_/volume_/rho;

        else if(coordinate_ > 0.09)
                        {
                                coefficient = faceAreas_[edge]*alfaCat_/volume_/rho*0;
                        }

                for(int i=1;i<=NC;i++)
                        dX[i] += (Rgas_[i]*gas_mixture->M()[i]-dmtot_*X[i])*coefficient;

                if (energyEquation_ == true)
                {

                        double Temp = 0.;
                        for (int i = 1; i<= NC; i++)
                        {
                        Temp = Temp +((Hi[i]*(rho*volume_*dX[i]+X[i]*dmtot_*faceAreas_[edge]*alfaCat_))/(rho*cpMix*volume_));
                        }
                        dX[indexT] += -Temp;
                        QReaction_ = -Temp*(rho*cpMix*volume_)/(faceAreas_[edge]*alfaCat_);
                        //cout << "QReaction_"<< endl;
                }
        }



    return(0);
}
```

171

Appendix E

The Gibbs free energy for the simulation results presented in section 8.4 is as observed in Figure 131 The results indicate that these are spontaneous reactions given that Gibbs free energy is negative.

Channel length=0.1 m   Channel length=0.01 m
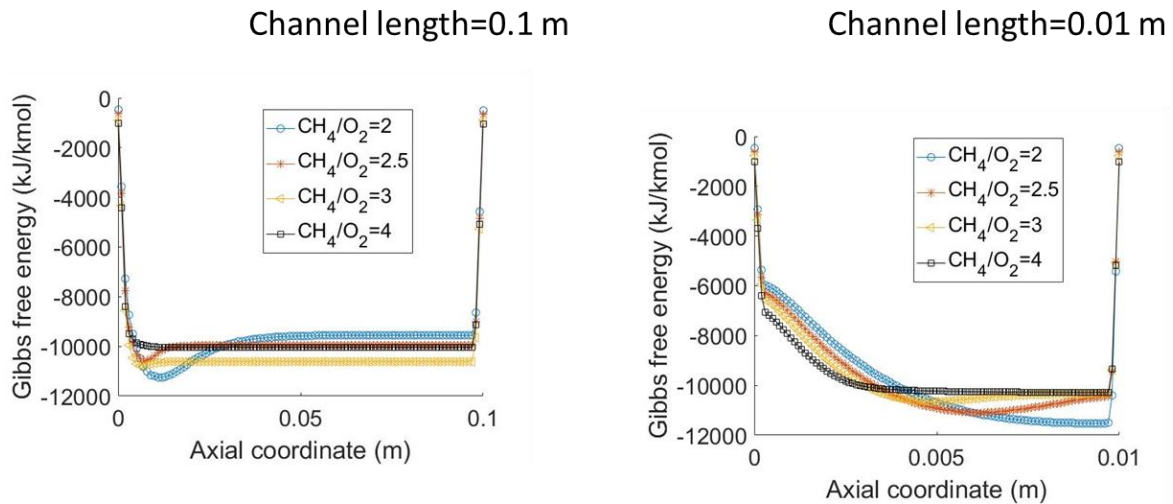
Figure 131: Gibbs free energy at various feedstock ratios
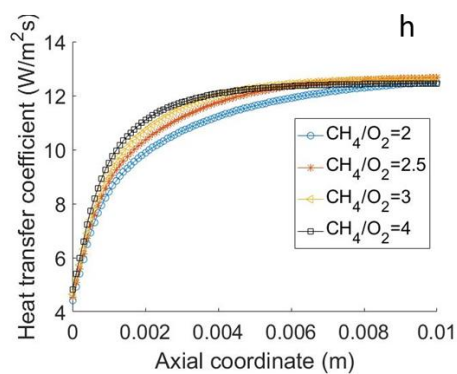
Figure 132: Heat transfer coefficient at various feedstock ratios
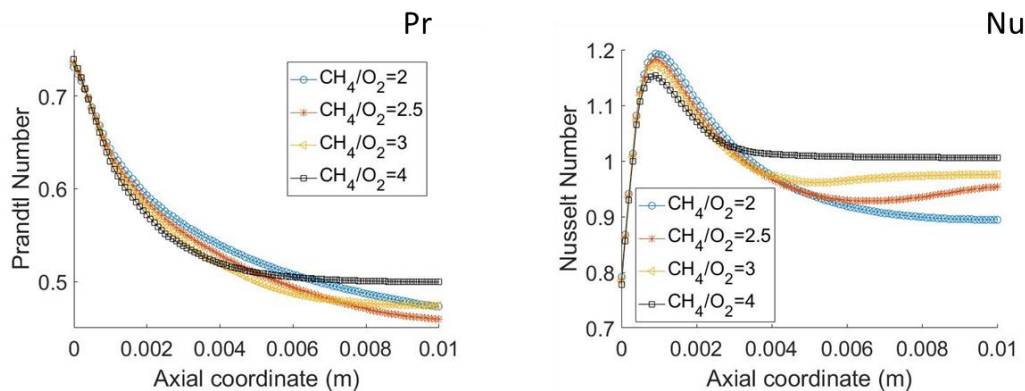
Figure 133: Nusselt and Prandtl numbers at various feedstock ratios

Table 15: Model input parameters (Quiceno et al., 2006)

```
MATERIAL MAT-1

SITE/PT_SURFACE/    SDEN/2.72E-9/
Pt(*)   H2O(*)  H(*)  OH(*)    CO(*)    C(*)
CH3(*)  CH2(*)  CH(*)  O(*)    CO2(*)
END
!!*****************************************************************
**
!!*********          CH4  Surface Reaction on Pt
!!*****************************************************************
**
! The activation energies must be in cal/mol

REACTIONS
!*****************************************************************
************
!**** 1.  ADSORPTION-DESORPTION
!*****************************************************************
*********************  A(cm,mol,s) b   Ea(cal/mol)***
H₂  +Pt(*) +Pt(*) =>H(*)+H(*)  4.600E-02  0.0   0.0

H(*) +H(*)=>H₂ +Pt(*) +Pt(*)   3.700E+18  0.0   16.098

O₂ +Pt(*)+Pt(*)=>O(*) +O(*)    1.89E+18    -0.5   0.0

O(*)+O(*) =>O₂ +Pt(*)+Pt(*)    3.700E+18   0.0   56.248

CH₄ +Pt(*)+Pt(*)=>CH₃(*) +H(*) 9.0009E-04  0.0   17.197

CH₃(*)+H(*)=>CH₄ +Pt(*)+Pt(*)  3.300E+18  0.0   11.942

H₂O+Pt(*)=>H₂O(*)              7.500E-01  0.0   0.0

H₂O(*)=>H₂O+Pt(*)             4.500E+12  0.0   9.984

CO₂+Pt(*) =>CO₂(*)            5.000E+01  0.0   0.0

CO₂(*) =>CO₂ +Pt(*)           1.000E+13  0.0   6.473

CO      +Pt(*)  =>CO(*)       0.840E+01  0.0  0.0

CO(*) =>CO +Pt(*)             1.000E+15  0.0   34.872


!*************************************************************
**
!**** 2.  SURFACE REACTIONS
***************************************************!
!*************************************************************
********************    A(cm,mol,s) b   Ea(cal/mol)***
H(*) +O(*)=>OH(*)+Pt(*)        1.280E+21 0.0     2.675

OH(*)+Pt(*)=>H(*)+O(*)        7.390E+19 0.0     18.463
```

```
H(*)+OH(*)=>H₂O(*)+Pt(*)          2.040E+21   0.0      15.816

H₂O(*)+Pt(*)=>H(*)+OH(*)          1.150E+19   0.0      24.219

OH(*)+OH(*)=>H₂O(*)+O(*)          7.400E+20   0.0      17.675

H₂O(*)+O(*)=>OH(*)+OH(*)          1.000E+20   0.0      10.294

C(*)+O(*)=>CO(*)+Pt(*)            3.700E+19   0.0       0.0

CO(*)+Pt(*)=>C(*)+O(*)            3.700E+19   0.0      56.487

CO(*)+O(*)=>CO2(*)+Pt(*)          3.700E+19   0.0      28.088

CO2(*)+Pt(*)=>CO(*)+O(*)          3.700E+19   0.0      41.392

CO(*)+OH(*)=>CO2(*)+H(*)          1.000E+19   0.0       9.243

CO2(*)+H(*)=>CO(*)+OH(*)          1.000E+19   0.0       2.006
!*************************************************************
**
!*************************************************************
*********************   A(cm,mol,s) b    Ea(cal/mol)***
CH₃(*)+Pt(*)=>CH₂(*)+H(*)      1.260E+22   0.0   16.791

CH₂(*)+H(*)=>CH₃(*)+Pt(*)      3.090E+22   0.0    0.0

CH₂(*)+Pt(*)=>CH(*)+H(*)       7.310E+22   0.0   14.068

CH(*)+H(*)=>CH₂(*)+Pt(*)       3.090E+22   0.0    0.0

CH(*)+Pt(*)=>C(*)+H(*)         3.090E+22   0.0    0.0

C(*)+H(*)=>CH(*)+Pt(*)         1.250E+22   0.0   32.961

H₂ +C(*)=>CH₂(*)               4.000E-02   0.0   7.0937

CH₂(*)=>C(*)+H₂                7.690E+13   0.0    5.995
!*****************************************************************
**
!*****************************************************************
*********************   A(cm,mol,s) b    Ea(cal/mol)***
CH₄+O(*)+Pt(*)=>CH₃(*)+OH(*)   5.000E+18  0.7   10.032

CH₄+OH(*)+Pt(*)=>CH₃(*)+H₂O(*) 1.000E+01  0.0    2.388

CH₃(*)+OH(*)=>CH₄+O(*)+Pt(*)   3.700E+21  0.0   20.995

CH₃(*)+H₂O(*)=>CH₄+OH(*)+Pt(*) 3.700E+21  0.0   26.416
!*****************************************************************
***************
END
```

Table 16: Species transport data for partial oxidation of methane on platinum (Kee et al., 2000)

Species Name	index	ε/k_B	σ	μ	α	Z_{rot}
H2	1	38.000	2.920	0.000	0.790	280.000
O2	1	107.400	3.458	0.000	1.600	3.800
H2O	2	572.400	2.605	1.844	0.000	4.000
H	0	145.000	2.050	0.000	0.000	0.000
O	0	80.000	2.750	0.000	0.000	0.000
OH	1	80.000	2.750	0.000	0.000	0.000
C	0	71.400	3.298	0.000	0.000	0.000
CH	1	80.000	2.750	0.000	0.000	0.000
CH2	1	144.000	3.800	0.000	0.000	0.000
CH3	1	144.000	3.800	0.000	0.000	0.000
CH4	2	141.400	3.746	0.000	2.600	13.000
CO	1	98.100	3.650	0.000	1.950	1.800
CO2	1	244.000	3.763	0.000	2.650	2.100
N2	1	97.530	3.621	0.000	1.760	4.000
N	0	71.400	3.298	0.000	0.000	0.000
AR	0	136.500	3.330	0.000	0.000	0.000
HE	0	10.200	2.576	0.000	0.000	0.000
Pt	0	10.200	2.576	0.000	0.000	0.000

Table 17: Species Thermodynamic data

```
THERMO ALL
 300.0  1000.0  3000.0
O(*)          O   1Pt 1      I   300.00           3000.00         1000.00          1
 0.00000000E+00 0.00000000E+00 0.00000000E+00 0.00000000E+00 0.00000000E+00       2
 0.00000000E+00 0.00000000E+00 0.00000000E+00 0.00000000E+00 0.00000000E+00       3
 0.00000000E+00 0.00000000E+00 0.00000000E+00 0.00000000E+00                      4
O2(*)         O   2Pt 1      I   300.00           3000.00         1000.00          1
 0.00000000E+00 0.00000000E+00 0.00000000E+00 0.00000000E+00 0.00000000E+00       2
 0.00000000E+00 0.00000000E+00 0.00000000E+00 0.00000000E+00 0.00000000E+00       3
 0.00000000E+00 0.00000000E+00 0.00000000E+00 0.00000000E+00                      4
H(*)          H   1Pt 1      I   300.00           3000.00         1000.00          1
 0.00000000E+00 0.00000000E+00 0.00000000E+00 0.00000000E+00 0.00000000E+00       2
 0.00000000E+00 0.00000000E+00 0.00000000E+00 0.00000000E+00 0.00000000E+00       3
 0.00000000E+00 0.00000000E+00 0.00000000E+00 0.00000000E+00                      4
H2(*)         H   2Pt 1      I   300.00           3000.00         1000.00          1
 0.00000000E+00 0.00000000E+00 0.00000000E+00 0.00000000E+00 0.00000000E+00       2
 0.00000000E+00 0.00000000E+00 0.00000000E+00 0.00000000E+00 0.00000000E+00       3
 0.00000000E+00 0.00000000E+00 0.00000000E+00 0.00000000E+00                      4
H2O(*)        O   1H  2Pt 1  I   300.00           3000.00         1000.00          1
 0.00000000E+00 0.00000000E+00 0.00000000E+00 0.00000000E+00 0.00000000E+00       2
 0.00000000E+00 0.00000000E+00 0.00000000E+00 0.00000000E+00 0.00000000E+00       3
 0.00000000E+00 0.00000000E+00 0.00000000E+00 0.00000000E+00                      4
OH(*)         O   1H  1Pt 1  I   300.00           3000.00         1000.00          1
 0.00000000E+00 0.00000000E+00 0.00000000E+00 0.00000000E+00 0.00000000E+00       2
 0.00000000E+00 0.00000000E+00 0.00000000E+00 0.00000000E+00 0.00000000E+00       3
 0.00000000E+00 0.00000000E+00 0.00000000E+00 0.00000000E+00                      4
Pt(*)         Pt 1          S   300.00           3000.00         1000.00          1
 0.00000000E+00 0.00000000E+00 0.00000000E+00 0.00000000E+00 0.00000000E+00       2
 0.00000000E+00 0.00000000E+00 0.00000000E+00 0.00000000E+00 0.00000000E+00       3
 0.00000000E+00 0.00000000E+00 0.00000000E+00 0.00000000E+00                      4
Pt            Pt 1          S   300.00           3000.00         1000.00          1
 0.00000000E+00 0.00000000E+00 0.00000000E+00 0.00000000E+00 0.00000000E+00       2
 0.00000000E+00 0.00000000E+00 0.00000000E+00 0.00000000E+00 0.00000000E+00       3
 0.00000000E+00 0.00000000E+00 0.00000000E+00 0.00000000E+00                      4
CO(*)         C   1O  1Pt 1  I   300.00           3000.00         1000.00          1
 0.00000000E+00 0.00000000E+00 0.00000000E+00 0.00000000E+00 0.00000000E+00       2
 0.00000000E+00 0.00000000E+00 0.00000000E+00 0.00000000E+00 0.00000000E+00       3
 0.00000000E+00 0.00000000E+00 0.00000000E+00 0.00000000E+00                      4
CO2(*)        C   1O  2Pt 1  I   300.00           3000.00         1000.00          1
 0.00000000E+00 0.00000000E+00 0.00000000E+00 0.00000000E+00 0.00000000E+00       2
 0.00000000E+00 0.00000000E+00 0.00000000E+00 0.00000000E+00 0.00000000E+00       3
 0.00000000E+00 0.00000000E+00 0.00000000E+00 0.00000000E+00                      4
C(*)          C   1Pt 1      I   300.00           3000.00         1000.00          1
 0.00000000E+00 0.00000000E+00 0.00000000E+00 0.00000000E+00 0.00000000E+00       2
 0.00000000E+00 0.00000000E+00 0.00000000E+00 0.00000000E+00 0.00000000E+00       3
 0.00000000E+00 0.00000000E+00 0.00000000E+00 0.00000000E+00                      4
CH(*)         C   1H  1Pt 1  I   300.00           3000.00         1000.00          1
 0.00000000E+00 0.00000000E+00 0.00000000E+00 0.00000000E+00 0.00000000E+00       2
 0.00000000E+00 0.00000000E+00 0.00000000E+00 0.00000000E+00 0.00000000E+00       3
 0.00000000E+00 0.00000000E+00 0.00000000E+00 0.00000000E+00                      4
CH2(*)        C   1H  2Pt 1  I   300.00           3000.00         1000.00          1
```

```
0.00000000E+00 0.00000000E+00 0.00000000E+00 0.00000000E+00 0.00000000E+00    2
 0.00000000E+00 0.00000000E+00 0.00000000E+00 0.00000000E+00 0.00000000E+00    3
 0.00000000E+00 0.00000000E+00 0.00000000E+00 0.00000000E+00                   4
CH3(*)          C  1H  3Pt 1     I   300.00       3000.00       1000.00         1
 0.00000000E+00 0.00000000E+00 0.00000000E+00 0.00000000E+00 0.00000000E+00    2
 0.00000000E+00 0.00000000E+00 0.00000000E+00 0.00000000E+00 0.00000000E+00    3
 0.00000000E+00 0.00000000E+00 0.00000000E+00 0.00000000E+00                   4
CH4(*)          C  1H  4Pt 1     I   300.00       3000.00       1000.00         1
 0.00000000E+00 0.00000000E+00 0.00000000E+00 0.00000000E+00 0.00000000E+00    2
 0.00000000E+00 0.00000000E+00 0.00000000E+00 0.00000000E+00 0.00000000E+00    3
 0.00000000E+00 0.00000000E+00 0.00000000E+00 0.00000000E+00                   4
H2              H  2           G   300.00       5000.00       1000.00           1
 .299142220E+01 .700064410E-03-.563382800E-07-.923157820E-11 .158275200E-14    2
-.835033546E+03-.135510641E+01 .329812400E+01 .824944120E-03-.814301470E-06    3
-.947543430E-10 .413487200E-12-.101252100E+04-.329409400E+01                   4
O2              O  2           G   300.00       5000.00       1000.00           1
 .369757685E+01 .613519690E-03-.125884200E-06 .177528100E-10-.113643500E-14    2
-.123392966E+04 .318917125E+01 .321293600E+01 .112748610E-02-.575614990E-06    3
 .131387700E-08-.876855390E-12-.100524900E+04 .603473900E+01                   4
H2O             H  2O  1       G   300.00       5000.00       1000.00           1
 .267214569E+01 .305629290E-02-.873026070E-06 .120099600E-09-.639161790E-14    2
-.298992115E+05 .686281125E+01 .338684200E+01 .347498200E-02-.635469590E-05    3
 .696858040E-08-.250658800E-11-.302081100E+05 .259023200E+01                   4
H               H  1           G   300.00       5000.00       1000.00           1
 .250000000E+01 .000000000E+00 .000000000E+00 .000000000E+00 .000000000E+00    2
 .254716200E+05-.460117600E+00 .250000000E+01 .000000000E+00 .000000000E+00    3
 .000000000E+00 .000000000E+00 .254716200E+05-.460117600E+00                   4
OH              H  1O  1       G   300.00       5000.00       1710.00           1
 .285376040E+01 .102994334E-02-.232666477E-06 .193750704E-10-.315759847E-15    2
 .369949720E+04 .578756825E+01 .341896226E+01 .319255801E-03-.308292717E-06    3
 .364407494E-09-.100195479E-12 .345264448E+04 .254433372E+01                   4
O               O  1           G   300.00       5000.00       1000.00           1
 .254205876E+01-.275506100E-04-.310280290E-08 .455106700E-11-.436805100E-15    2
 .292307989E+05 .492030884E+01 .294642800E+01-.163816600E-02 .242103100E-05    3
-.160284300E-08 .389069610E-12 .291476400E+05 .296399500E+01                   4
CO              C  1O  1       G   300.00       5000.00       1000.00           1
 .302507617E+01 .144268900E-02-.563082720E-06 .101858100E-09-.691095110E-14    2
-.142683499E+05 .610822521E+01 .326245100E+01 .151194100E-02-.388175520E-05    3
 .558194380E-08-.247495100E-11-.143105400E+05 .484889700E+01                   4
CO2             C  1O  2       G   300.00  5000.00 1000.00                      1
 .445362582E+01 .314016800E-02-.127841100E-05 .239399610E-09-.166903300E-13    2
-.489669524E+05-.955420007E+00 .227572400E+01 .992207230E-02-.104091100E-04    3
 .686668590E-08-.211728010E-11-.483731400E+05 .101884900E+02                   4
CH4             C  1H  4       G   300.00  5000.00 1000.00                      1
 .168346564E+01 .102372400E-01-.387512820E-05 .678558490E-09-.450342310E-13    2
-.100807773E+05 .962347575E+01 .778741700E+00 .174766800E-01-.278340900E-04    3
 .304970800E-07-.122393100E-10-.982522800E+04 .137221900E+02                   4
CH              C  1H  1       G   300.00  5000.00 1000.00                      1
 .219622115E+01 .234038100E-02-.705820130E-06 .900758220E-10-.385504010E-14    2
 .708672121E+05 .917838138E+01 .320020200E+01 .207287490E-02-.513443090E-05    3
 .573388980E-08-.195553300E-11 .704525700E+05 .333158700E+01                   4
```

```
CH2            C  1H  2      G    300.00  5000.00 1000.00                        1
 .363640757E+01 .193305600E-02-.168701600E-06-.100989900E-09 .180825510E-13     2
 .453413341E+05 .215656196E+01 .376223700E+01 .115981900E-02 .248958490E-06     3
 .880083620E-09-.733243490E-12 .453679000E+05 .171257700E+01                    4
CH3            C  1H  3      G    300.00  5000.00 1000.00                        1
 .284405718E+01 .613797410E-02-.223034500E-05 .378516110E-09-.245215900E-13     2
 .164378004E+05 .545265727E+01 .243044200E+01 .111241000E-01-.168022000E-04     3
 .162182910E-07-.586495220E-11 .164237800E+05 .678979400E+01                    4
C              C  1          G    300.00  5000.00 1000.00                        1
 .249266888E+01 .479889284E-04-.724335020E-07 .374291029E-10-.487277893E-14     2
 .854512953E+05 .480150373E+01 .255423955E+01-.321537724E-03 .733792245E-06     3
-.732234889E-09 .266521446E-12 .854438832E+05 .453130848E+01                    4
N2             N  2          G    300.00  5000.00 1000.00                        1
 .292663788E+01 .148797700E-02-.568476030E-06 .100970400E-09-.675335090E-14     2
-.922795384E+03 .598054018E+01 .329867700E+01 .140823990E-02-.396322180E-05     3
 .564151480E-08-.244485400E-11-.102090000E+04 .395037200E+01                    4
N              N  1          G    300.00  5000.00 1000.00                        1
 .245026778E+01 .106614600E-03-.746533710E-07 .187965200E-10-.102598400E-14     2
 .561160257E+05 .444874779E+01 .250307100E+01-.218001810E-04 .542052910E-07     3
-.564755990E-10 .209990390E-13 .560988900E+05 .416756600E+01                    4
AR             AR 1          G    300.00  5000.00 1000.00                        1
 .312500009E+01-.140625050E-02 .937500490E-06-.156250080E-09 .000000000E+00     2
-.940687583E+03 .103823694E+01 .250000000E+01 .000000000E+00 .000000000E+00     3
 .000000000E+00 .000000000E+00-.745375100E+03 .436600100E+01                    4
HE             HE 1          G    300.00  5000.00 1000.00                        1
 .250000000E+01 .000000000E+00 .000000000E+00 .000000000E+00 .000000000E+00     2
-.745375000E+03 .928723974E+00 .250000000E+01 .000000000E+00 .000000000E+00     3
 .000000000E+00 .000000000E+00-.745375000E+03 .928723974E+00                    4
END
```

Upon applying the kinetic interpreter to the thermodynamic data in Table 17, the species entropy coeffiecients, specif heat coefficients and enthalpy coefficients were found to be as presented in Tables 18, 19 and 20.

Table 18: Species entropy coefficients

```
--------------------------------------------------------------------------------------------------------------------------------
            ENTROPY COEFFICIENTS

   S/R = A*lnT + B*T + C*T^2 + D*T^3 + E*T^4 + F  [-]

  Species          S(298K)[J/kmol/K] S(1000K)[J/kmol/K]   LT-HT        A(LT)        B(LT)          C(LT)          D(LT)          E(LT)          F(LT)          A(HT)          B
(HT)     C(HT)        D(HT)           E(HT)           F(HT)
--------------------------------------------------------------------------------------------------------------------------------

  1. H2            1.305810e+05  1.661073e+05  1.000000e+03  3.298124e+00   8.249441e-04   -4.071507e-07   -3.158478e-11   1.033718e-13   -3.294094e+00   2.991422e+00
7.000644e-04   -2.816914e-08   -3.077193e-12   3.956880e-16   -1.355106e+00
  2. O2           2.050299e+05  2.435085e+05  1.000000e+03  3.212936e+00   1.127486e-03   -2.878075e-07   4.379590e-10   -2.192138e-13   6.034739e+00   3.697577e+00
6.135197e-04   -6.294210e-08   5.917603e-12   -2.841088e-16   3.189171e+00
  3. H2O          1.886992e+05  2.326349e+05  1.000000e+03  3.386842e+00   3.474982e-03   -3.177348e-06   2.322860e-09   -6.266470e-13   2.590232e+00   2.672146e+00
3.056293e-03   -4.365130e-07   4.003320e-11   -1.597904e-15   6.862811e+00
  4. O            1.609349e+05  1.866807e+05  1.000000e+03  2.946428e+00   -1.638166e-03   1.210515e-06   -5.342810e-10   9.726740e-14   2.963995e+00   2.542059e+00
-2.755061e-05   -1.551401e-09   1.517022e-12   -1.092013e-16   4.920309e+00
  5. OH           1.838074e+05  2.196948e+05  1.710000e+03  3.418962e+00   3.192558e-04   -1.541464e-07   1.214692e-10   -2.504887e-14   2.544334e+00   2.853760e+00
1.029943e-03   -1.163332e-07   6.458357e-12   -7.893996e-17   5.787568e+00
  6. H            1.145950e+05  1.397600e+05  1.000000e+03  2.500000e+00   0.000000e+00   0.000000e+00   0.000000e+00   0.000000e+00   -4.601176e-01   2.500000e+00
0.000000e+00   0.000000e+00   0.000000e+00   0.000000e+00   -4.601176e-01
  7. CO           1.975345e+05  2.344519e+05  1.000000e+03  3.262451e+00   1.511941e-03   -1.940878e-06   1.860648e-09   -6.187377e-13   4.848897e+00   3.025076e+00
1.442689e-03   -2.815414e-07   3.395270e-11   -1.727738e-15   6.108225e+00
  8. CO2          2.137190e+05  2.692699e+05  1.000000e+03  2.275724e+00   9.922072e-03   -5.204555e-06   2.288895e-09   -5.293200e-13   1.018849e+01   4.453626e+00
3.140168e-03   -6.392055e-07   7.979987e-11   -4.172582e-15   -9.554200e-01
  9. CH4          1.860428e+05  2.474970e+05  1.000000e+03  7.787417e-01   1.747668e-02   -1.391705e-05   1.016569e-08   -3.059828e-12   1.372219e+01   1.683466e+00
1.023724e-02   -1.937564e-06   2.261862e-10   -1.125856e-14   9.623476e+00
  10. CH          1.829173e+05  2.192180e+05  1.000000e+03  3.200202e+00   2.072875e-03   -2.567215e-06   1.911297e-09   -4.888832e-13   3.331587e+00   2.196221e+00
2.340381e-03   -3.529101e-07   3.002527e-11   -9.637600e-16   9.178381e+00
  11. CH2         1.954679e+05  2.419137e+05  1.000000e+03  3.762237e+00   1.159819e-03   1.244792e-07   2.933612e-10   -1.833109e-13   1.712577e+00   3.636408e+00
1.933056e-03   -8.435080e-08   4.520638e-15   2.156562e+00
  12. CH3         1.940320e+05  2.514422e+05  1.000000e+03  2.430442e+00   1.112410e-02   -8.401100e-06   5.406097e-09   -1.466238e-12   6.789794e+00   2.844057e+00
6.137974e-03   -1.115172e-06   1.261720e-10   -6.130398e-15   5.452657e+00
  13. C           1.580902e+05  1.832780e+05  1.000000e+03  2.554240e+00   -3.215377e-04   3.668961e-07   -2.440783e-10   6.663036e-14   4.531308e+00   2.492669e+00
4.798893e-05   -3.621675e-08   1.247637e-11   -1.218195e-15   4.801504e+00
  14. N           1.531794e+05  1.783443e+05  1.000000e+03  2.503071e+00   -2.180018e-05   2.710265e-08   -1.882520e-11   5.249760e-15   4.167566e+00   2.450268e+00
1.066146e-04   -3.732669e-08   6.265507e-12   -2.564960e-16   4.448748e+00
  15. N2          1.914976e+05  2.280885e+05  1.000000e+03  3.298677e+00   1.408240e-03   -1.981611e-06   1.880505e-09   -6.112135e-13   3.950372e+00   2.926638e+00
1.487977e-03   -2.842380e-07   3.365680e-11   -1.688338e-15   5.980540e+00
  16. Ar          1.547216e+05  1.798866e+05  1.000000e+03  2.500000e+00   0.000000e+00   0.000000e+00   0.000000e+00   0.000000e+00   4.366001e+00   3.125000e+00
-1.406250e-03   4.687502e-07   -5.208336e-11   0.000000e+00   1.038237e+00
  17. He          1.261425e+05  1.513075e+05  1.000000e+03  2.500000e+00   0.000000e+00   0.000000e+00   0.000000e+00   0.000000e+00   9.287240e-01   2.500000e+00
0.000000e+00   0.000000e+00   0.000000e+00   0.000000e+00   9.287240e-01
```

Table 19: Species enthalpy coefficients

```
--------------------------------------------------------------------------------------------------------------------------------
            ENTHALPY COEFFICIENTS

   H/(RT) = A + B*T + C*T^2 + D*T^3 + E*T^4 + F/T  [-]

  Species       H(298K)[J/kmol]  H(1000K)[J/kmol]   LT-HT        A(LT)        B(LT)          C(LT)          D(LT)          E(LT)          F(LT)          A(HT)          B
(HT)     C(HT)        D(HT)           E(HT)           F(HT)
--------------------------------------------------------------------------------------------------------------------------------

  1. H2           -1.882892e+03  2.066684e+07  1.000000e+03  3.298124e+00   4.124721e-04   -2.714338e-07   -2.368859e-11   8.269744e-14   -1.012521e+03   2.991422e+00
3.500322e-04   -1.877943e-08   -2.307895e-12   3.165504e-16   -8.350335e+02
  2. O2           -5.244966e+03  2.272057e+07  1.000000e+03  3.212936e+00   5.637431e-04   -1.918717e-07   3.284693e-10   -1.753711e-13   -1.005249e+03   3.697577e+00
3.067598e-04   -4.196140e-08   4.438203e-12   -2.272870e-16   -1.233930e+03
  3. H2O          -2.418513e+08  -2.158533e+08  1.000000e+03  3.386842e+00   1.737491e-03   -2.118232e-06   1.742145e-09   -5.013176e-13   -3.020811e+04   2.672146e+00
1.528146e-03   -2.910087e-07   3.002490e-11   -1.278324e-15   -2.989921e+04
  4. O            2.491954e+08  2.640598e+08  1.000000e+03  2.946428e+00   -8.190830e-04   8.070103e-07   -4.007107e-10   7.781392e-14   2.914764e+04   2.542059e+00
-1.377531e-05   -1.034268e-09   1.137767e-12   -8.736102e-17   2.923080e+04
  5. OH           3.727891e+07  5.819735e+07  1.710000e+03  3.418962e+00   1.596279e-04   -1.027642e-07   9.110187e-11   -2.003910e-14   3.452644e+03   2.853760e+00
5.149717e-04   -7.755549e-08   4.843768e-12   -6.315197e-17   3.699497e+03
  6. H            2.179771e+08  2.325690e+08  1.000000e+03  2.500000e+00   0.000000e+00   0.000000e+00   0.000000e+00   0.000000e+00   2.547162e+04   2.500000e+00
0.000000e+00   0.000000e+00   0.000000e+00   0.000000e+00   2.547162e+04
  7. CO           -1.105457e+08  -8.884453e+07  1.000000e+03  3.262451e+00   7.559705e-04   -1.293918e-06   1.395486e-09   -4.949902e-13   -1.431054e+04   3.025076e+00
7.213445e-04   -1.876942e-07   2.546452e-11   -1.382190e-15   -1.426835e+04
  8. CO2          -3.935542e+08  -3.601232e+08  1.000000e+03  2.275724e+00   4.961036e-03   -3.469703e-06   1.716671e-09   -4.234560e-13   -4.837314e+04   4.453626e+00
1.570084e-03   -4.261370e-07   5.984990e-11   -3.338066e-15   -4.896695e+04
  9. CH4          -7.489933e+07  -3.666485e+07  1.000000e+03  7.787417e-01   8.738340e-03   -9.278030e-06   7.624270e-09   -2.447862e-12   -9.825228e+03   1.683466e+00
5.118620e-03   -1.291709e-06   1.696396e-10   -9.006846e-15   -1.008078e+04
  10. CH          5.941794e+08  6.154373e+08  1.000000e+03  3.200202e+00   1.036437e-03   -1.711477e-06   1.433472e-09   -3.911066e-13   7.045257e+04   2.196221e+00
1.170190e-03   -2.352734e-07   2.251896e-11   -7.710080e-16   7.086721e+04
  11. CH2         3.869894e+08  4.146123e+08  1.000000e+03  3.762237e+00   5.799095e-04   8.298616e-08   2.200209e-10   -1.466487e-13   4.536790e+04   3.636408e+00
9.665280e-04   -5.623387e-08   -2.524747e-11   3.616510e-15   4.534133e+04
  12. CH3         1.456942e+08  1.803999e+08  1.000000e+03  2.430442e+00   5.562050e-03   -5.600733e-06   4.054573e-09   -1.172990e-12   1.642378e+04   2.844057e+00
3.068987e-03   -7.434483e-07   9.462903e-11   -4.904318e-15   1.643780e+04
  13. C           7.166727e+08  7.312752e+08  1.000000e+03  2.554240e+00   -1.607689e-04   2.445974e-07   -1.830587e-10   5.330429e-14   8.544388e+04   2.492669e+00
2.399446e-05   -2.414450e-08   9.357276e-12   -9.745558e-16   8.545130e+04
  14. N           4.726291e+08  4.872209e+08  1.000000e+03  2.503071e+00   -1.090009e-05   1.806843e-08   -1.411890e-11   4.199808e-15   5.609889e+04   2.450268e+00
5.330730e-05   -2.488446e-08   4.699130e-12   -2.051968e-16   5.611603e+04
  15. N2          -2.931729e+03  2.146986e+07  1.000000e+03  3.298677e+00   7.041200e-04   -1.321074e-06   1.410379e-09   -4.889708e-13   -1.020900e+03   2.926638e+00
7.439885e-04   -1.894920e-07   2.524260e-11   -1.350670e-15   -9.227954e+02
  16. Ar          -3.118755e+03  1.458876e+07  1.000000e+03  2.500000e+00   0.000000e+00   0.000000e+00   0.000000e+00   0.000000e+00   -7.453751e+02   3.125000e+00
-7.031252e-04   3.125002e-07   -3.906252e-11   0.000000e+00   -9.406876e+02
  17. He          -3.117923e+03  1.458876e+07  1.000000e+03  2.500000e+00   0.000000e+00   0.000000e+00   0.000000e+00   0.000000e+00   -7.453750e+02   2.500000e+00
0.000000e+00   0.000000e+00   0.000000e+00   0.000000e+00   -7.453750e+02
```

Table 20: Species specific heat coefficients

```
          SPECIFIC HEAT COEFFICIENTS

     Cp = A + B*T + C*T^2 + D*T^3 + E*T^4  [J/kg/K]
```

Species	Cp(298K)	Cp(1000K)	LT-HT	A(LT)	B(LT)	C(LT)	D(LT)	E(LT)	A(HT)	B(HT)	C(HT)	D(HT)	E(HT)
1. H2	1.432099e+04	1.496067e+04	1.000000e+03	1.360225e+04	3.402265e+00	-3.358372e-03	-3.907894e-07	1.705319e-09	1.360225e+04	3.402265e+00	-3.358372e-03	-3.907894e-07	1.705319e-09
2. O2	9.161200e+02	1.091817e+03	1.000000e+03	8.348595e+02	2.929696e-01	-1.495696e-04	3.414020e-07	-2.278449e-10	8.348595e+02	2.929696e-01	-1.495696e-04	3.414020e-07	-2.278449e-10
3. H2O	1.856601e+03	2.293398e+03	1.000000e+03	1.563129e+03	1.603808e+00	-2.932883e-03	3.216209e-06	-1.156865e-09	1.563129e+03	1.603808e+00	-2.932883e-03	3.216209e-06	-1.156865e-09
4. O	1.368804e+03	1.307281e+03	1.000000e+03	1.531218e+03	-8.513325e-01	1.258177e-03	-8.329757e-07	2.021942e-10	1.531218e+03	-8.513325e-01	1.258177e-03	-8.329757e-07	2.021942e-10
5. OH	1.708934e+03	1.806007e+03	1.710000e+03	1.671478e+03	1.560793e-01	-1.507196e-04	1.781533e-07	-4.898404e-11	1.671478e+03	1.560793e-01	-1.507196e-04	1.781533e-07	-4.898404e-11
6. H	2.062119e+04	2.062119e+04	1.000000e+03	2.062119e+04	0.000000e+00	0.000000e+00	0.000000e+00	0.000000e+00	2.062119e+04	0.000000e+00	0.000000e+00	0.000000e+00	0.000000e+00
7. CO	1.037896e+03	1.187246e+03	1.000000e+03	9.684229e+02	4.488032e-01	-1.152257e-03	1.656939e-06	-7.346621e-10	9.684229e+02	4.488032e-01	-1.152257e-03	1.656939e-06	-7.346621e-10
8. CO2	8.450963e+02	1.235218e+03	1.000000e+03	4.299444e+02	1.874541e+00	-1.966556e-03	1.297298e-06	-4.000101e-10	4.299444e+02	1.874541e+00	-1.966556e-03	1.297298e-06	-4.000101e-10
9. CH4	2.189941e+03	4.498040e+03	1.000000e+03	4.035915e+02	9.057483e+00	-1.442533e-02	1.580545e-05	-6.343158e-09	4.035915e+02	9.057483e+00	-1.442533e-02	1.580545e-05	-6.343158e-09
10. CH	2.234143e+03	2.501557e+03	1.000000e+03	2.043779e+03	1.323822e+00	-3.279056e-03	3.661895e-06	-1.248883e-09	2.043779e+03	1.323822e+00	-3.279056e-03	3.661895e-06	-1.248883e-09
11. CH2	2.458406e+03	3.152142e+03	1.000000e+03	2.230055e+03	6.874792e-01	1.475694e-04	5.216669e-07	-4.346279e-10	2.230055e+03	6.874792e-01	1.475694e-04	5.216669e-07	-4.346279e-10
12. CH3	2.563887e+03	3.929492e+03	1.000000e+03	1.344052e+03	6.151707e+00	-9.291736e-03	8.968831e-06	-3.243360e-09	1.344052e+03	6.151707e+00	-9.291736e-03	8.968831e-06	-3.243360e-09
13. C	1.734961e+03	1.731134e+03	1.000000e+03	1.768140e+03	-2.225804e-01	5.079584e-04	-5.068803e-07	1.844961e-10	1.768140e+03	-2.225804e-01	5.079584e-04	-5.068803e-07	1.844961e-10
14. N	1.484019e+03	1.483983e+03	1.000000e+03	1.485806e+03	-1.294044e-02	3.217590e-05	-3.352354e-08	1.246489e-11	1.485806e+03	-1.294044e-02	3.217590e-05	-3.352354e-08	1.246489e-11
15. N2	1.037719e+03	1.169485e+03	1.000000e+03	9.790364e+02	4.179609e-01	-1.176271e-03	1.674383e-06	-7.256245e-10	9.790364e+02	4.179609e-01	-1.176271e-03	1.674383e-06	-7.256245e-10
16. Ar	5.203303e+02	5.203303e+02	1.000000e+03	5.203303e+02	0.000000e+00	0.000000e+00	0.000000e+00	0.000000e+00	5.203303e+02	0.000000e+00	0.000000e+00	0.000000e+00	0.000000e+00
17. He	5.192645e+03	5.192645e+03	1.000000e+03	5.192645e+03	0.000000e+00	0.000000e+00	0.000000e+00	0.000000e+00	5.192645e+03	0.000000e+00	0.000000e+00	0.000000e+00	0.000000e+00

Table 21: Gas-phase reaction mechanism and kinetic data (Quiceno et al., 2006)

Reaction	A (mol, cm, s)	b	Ea (kJ/mol)
$O_2 + H = OH + O$	9.756×10^{13}	0.0	62.10
$H_2 + OH = H_2O + H$	1.000×10^8	1.600	13.80
$H + O_2 + M_3 = HO_2 + M_3$	2.100×10^{18}	0.800	0.0
$HO_2 + H = OH + OH$	1.500×10^{14}	0.0	3.80
$HO_2 + H = H_2 + O_2$	3.000×10^{13}	0.0	4.00
$HO_2 + H = H_2O + O$	3.000×10^{13}	0.0	7.20
$HO_2 + OH = H_2O + O_2$	6.000×10^{13}	0.0	0.0
$HO_2 + HO_2 = H_2O_2 + O_{2a}$	4.220×10^{14}	0.0	50.14
$HO_2 + HO_2 = H_2O_2 + O_{2a}$	1.320×10^{11}	0.0	6.82
$H_2O_2 + OH = H_2O + HO_2$	5.400×10^{12}	0.0	4.20
$OH + OH + M_1 = H_2O_2 + M_1$	7.230×10^{13}	0.370	0.0
Low	5.530×10^{19}	0.760	0.0
Troe	0.50, 0.0	0.0	0.0
$CO + OH = CO_2 + H$	4.760×10^7	1.230	0.29
$CO + HO_2 = CO_2 + OH$	1.500×10^{14}	0.0	98.70
$CO + CH_3O = CO_2 + CH_3$	1.580×10^{13}	0.0	49.40
$CHO + M_1 = CO + H + M_1$	4.500×10^{14}	0.0	66.00
$CHO + O_2 = CO + HO_2$	2.400×10^{12}	0.0	0.0
$CHO + O_2 = CO_2 + OH$	0.600×10^{12}	0.0	0.0
$CHO + HO_2 = OH + CO_2 + H$	3.000×10^{13}	0.0	0.0
$CH_2O + H = CHO + H_2$	1.270×10^8	1.62	9.00
$CH_2O + O = CHO + OH$	4.150×10^{11}	0.57	11.60
$CH_2O + OH = CHO + H_2O$	3.400×10^9	1.18	1.87
$CH_2O + HO_2 = CHO + H_2O_2$	3.000×10^{12}	0.0	54.7
$CH_2O + CH_3 = CHO + CH_4$	7.830×10^8	6.1	8.20
$CH_2O + O_2 = CHO + HO_2$	6.000×10^{13}	0.0	70.70
$CH_3 + O_2 = CH_2O + OH$	3.300×10^{11}	0.0	37.40
$CH_3 + HO_2 = CH_3O + OH$	1.800×10^{13}	0.0	0.0
$CH_3 + HO_2 = CH_4 + O_2$	3.600×10^{12}	0.0	0.0
$CH_3 + CH_3 + M_1 = C_2H_6 + M_1$	3.610×10^{13}	0.0	0.0
Low	3.630×10^{41}	7.000	11.60
Troe	0.620, 73.0	1180.0	0.0
$CH_3O + M_1 = CH_2O + H + M_1$	5.000×10^{13}	0.0	105.0
$CH_3O + O_2 = CH_2O + HO_2$	3.000×10^{10}	0.0	7.3
$CH_2O + CH_3O = CH_3OH + CHO$	1.150×10^{11}	0.0	5.2
$CH_3 + O_2 ! O + CH_3O$	0.600×10^{14}	0.0	131.0
$CH_2OH + O_2 = CH_2O + HO_2$	1.570×10^{15}	0.0	0.0
$CH_3 + O_2 + M_1 = CH_3O_2 + M_1$	7.800×10^8	1.2	0.0
Low	1.650×10^{26}	3.30	0.0
Troe	0.495, 2325.5	10.0	0.0
$CH_3O_2 + CH_2O = CH_3O_2H + CHO$	2.000×10^{12}	0.0	48.74
$CH_3O_2 + CH_3 = CH_3O + CH_3O$	2.400×10^{13}	0.0	0.0
$CH_3O_2 + HO_2 = CH_3O_2H + O_2$	2.400×10^{11}	0.0	6.6
$CH_4 + H = H_2 + CH_3$	1.330×10^4	3.00	33.60
$CH_4 + O = OH + CH_3$	6.923×10^8	1.56	35.50
$CH_4 + OH = H_2O + CH_3$	1.000×10^7	1.83	11.60
$CH_4 + HO_2 = H_2O_2 + CH_3$	1.100×10^{13}	0.0	103.10
$CH_4 + CH_3O = CH_3OH + CH_3$	4.300×10^{12}	0.0	42.00
$CH_4 + CH_3O_2 = CH_3O_2H + CH_3$	1.8100×10^{11}	0.0	77.80
$CH_3OH + H = CH_2OH + H_2$	1.640×10^{07}	2.0	18.89
$CH_3OH + OH = CH_2OH + H_2O$	1.440×10^{06}	2.0	3.5
$CH_3OH + OH = CH_3O + H_2O$	1.640×10^{13}	0.0	7.1
$CH_3OH + HO_2 = CH_2OH + H_2O_2$	9.640×10^{10}	0.0	52.58
$CH_3OH + CH_3 = CH_4 + CH_2OH$	9.000×10^{12}	0.0	41.1
$CH_3O_2H = CH_3O + OH$	6.000×10^{14}	0.0	177.10
$CH_3O_2 + H_2O_2 = CH_3O_2H + HO_2$	2.400×10^{12}	0.0	41.8
$CH_3 + CO + M_1 = CH_3CO + M_1$	5.058×10^{11}	0.0	28.77
$C_2H_4 + CH_3O = OXIRAN + CH_3$	1.000×10^{11}	0.0	60.61
$CH_3CHO + OH = CH_3CHO + H_2O$	2.300×10^{10}	0.73	4.6
$CH_3CHO + HO_2 = CH_3CO + H_2O_2$	3.100×10^{12}	0.0	50.0
$CH_3CHO + CH_3 = CH_3CO + CH_4$	2.050×10^{06}	5.6	10.3

Table 21 continued

Reaction	A (mol, cm, s)	b	Ea (kJ/mol
$CH_3CO + O = CO_2 + CH_3$	4.818×10^{23}	0.0	0.0
$C_2H_4 + H + M_1 = C_2H_5 + M_1$	2.000×10^{09}	1.28	5.4
Low	16.980×10^{18}	0.0	3.2
Troe	0.760, 40.0	1025.0	0.0
$C_2H_5 + M_1 = C_2H_4 + H + M_1$	8.200×10^{13}	0.0	166.8
Low	3.400×10^{17}	0.0	139.6
Troe	0.750, 97.0	1379.0	0.0
$C_2H_6 + H = C_2H_5 + H_2$	1.150×10^{09}	1.9	31.1
$C_2H_6 + OH = C_2H_5 + H_2O$	6.200×10^{06}	2.0	3.6
$C_2H_6 + HO_2 = C_2H_5 + H_2O_2$	1.333×10^{13}	0.0	85.6
$C_2H_6 + CH_3 = C_2H_5 + CH_4$	1.000×10^{13}	0.0	56.54
$C_2H_6 + CH_3O = CH_3OH + C_2H_5$	2.409×10^{11}	0.0	29.68
$OXIRAN + H = C_2H_3O + H_2$	8.010×10^{13}	0.0	40.50
$OXIRAN + OH = C_2H_3O + H2O$	6.625×10^{12}	0.0	12.14
$OXIRAN + CH_3 = C_2H_3O + CH_4$	1.072×10^{12}	0.0	49.47
$OXIRAN = CH_3CHO$	6.310×10^{13}	0.0	247.71
$OXIRAN = CH_4 + CO$	1.210×10^{13}	0.0	239.46
$OXIRAN = CH_3 + CHO$	3.630×10^{13}	0.0	239.46
$C_2H_5 + M_1 + O_2 = C_2H_5O_2 + M_1$	2.002×10^{42}	-10.3	25.44
$C_2H_5O_2 \rightarrow DC_2OOH$	2.080×10^{12}	0.0	138.0
$DC_2OOH \rightarrow C_2H_5O_2$	8.500×10^{09}	-0.09	69.5
$DC_2OOH \rightarrow OXIRAN + OH$	1.300×10^{10}	0.0	65.5
$C_2H_5O_2 + HO_2 = C_2H_5OOH + O_2$	9.697×10^{10}	0.0	-10.47
$C_2H_5O_2 + CH2O \rightarrow C_2H_5OOH + CHO$	1.000×10^{12}	0.0	42.0
$C_2H_5OOH + CHO \rightarrow C_2H_5O_2 + CH_2O$	2.700×10^{06}	1.0	0.688